THÈSE

UNIVERSITE DE PAU ET DES PAYS DE L'ADOUR
École doctorale des Sciences Exactes et leurs Applications

Soutenue le 9/12/2020

par **Julen Vadillo Del Ser**

pour obtenir le grade de docteur
de l'Université de Pau et des Pays de l'Adour
Spécialité : CHIMIE. Spécialité Polymères

Design, synthesis and characterization of inks based in waterborne polyurethane urea dispersions suitable for direct ink writing 3D-printing

MEMBRES DU JURY

RAPPORTEURS

• Philippe POULIN	Directeur de Recherche CNRS / CRPP, Bordeaux
• Rafael Antonio BALART GIMENO	Professeur / High Polytechnic School, Valence

EXAMINATEURS

• Corinne NARDIN	Professeur / Université de Pau et des Pays de l'Adour, Pau
• Frédéric PERUCH	Directeur de recherche / LCPO, Bordeaux

DIRECTEURS

• Christophe DERAIL	Professeur / Université de Pau et des Pays de l'Adour, Pau
• Arantxa ECEIZA	Professeur / University of Basque Country, San Sebastian

UNIVERSITÉ DE PAU ET DES PAYS DE L'ADOUR

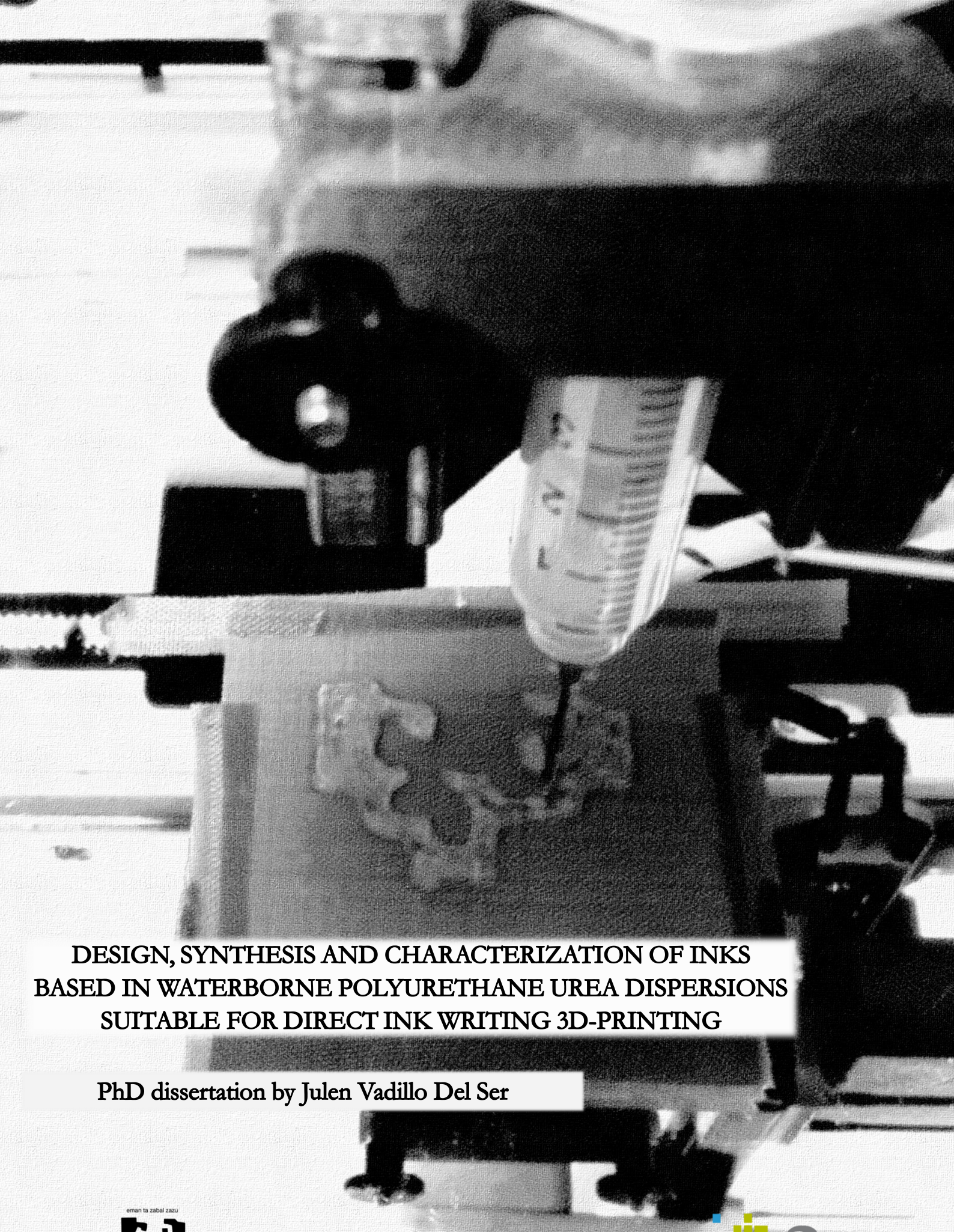

DESIGN, SYNTHESIS AND CHARACTERIZATION OF INKS BASED IN WATERBORNE POLYURETHANE UREA DISPERSIONS SUITABLE FOR DIRECT INK WRITING 3D-PRINTING

PhD dissertation by Julen Vadillo Del Ser

eman ta zabal zazu
Universidad del País Vasco
Euskal Herriko Unibertsitatea

Université de Pau et des Pays de l'Adour

Design, synthesis and characterization of inks based in waterborne polyurethane urea dispersions suitable for direct ink writing 3D-printing

PhD dissertation presented by

JULEN VADILLO DEL SER

in fulfilment of the requirements to obtain

the degree of doctor in

Renewable materials engineering by the University of Basque Country (UPV/EHU)

and

Chemistry specialized in polymers by the Université de Pau et des Pays de l'Adour (UPPA)

Under the supervision of

Prof. Arantxa Eceiza

Prof. Christophe Derail

ACKNOWLEDGEMENTS

This manuscript is the result of three years of work. What I am sure of is that this work has only been made possible by the help of many people. Thus, I would like to use these pages to thank to these people properly.

Firstly, I would like to express my earnest gratitude to my supervisors, Dr. Arantxa Eceiza and Dr. Christophe Derail for giving me the opportunity to work with them. I only have find nothing but good advices, constructive feedback and what I consider more important, confidence in my work, which provided me a very comfortable atmosphere to work.

Furthermore, I would like to thank to the University of Pau et des Pays de l'Adour (UPPA) and the University of Basque country (UPV/EHU) for making possible this thesis in a cotutelle framework. Additionally, thanks to the UPPA for the financial assistance granted to carry out this doctoral thesis.

I would also like to thank the General Services (SGIKER) of the UPV/EHU for the technical support provided these three years. Specially I would like to thank to Dr. Loli Martin, who has always been there, ensuring that everything is going fine in the lab and willing to help and provide technical assistance.

Moreover, I would like to express my gratitude to my colleagues of the 'Materials + Technologies' Group (GMT) of the Department of Chemical and Environmental Engineering (UPV/EHU) for their support during all the thesis. Specially to Dr. Maria Angeles Corcuera, who in her last year prior to retirement has always been willing to help. I have been always very comfortable working with all the people in the lab, with the people who was here when I started with the PhD and are not now in the lab, but also with the new colleagues who have arrived later. Thanks to all of you sincerely. Specially I would like to thank to Izaskun Larraza for her support. Our work has been gone in parallel and I have always had your help. Also I want to thank to Olatz Guaresti for her support in the bad days and good advices. Additionally, I would like to extend my thanks to the personal of the other research groups of the Faculty of Engineering of Gipuzkoa for contributing to a good working atmosphere. Specially I would like to thank to Amaia Morales and Fabio Hernandez for their friendship, support and for been there always in good but also in bad times.

Regarding my period in UPPA, firstly I would like to thank to all the personal of the Institut des Sciences Analytiques et de Physico-Chimie pour l'Environnement et les Matériaux (IPREM) for they support and help during my time in France. I would like to express my gratitude to Anthony Laffore for his support and technical help of the use of the rheometer and to Virginie Pellerin for her support with the SEM and AFM. My period in UPPA would be more difficult without the presence of Laia, Garbiñe and specially Laura. Thanks to all of you for easing my integration in Pau. Additionally, thanks to Dr. Maud Save for her good advices and positive feedback specially the first year.

In a more personal way I would like to thank to my friends for always been there. Probably without knowing anything about my work you have contribute a lot being always there after a bad day, always willing to listen. Thanks for all of you. Specially I would like to thank to Amaia Martinez for her friendship and for always been there. Additionally, I would like to thank to Andrea, who has suffered me in the last months being always patience and positive with my work.

Finally, I would like to thank to my family for their unconditional support and for always been interested in my work. Specially to my father, mother and my brother Jon, thanks for always been there and support me always, love you.

In memory of Aritz,

Your memory helps me to keep on going

SUMMARY

A series of waterborne polyurethane urea dispersions were prepared to study their viability as inks for direct ink writing 3D-printing. In this context, waterborne polyurethane urea dispersions were successfully synthesized using a hydrophilic polyethylene glycol (PEG) and a hydrophobic polycaprolactone (PCL) as soft segment to ease the physical gelation of the inks. The PCL/PEG ratio as well as the molecular mass of the PEG has been modified and the resulting dispersions, as well as the films prepared from the dispersions, were characterized from the physicochemical, mechanical, thermomechanical and morphological viewpoints to select the better formulation that fulfils with the required end-use properties, particularly for 3D-printing process. Once the selection of the composition of the waterborne polyurethane urea was stablished, inks with different solid content were prepared, analysed by means of rheology and subsequently printed so as to establish relationships between the rheological behaviour and the 3D-printing performances.

To pilot the rheological behaviour and the printing performances, cellulose nanocrystals were used as viscosity modulator. Different cellulose contents were added to the waterborne polyurethane urea ink using two different methods called the *in situ* and the *ex situ* methods which differ in the moment of the addition of the nanoentities. The composites prepared from both methods were analysed from the rheological viewpoint and printed in the aim to select the best compositions, as well as to compare both incorporation methods. Additionally, the physicochemical, mechanical and thermomechanical properties of the printed pieces were studied to ensure the successful reinforcement of the cellulose nanocrystals into the composites. It was seen that the different addition methods resulted in different disposition of the cellulose nanocrystals leading to the obtain of nanocomposites presenting different rheological, mechanical and thermomechanical properties.

Two potential applications were studied to demonstrate their viability. In the first one, shape customized scaffolds were prepared *via* 3D-printing and freeze drying using a previously developed waterborne polyurethane urea ink with *in situ* addition of different contents of cellulose nanocrystals, as well as crosslinking by immersion in $CaCl_2$ before freeze drying. The morphology, mechanical and physicochemical properties of the prepared scaffolds were evaluated and tested as an absorption material against cationic methylene blue dye presenting an interesting absorption capacity. For the second application, inks based on a waterborne

polyurethane urea with *Salvia* extracts incorporated by *in situ* method and different contents of *ex situ* added cellulose nanocrystals were developed in order to prepare scaffolds with antimicrobial properties. The antimicrobial activity of the scaffolds was tested successfully against Gram positive *Staphylococcus aureus* and Gram negative *Escherichia coli*. Additionally, the influence of the inclusions of *Salvia* extracts on the rheological properties of the inks and the properties of the dispersion were studied.

RESUME

Une série de dispersions de polyuréthane urée en phase aqueuse ont été préparées pour étudier leur utilisation comme encres pour l'impression 3D par écriture directe. Dans ce contexte, ces dispersions aqueuses de polyuréthane urée ont été synthétisées avec succès en utilisant un polyéthylène glycol hydrophile (PEG) et un polycaprolactone hydrophobe (PCL) comme segment mou pour faciliter la gélification physique des encres. Le rapport PCL/PEG ainsi que la masse molaire du PEG ont été modifiés et les dispersions résultantes, ainsi que les films préparés à partir de celles-ci, ont été caractérisés du point de vue physico-chimique, mécanique, thermomécanique et morphologique afin de sélectionner la meilleure formulation répondant aux propriétés requises pour l'utilisation finale, en particulier pour le processus d'impression 3D. Une fois le choix de la composition en phase aqueuse arrêté, des encres avec différents taux de solides ont été préparées, analysées au moyen de la rhéologie et ensuite imprimées afin d'établir les relations entre le comportement rhéologique et les performances d'impression 3D.

Pour adapter le comportement rhéologique et les performances d'impression, des nanocristaux de cellulose ont été utilisés comme modulateur de viscosité. Différentes teneurs de nanocristaux ont été ajoutées à l'encre polyuréthane en utilisant deux méthodes différentes dites in situ et ex situ, qui diffèrent par le moment de l'ajout des nanocharges durant la préparation. Les composites préparés à partir des deux méthodes ont été analysés du point de vue rhéologique et imprimés dans le but de sélectionner les meilleures compositions, ainsi que de comparer les deux méthodes d'incorporation. En outre, les propriétés physico-chimiques, mécaniques et thermomécaniques des pièces imprimées ont été étudiées pour mesurer l'efficacité du renforcement des nanocristaux de cellulose. Il a été constaté que les différentes méthodes d'addition ont entraîné une dispersion différente des nanocristaux de cellulose, ce qui a permis d'obtenir des nanocomposites présentant des propriétés rhéologiques, mécaniques et thermomécaniques différentes.

Deux applications potentielles ont été étudiées pour démontrer leur capacité finale. Dans la première, des pièces de forme personnalisée ont été préparées par impression 3D suivi d'une lyophilisation à l'aide d'une encre polyuréthane urée aqueuse préalablement mise au point, avec addition *in situ* de différentes teneurs en nanocristaux de cellulose, ainsi qu'une réticulation par immersion dans du $CaCl_2$ avant lyophilisation. La morphologie, les propriétés

mécaniques et physico-chimiques des pièces préparées ont été évaluées et nous avons également démontré leur capacité comme matériau d'absorption en utilisant le marqueur bleu de méthylène cationique. Pour la seconde application, les encres additionnées d'extraits de *sauge* par méthode *in situ* et différentes teneurs en nanocristaux de cellulose ajoutés *ex situ* ont été développées afin de préparer des pièces à propriété antimicrobienne. L'activité antimicrobienne des pièces a été testée avec succès contre Staphylococcus aureus à Gram positif et Escherichia coli à Gram négatif. En outre, l'influence des inclusions d'extraits de sauge sur les propriétés rhéologiques des encres et les propriétés de la dispersion ont été étudiées.

INDEX

INTRODUCTION.

CHAPTER 1. State of art

CHAPTER 2. Materials and methods

INTRODUCTION

INTRODUCTION

Motivation

The demand for the development of new fabrication techniques, which can satisfy the actual demand of advanced materials for multiple applications, is one of today's big challenges. Not only those new fabrication techniques must be able to process new materials successfully but also they have to respect the increasing environmental awareness, which represent a boost on the development of more environmentally friendly manufacturing techniques. In the last years, the 3D-printing, also known as additive manufacturing, has gained increasing interest due to the possibility of the direct production of customized complex components from a wide variety of materials such as polymers, metals and ceramics among others. Is by definition a versatile layer-by-layer fabrication technology of 3D objects through progressive adding of materials directly guided by predefined digital models. It comprises a number of fabrication techniques which can be used depending the raw material and the application field so as to obtain the desirable end use material.

One example of this type of more environmental friendly fabrication technique is that of the direct ink writing 3D-printing (DIW 3D-printing). This advanced manufacturing technique represents an interesting alternative to other 3D-printing based conventional techniques due to the possibility of obtaining complex 3D designs using aqueous based viscous systems, resulting into an eco-friendlier fabrication technique, representing an approach more in line with the actual environmental awareness policies. In this context, the development of suitable inks for this novel technology can be considered as an important challenge, since the printing process requires inks which must fulfill a specific rheological behaviour. Taking this into account, the rheology plays a major role as far as the design of the ink is concerned.

Despite many type of materials can be used as printing inks for DIW 3D-printing, regarding the water based materials, the waterborne polyurethane urea dispersions (WBPUU) have taken increasing importance during the last years. The possibility of obtaining polyurethanes being synthesized by a solvent free method which implies low amount of organic compounds compared with the traditional methods is a key point for an environmental friendly approach. Waterborne polyurethane urea dispersions represent a promising material for DIW 3D-printing, presenting an important advantage during printing due to the absence of volatile organic compounds, enabling the obtaining of polyurethane urea pieces with a customized design by a more environmental friendly way.

Furthermore, the possibility of dispersing hydrophilic nanoentities into the WBPUU inks represents an interesting approach so as to provide new functionalities to the potential inks as well as to modulate their rheological properties so as to improve the printing performance. Indeed, some water dispersible nanoentities, such as environmental friendly nanocellulose represent a suitable candidate in order to pilot the rheological properties of the inks, modifying the printing performance, as well as providing a modification of the properties of the printed pieces. Additionally, other hydrophilic, environmental friendly compounds such as plant extracts, will provide to the WBPUU systems new functionalities such as antimicrobial properties. In this way, the different incorporation routes of the nanoentities and compounds as well as their content in the WBPUU based formulation can result into a different modification of the properties of both inks and system printed from the inks, leading to a modulation of the final properties of the end use material towards the desired application.

Therefore, in this work a series of WBPUU inks based on the combination of hydrophilic polyethylenglycol (PEG) and hydrophobic polycaprolactone diol (PCL) will be synthesized. Different ratios of both polyols will be studied so as to select the best combination that will favour the sol-gel transition. Once the WBPUU ink composition is determined, the influence of the solid content into the printing performance will be studied in order to study its influence and determine the parameters which gives the best printing performance. Apart from that, cellulose nanocrystals (CNC) will be added in different amounts and by different strategies to the WBPUU ink, and their influence into both the printing performance of the inks and the properties of the final material will be studied. In the last part two potential applications of the prepared WBPUU inks will be proposed: (i) the preparation of WBPUU scaffolds for cationic dyes absorption and (ii) the addition of *Salvia* extract to the WBPUU inks so as to obtain materials with antimicrobial properties.

General objectives

The principal objective of this work was the design of a suitable waterborne polyurethane urea ink for DIW 3D-printing. For that purpose, the ratios of reactants as well as the solid content of the synthesized inks were studied. Moreover, the ink was posteriorly modified with the addition of nanoentities such as cellulose nanocrystals or active compounds from plant extracts at different steps of the synthesis leading to the formation of composite inks with different rheological behaviour. In the last part of the work two potential applications were studied so as to analyze their viability, the absorption of cationic dyes and the obtaining of an ink presenting antibacterial properties.

Hence, apart from the Chapter 1 and 2, which contain the state of art and the specifications of the reactants and characterization methods, respectively, the work has been divided as follows:

- In Chapter 3, different WBPUU dispersions are synthesized varying the soft segment composition (PCL/PEG) so as to study its influence on the obtained dispersions and films properties. Additionally, the influence of the molecular mass of the used polyethylenglycol into dispersions and films is also analyzed.

- In Chapter 4, WBPUU based dispersions with different solid contents are prepared and analyzed from the rheological viewpoint and subsequently printed in order to study the ideal solid content percentage for a successful DIW 3D-printing.

- In Chapter 5, WBPUU-CNC nanocomposites based inks are synthesized by *in situ* method, that is, adding CNC during the phase inversion step, analyzed from the rheological viewpoint and subsequently printed. The influence of the loaded CNC content on the rheological properties of the inks as well as on the properties of the printed pieces is studied.

- In Chapter 6, WBPUU-CNC nanocomposites based inks are prepared by *ex situ* method, by loading the CNC to the previously synthesized WBPUU, and analyzed from the rheological viewpoint and subsequently printed. The influence of the loaded CNC content on the rheological properties of the inks as well as on the properties of the printed pieces is studied. Additionally, a comparison of the results obtained in this chapter with the ones obtained by *in situ* method in Chapter 5 is stablished.

- In Chapter 7, WBPUU-CNC nanocomposite based inks prepared *in situ* are printed and subsequently freeze dried in order to prepare porous scaffolds. The influence of different amounts of CNC on the properties of the scaffolds is studied. Additionally, some printed pieces are immersed in $CaCl_2$ so as to promote a chemical crosslinking and modify the properties of the scaffolds. The scaffold that presented the best results are tested as an absorption material for the cationic methylene blue dye. In the second part of the chapter, WBPUU-*Salvia* and WBPUU-CNC-*Salvia* nanocomposites based inks are prepared and printed. The WBPUU-*Salvia* inks were prepared by adding a 3 wt% *Salvia* extract *in situ* and posteriorly different CNC contents were added by ex situ method to the prepared WBPUU-*Salvia* inks. The rheology of the obtained inks as well as the antibacterial properties of the printed pieces are evaluated in order to study their viability as antimicrobial material.

- In Chapter 8, the main conclusions of the work as well as the proposed future work lines are presented.

CHAPTER 1

STATE OF ART

1.1 Polyurethanes and polyurethane ureas

Polyurethanes and polyurethane ureas are a family of polymers whose properties can be modulated by their composition and, thus, can be used in a wide range of applications fields such as automotive, textile, adhesive, electronics, coatings, membranes, and biomedicine among others [1–8].

The polyurethane chemistry consists on the formation of urethane groups, which are formed by the polycondensation of isocyanate and hydroxyl groups. Additionally, in the case of polyurethane urea, urea groups are also formed by the reaction of isocyanate and amine groups. Both groups formations are represented in **Figure 1.1**.

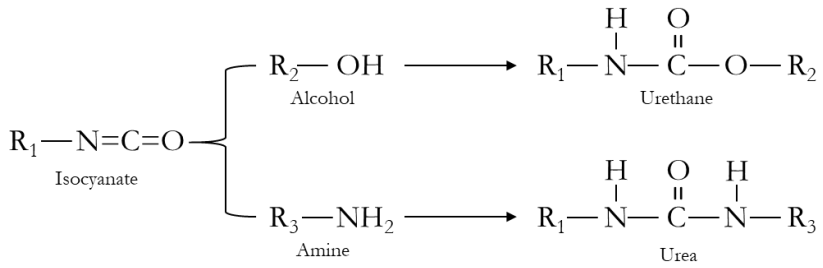

Figure 1.1 Scheme of the formation of urethane and urea groups

The principal difference of both groups is the different ability of forming hydrogen bonding. The extra secondary amine group of the urea group comparing to the urethane single one results in stronger interactions and hence in stiffer materials [9]. Additionally, this higher

hydrogen bonding capacity results in an increase of the thermal stability compared to urethanes [10].

The composition of polyurethane and polyurethane urea is usually segmented in two alternating blocks; the hard segment (HS), composed by the isocyanate and the chain extender both with hydroxyl or amina groups, respectively, and the soft segment (SS) which is formed by a polyol. These two segments are thermodynamically incompatible, which result in the separation of phases and the formation of microdomains. Generally, the hard segment provides stiffness to the material whereas the soft segment confers flexibility. However, depending on the reagents and the composition of the system, both hard and soft segments can form amorphous and crystalline ordered domains piloting the properties of the final material.

1.2 Waterborne polyurethanes and polyurethane ureas (WBPU and WBPUU)

Since classic polyurethane and polyurethane urea are hydrophobic, organic solvents are necessary for their synthesis, manipulation and processing. This fact confronts against the increasing environmental awareness, which boosts the finding of more environmentally friendly alternatives. In this context, the development of waterborne polyurethane and waterborne polyurethane urea dispersions has resulted to be a viable alternative, since the use of organic solvents can be avoided by the addition of an internal emulsifier, thereby enabling the substitution of the aforementioned organic solvent by water, which is more environmentally friendly [2,11]. The presence of an internal emulsifier, covalently bonded in the polymer backbone, gives stability to the particles formed during the addition of water in the phase inversion step.

1.2.1 Reactants

The versatility of the waterborne polyurethanes and polyurethane ureas arises from the wide range of combination of reactants that can be used for their formulation and are mainly composed by a polyol, an isocyanate, a chain extender and an internal emulsifier. The choice of the appropriate composition would determine the mechanical and thermal properties as well as its hydrophobic/hydrophilic behaviour and its biodegradability.

1.2.1.1 Polyols

Polyols, which are the main compound of the soft segment, are medium size molecular mass macromolecules containing hydroxyl groups. Among others, functionality and molecular

mass are the main selecting criteria and will influence the properties of the final WBPU or WBPUU.

Taking into consideration the functionality of the polyol, different types of polyurethane and polyurethane ureas can be obtained. The use of difunctional polyols, which are the most commonly used in WBPU and WBPUU synthesis, result in single chained thermoplastic polyurethanes [12]. Contrary, polyols presenting higher functionality, result in thermoset polymers presenting a crosslinked network [13]. Moreover, different molecular masses of the polyols result in different viscosities of the final dispersion [14], and the microstructure formed by the SS can also been affected [15].

Focusing on their nature, different types of polyols can be used for the synthesis of WBPU and WBPUU, polyethers, polyesters and polycarbonates are the more common ones. Polyesters generally present outstanding resistance to light and aging, becoming a good choice for outdoors applications [16] and they also exhibit higher strength comparing to polyethers [16,17]. Those latter ones are more sensitive to light and oxygen but improve the chain flexibility as well as the dispersion in water. Polycarbonates, conversely, are claimed to present lower oxidation sensitivity compared to polyethers [18], better hydrolytic stability than polyesters [19], and in general better mechanical properties [20].

Additionally, apart from the aforementioned polyols, which have a synthetic source, in the last year the use of polyols coming for renewable sources has gained increasing interest. In this context, polyols coming from vegetal oils such as Castor oil [21,22] or Tung oil [23] are used in order to obtain more environmental friendly WBPU or WBPUU.

Although most of the polyols used in this synthesis are generally hydrophobic, the use of hydrophilic polyols, that can act also as internal emulsifier, in WBPU and WBPUU synthesis has been also reported in the literature, mainly, in order to obtain hydrogels. It has been observed that dispersions containing polyethylenglycol (PEG), also known as polyethylene oxide) (PEO), with high solid content (above 30 wt%) tends to form physical gels [24,25]. However, in the last years the use of more than one polyol as SS has drawn increasing interest. The combination of different polyols allows to modify the properties of the final material as well as to incorporate new functionalities [26]. Concretely, in the case of the combination of a hydrophobic and a hydrophilic polyol the possibility of obtaining WBPU/WBPUU based hydrogels but maintaining the properties of hydrophobic polyols has been studied in the literature as a potential material, principally for biomedical applications [27,28].

1.2.1.2 Isocyanates

For among the wide range of isocyanates, diisocyanates are the most common ones for the synthesis of WBPU and WBPUU. Depending on their structures, they can be divided into two main categories: aromatics and aliphatics. The structure of the diisocyanate is an important factor for the polymer design, affecting the crystallinity of WBPU and WBPUU and therefore to the mechanical properties of the final material [29]. Additionally, the diisocyanates also affect the reactivity in the synthesis, but also the biodegradability and the biocompatibility [30,31] of the end use material.

Aromatic diisocyanates, which are usually used in the synthesis of industrial polyurethane and polyurethane ureas, present limitations for the synthesis of WBPU and WBPUU. Their higher reactivity with water and the higher resulting viscosity when are used, makes the dispersion process in water difficult [32]. Taking this issue into account, aliphatic diisocyanates result to be a better option for the WBPU and WBPUU synthesis. Moreover, this type of diisocyanates present better resistance against thermal and hydrolytic attack comparing with aromatic ones [33]. 4,4'-Dicyclohexyl methane diisocyanate (H_{12}MDI) and 1,6-hexamethylene diisocyanate (HDI) are examples of aliphatic diisocyanate reported in the literature for the synthesis of WBPU and WBPUU, but among others, isophorone diisocyanate (IPDI) is probably one of the most used. This diisocyanate presents low reactivity with water, which allows to obtain a more controllable process and thus a more stable final product [32,33]. Additionally, its cyclic and asymmetrical structure leads to less ordered structures and thus, eases the diffusion of water during the dispersion step [34].

1.2.1.3 Chain extender

Regarding the chain extenders, usually they are low molecular mass diols or diamines [35], which lead to the formation of WBPU and WBPUU respectively. Nevertheless, chain extenders presenting higher functionalities than two can be used in order to obtain crosslinked WBPU or WBPUU dispersions.

The most commonly used diols include ethylene glycol (EG) and 1,4-butanediol (1,4-BD), whereas the most used diamine is the ethylene diamine (EDA) [34]. As explained before, the use of diamine leads to the formation of urea linkages, which leads to an improvement of both mechanical properties and thermal stability due to the stronger hydrogen bonding interaction of the extra amine group [36].

1.2.1.4 Internal emulsifier

The internal emulsifier plays a major role in the formation of WBPU and WBPUU since its inclusion allows the formation of stable dispersions in water. Depending on their nature, internal emulsifier can be divided into non-ionic and ionic. The former consists on the inclusion of a hydrophilic segment such as PEG into the polymer backbone so as to stabilize the dispersion [37]. This strategy involves some limitations because its weaker hydrophilic behaviour compared to ionic emulsifier hinders the dispersion in water [38].

In turn, the ionic emulsifiers can be classified into cationic and anionic, depending on the functional group that confers hydrophilicity to the system. These ionic groups, completely or partially neutralized by the presence of counterions, can be cationic like quaternary ammonium groups and anionic like carboxylated or sulfonated groups [1,37,39]. Generally, the use of anionic emulsifiers has been more reported in the literature, however, the use of cationic emulsifier has also been reported for many applications. The most commonly used internal emulsifiers are 2,2-bis(hydroxymethyl) propionic acid (DMPA) and N-methyldiethanolamine (MDEA) as anionic and cationic internal emulsifiers, respectively [40–42].

1.2.1.5 Catalyst

In order to improve the reactivity of the WBPU and WBPUU reactants during the synthesis, catalysts are used in the first step of the reaction with the aim of accelerating the reaction between hydroxyl and isocyanate groups at lower temperatures. The most widely used catalysts in WBPU and WBPUU synthesis are tertiary amines such as 1,4-diazabicyclo octane (DABCO) and organo tin compounds as dibutyltin dilaurate (DBTDL) [43]. However, some authors reported the use of less harmful catalyst such as zirconium based compounds [32,44].

1.2.2 Synthesis procedure

The synthesis procedure of WPBU and WPBUU is a complex process which classically comprises two steps. In the first one, the formation of the prepolymer backbone is carried out, by reacting firstly the polyol and the diisocyanate (usually in presence of a catalyst) and posteriorly with the internal emulsifier. Besides the second one comprises the chain extension of the prepolymer backbone to form the final polyurethane or polyurethane urea chain. **Figure 1.2** shows a general scheme of WPBU and WPBUU synthesis process.

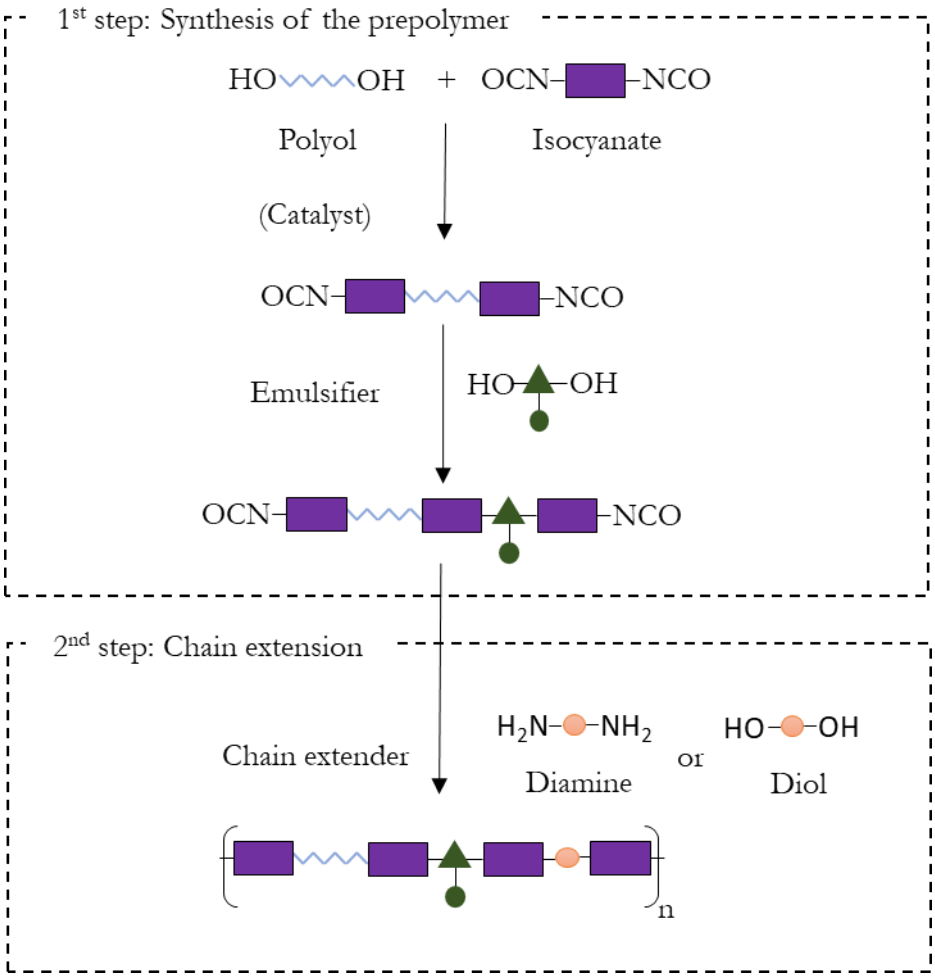

Figure 1.2 WBPU and WBPUU synthesis procedure

Notwithstanding, in the case of WBPU and WBPUU an additional step named phase inversion is required so as to obtain the desired dispersion. Depending when this step is carried out, the dispersion in homogeneous medium (chain extension before phase inversion), or the dispersion in heterogeneous medium (chain extension after phase inversion) can be performed [45]. Normally this phase inversion step is carried out with deionized water, but in a recent work, *Fang et al.* synthesized successfully a series of WBPU of different compositions using snow as dispersant [46]. The chain extender's nature plays an important role in the selection of the most appropriate medium for phase inversion. In general, diol chain extensions are performed before phase inversion so as to avoid side reactions owing to its lower reactivity with isocyanates comparing with water. Contrary, diamine chain extenders, which show higher reactivity than diols and also than water, can be added before or after the phase inversion, leading thus to a dispersion in homogeneous and heterogeneous media, respectively.

The stabilization of the ionic WBPU and WBPUU particles is produced by the electronic double layer mechanism produced by the ionic emulsifier and a counterion added before the phase inversion in order to maintain the electrical neutrality of the ionic center [47]. Contrary, in the case of non-ionic emulsifiers, the stabilization mechanism is based on entropic repulsion. The hydrophilic segments of the polymer chain are situated towards the water, and thus, when particles are approaching each other, the mobility of this segment is reduced, decreasing the entropy and hence, stabilizing the dispersion. When the dispersion is formed, the ionic groups of the particles, surrounded by the counterions forming the electrical double layer [48], as well as the non-ionic hydrophilic domains are arranged in the surface forming the shell of the particle [49,50]. Conversely, hydrophobic domains will be situated in the center of particles forming the core of the particles [51]. **Figure 1.3** illustrates the formation mechanism of ionic WBPU and WBPUU dispersions.

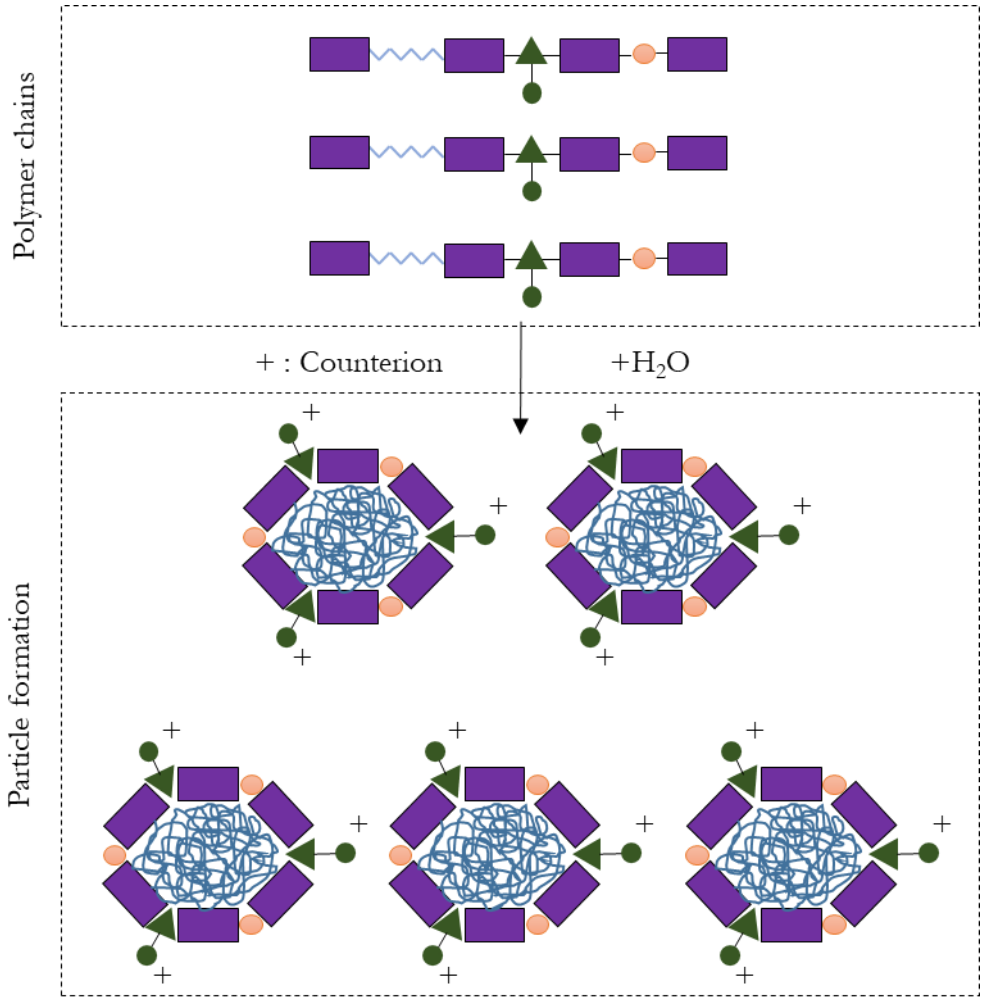

Figure 1.3 Formation mechanism of the WBPU and WBPUU particles

1.3 Cellulose nanocrystals

Cellulose is one of the most common renewable materials in the world, and due to its availability, low toxicity, biocompatibility and biodegradability, it has been extensively explored for producing new materials, especially in the form of micro or nanoscale with different morphology and crystallinity. Cellulose is a high molecular mass homopolymer composed of D-glucose units linked by β(1,4) glyosidic bonds, as can be observed in **Figure 1.4**.

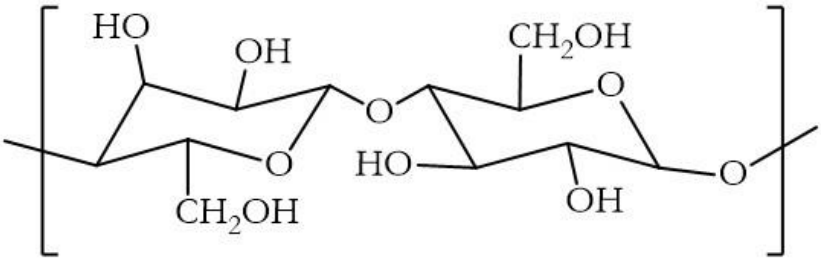

Figure 1.4 Chemical structural unit of cellulose

Cellulose nanocrystals (CNC), which represent the crystalline region of the cellulose, have been widely used as reinforcement for nanocomposites in many applications fields such as tissue engineering [52], food packaging [53], water filtration [54] or electronics [55] among others.

This crystalline fraction, is extracted from cellulose through different methods such as acid hydrolysis, combined mechanical shearing, and enzymatic hydrolysis in which the amorphous or disordered regions of cellulose are hydrolyzed, and the crystalline regions with higher resistance to acid attack remain intact and result in CNC [56,57]. The source of the cellulose, as well as, the hydrolysis conditions influence the final properties of the CNC [58,59]. Regarding those properties, the most remarkable ones are the high aspect ratio and high specific mechanical properties such as a high tensile strength and modulus [60,61].

Different types of polymers have been used as matrices to prepare composites reinforced by CNC. Due to its hydrophilic nature, surfactants or a modification of the CNC are needed so as to obtain homogeneous dispersions of the particles in non-polar polymers [62]. In this context the use of polymers dispersed in water allows to overcome this limitations, facilitating a good dispersion of the nanoentities without the addition of surfactant or chemical modifications [63].

Focusing on WBPU and WBPUU, the possibility of easily dispersing CNC into the water medium has earned increasing attention for the preparation of WBPU/CNC and WBPUU/CNC composites [64–66]. In this case, the addition of the nanoentities can be done in different steps, resulting in composites with different properties. Usually, the addition of CNC is carried out after the synthesis of the WBPU and WBPUU adding the nanoentities to the polymer dispersion by mechanical stirring, which is known as *ex situ* method and leads to the formation of physical bonding between the CNC and the polymer matrix. However, it has been also reported the option of adding the CNC dispersed in water during the phase inversion as a part of the synthesis itself. As a result, the CNC could react chemically with the free isocyanate groups of the polyurethane prepolymer, stablishing a chemical bonding that modifies the properties of the final composite. This preparation route is known as *in situ* method [67,68].

1.4 Plants extracts

The use of water dispersible plant extracts in order to be incorporated into WBPU and WBPUU represent and interesting strategy so as to provide to the final composite particular enhanced properties related principally to the antibacterial and antimicrobial properties. In this context, this extracts obtained from natural sources can be added to the dispersion easily following the same methodology as was used for the cellulose nanocrystals, representing an example of the use of environmental friendly additives to functionalize the matrix.

Different methods can be used so as to make the extraction of this compounds such as the decoction or infusion among others [69], by using different solvents [70], and depending the conditions of this process the composition of the obtained extracts can be varied.

Regarding the addition process, as happened with the CNC addition, the literature showed two principal methods, the *in situ* and the *ex situ* method. The former takes advantage of the dispersability of the extracts in the water to add them during the synthesis of the WBPU and WBPUU, specifically in the phase inversion previously dispersed in the water. The latter comprise the mixing of the extracts and the synthesized dispersion by vigorous mechanical stirring [71].

The use of medicinal plants in order to obtain valuable extracts for their use in potential antibacterial applications has been exhaustively studied in the literature [72]. Extract obtained from *Salvia officinalis L.*, represents an example of these aforementioned water dispersible plant extracts presenting in this case antibacterial, antioxidant and anti-inflammatory

properties [73,74]. These properties can be attributed to the bioactive compounds of the plants which comprise normally alkaloids, flavonoids, tannins and phenolic compounds among others, and whose composition depends on the type of plant and the growing conditions [75–77].

1.5 3D-printing

3D-printing, also known as additive manufacturing (AM), is a fabrication technique based on the principle of layered manufacturing, which allows the fabrication of a wide range of structures and complex geometries from three dimensional (3D) model data [78,79].

Despite the first early developments of this fabrication technique dating back to the early 80s [80,81], in the last decade, the 3D-printing industry has exploded due to the reduced manufacturing costs of 3D printers and to their improved printing precision and speed. Likewise, this increasing interest in AM has led to the development of new techniques and more interesting materials allowing to widen the application fields of this fabrication technique such as, energy storage [82], tissue engineering [83], automotive [84] or sensors [85] among others.

Although stereo lithography (SLA) is the oldest 3D-printing technique, nowadays from the different developed methods for 3D-printing, fused deposition modelling (FDM) is the most popular one. However, many different techniques have been developed during the years, with different working principles, materials and applications. Apart from FDM and SLA, the main printing techniques englobe the selective laser sintering (SLS), selective laser melting (SLM), liquid binding in three dimensional printing (3DP), direct ink writing (DIW), direct energy deposition (DED) and laminated object manufacturing (LOM).

Every method presents their advantages and drawbacks as well as material limitations. In the **Table 1.1** a synthesis of the main methods for additive manufacturing is displayed.

Table 1.1 Summary of the main methods for additive manufacturing

Method	Working principle	Materials	Benefits	Drawbacks	Applications	References
Fused deposition modeling (FDM)	Extrusion and deposition	Filaments, principally of thermoplastic polymers	High speed Low cost	Weak mechanical properties Material limitation	Prototyping	[86–88]
Stereo lithography (SLA)	Laser scanning and UV induced curing	Resin with photoactive monomer	High resolution High quality	High cost Material limitation Cytotoxicity	Biomedical Prototyping	[89,90]
Selective laser sintering (SLS)	Laser energy to sinter powder material	Metals Polymers	Good strength	Slow printing Expensive	Biomedical Electronics Aerospace	[91,92]
Liquid binding in 3D-printing (3DP)	Joining of powder particles by a binding agent	Ceramic Polymers	High resolution	High porosity in the binder method	Biomedical Electronics	[93]
Direct ink writing (DIW)	Pressurized o mechanized syringe extrusion	Polymers Hydrogels	High resolution	Low mechanical strength	Biomedical Electronics	[94,95]
Direct energy deposition (DED)	Melting of the deposited material	Metals Ceramic Polymers	Controlled microstructure	Low surface quality	Aerospace Biomedical	[96,97]
Laminated object manufacturing (LOM)	Layer-by-layer cutting and lamination of sheets or rolls of materials	Polymer composites Ceramics Metal rolls	Low cost Wide range of materials Manufacturing of larger structures	Inferior surface quality Limitation in manufacturing for complex shapes	Paper manufacturing Electronics Smart structures	[98]

1.5.1 Direct ink writing 3D-printing

The extrusion based direct ink writing (DIW), so called extrusion based 3D-printing, has gained in the last years an increasing interest in several fields due to the possibility of designing complex devices overcoming drawbacks of the classic 3D-printing, among others, the use of volatile organic compounds or crosslinkers. This printing technique, mostly referred in the bibliography as micro-extrusion, has evolved from the conventional fused deposition modeling, and consists on the extrusion of the material through a needle pushed by pneumatic pressure [99], a piston, or a rotating screw [100]. **Figure 1.5** illustrates the different extrusion mechanism for DIW. Depending on the physicochemical parameters of the ink, the printing device and the needle diameter, a thread with a width range of diameters from 45 μm [101] to 1200 μm [102] can be printed with high precision. Additionally, curing reactions can be performed by dispensing two reactive components using mixing nozzles or being induced either by heat or UV light [103].

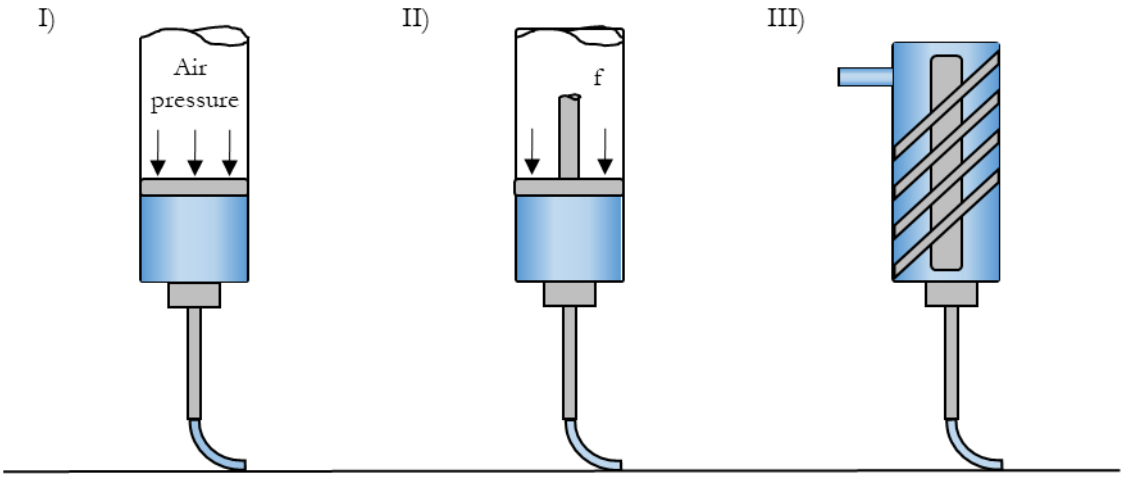

Figure 1.5 Graphical illustration of the extrusion mechanism for DIW 3D-printing: I) pneumatic pressure based, II) piston based and III) rotating screw based

The pneumatic extrusion system uses compressed gas as driving force for the extrusion, which is normally air or N_2 in the case of printing of biological inks [104]. This type of system is more complicated to build and operate than motor driven systems since it involves the use of compressed gas, but it presents some advantages such as its capacity of extruding a wide range of viscoelastic inks [105], and its faster response time due to the quick pressurization and depressurization of the syringe cartridge.

Contrary, the motor driven piston system provides better control of the extrusion rate since there is constant volume displacement. However, its time delay in the set up to start and stop

the extrusion process may result in an inaccurate print [106]. Finally, regarding rotating screw system, its design allows a continuous printing due to the possibility of continuous alimentation. Additionally, the use of the screw during printing also helps to mix the material avoiding phase separation or inhomogeneity in systems with more than one component [107]. Nevertheless, there are also some important drawbacks such as the possibility of cross contamination since the materials are not stored separately, as well as the impossibility of using delicate materials such as cells since shear force would damage the cell membrane [108].

Despite some noteworthy advances that DIW presents compared with other printing technologies such as the possibility of printing biomaterials with high viscosities as well as its room temperature process this technology still presents some drawbacks such as its low printing speed or the need of specific matching of materials densities to preserve intricate shapes [109]. One of the major challenges of this novel technology involves the development of clear technical parameters which can lead to its optimal use. Since its recent development, multiple contradictions have appeared between authors about the ideal parameters, and hence, it is difficult to establish the best protocol.

1.5.1.1 Materials for direct ink writing 3D-printing

As was aforementioned, one of the most critical parameters and hence, limitation of the DIW 3D-printing is the need of materials (also called inks in the 3D-printing field) that match with the special requirements of this AM technology. Concretely, the extrusion mechanism requires inks that reduce their viscosity as a result of an applied stress so as to successfully pass through the needle and then, recover their initial stage in order to support the designed multilayered complex design.

Taking those limitations into account, different approaches have been proposed in the literature. Principally, inks can be divided into three categories: hot melt extrusion inks, cold extrusion inks and gel forming inks.

The former, which is also known as phase change inks [110], englobes materials which requires an initial heating step to allow the ink to flow out of the nozzle followed by a cooling step to solidify the ink. This behaviour is similar to the one observed in the filament of FDM, however, in this case the temperatures are much lower, just enough to maintain the ink above its gel point before printing. After the printing performance, contrary, the bed temperature is below the gel point, allowing to the sol formation. Gel points below room temperature require the use of ice bath or a Peltier device to reduce the temperature.

Gel forming inks englobe all those systems which use the chemical or physical crosslinking of the inks before or after the printing process. In contrast to hot melt extrusion inks, in this case instead of the temperature, the addition of anionic compounds or UV light is used for provoking the gelation of the printed ink.

Regarding the addition of anionic species, many authors reported the use of divalent ions such as calcium or monovalent such as potassium to crosslink anionic biopolymers like alginate or carrageenan in order to obtain printable gels [111,112], mainly for biomedical applications due to the biocompatibility of the resulting inks. Additionally, also the combination of alginate with other compounds has been reported in the literature as potential inks. Alginate/gelatin [113], gelatin/hyaluronic [114,115], gelatin/alginate/hepatoyle [116], alginate/Pluronic F127 [117], and alginate/chitosan/polyelectrolyte complexes [118] are examples of successful combinations of compounds to prepare gel forming inks. However, the poor mechanical properties of the printed materials have led to the use of reinforcements as well as to improve the printing performance and the mechanical properties of the printed material. In this context, cellulose derivatives have been extensively studied as fillers to improve the printability as well as the interfacial adhesion of the inks, in the form of nanofibers [119], nanocrystals [120], carboxymethyl cellulose [121] and methylcellulose [122] among others. Other works are focused on improving the mechanical properties of the resulting piece by adding to alginate based inks carbon derived entities such as graphene oxide [123,124] or carbon nanotubes [125], resulting not only in a mechanical reinforcement but also in some cases in an interesting electrical conductivity.

As far as UV cured inks is concerned, photopolymers such as gelatin methacrylate [126] or resins with UV initiators [127,128] are examples of inks that can be cured by UV after being printed. As the UV light and the intermediate free radicals can kill cells, this approach presents some limitations which are well known and studied to avoid this type of problems.

Cold extrusion inks, contrary, comprise all those which their printing processes do not require the application of temperature and only rely on the ink's rheology for the printing. The ink must be able to be extruded but at the same way to form self-supporting layers [129]. The addition of additives or thickeners and the modification of the composition are usually used in order to adapt the rheology and allow a successful printing process. The use of this type of inks presents an important advantage against other types of inks, that is the absence of extra processing of the ink such as the application of temperature, crosslinkers or UV

light. However, this absence of "second" processing step also represents a greater limitation of the materials, due to the special conditions that the ink has to fulfil to be successfully printed. Numerous formulations have been developed during the last years to achieve this special conditions such as polycaprolactone/starch blends [130], hydroxyapatite [131], mesoporous bioactive glass/polyvinyl acetate [132], polylactic acid/polyethylenglycol in chloroform [133], poly (hydroxymethylglycolide-co-ε-caprolaptone) [134] and graphene dispersion [135] represent examples of development of suitable cold extrusion inks.

In this context, regarding polyurethane based inks, waterborne polyurethane and polyurethane ureas with different compositions have been proposed as suitable inks, mostly as cold extrusion inks. Polycaprolactone [136], polycaprolactone/polyether block amide/ hyaluronic acid [137], polycaprolactone/polyethylenglycol [138], polycaprolactone/polylactic acid/poly(-L-lactic) acid [139], polycaprolactone/polyether block amide [140], peptinucleic acid/carbon nanotubes [141], polycaprolactone/polyether block amide, polycaprolactone/polyether block amide/polyethylenglycol [142], polycaprolactone/poly(L-lactide)/poly(ethylene oxide) [28] represent examples in the literature for the development of inks based on different formulations of waterborne polyurethanes and polyurethane ureas.

1.5.1.2 Impact of rheology on DIW 3D-printing

Although the DIW 3D-printing represents an interesting fabrication technique, the correct development of suitable materials is still an important challenge in order to ensure the viability of this AM. The extrusion rate, printing speed and printer resolution are some important 3D-printing parameters, which are directly linked to the rheological properties of the ink.

Overall, the materials suitable for DIW 3D-printing are required to decrease their viscosity in order to flow easily under pressure, and posteriorly be able to recover the initial stage so as to retain their shape quickly for a long time, and maintain sufficient integrity after fabrication. In the **Figure 1.6** a graphical illustration of the different stages of the DIW 3D-printing process is displayed.

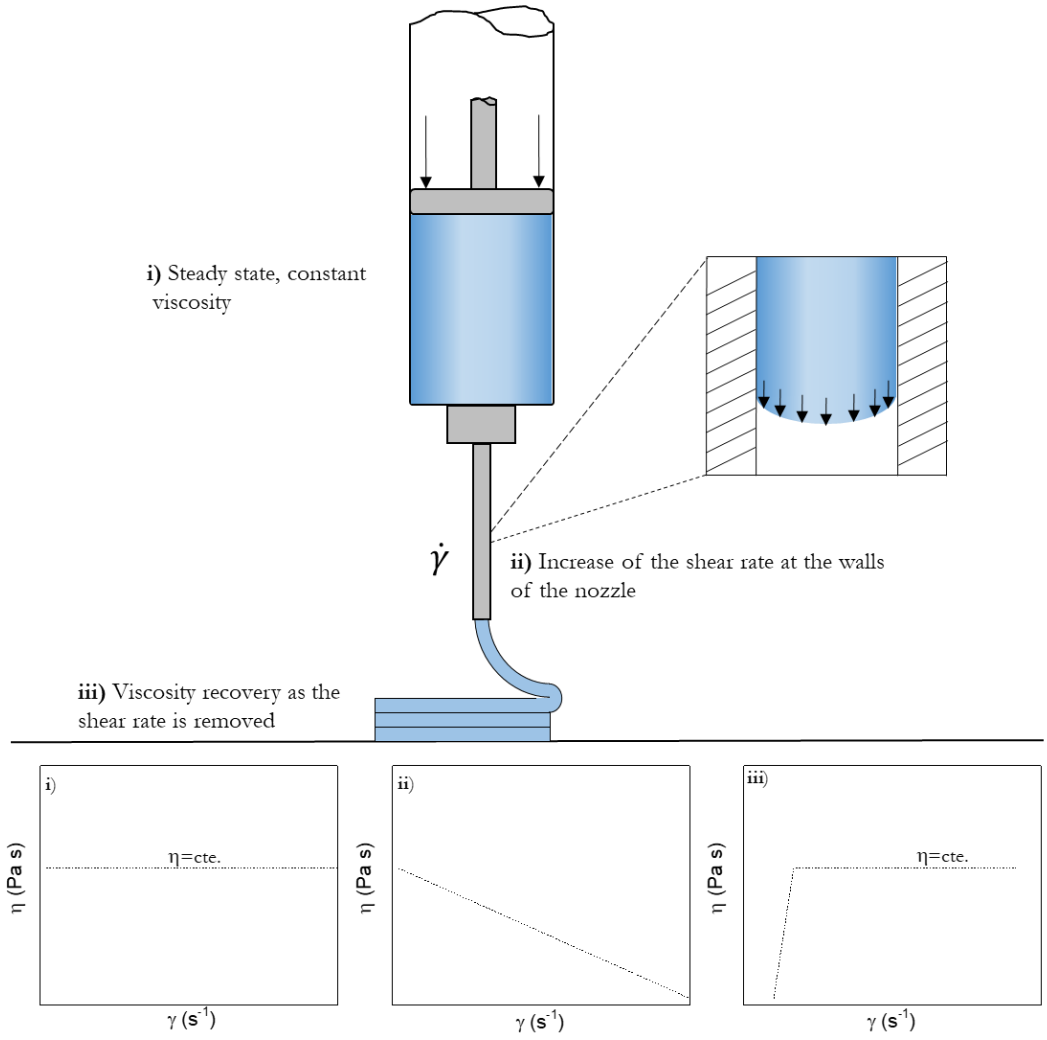

Figure 1.6 Graphical illustration of the different steps of the DIW 3D-printing at their rheological correspondence

In general terms, so as to determine the suitability of the inks, authors agree to explore (i) the processability of the ink, also known as "printability" and ii) the printing fidelity and the strength of the printed construct to self-sustain a 3D structure post printing, according to the rheological properties of the inks.

Normally, the analysis of the rheological parameters is carried out for cold extrusion inks, measuring the viscosity as a function of the shear rate and determining the elastic and viscous components by oscillatory measurements in order to obtain the desired parameters. The **Figure 1.7** propose a tentative of the relationship between rheological parameters and 3D-printing process.

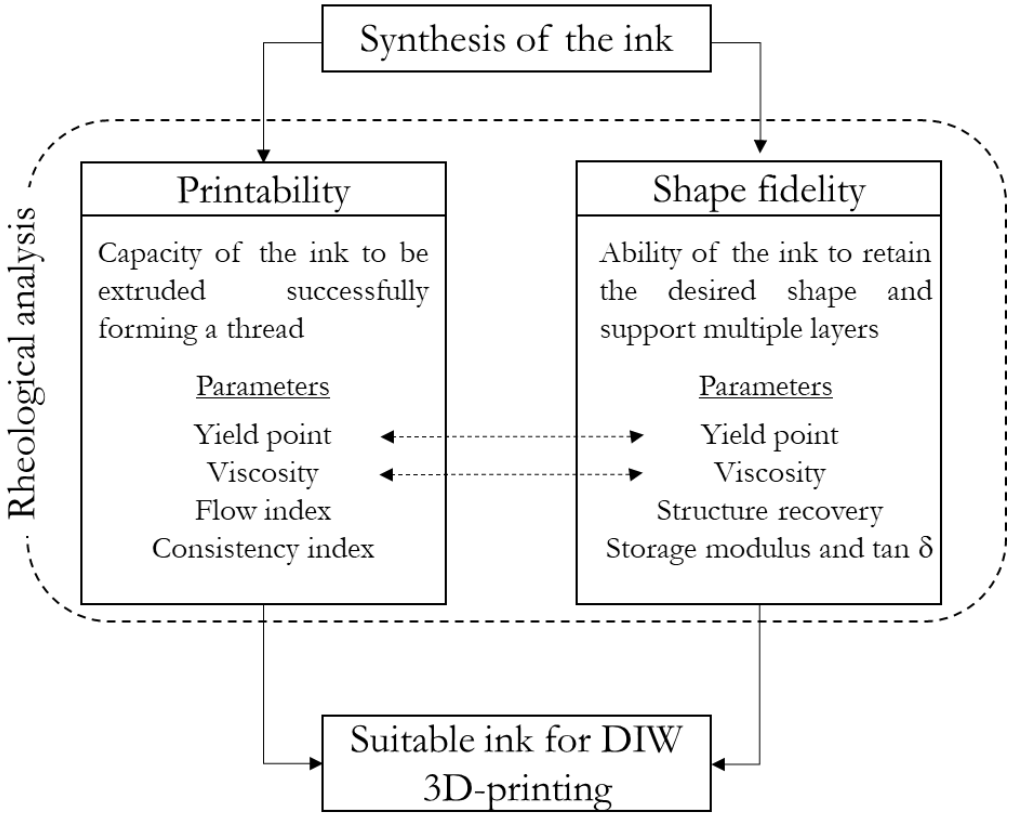

Figure 1.7 Scheme of the rheological analysis of the inks for DIW 3D-printing

For gel forming inks that undergo phase transition, contrary, the rheology is measured as function of time and temperature in order to determine the conditions under which the phase change occurs. This will help to determine the optimal printing conditions such as printing temperature.

1.5.1.2.1 Printability of the inks

The printability is commonly defined as the capacity of an ink to be extruded successfully forming a continuous and homogeneous thread. **Figure 1.8** illustrates the ideal extrusion process as well as the undesired under-extrusion and over-extrusion phenomena. The former, happens when not enough ink is extruded or the printing speed is too fast and as a result, an inhomogeneous thread is obtained, whereas in the latter, too much ink is being extruded or the speed is too low, resulting in a too big thread, which can result in problems to represent the details of the 3D design as well as the possibility of dragging already printed areas.

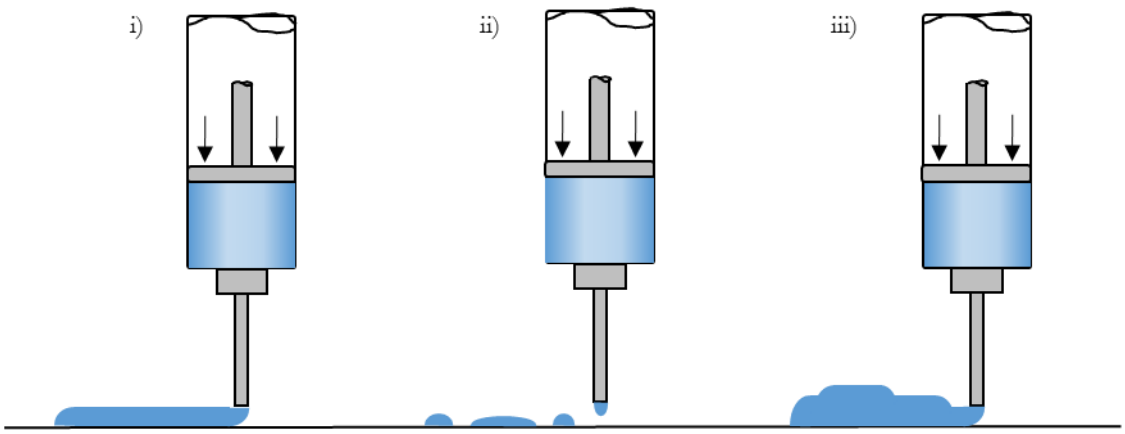

Figure 1.8 Different examples of printability of the inks: i) desired extrusion, ii) under-extrusion and iii) over-extrusion

One can notice that some authors define the "printability" of an ink as the overall ability of a material to make a 3D object by layer-by-layer deposition and to support its structure once printed [129] without discussed the end use properties.

The viscosity is defined as the ratio of the shear stress over the shear rate. Depending on the variation of the viscosity as a function of the shear rate, the materials can be divided into two categories: Newtonian and non-Newtonian fluids. The viscosity of a Newtonian fluid is constant whatever the shear rate (the shear stress varies linearly with the shear rate). For non-Newtonian fluids, contrary, the shear stress varies non-linearly with shear rate and one can define pseudoplastic materials and dilatant ones, depending the decreasing (shear thinning) and increasing (shear thickening) tendency of the viscosity as the shear rate increases respectively. Additionally, Bingham, plastics are defined as a material that behaves as a rigid body at low stresses but flows as a Newtonian fluid at high stresses. In the **Figure 1.9** a representation of the different behaviors is displayed.

The viscosity of a polymer solution is predominantly determined by the polymer concentration and molecular weight [23] thus, these two parameters have to be taken into consideration in order to design printable materials by DIW 3D-printing.

For DIW 3D-printing, pseudoplastic materials are the ones that are recommendable. Their capacity of decreasing their viscosity as the shear rate increases gives them the ideal behaviour for the micro-extrusion process. At high shear rates (printing state) the viscosity decreases drastically up to the point that becomes easily extruded forming a continuous nozzle, whereas at low shear rates (steady state) the high viscosity of the ink allows to maintain the given shape.

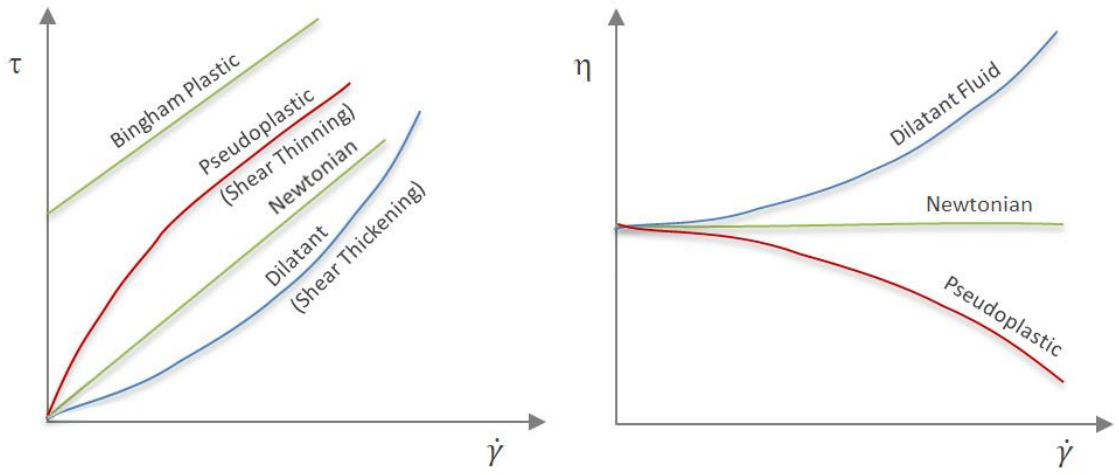

Figure 1.9 Representation of the different materials divided by their behaviour against the shear rate. Shear stress (left), viscosity (right).

During the shear process, the macromolecules are more or less oriented in the shear direction (in this case the extrusion direction). The resistance to flow is lower when the orientation is more significant. In the case of the polymer chains, which are entangled in steady state, the applied shear rate unravels the polymer chains, up to the point that at high rates the chains are not in contact with each other. For dispersions, contrary, the applied shear rate causes particles orientation in the flow direction. Additionally, a shear load can also break agglomerates or change the particles network. This type of behaviour leads to a decrease of the resistance to flow which is traduced in lower viscosity and a better properties for printing [143].

Generally, the viscosity influences the shape fidelity of the printed piece, being higher as the viscosity increases. However, it also influences the printability, since high viscosities require high shear stresses which can lead to extrusion problems.

In the **Table 1.2** the viscosity values in steady and printing state of different systems observed in the literature are displayed. As can be observed, a wide range of viscosity values allows to possible extrusion, however, a shear thinning behaviour is observed in all of them, presenting much lower viscosities when are extruded.

Table 1.2 Viscosity and shear rate values of inks during and after extrusion in literature

Extrusion viscosity (Pa s)	Extrusion shear rate (s^{-1})	Newtonian or steady state (Pa s)	Newtonian or steady shear rate (s^{-1})	References
10-100	50	10000	0.01	[144]
28.6	26	400	0	[145]
2.72	96	15	0.1	[142]
35	28	2560	0.14	[146]
10-100	100	10000	0.1	[147]

For non-Newtonian fluids, the nonlinear variation of the shear stress as a function of the shear rate can be described by the power law (**Equation 1.1**) and the Herschel Bulkley model (**Equation 1.2**)

$$\tau = K\,\dot{\gamma}^{n} \qquad (1.1)$$

$$\tau = \tau_y + K\,\dot{\gamma}^{n} \qquad (1.2)$$

where τ is the shear stress (Pa), $\dot{\gamma}$ is the shear rate (s^{-1}), K is the consistency index (Pa s^n), n is the flow index (dimensionless), and τ_y is the yield point.

The n index, defines the nature of the variation of the shear stress as a function of the shear rate. Values of $n>1$ are related to materials with shear thickening behaviour, whereas $n<1$ is characteristic of materials that present shear thinning behaviour. Low values indicate a strong shear thinning behaviour, which eases the extrudability of the inks, leading to improve its printability [145,148,149]. Conversely, the K index is related to the apparent viscosity of the fluid at a shear rate of 1 s^{-1} [150], where high values can lead to the extrudability problems of the ink. Some authors suggest the possibility that the consistency index reflects individual structural characteristic, whereas flow index reflects the structural property of the whole suspension [151].

The power law model allows to describe the behaviour of the shear stress as a function of the shear rate for most of the non-Newtonian fluids. However, in order to describe the behaviour of the inks that are solid at rest and only starts to flow after a certain applied stress the inclusion of more parameters is needed. In this context the Herschel Bulkley model, which takes into consideration this applied stress under the name of yield point represents a more accurate model.

The yield point, also called yield stress is by definition a measure of the stress at which the network structure of the material starts to break down and hence starts flowing. The determination of this parameter is of the major importance for the evaluation of the capability of the printability of the material because the DIW 3D printer must apply a stress higher than the τ_y so as to start extruding the material through the nozzle. High τ_y values will result in inhomogeneous, non-continuous flow or even lead to the impossibility of extruding the material. Anyway, since the ink has to be extruded through the nozzle, its diameter plays also a major role in the printability, resulting more difficult to extrude successfully as the diameter of the nozzle decreases. Apart from the influence on the printability, the yield point also influences the ability of the material to keep its shape under gravity and under the stresses generated by material layers deposited on top of it [152,153]. Thus, an ink suitable for 3D-printing should possess a yield point low enough to ensure its correct extrusion but not too low after the printing to avoid spreading of the printed object under its own weight.

The determination of the yield point which is carried out in a stress ramp is a process that does not present a consensus in the consulted literature, since many authors propose their own interpretation of the yield point determination. Generally, all methods are related with the deviation of the storage modulus from the constant plateau observed at low shear stresses and only differed on the stress value where the τ_y is taken. In the **Table 1.3** some of the different yield point determination methods based on the stress ramp observed in the literature are enlisted. As well, in **Figure 1.10** an example of the different yield point calculated from the mentioned methods are represented in a stress ramp.

Table 1.3 Different yield point determination methods

Author	Determination method	References
Lille et al. **and** ***Cyriac et al.***	Deviation of the G' from linearity	[152,154]
Shih et al.	Intercept between G' and G"	[155]
Sharma et al.	10% of deviation of the G' from linearity	[156]
De Graef et al.	Onset of the drop of the G*	[157]

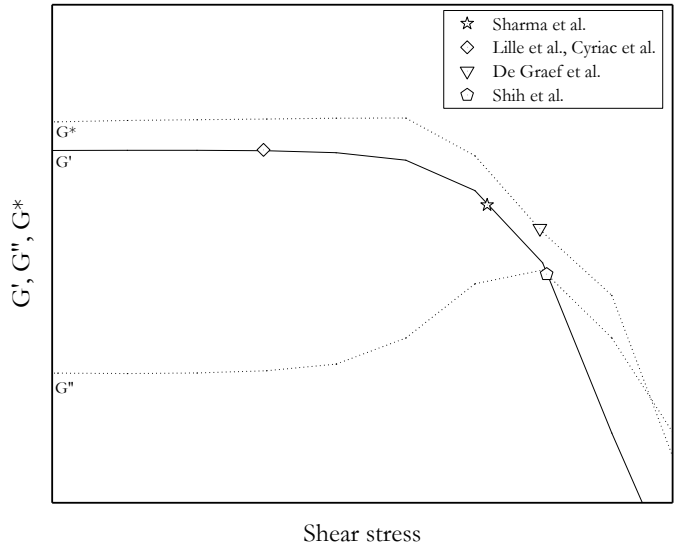

Figure 1.10 Representation of the different enlisted methods for the determination of yield point

As can be observed, the different interpretations of the determination of the yield point lead to very different τ_y values, which can represent and issue as far as a correct correlation with the printing performance is concerned. For that reason, for comparing the different values provided in the literature, the determination method as well as the capacity of the DIW 3-printer to apply the stress must be taken into consideration. Anyway in the **Table 1.4** the printable yield point ranges of inks observed in the literature are enlisted observing a wide variety of yield point ranges.

Table 1.4 Some example of yield point values of inks in the literature

Yield point range (Pa)	Type of ink	References
419-1419	Yeast extracts	[158]
1-10	Geopolymer paste	[159]
99-160	Poly(ethylene glycol) diacrylate	[160]
8-80	Graphene oxide solution	[161]

Apart from the yield point, most of the authors reported the flow stress, or flow point (τ_f), as the crossover between G' and G" in order to reflect the point where the ink starts flowing like a liquid. Additionally, the flow transition index, (FTI) is proposed as a dimensionless

parameter, which consist on the ratio between the flow point and the yield point (τ_f/τ_y) [161], and is used in order to characterize the breaking behaviour of the inner structure of the ink, which illustrates the brittle behaviour of the soft material as FTI approaches to 1 [143].

In conclusion, the most important characteristics that a suitable ink must have for a good printability is having a shear thinning behaviour, a low enough viscosity and a yield point lower than the limitations of the DIW equipment but high enough not to compromise the shape fidelity.

1.5.1.2.2 Shape fidelity of the inks

Contrary to printability, the shape fidelity comprises other parameters and requires other type of tests even if some of the parameters mentioned for the printability have their influence on the shape fidelity and vice versa. In this case, oscillatory measurements allow to determine the storage and loss moduli and as consequence the capacity of the printed piece of maintaining the given shape as well as to avoid the collapse of the structure due to their own weight.

The storage and loss moduli obtained by spectromechanical analysis are the key parameters in order to determine the capacity of the ink of maintaining the given shape as well as to support multiple layers without collapsing for its own weight. Generally, for cold extrusion inks a G' over G" is desired, indicating a elastic behaviour. In the case of gel forming inks, contrary, the systems usually present G" over G' before gelation and G' over G" after the gelation of the ink which will ease initially the printing process and once printed stablish a solid structure. Focusing on the moduli values, systems presenting low values of storage modulus, normally exhibit a less structured network compared with the ones with higher G' values, which are correlated to highly structured systems Thus, the latter ones are desirable in order to obtain inks with good shape fidelity which can also support multiple layers without collapsing. According to *Li et al.*, empirically, a storage modulus above 10^3 Pa is necessary to support highly stable 3D structure of multiple layers [162].

In addition to the storage modulus, the yield point has also influence on the capacity of maintaining the shape since a very low value can lead to the flow of the lower layers as a result of the own weight of the 3D construction. Additionally, the relationship between the storage and loss moduli, which is known as the tangent of the phase angle δ ($\tan \delta = G''/G'$), gives useful information about the structuration of the network of the

inks. High values of tan δ represent a more viscous behaviour, leading to systems that cannot maintain the given shape and are not able to support layers, whereas lower values of tan δ are desirable so as to obtain inks with good shape maintaining properties owing to their elastic behaviour. However, very low values of tan δ can result in a too high elastic behaviour, avoiding good adhesion between each layer and leading to problems of cohesion between layers as well as difficulties in printing corners due to material drag. In the **Table 1.5** an example of different storage modulus and tan δ values for printable materials are displayed. **Figure 1.11** illustrates the storage modulus and tan δ of printable and not printable materials of cold extrusion and gel forming inks observed in the literature.

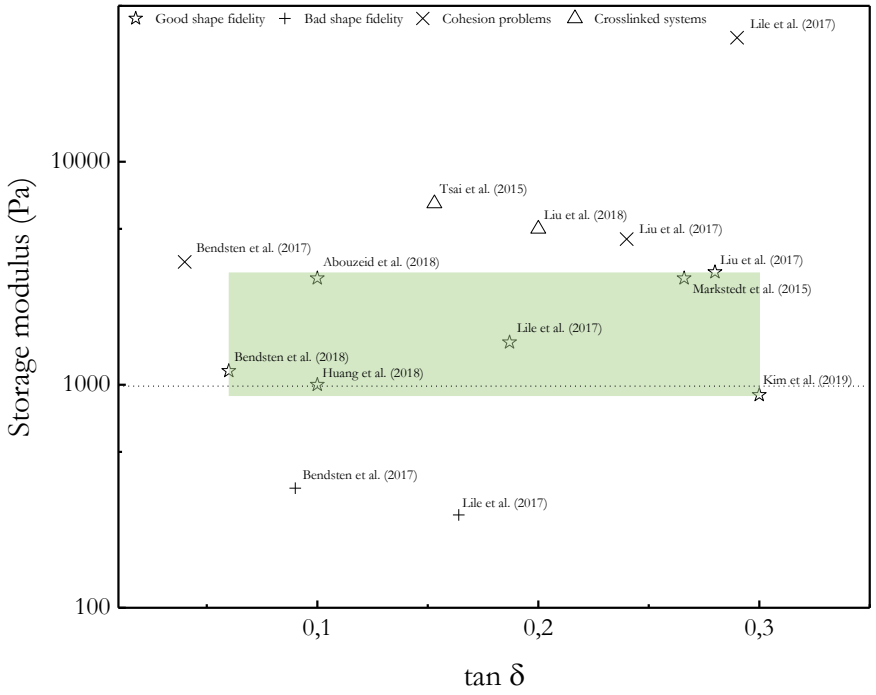

Figure 1.11 Comparison of the storage modulus and tan δ of different printed systems in the literature. (…) Good shape fidelity lower limit proposed by *Li et al.*, green region represents the ideal storage modulus and tan δ values square obtained from the consulted literature data [28,152,164,166–169].

Table 1.5 Storage modulus and tan δ values of inks in the literature

Storage modulus (Pa)	tan δ	Type of ink	Reference
2000-3000	0.20-0.30	Mashed potatoes	[163]
1500	0.19	Cellulose nanofibers/alginate	[164]
1500	0.18	Protein and fiber paste	[152]
3000	0.30	Polylactide-co-glycolide/graphene	[165]

Analysing the **Figure 1.11**, one can observe that all the reported systems presenting a good shape fidelity exhibit a storage modulus values in the range 900-3000 Pa and tan δ values between 0.06-0.3. Out of these values, systems presenting lower values of storage modulus showed bad shape fidelity, whereas inks presenting upper values showed cohesion problems between layers. Apart from that, posteriorly crosslinked systems presented storage modulus values in the range of the latter, however, since the crosslinking process happens after the printing process there is not any cohesion problems between layers.

Apart from the structuration of the inks, their capacity of recovering their initial state has to be studied in order to ensure that the ink is going to be able to maintain their structure after being processed. For that, in the literature, many tests, named as "shape recovery test" have been proposed so as to study this phenomenon. The principal one, is shown in **Figure 1.12**. The variation of the viscosity as a function of time by applying different shear rates simulates the different steps of the printing process: i) the shear rate is fixed to 1 s^{-1} to simulate the steady state of the ink, ii) the shear rate has been increased to 100 s^{-1} simulating the printing conditions and iii) the shear rate is reduced again until 1 s^{-1} simulating the recovery of the ink after being printed. The ratio between the viscosity measured in the first step and the one measured in the last one will indicate the recovery capacity of the system. Obviously, high values of structure recovery are needed so as to obtain inks which maintain their properties after the printing performance. In fact, according to the literature, *Peak et al.* reported that recovery percentages above 80% are significant for 3D-printing applications[147].

In this context, in **Table 1.6** the recovery values of different systems are displayed for comparative purposes. Apart from this test, other authors propose an alternative recovery test which is based on the variation of G' and G" as a function of time applying different shear stresses. The mechanism of the test follows the same way of the displayed one in the **Figure 1.12**, and presents a G' over G" at low rates and G" over G' at the printing stage, illustrating the flow of the ink during its extrusion [170,171].

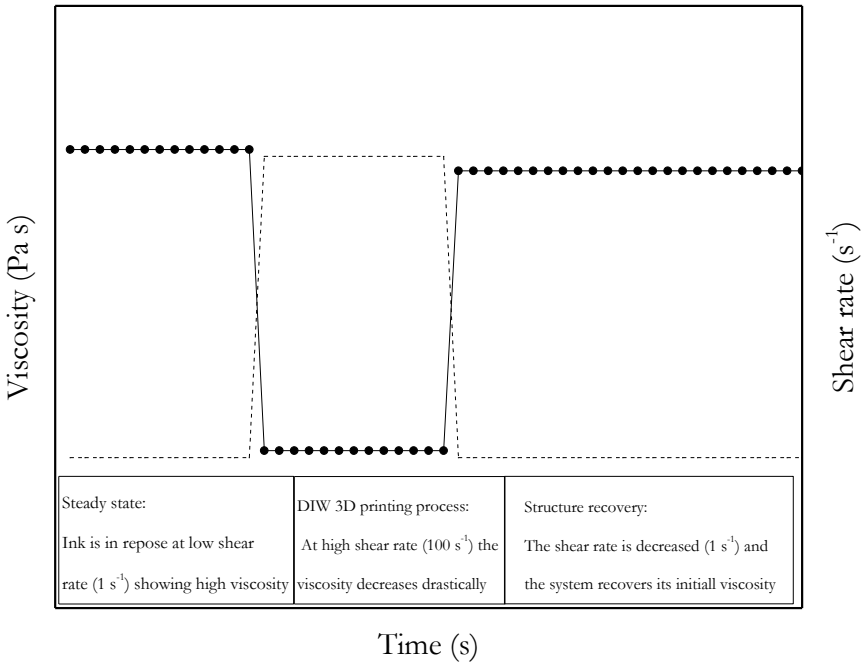

Figure 1.12 Scheme of the structure recovery test

Table 1.6 Structure recovery percentage values observed in the literature

Structure recovery (%)	Type of ink	Reference
85.5	Calcium alginate/ Graphene oxide	[124]
90-95	Laponite/alginate	[172]
>80%	PEG/laponite	[147]
66%	Cellulose nanofibers/alginate	[164]
>80%	Calcium alginate/carrageenan	[169]

In conclusion, regarding the shape fidelity, suitable inks for DIW 3D-printing have to present high enough storage modulus and low enough tan δ to support successfully the 3D-printing design and not collapse by their own weight, and also must present significantly high percentages of viscosity recovery so as to be able to recover their initial step.

1.5.1.3 Applications of DIW 3D-printing

As mentioned previously, the DIW 3D-printing presents multiple fields of application due to the aforementioned advantages compared with other advanced manufacturing techniques. Mainly they can be divided in the following categories: tissue engineering, wound dressing, functional materials, and others. The **Figure 1.13** shows the multiple application fields of this fabrication technique.

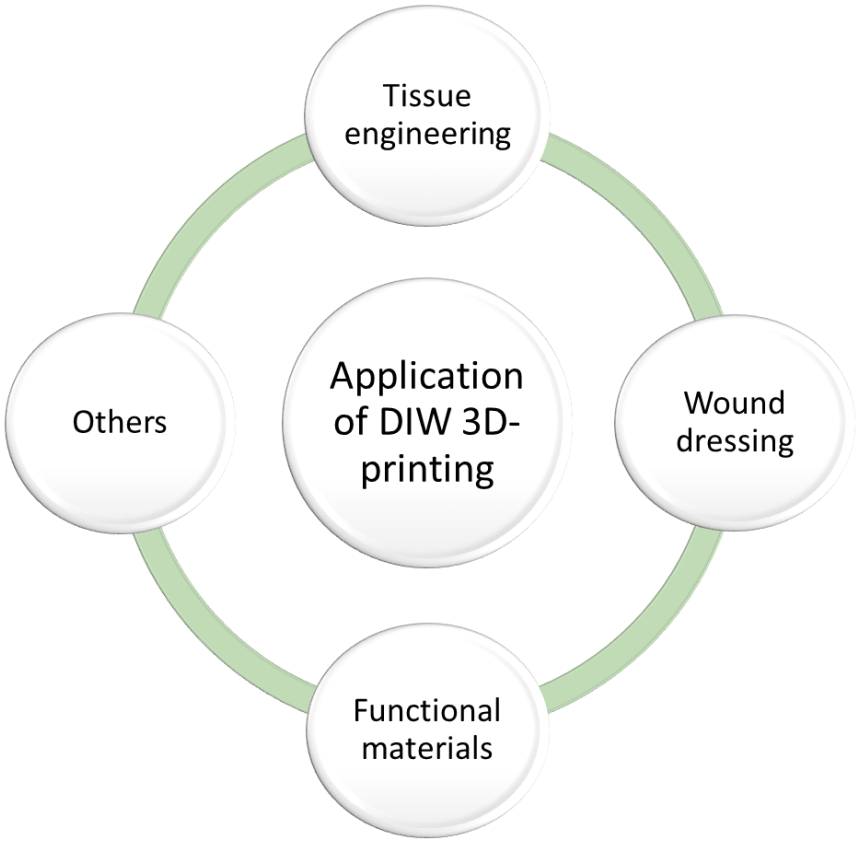

Figure 1.13 Graphical illustration of the principal application field of DIW 3D-printing

The materials used for the design of the inks used in DIW 3D-printing are usually biocompatible. In this context, the use of this technique in the tissue engineering field has been extensively studied in the literature: carbon nanotubes/agarose based ink for the printing of conductive scaffolds for biosensors or organ printing [173], nanocrystalline hydroxyapatite/alginate/gelatin based ink for the printing of scaffolds which promotes osteogenic differentiation for bone tissue engineering [174], nanocrystalline hydroxyapatite/collagen based ink for the internal microchannel generation for vascularized tissue engineering scaffolds [175], nanocrystalline hydroxyapatite/chitosan based ink for improve the cell viability, proliferation and osteogenic differentiation in bone tissue engineering [176] and nanocellulose/alginate gelatin based ink for printing scaffolds with

controlled pore size for tissue regeneration [177], represent among others examples of a promising use of DIW 3D-printing in this field.

Regarding the wound dressing applications, *Leppiniemi et al.* printed a nanocellulose/alginate hydrogel whose absorbing water capacity in moist conditions suggests its potential in wound dressings [178]. Moreover, *Maver et al.* combined DIW 3D-printing and electrospinning to design a carboxymethyl cellulose based scaffold which contained lidocaine and presented a good drug release [179]. *Reese et al.* also proposed a nanocellulose based compound, concretely, carboxymethylated periodate oxidized nanocellulose, as a 3D-printing construct which presented a potential to carry and release antimicrobial components not showing bacterial growth in the printed scaffold [180]. Finally, *Intini et al.* fabricated a chitosan based scaffold which exhibited excellent biocompatibility and cytotoxicity toward two different skin associated human cell lines, being a promising material for wound dressing applications [181].

Moreover, in the literature, DIW 3D-printing has also been reported as an advanced manufacturing technique for the printing of functional materials. *Zhong et al.* designed a printable and conductive ink containing graphene for the fabrication of self-sensing composites [182], whereas *Wu et al.* used DIW 3D-printing in order to fabricate a polybutylene succinate/graphene composite which presented self-healing properties for its application in autonomous structures [183].

The water treatment, desalinization and membrane separation fields also presented developments based on the DIW 3D-printing. For example, *Appuhamillage et al.* developed an ink based on chitosan and diacrylated Pluronic F-127 to construct hydrogels for heavy metal ion removal (Cu^{2+}, Pb^{2+}, Cd^{2+}, Hg^{2+}) [184], whereas *Li et al.* printed a highly porous all in one evaporator for high efficiency solar steam generation [185]. Finally, many soft and flexible graphene foam structures can be fabricated by DIW 3D-printing [186]. These structures demonstrate a great potential in energy storage field owing to their large superficial area, high electrical conductivity and lightweight features. Moreover, some interesting soft sensors [187] and robots can also be developed by DIW 3D-printing [188].

1.6 References

[1] D.K. Chattopadhyay, K.V.S.N. Raju, Structural engineering of polyurethane coatings for high performance applications, Prog. Polym. Sci. 32 (2007) 352–418.

https://doi.org/10.1016/j.progpolymsci.2006.05.003.

[2] H. Honarkar, Waterborne polyurethanes: A review, J. Dispers. Sci. Technol. 39 (2018) 507. https://doi.org/10.1080/01932691.2017.1327818.

[3] H. Hao, J. Shao, Y. Deng, S. He, F. Luo, Y. Wu, J. Li, H. Tan, J. Li, Q. Fu, Synthesis and characterization of biodegradable lysine-based waterborne polyurethane for soft tissue engineering applications, Biomater. Sci. 4 (2016) 1682–1690. https://doi.org/10.1039/c6bm00588h.

[4] Z. Wang, Z. Hou, Y. Wang, Fluorinated waterborne shape memory polyurethane urea for potential medical implant application, J. Appl. Polym. Sci. 127 (2012) 710–716. https://doi.org/10.1002/app.37862.

[5] Z.H. Fang, H.Y. Duan, Z.H. Zhang, J. Wang, D.Q. Li, Y.X. Huang, J.J. Shang, Z.Y. Liu, Novel heat-resistance UV curable waterborne polyurethane coatings modified by melamine, Appl. Surf. Sci. 257 (2011) 4765–4768. https://doi.org/10.1016/j.apsusc.2010.10.082.

[6] G. Woods, The ICI polyurethanes book, 2nd ed., Jon Wiley & Sons, 1990.

[7] M. Marzec, J. Kucińska-Lipka, I. Kalaszczyńska, H. Janik, Development of polyurethanes for bone repair, Mater. Sci. Eng. C. 80 (2017) 736–747. https://doi.org/10.1016/j.msec.2017.07.047.

[8] P.M. Kapatel, R.H. Patel, Green approach for the development of novel flame retardant waterborne polyurethanes: Synthesis and its characterizations, Mater. Today Proc. 23 (2020) 389–399. https://doi.org/10.1016/j.matpr.2020.02.058.

[9] I. Yilgör, E. Yilgör, G.L. Wilkes, Critical parameters in designing segmented polyurethanes and their effect on morphology and properties: A comprehensive review, Polym. (United Kingdom) 58 (2015) A1–A36. https://doi.org/10.1016/j.polymer.2014.12.014.

[10] F.M.B. Coutinho, M.C. Delpech, T.L. Alves, A.A. Ferreira, Degradation profiles of cast films of polyurethane and poly (urethane-urea) aqueous dispersions based on hydroxy- terminated polybutadiene and different diisocyanates, Polym. Degrad. Stab. 81 (2003) 19–27. https://doi.org/10.1016/S0141-3910(03)00058-2.

[11] H. Lee, S. Wu, R. Jeng, Effects of sulfonated polyol on the properties of the

resultant aqueous polyurethane dispersions, Colloids Surf. A 276 (2006) 176–185. https://doi.org/10.1016/j.colsurfa.2005.10.034.

[12] V. García-Pacios, Y. Iwata, M. Colera, J.M. Martín-Martínez, Influence of the solids content on the properties of waterborne polyurethane dispersions obtained with polycarbonate of hexanediol, Int. J. Adhes. 31 (2011) 787–794. https://doi.org/10.1016/j.ijadhadh.2011.05.010.

[13] J. Hong, X.-Q. Yang, X. Wan, Z. Zheng, Z.S. Petrovic, Z. Zheng, J. Hong, Z.S. Petrovic, High value polyurethane resins from rubber seed oil, Polym. Int. 66 (2017) 126–132. https://doi.org/10.1002/pi.5256

[14] M. Pohl, E. Danieli, M. Leven, W. Leitner, Dynamics of polyether polyols and polyether carbonate polyols, macromolecules 49 (2016) 8995–9003. https://doi.org/10.1021/acs.macromol.6b01601.

[15] K. Gorna, S. Polowinski, S. Gogolewski, Synthesis and characterization of biodegradable poly (ε -caprolactone urethane). I . Effect of the polyol molecular weight , catalyst , and chain extender on the molecular and physical characteristics, J. Polym. Sci. Part A Polym. Chem. 40 (2002) 156–170. https://doi.org/10.1002/pola.10096.

[16] S.M. Cakić, I.S. Ristić, O.Z. Ristić, Thermal Analysis of Polyurethane Dispersions Based on Different Polyols, in: F. Zafar, E. Sharmin (Eds.), Polyurethane, IntechOpen, London, 2012, 79–100. https://doi.org/10.5772/35800.

[17] X. Jiang, J. Li, M. Ding, H. Tan, Q. Ling, Y. Zhong, Q. Fu, Synthesis and degradation of nontoxic biodegradable waterborne polyurethanes elastomer with poly (ε -caprolactone) and poly (ethylene glycol) as soft segment, Eur. Polym. J. 43 (2007) 1838–1846. https://doi.org/10.1016/j.eurpolymj.2007.02.029.

[18] R.S. Labow, E. Meek, J.P. Santerre, Hydrolytic degradation of poly (carbonate) - urethanes by monocyte-derived macrophages, Biomaterials 22 (2001) 3025–3033. https://doi.org/10.1016/s0142-9612(01)00049-7

[19] E.M. Christenson, M. Dadsetan, M. Wiggins, J.M. Anderson, A. Hiltner, Poly (carbonate urethane) and poly (ether urethane) biodegradation: In vivo studies, J. Biomed. Mater. Res. Part A. 69 (2004) 407–416. https://doi.org/10.1002/jbm.a.30002.

[20] S.M. Cakić, M. Špírková, I.S. Ristić, J.K. B-Simendić, M. M-Cincović, R. Poręba, The waterborne polyurethane dispersions based on polycarbonate diol: Effect of ionic content, Mater. Chem. Phys. 138 (2013) 277–285. https://doi.org/10.1016/j.matchemphys.2012.11.057.

[21] W. Zhang, Y. Zhang, H. Liang, D. Liang, H. Cao, C. Liu, High bio-content castor oil based waterborne polyurethane/sodium lignosulfonate composites for environmental friendly UV absorption application, Ind. Crop. Prod. 142 (2019) 111836. https://doi.org/10.1016/j.indcrop.2019.111836.

[22] Y. Zhang, W. Zhang, X. Wang, Q. Dong, X. Zeng, R.L. Quirino, Q. Lu, Q. Wang, C. Zhang, Waterborne polyurethanes from castor oil-based polyols for next generation of environmentally-friendly hair-styling agents, Prog. Org. Coatings. 142 (2020) 105588. https://doi.org/10.1016/j.porgcoat.2020.105588.

[23] L. Man, Y. Feng, Y. Hu, T. Yuan, Z. Yang, A renewable and multifunctional eco-friendly coating from novel tung oil-based cationic waterborne polyurethane dispersions, J. Clean. Prod. 241 (2019) 118341. https://doi.org/10.1016/j.jclepro.2019.118341.

[24] H.J. Yoo, H. Do Kim, Synthesis and properties of waterborne polyurethane hydrogels for wound healing dressings, J. Biomed. Mater. Res. - Part B Appl. Biomater. 85 (2008) 326–333. https://doi.org/10.1002/jbm.b.30950.

[25] J.H. Jeong, Y.C. Han, J.H. Yang, D.S. Kwak, H.M. Jeong, Waterborne polyurethane modified with poly(ethylene glycol) macromer for waterproof breathable coating, Prog. Org. Coatings. 103 (2017) 69–75. https://doi.org/10.1016/j.porgcoat.2016.10.004.

[26] M. Fuensanta, J.A. Jofre-Reche, F. Rodríguez-Llansola, V. Costa, J.I. Iglesias, J.M. Martín-Martínez, Structural characterization of polyurethane ureas and waterborne polyurethane urea dispersions made with mixtures of polyester polyol and polycarbonate diol, Prog. Org. Coatings. 112 (2017) 141–152. https://doi.org/10.1016/j.porgcoat.2017.07.009.

[27] S.H. Hsu, C.W. Chen, K.C. Hung, Y.C. Tsai, S. Li, Thermo-responsive polyurethane hydrogels based on poly(ε-caprolactone) diol and amphiphilic polylactide-poly(ethylene glycol) block copolymers, Polymers 8 (2016). https://doi.org/10.3390/polym8070252.

[28] Y.C. Tsai, S. Li, S.G. Hu, W.C. Chang, U.S. Jeng, S.H. Hsu, Synthesis of thermoresponsive amphiphilic polyurethane gel as a new cell printing material near body temperature, ACS Appl. Mater. Interfaces 7 (2015) 27613–27623. https://doi.org/10.1021/acsami.5b10697.

[29] D. Lee, H. Tsai, Properties of segmented polyurethanes derived from different diisocyanates, J. Appl. Polym. Sci. 75 (1999) 167–174. https://doi.org/10.1002/(SICI)1097-4628(20000103)75:1<167::AID-APP19>3.0.CO;2-N.

[30] Y.W. Tang, R.S. Labow, J.P. Santerre, Enzyme-induced biodegradation of polycarbonate polyurethanes : Dependence on hard-segment concentration, J. Biomed. Mater. Res. 56 (2001) 516–528. https://doi.org/10.1002/1097-4636(20010915)56:4<516::aid-jbm1123>3.0.co;2-b.

[31] Y.W. Tang, R.S. Labow, J.P. Santerre, Isolation of methylene dianiline and aqueous-soluble biodegradation products from polycarbonate-polyurethanes, Biomaterials 24 (2003) 2805–2819. https://doi.org/10.1016/S0142-9612(03)00081-4.

[32] S.M. Cakic, J. V. Stamenkovic, D.M. Djordjevic, I.S. Ristic, Synthesis and degradation profile of cast films of PPG-DMPA-IPDI aqueous polyurethane dispersions based on selective catalysts, Polym. Degrad. Stab. 94 (2009) 2015–2022. https://doi.org/10.1016/j.polymdegradstab.2009.07.015.

[33] K. Wang, Y. Peng, R. Tong, Y. Wang, Z. Wu, The effects of isocyanate index on the properties of aliphatic waterborne polyurethaneureas, J. Appl. Polym. Sci. 118 (2010) 920–927. https://doi.org/10.1002/app.

[34] P. Król, Synthesis methods, chemical structures and phase structures of linear polyurethanes. Properties and applications of linear polyurethanes in polyurethane elastomers, copolymers and ionomers, Prog. Mater. Sci. 52 (2007) 915–1015. https://doi.org/10.1016/j.pmatsci.2006.11.001.

[35] S.K. Lee, B.K. Kim, High solid and high stability waterborne polyurethanes via ionic groups in soft segments and chain termini, J. Colloid Interface Sci. 336 (2009) 208–214. https://doi.org/10.1016/j.jcis.2009.03.028.

[36] S. Sakurai, Y. Okamoto, H. Sakaue, T. Nakamura, L. Banda, S. Nomura, Structure and properties of segmented poly (urethaneurea) s with relatively short hard-

segment chains, J. Polym. Sci. Part B. 38 (2000) 1716–1728. https://doi.org/10.1002/1099-0488(20000701)38:13<1716::AID-POLB50>3.0.CO;2-X

[37] M. Barikani, M.V. Ebrahimi, S.M.S. Mohaghegh, Preparation and characterization of aqueous polyurethane dispersions containing ionic centers, J. Appl. Polym. Sci. 104 (2006) 3931–3937. https://doi.org/10.1002/app.

[38] B. Li, D. Peng, N. Zhao, Q. Mu, J. Li, The physical properties of nonionic waterborne polyurethane with a polyether as side chain, J. Appl. Polym. Sci. 127 (2013) 1848–1852. https://doi.org/10.1002/app.37915.

[39] O. Jaudouin, J. Robin, J.-M. Lopez-Cuesta, D. Perrin, C. Imbert, Ionomer-based polyurethanes: a comparative, Polym. Int. 61 (2012) 495–510. https://doi.org/10.1002/pi.4156.

[40] A.M. Nelson, T.E. Long, Synthesis, properties , and applications of ion-containing polyurethane segmented copolymers, Macromol. Chem. Phys. 215 (2014) 2161–2174. https://doi.org/10.1002/macp.201400373.

[41] X. Dang, G. Wang, D. Wang, T. Pan, L. Zhou, X. Shi, Distribution of hydrophilic monomer units and its effect on the property of the water dispersion of polyurethaneurea anionomer, J. Appl. Polym. Sci. 103 (2007) 634–640. https://doi.org/10.1002/app.

[42] T.F. Garrison, Z. Zhang, H. Kim, D. Mitra, Y. Xia, D.P. Pfister, B.F. Brehm-stecher, R.C. Larock, M.R. Kessler, Thermo-mechanical and antibacterial properties of soybean oil-based cationic polyurethane coatings: Effects of amine ratio and degree of crosslinking, Macromol. Mater. Eng. 299 (2014) 1042–1051. https://doi.org/10.1002/mame.201300423.

[43] C. Hepburn, Polyurethane Elastomers, Springer Netherlands, 1992.

[44] H. Sardon, L. Irusta, Synthesis of isophorone diisocyanate (IPDI) based waterborne polyurethanes: Comparison between zirconium and tin catalysts in the polymerization process, Prog. Org. Coatings. 66 (2009) 291–295. https://doi.org/10.1016/j.porgcoat.2009.08.005.

[45] A. Santamaria-Echart, I. Fernandes, A. Saralegi, M.R.P.F.N. Costa, F. Barreiro, M.A. Corcuera, A. Eceiza, Synthesis of waterborne polyurethane-urea dispersions with

chain extension step in homogeneous and heterogeneous media, J. Colloid Interface Sci. 476 (2016) 184–192. https://doi.org/10.1016/j.jcis.2016.05.016.

[46] C. Fang, S. Pan, Z. Wang, X. Zhou, W. Lei, Y. Cheng, Synthesis of waterborne polyurethane using snow as dispersant: Structures and properties controlled by polyols utilization, J. Mater. Sci. Technol. 35 (2019) 1491–1498. https://doi.org/10.1016/j.jmst.2019.03.017.

[47] D.J. Hourston, G.D. Williams, R. Satguru, J.C. Padget, D. Pears, The influence of the degree of neutralization , the ionic moiety , and the counterion on water-dispersible polyurethanes, J. Appl. Polym. Sci. 74 (1999) 556–566. https://doi.org/10.1002/(SICI)1097-4628(19991017)74:3<556::AID-APP10>3.0.CO;2-D

[48] S.-H. Son, H.-J. Lee, J. Kim, Effects of carboxyl groups dissociation and dielectric constant on particle size of polyurethane dispersions, Colloids Surfaces A 133 (1998) 295–301. https://doi.org/10.1016/S0927-7757(97)00201-X

[49] L. Lei, L. Zhong, X. Lin, Y. Li, Z. Xia, Synthesis and characterization of waterborne polyurethane dispersions with different chain extenders for potential application in waterborne ink, Chem. Eng. J. 253 (2014) 518–525. https://doi.org/10.1016/j.cej.2014.05.044.

[50] I. Díez-García, A. Santamaría-Echart, A. Eceiza, A. Tercjak, Synthesis and characterization of environmentally-friendly waterborne poly(urethane-urea)s, Eur. Polym. J. 99 (2018) 240–249. https://doi.org/10.1016/j.eurpolymj.2017.12.026.

[51] J. Bullermann, S. Friebel, T. Salthammer, R. Spohnholz, Novel polyurethane dispersions based on renewable raw materials - Stability studies by variations of DMPA content and degree of neutralisation, Prog. Org. Coatings. 76 (2013) 609–615. https://doi.org/10.1016/j.porgcoat.2012.11.011.

[52] C.R. Silva, P.S. Babo, M. Gulino, L. Costa, M. Joaquim, J. Silva-Correia, R.M.A. Domingues, R.L. Reis, E. Manuela, Injectable and tunable hyaluronic acid hydrogels releasing chemotactic and angiogenic growth factors for endodontic regeneration, Acta Biomater. 77 (2018) 155–171. https://doi.org/10.1016/j.actbio.2018.07.035.

[53] S. Huang, X. Liu, C. Chang, Y. Wang, Recent developments and prospective food-related applications of cellulose nanocrystals: a review, Cellulose 3 (2020).

https://doi.org/10.1007/s10570-020-02984-3.

[54] C. Calvino, N. Macke, R. Kato, S.J. Rowan, Development, processing and aplications of bio-sourced cellulose nanocrystal composites, Prog. Polym. Sci. In Press (2020). https://doi.org/10.1016/j.progpolymsci.2020.101221.

[55] M. Kaushik, A. Moores, Nanocelluloses as versatile supports for metal nanoparticles and their applications in catalysis, Green Chem. 18 (2016) 622–637. https://doi.org/10.1039/C5GC02500A.

[56] M.A. Mohamed, W.N.W. Salleh, J. Jaafar, A.F. Ismail, M.A. Mutalib, A.B. Mohamad, M.F.M. Zain, N.A. Awang, Z. Adlan, M. Hir, Physicochemical characterization of cellulose nanocrystal and nanoporous self-assembled CNC membrane derived from Ceiba Pentandra, Carbohydr. Polym. (2016). https://doi.org/10.1016/j.carbpol.2016.11.078.

[57] I. Capron, O.J. Rojas, R. Bordes, Behavior of nanocelluloses at interfaces, Curr. Opin. Colloid Interface Sci. 29 (2017) 83–95. https://doi.org/10.1016/j.cocis.2017.04.001.

[58] Y. Habibi, L.A. Lucia, O.J. Rojas, Cellulose nanocrystals: Chemistry, self-Assembly , and applications, Chem. Rev. 110 (2010) 3479–3500. https://doi.org/10.1021/cr900339w.

[59] M. Hasani, E.D. Cranston, G. Westman, D.G. Gray, Cationic surface functionalization of cellulose nanocrystals, Soft Matter. 4 (2008) 2238–2244. https://doi.org/10.1039/b806789a.

[60] W. Chen, H. Yu, Q. Li, J. Li, Ultralight and highly flexible aerogels with long cellulose I nanofibers, Soft Matter. 7 (2011) 10360–10368. https://doi.org/10.1039/c1sm06179h.

[61] M.A.S.A. Samir, F. Alloin, A. Dufresne, Review of recent research into cellulosic whiskers, their properties and their application in nanocomposite field, Biomacromolecules. 6 (2005) 612–626. https://doi.org/10.1021/bm0493685.

[62] Y. Chimeni, G.K. Yoya, T. Stevanovic, D. Rodrigue, Surface modification of cellulosic materials for polyethylene composite applications, Polym. Compos. 40 (2017) E202–E213. https://doi.org/10.1002/pc.24602.

[63] M. Mariano, N. El Kissi, A. Dufresne, Cellulose Nanocrystals and related nanocomposites: Review of some properties and challenges, J. Polym. Sci. Part B Polym. Phys. 52 (2014) 791–806. https://doi.org/10.1002/polb.23490.

[64] G. Mondragon, A. Santamaria-Echart, M.E. V. Hormaiztegui, A. Arbelaiz, C. Peña-Rodriguez, V. Mucci, M. Corcuera, M.I. Aranguren, A. Eceiza, Nanocomposites of waterborne polyurethane reinforced with cellulose nanocrystals from sisal fibres, J. Polym. Environ. 26 (2017) 1869–1880. https://doi.org/10.1007/s10924-017-1089-z.

[65] S.M. Choi, M.W. Lee, E.J. Shin, One-pot processing of regenerated cellulose nanoparticles/waterborne polyurethane, Polymers 11 (2019). https://doi.org/10.3390/polym11020356.

[66] P. Zhang, Y. Lu, M. Fan, P. Jiang, Y. Dong, Modified cellulose nanocrystals enhancement to mechanical properties and water resistance of vegetable oil-based waterborne polyurethane, J. Appl. Polym. Sci. 136 (2019) 48228–48236. https://doi.org/10.1002/app.48228.

[67] A. Santamaria-Echart, L. Ugarte, A. Arbelaiz, N. Gabilondo, M.A. Corcuera, A. Eceiza, Two different incorporation routes of cellulose nanocrystals in waterborne polyurethane nanocomposites, Eur. Polym. J. 76 (2016) 99–109. https://doi.org/10.1016/j.eurpolymj.2016.01.035.

[68] W. Lei, X. Zhou, C. Fang, Y. Song, Y. Li, Eco-friendly waterborne polyurethane reinforced with cellulose nanocrystal from office waste paper by two different methods, Carbohydr. Polym. 209 (2019) 299–309. https://doi.org/10.1016/j.carbpol.2019.01.013.

[69] M. Carocho, M.J.R.. Calhelha, A. Queiroz, P. Morales, M. Sokovic, I.C.F.R. Ferreira, Infusions and decoctions of castanea sativa flowers as effective antitumor and antimicrobial matrices, Ind. Crop. Prod. 62 (2014) 42–46. https://doi.org/10.1016/j.indcrop.2014.08.016.

[70] K. Rashed, A. Ciric, J. Glamoclija, R.C. Calhelha, I.C.F.R. Ferreira, M. Sokovíc, Antimicrobial and cytotoxic activities of Alnus rugosa L . aerial parts and identification of the bioactive components, Ind. Crops Prod. 59 (2014) 189–196. https://doi.org/10.1016/j.indcrop.2014.05.017.

[71] A. Santamaria-Echart, I. Fernandes, F. Barreiro, A. Retegi, Development of waterborne polyurethane-ureas added with plant extracts: Study of different incorporation routes and their influence on particle size, thermal, mechanical and antibacterial properties, Prog. Org. Coatings. 117 (2018) 76–90. https://doi.org/10.1016/j.porgcoat.2018.01.006.

[72] A.A. Mostafa, A.A. Al-askar, K.S. Almaary, T.M. Dawoud, E.N. Sholkamy, M.M. Bakri, Antimicrobial activity of some plant extracts against bacterial strains causing food poisoning diseases, Saudi J. Biol. Sci. 25 (2018) 361–366. https://doi.org/10.1016/j.sjbs.2017.02.004.

[73] N. Martins, L. Barros, C. Santos-buelga, M. Henriques, S. Silva, I.C.F.R. Ferreira, Evaluation of bioactive properties and phenolic compounds in different extracts prepared from Salvia officinalis L , Food Chem. 170 (2014) 378–385. https://doi.org/10.1016/j.foodchem.2014.08.096.

[74] M. Ghorbanpour, M. Hatami, K. Kariman, P. Dahaji, Phytochemical variations and enhanced efficiency of antioxidant and antimicrobial ingredients in salvia officinalis as inoculated with different Rhizobacteria, Chem. Biodivers. 13 (2016) 319–330. https://doi.org/10.1002/cbdv.201500082.

[75] O. Stefanovic, L. Comic, Synergistic antibacterial interaction between Melissa officinalis extracts and antibiotics, J. Appl. Pharm. Sci. 02 (2012) 1–5.

[76] B. Pawlikowska-Pawlega, L.E. Misiak, B. Zarzyka, R. Paduch, A. Gawron, I. Gruszecki, FTIR , 1 H NMR and EPR spectroscopy studies on the interaction of flavone apigenin with dipalmitoylphosphatidylcholine liposomes, Biochim. Biophys. Acta 1828 (2013) 518–527. https://doi.org/10.1016/j.bbamem.2012.10.013.

[77] R. Venkataswamy, A. Doss, H.M. Mubarack, M. Sukumar, Phytochemical , HPTLC finger printing and antibacterial activity of Acacia nilotica (L .) Delile, Hygeia. J. Drugs Med. 2 (2010) 38–42.

[78] Q. Yan, H. Dong, J. Su, J. Han, B. Song, Q. Wei, Y. Shi, A review of 3D printing technology for medical applications, Engineering 4 (2018). https://doi.org/10.1016/j.eng.2018.07.021.

[79] T.D. Ngo, A. Kashani, G. Imbalzano, K.T.Q. Nguyen, D. Hui, Additive manufacturing (3D printing): A review of materials , methods , applications and

challenges, Compos. Part B. 143 (2018) 172–196. https://doi.org/10.1016/j.compositesb.2018.02.012.

[80] H. Kodama, Automatic method for fabricating a three-dimensional plastic model with photo-hardening polymer, Rev. Sci. Instrum. 52 (1981) 1770–1773. https://doi.org/10.1063/1.1136492.

[81] H. Kodama, A scheme for three-dimensional display by automatic fabrication of three-dimensional model, IEICE Trans. Electron. J64-C (1981) 237–241.

[82] A. Ambrosi, R.D. Webster, 3D printing for aqueous and non-aqueous redox flow batteries, Curr. Opin. Electrochem. 20 (2020) 28–35. https://doi.org/10.1016/j.coelec.2020.02.005.

[83] S. Bose, S. Vahabzadeh, A. Bandyopadhyay, Bone tissue engineering using 3D printing, Mater. Today. 16 (2013) 496–504. https://doi.org/10.1016/j.mattod.2013.11.017.

[84] C. Wee, J. Lim, K.Q. Le, Q. Lu, C.H. Wong, An overview of 3D printing in the manufacturing, aerospace, and automotive industries, Smart Manuf. 35 (2016) 18–22. https://doi.org/10.1109/MPOT.2016.2540098

[85] Y. Ni, R. Ji, K. Long, T. Bu, K. Chen, S. Zhuang, A review of 3D-printed sensors, Appl. Spectrosc. Rev. 52 (2017) 623–652. https://doi.org/10.1080/05704928.2017.1287082.

[86] M. Nikzad, S.H. Masood, I. Sbarski, Thermo-mechanical properties of a highly filled polymeric composites for fused deposition modeling, Mater. Des. 32 (2011) 3448–3456. https://doi.org/10.1016/j.matdes.2011.01.056.

[87] W. Zhong, F. Li, Z. Zhang, L. Song, Z. Li, Short fiber reinforced composites for fused deposition modeling, Mater. Sci. Eng. A. 301 (2001) 125–130. https://doi.org/10.1016/S0921-5093(00)01810-4.

[88] S. Hwang, E.I. Reyes, K. Moon, R.C. Rumpf, N.S. Kim, Thermo-mechanical characterization of metal/polymer composite filaments and printing parameter study for fused deposition modeling in the 3D printing process, J. Electron. Mater. 44 (2015) 771–777. https://doi.org/10.1007/s11664-014-3425-6.

[89] X. Wang, M. Jiang, Z. Zhou, J. Gou, D. Hui, 3D printing of polymer matrix

composites: A review and prospective, Compos. Part B. 110 (2017) 442–458. https://doi.org/10.1016/j.compositesb.2016.11.034.

[90] M. Kurimoto, Y. Yamashita, H. Ozaki, T. Kato, T. Funabashi, Y. Suzuoki, 3D Printing of conical insulating spacer using alumina/UV-cured-resin composite, Annu. Rep. Conf. Electr. Insul. Dielectr. Phenom. (2015) 463–466. https://doi.org/10.1109/CEIDP.2015.7352047.

[91] J. Kruth, P. Mercelis, J. Van Vaerenbergh, L. Froyen, M. Rombouts, Binding mechanisms in selective laser sintering and selective laser melting, Rapid Prototyp. J. 11 (2005) 26–36. https://doi.org/10.1108/13552540510573365.

[92] Q. Yang, H. Li, Y. Zhai, X. Li, P. Zhang, The synthesis of epoxy resin coated Al_2O_3 composites for selective laser sintering 3D printing, Rapid Prototyp. J. 6 (2018) 1059–1066. https://doi.org/10.1108/RPJ-09-2017-0189.

[93] P. Shakor, S. Nejadi, G. Paul, J. Sanjayan, Automation in construction dimensional accuracy, flowability, wettability, and porosity in inkjet 3DP for gypsum and cement mortar materials, Autom. Constr. 110 (2020) 102964. https://doi.org/10.1016/j.autcon.2019.102964.

[94] S. V Murphy, A. Atala, Review 3D bioprinting of tissues and organs, Nat. Publ. Gr. 32 (2014) 773–785. https://doi.org/10.1038/nbt.2958.

[95] J.E. Smay, J.C. Iii, J.A. Lewis, Colloidal inks for directed assembly of 3-D periodic structures, Langmuir 84 (2002) 5429–5437. https://doi.org/10.1021/la0257135.

[96] H. Hsu, Y. Lo, M. Lee, Vision-based inspection system for cladding height measurement in direct energy deposition (DED), Addit. Manuf. 27 (2019) 372–378. https://doi.org/10.1016/j.addma.2019.03.017.

[97] S.J. Wolff, S. Lin, E.J. Faierson, W.K. Liu, G.J. Wagner, J. Cao, A framework to link localized cooling and properties of directed energy deposition (DED) -processed Ti-6Al-4V, Acta Mater. 132 (2017) 106–117. https://doi.org/10.1016/j.actamat.2017.04.027.

[98] I. Gibson, D. Rosen, B. Stucker, Additive manufacturing technologies: 3D printing, rapid prototyping, and direct digital manufacturing, Springer-Verlag New York, 2015.

[99] H. Kang, S.J. Lee, I.K. Ko, C. Kengla, J.J. Yoo, A. Atala, A 3D bioprinting system to produce human-scale tissue constructs with structural integrity, Nat. Biotechnol. 34 (2016) 312–319. https://doi.org/10.1038/nbt.3413.

[100] J. Visser, B. Peters, T.J. Burger, J. Boomstra, W.J.A. Dhert, F.P.W. Melchels, J. Malda, Biofabrication of multi-material anatomically shaped tissue constructs, Biofabrication 5 (2013) 1–9. https://doi.org/10.1088/1758-5082/5/3/035007.

[101] D.B. Kolesky, R.L. Truby, A.S. Gladman, T.A. Busbee, K.A. Homan, J.A. Lewis, 3D Bioprinting of vascularized, heterogeneous cell-laden tissue constructs, Adv. Mater. 26 (2014) 3124–3130. https://doi.org/10.1002/adma.201305506.

[102] D.L. Cohen, E. Malone, H. Lipson, L.J. Bonassar, Direct freeform fabrication of seeded hydrogels in arbitrary geometries, Tissue Eng. 12 (2006) 1325–1335. doi: 10.1089/ten.2006.12.1325.

[103] T. Billiet, M. Vandenhaute, J. Schelfhout, S. Van Vlierberghe, P. Dubruel, Biomaterials A review of trends and limitations in hydrogel-rapid prototyping for tissue engineering, Biomaterials 33 (2012) 6020–6041. https://doi.org/10.1016/j.biomaterials.2012.04.050.

[104] T.J. Hinton, Q. Jallerat, R.N. Palchesko, J.H. Park, M.S. Grodzicki, H. Shue, M.H. Ramadan, A.R. Hudson, A.W. Feinberg, Three-dimensional printing of complex biological structures by freeform reversible embedding of suspended hydrogels, Biomed. Eng. 1 (2015). https://doi.org/10.1126/sciadv.1500758.

[105] K. Hölzl, S. Lin, L. Tytgat, S. Van Vlierberghe, L. Gu, A. Ovsianikov, Bioink properties before , during and after 3D bioprinting, Biofabrication 8 (2016) 1–19. https://doi.org/10.1088/1758-5090/8/3/032002.

[106] W. Li, A. Ghazanfari, M.C. Leu, R.G. Landers, Methods of extrusion on demand for high solids loading ceramic paste in freeform extrusion fabrication, Int. Solid Free. Fabr. Symp. (2015) 332–345.

[107] W. Wang, L. Yao, T. Zhang, C. Cheng, D. Levine, H. Ishii, Transformative appetite: shape-changing food transforms from 2D to 3D by Water Interaction through Cooking, in: Proc. 2017 CHI Conf. Hum. Factors Comput. Syst. (2017).

[108] L. Ouyang, R. Yao, Y. Zhao, W. Sun, Effect of bioink properties on printability and cell viability for 3D bioplotting of embryonic stem cells, Biofabrication 8 (2016) 1–

12. https://doi.org/10.1088/1758-5090/8/3/035020.

[109] R. Chang, J.A.E. Nam, W.E.I. Sun, Effects of dispensing pressure and nozzle diameter direct cell writing, Tissue Eng. Part A. 14 (2008). https://doi.org/10.1089/ten.a.2007.0004.

[110] A. Pekarovicova, H. Bhide, P.D. Fleming III, J. Pekarovic, Phase-Change Inks, J. Coatings Technol. 75 (2003) 65–72. https://doi.org/10.1007/BF02697924.

[111] J. Jia, D.J. Richards, S. Pollard, Y. Tan, J. Rodriguez, R.P. Visconti, T.C. Trusk, M.J. Yost, H. Yao, R.R. Markwald, Y. Mei, Engineering alginate as bioink for bioprinting, Acta Biomater. 10 (2014) 4323–4331. https://doi.org/10.1016/j.actbio.2014.06.034.

[112] B. Ye, H. Xu, B. Bao, L. Zhang, 3D-printed air-blast microfluidic nozzles for preparing calcium alginate microparticles, RSC Adv. 7 (2017) 48826–48834. https://doi.org/10.1039/C7RA08611C.

[113] D. Bociaga, M. Bartniak, J. Grabarczyk, K. Przybyszewska, Sodium alginate/gelatine hydrogels for direct bioprinting—The effect of composition selection and applied solvents on the bioink properties, Materials 12 (2019) 2669–2681. doi: 10.3390/ma12172669.

[114] T. Zhang, Y. Yan, X. Wang, Z. Xiong, F. Lin, R. Wu, R. ZHang, Compatible polymers three-dimensional gelatin and gelatin/hyaluronan hydrogel structures for traumatic brain, J. Bioact. Compat. Polyerms. 22 (2007) 19–29. https://doi.org/10.1177/0883911506074025.

[115] C. Antich, J. De Vicente, G. Jiménez, C. Chocarro, E. Carrillo, E. Montañez, P. Gálvez-Martín, J. Marchal, Bio-inspired hydrogel composed of hyaluronic acid and alginate as a potential bioink for 3D bioprinting of articular cartilage engineering constructs, Acta Biomater. 106 (2020) 114–123. https://doi.org/10.1016/j.actbio.2020.01.046.

[116] Y. Yan, X. Wang, Z. Xiong, H. Liu, F. Liu, F. Lin, R. Wu, R. Zhang, Q. Lu, Direct construction of a three-dimensional structure with cells and hydrogel, J. Bioact. Compat. Polym. 20 (2005) 259–269. https://doi.org/10.1177/0883911505053658.

[117] J.P.K. Armstrong, M. Burke, B.M. Carter, S.A. Davis, A.W. Perriman, 3D bioprinting using a templated porous bioink, Adv. Healthc. Mater. 5 (2016) 1724–1730. https://doi.org/10.1002/adhm.201600022.

[118] R. Bushkalova, M. Farno, C. Tenailleau, B. Duployer, D. Cussac, A. Parini, B. Sallerin, S. Girod, Alginate-chitosan PEC scaffolds: A useful tool for soft tissues cell therapy, Int. J. Pharm. 571 (2019) 118692. https://doi.org/10.1016/j.ijpharm.2019.118692.

[119] K. Markstedt, A. Mantas, I. Tournier, D. Ha, P. Gatenholm, 3D bioprinting human chondrocytes with nanocellulose−alginate bioink for cartilage tissue engineering applications, Biomacromolecules 16 (2015) 1489–1496. https://doi.org/10.1021/acs.biomac.5b00188.

[120] Y. Wu, Z. Yuan, W. Lin, C. Andrew, K.C. Tam, X.S. Tang, 3D bioprinting of liver-mimetic construct with alginate/cellulose nanocrystal hybrid bioink, Bioprinting 9 (2017) 1–6. https://doi.org/10.1016/j.bprint.2017.12.001.

[121] A. Habib, V. Sathish, S. Mallik, B. Khoda, 3D printability of alginate-carboxymethyl cellulose hydrogel, Materials 11 (2018) 454. https://doi.org/10.3390/ma11030454.

[122] H. Li, Y.J. Tan, K.F. Leong, L. Li, 3D bioprinting of highly thixotropic alginate / methylcellulose hydrogel with strong interface bonding 3D bioprinting of highly thixotropic alginate / methylcellulose hydrogel with strong interface bonding, Appl. Mater. Interfaces 9 (2017) 1–29. https://doi.org/10.1021/acsami.7b04216

[123] T.M. Valentin, A.K. Landauer, L.C. Morales, E.M. Dubois, S. Shukla, M. Liu, L.H. Stephens, C. Franck, P. Chen, I.Y. Wong, Alginate-graphene oxide hydrogels with enhanced ionic tunability and chemomechanical stability for light-directed 3D printing, Carbon 143 (2019) 447–456. https://doi.org/10.1016/j.carbon.2018.11.006.

[124] H. Li, S. Liu, L. Li, Rheological study on 3D printability of alginate hydrogel and effect of graphene oxide, Int. J. Bioprinting. 2 (2016) 54–66. https://doi.org/10.18063/IJB.2016.02.007.

[125] L. Li, S. Qin, J. Peng, A. Chen, Y. Nie, T. Liu, K. Song, Engineering gelatin-based alginate / carbon nanotubes blend bioink for direct 3D printing of vessel constructs, Int. J. Biol. Macromol. 145 (2020) 262–271. https://doi.org/10.1016/j.ijbiomac.2019.12.174.

[126] S. Wang, J.M. Lee, W.Y. Yeong, Smart hydrogels for 3D bioprinting, Int. J. Bioprinting 1 (2015) 3–14. http://dx.doi.org/10.18063/IJB.2015.01.005.

[127] C. Lin, Y. Lin, Y. Lai, S. Lee, Mechanical properties, accuracy, and cytotoxicity of UV-polymerized 3D printing resins composed of Bis-EMA , J. Prosthet. Dent. 123 (2020) 349–354. https://doi.org/10.1016/j.prosdent.2019.05.002.

[128] S.Y. Hong, Y.C. Kim, M. Wang, H. Kim, D. Byun, Experimental investigation of mechanical properties of UV-curable 3D printing materials, Polymer (Guildf) 145 (2018) 88–94. https://doi.org/10.1016/j.polymer.2018.04.067.

[129] F.C. Godoi, S. Prakash, P.B.R. Bhandari, 3D Printing technologies applied for food design: Status and prospects, J. Food Eng. 179 (2016) 44–54. https://doi.org/10.1016/j.jfoodeng.2016.01.025.

[130] J.M. Sobral, S.G. Caridade, R.A. Sousa, J.F. Mano, R.L. Reis, Three-dimensional plotted scaffolds with controlled pore size gradients: Effect of scaffold geometry on mechanical performance and cell seeding efficiency, Acta Biomater. 7 (2011) 1009–1018. https://doi.org/10.1016/j.actbio.2010.11.003.

[131] R. Detsch, F. Uhl, U. Deisinger, G. Ziegler, 3D-Cultivation of bone marrow stromal cells on hydroxyapatite scaffolds fabricated by dispense-plotting and negative mould technique, J. Mater. Sci. Mater. Med. 19 (2008) 1491–1496. https://doi.org/10.1007/s10856-007-3297-x.

[132] C. Wu, Y. Luo, G. Cuniberti, Y. Xiao, M. Gelinsky, Three-dimensional printing of hierarchical and tough mesoporous bioactive glass scaffolds with a controllable pore architecture, excellent mechanical strength and mineralization ability, Acta Biomater. 7 (2011) 2644–2650. https://doi.org/10.1016/j.actbio.2011.03.009.

[133] T. Serra, J.A. Planell, M. Navarro, High-resolution PLA-based composite scaffolds via 3-D printing technology, Acta Biomater. 9 (2013) 5521–5530. https://doi.org/10.1016/j.actbio.2012.10.041.

[134] H. Seyednejad, D. Gawlitta, R. V Kuiper, A. De Bruin, C.F. Van Nostrum, T. Vermonden, W.J.A. Dhert, W.E. Hennink, In vivo biocompatibility and biodegradation of 3D-printed porous scaffolds based on a hydroxyl-functionalized poly (ε -caprolactone), Biomaterials 33 (2012) 4309–4318. https://doi.org/10.1016/j.biomaterials.2012.03.002.

[135] S. Ling, W. Kang, S. Tao, C. Zhang, Highly concentrated graphene oxide ink for facile 3D printing of supercapacitors, Nano Mater. Sci. 1 (2019) 142–148.

https://doi.org/10.1016/j.nanoms.2019.05.003.

[136] R. Chen, C. Huang, S. Hsu, Composites of waterborne polyurethane and cellulose nanofibers dor 3D printing and bioapplications, Carbohydr. Polym. (2019). https://doi.org/10.1016/j.carbpol.2019.02.025.

[137] K. Hung, C. Tseng, L. Dai, S. Hsu, Water-based polyurethane 3D printed scaffolds with controlled release function for customized cartilage tissue engineering, Biomaterials 83 (2016) 156–168. https://doi.org/10.1016/j.biomaterials.2016.01.019.

[138] Z. Yang, G. Wu, Effects of soft segment characteristics on the properties of biodegradable amphiphilic waterborne polyurethane prepared by a green process, J. Mater. Sci. 55 (2020) 3139–3156. https://doi.org/10.1007/s10853-019-04237-6.

[139] Y. Wang, U. Jeng, S. Hsu, Biodegradable water-based polyurethane shape memory elastomers for bone tissue engineering, ACS Biomater. Sci. Eng. 4 (2018) 1397–1406. https://doi.org/10.1021/acsbiomaterials.8b00091.

[140] C. Hsieh, C. Liao, N. Dai, C. Tseng, B.L. Yen, S. Hsu, 3D printing of tubular scaffolds with elasticity and complex structure from multiple waterborne polyurethanes for tracheal tissue engineering, Appl. Mater. Today 12 (2018) 330–341. https://doi.org/10.1016/j.apmt.2018.06.004.

[141] X. Zhou, J. Deng, C. Fang, R. Yu, W. Lei, X. He, C. Zhang, Preparation and characterization of lysozyme @ carbon nanotubes / waterborne polyurethane composite and the potential application in printing inks, Prog. Org. Coatings. 142 (2020) 105600. https://doi.org/10.1016/j.porgcoat.2020.105600.

[142] K. Hung, C. Tseng, S. Hsu, Synthesis and 3D printing of biodegradable polyurethane elastomer by a water-based process for cartilage tissue engineering applications, Adv. Healthc. Mater. 3 (2014) 1578–1587. https://doi.org/10.1002/adhm.201400018.

[143] T.G. Mezger, The rheology handbook, Vincentz Network GmbH & Co., Hannover, 2006.

[144] G. Siqueira, D. Kokkinis, R. Libanori, M.K. Hausmann, A.S. Gladman, A. Neels, P. Tingaut, T. Zimmermann, J.A. Lewis, A.R. Studart, Cellulose nanocrystal inks for 3D printing of textured cellular architectures, Adv. Funct. Mater. 27 (2017) 1604619.

https://doi.org/10.1002/adfm.201604619.

[145] M. Faes, H. Valkenaers, F. Vogeler, J. Vleugels, E. Ferraris, Extrusion-based 3D printing of ceramic components, Procedia CIRP 28 (2015) 76–81. https://doi.org/10.1016/j.procir.2015.04.028.

[146] A. Derossi, R. Caporizzi, D. Azzollini, C. Severini, Application of 3D printing for customized food. A case on the development of a fruit-based snack for children, J. Food Eng. 220 (2017) 65–75. https://doi.org/10.1016/j.jfoodeng.2017.05.015.

[147] C.W. Peak, J. Stein, K.A. Gold, A.K. Gaharwar, Nanoengineered colloidal inks for 3D bioprinting, Langmuir 34 (3) (2017) 917–925. https://doi.org/10.1021/acs.langmuir.7b02540.

[148] W.J. Costakis, L.M. Rueschhoff, A.I. Diaz-cano, J.P. Youngblood, R.W. Trice, Additive manufacturing of boron carbide via continuous filament direct ink writing of aqueous ceramic suspensions, J. Eur. Ceram. Soc. 36 (2016) 3249–3256. https://doi.org/10.1016/j.jeurceramsoc.2016.06.002.

[149] E. Feilden, E. García-Tuñon, F. Giuliani, E. Saiz, L. Vandeperre, Robocasting of structural ceramic parts with hydrogel inks, J. Eur. Ceram. Soc. 36 (2016) 2525–2533. https://doi.org/10.1016/j.jeurceramsoc.2016.03.001.

[150] D. Chimene, C.W. Peak, J.L. Gentry, J.K. Carrow, L.M. Cross, E. Mondragon, G.B. Cardoso, R. Kaunas, A.K. Gaharwar, Nanoengineered ionic–covalent entanglement (NICE) bioinks for 3D bioprinting, ACS Appl. Mater. Interfaces 10 (2018) 9957–9968. https://doi.org/10.1021/acsami.7b19808.

[151] A.I. Koponen, The effect of consistency on the shear rheology of aqueous suspensions of cellulose micro- and nanofibrils: a review, Cellulose 0123456789 (2019). https://doi.org/10.1007/s10570-019-02908-w.

[152] M. Lille, A. Nurmela, E. Nordlund, S. Metsa-Kortelainen, N. Sozer, Applicability of protein and fiber-rich food materials in extrusion-based 3D printing, J. Food Eng. 220 (2018) 20–27. https://doi.org/10.1016/j.jfoodeng.2017.04.034.

[153] A. Hiller, K. Borchers, G.E.M. Tovar, A. Southan, Impact of intermediate UV curing and yield stress of 3D printed poly (ethylene glycol) diacrylate hydrogels on interlayer connectivity and maximum build height, Addit. Manuf. 18 (2017) 136–144. https://doi.org/10.1016/j.addma.2017.10.008.

[154] F. Cyriac, P.M. Lugt, R. Bosman, On a new method to determine the yield stress in lubricating grease, Tribol. Trans. 58 (2015) 1021–1030. https://doi.org/10.1080/10402004.2015.1035414.

[155] W.Y. Shih, W. Shih, I.A. Aksay, Elastic and yield behavior of strongly flocculated colloids, J. Am. Ceram. Soc. 82 (3) (2004) 616–624. https://doi.org/10.1111/j.1151-2916.1999.tb01809.x.

[156] M. Sharma, E. Kristo, M. Corredig, L. Duizer, Effect of hydrocolloid type on texture of pureed carrots: Rheological and sensory measures, Food Hydrocoll. 63 (2017) 478–487. https://doi.org/10.1016/j.foodhyd.2016.09.040.

[157] V. De Graef, F. Depypere, M. Minnaert, K. Dewettinck, Chocolate yield stress as measured by oscillatory rheology, Food Res. Int. 44 (2011) 2660–2665. https://doi.org/10.1016/j.foodres.2011.05.009.

[158] C.A. Hamilton, G. Alici, 3D printing vegemite and marmite: Redefining "breadboards," J. Food Eng. 220 (2017) 83–88. https://doi.org/10.1016/j.jfoodeng.2017.01.008.

[159] D. Zhang, D. Wang, X. Lin, T. Zhang, The study of the structure rebuilding and yield stress of 3D printing geopolymer pastes, Constr. Build. Mater. 184 (2018) 575–580. https://doi.org/10.1016/j.conbuildmat.2018.06.233.

[160] S. Joas, G.E.M. Tovar, O. Celik, C. Bonten, A. Southan, Extrusion-based 3D printing of poly(ethylene glycol) diacrylate hydrogels containing positively and negatively charged groups, Gels 4 (2018) 69. https://doi.org/10.3390/gels4030069.

[161] A. Corker, H.C. Ng, E. Garcı, R.J. Poole, 3D printing with 2D colloids: designing rheology protocols to predict printability of sof-materials, Soft Matter. 15 (2019) 1444–1456. https://doi.org/10.1039/c8sm01936c.

[162] L. Li, Q. Lin, M. Tang, A.J.E. Duncan, C. Ke, Advanced polymer designs for direct-ink-write 3D printing, Chem. Eur. J. (2019) 1–15. https://doi.org/10.1002/chem.201900975.

[163] Z. Liu, M. Zhang, B. Bhandari, C. Yang, Impact of rheological properties of mashed potatoes on 3D printing, J. Food Eng. 220 (2017) 76–82. https://doi.org/10.1016/j.jfoodeng.2017.04.017.

[164] R.E. Abouzeid, R. Khiari, D. Beneventi, A. Dufresne, Biomimetic mineralization of three-dimensional printed alginate/TEMPO-oxidized cellulose nanofibril scaffolds for bone tissue engineering, Biomacromolecules 19 (2018) 4442–4452. https://doi.org/10.1021/acs.biomac.8b01325.

[165] H. Guo, R. Lv, S. Bai, Nano materials science recent advances on 3D printing graphene-based composites, Nano Mater. Sci. 1 (2019) 101–115. https://doi.org/10.1016/j.nanoms.2019.03.003.

[166] S.T. Bendtsen, S.P. Quinnell, M. Wei, Development of a novel alginate-polyvinyl alcohol-hydroxyapatite hydrogel for 3D bioprinting bone tissue engineered scaffolds, J. Biomed. Mater. Res. Part A. 105 (2017) 1457–1468. https://doi.org/10.1002/jbm.a.36036.

[167] Q. Liu, Q. Li, S. Xu, Q. Zheng, X. Cao, Preparation and properties of 3D printed alginate–chitosan polyion complex hydrogels, Polymers 10 (2018) 664. https://doi.org/10.3390/polym10060664.

[168] L. Guo, S. Huang, J. Qu, Synthesis and properties of high-functionality hydroxyl-terminated polyurethane dispersions, Prog. Org. Coatings. 119 (2018) 214–220. https://doi.org/10.1016/j.porgcoat.2018.02.033.

[169] M. Hwan Kim, Y. Wook Lee, W. Jung, J. Oh, S.Y. Nam, Enhanced rheological behaviors of alginate hydrogels with carrageenan for extrusion-based bioprinting, J. Mech. Behav. Biomed. Mater. 98 (2019) 187–194. https://doi.org/10.1016/j.jmbbm.2019.06.014.

[170] S.A. Wilson, L.M. Cross, C.W. Peak, A.K. Gaharwar, Shear-thinning and thermo-reversible nanoengineered inks for 3D bioprinting, ACS Appl. Mater. Interfaces 9 (2017) 43449–43458. https://doi.org/10.1021/acsami.7b13602.

[171] A.K. Gaharwar, R.K. Avery, A. Assmann, A. Paul, G.H. Mckinley, A. Khademhosseini, B.D. Olsen, Shear-thinning nanocomposite hydrogels for the treatment of hemorrhage, ACS Nano 8 (2014) 9833–9842. https://doi.org/10.1021/nn503719n.

[172] J.L. Davila, M.A. D'Ávila, Rheological evaluation of laponite/alginate inks for 3D extrusion-based printing, Int. J. Adv. Manuf. Technol. 101 (2019) 675–686. https://doi.org/10.1007/s00170-018-2876-y

[173] A. Nadernezhad, N. Khani, G.A. Skvortsov, B. Toprakhisar, E. Bakirci, Y. Menceloglu, S. Unal, B. Koc, Multifunctional 3D printing of heterogeneous hydrogel structures, Sci. Rep. 6 (2016) 1–12. https://doi.org/10.1038/srep33178.

[174] T. Pan, W. Song, X. Cao, Y. Wang, 3D Bioplotting of gelatin/alginate scaffolds for tissue engineering : Influence of crosslinking degree and pore architecture on physicochemical properties, Mater. Sci. Technol. 32 (2016) 889–900. https://doi.org/10.1016/j.jmst.2016.01.007.

[175] E. Sachols, D. Gotora, J. Czernuszka, Collagen scaffolds reinforced with biomimetic composite nano-sized carbonate-cubstituted hydroxyapatite crystals and shaped by rapid prototyping to contain internal microchannels, Tissue Eng. 12 (2006) 2479–2587. https://doi.org/10.1089/ten.2006.12.2479.

[176] T. Demirtas, G. Irmak, M. Gümüsderelioglu, A bioprintable form of chitosan hydrogel for bone tissue engineering, Biofabrication 9 (2017).035003. doi: 10.1088/1758-5090/aa7b1d.

[177] S. Sultan, A. Mathew, 3D printed scaffolds with gradient porosity based on cellulose nanocrystal hydrogel, Nanoscale 10 (2018) 4421–4431. https://doi.org/10.1039/C7NR08966J.

[178] J. Leppiniemi, P. Lahtinen, A. Paajanen, R. Mahlberg, S. Metsä-kortelainen, H. Pajari, I.M. Vikholm-Lundin, P. Pursula, V.P. Hytönen, 3D printable bioactivated nanocellulose-alginate hydrogels, ACS Appl. Mater. Interfaces. 9 (2017) 21959–21970. https://doi.org/10.1021/acsami.7b02756.

[179] T. Maver, D.M. Smrke, M. Kurecic, L. Gradisnik, U. Maver, K. Kleinschek, Combining 3D printing and electrospinning for preparation of pain- relieving wound-dressing materials, J. Sol-Gel Sci. Technol. 88 (2018) 33–48. https://doi.org/10.1007/s10971-018-4630-1.

[180] A. Rees, L.C. Powell, G. Chinga-Carrasco, D.T. Gethin, K. Syverud, K.E. Hill, D.W. Thomas, 3D bioprinting of carboxymethylated-periodate oxidized nanocellulose constructs for wound dressing applications, Biomed. Res. Int. 2015 (2015) 1–7. https://doi.org/10.1155/2015/925757.

[181] C. Intini, L. Elviri, J. Cabral, S. Mros, C. Bergonzi, A. Bianchera, L. Flammini, P. Govoni, E. Barocelli, R. Bettini, M. Mcconnell, 3D-printed chitosan-based scaffolds:

An in vitro study of human skin cell growth and an in-vivo wound healing evaluation in experimental diabetes in rats, Carbohydr. Polym. 199 (2018) 593–602. https://doi.org/10.1016/j.carbpol.2018.07.057.

[182] J. Zhong, G. Zhou, P. He, Z. Yang, D.-C. Jia, 3D printing strong and conductive geo-polymer nanocomposite structures modi fi ed by graphene oxide, Carbon 117 (2017) 421–426. https://doi.org/10.1016/j.carbon.2017.02.102.

[183] T. Wu, E. Gray, B. Chen, A self-healing, adaptive and conductive polymer composite ink for 3D printing of gas sensors, J. Mater. Chem. C 6 (2018) 6200–6207. https://doi.org/10.1039/c8tc01092g.

[184] G.A. Appuhamillage, D.R. Berry, C.E. Benjamin, M.A. Luzuriaga, J.C. Reagan, J.J. Gassensmith, R.A. Smaldone, A biopolymer-based 3D printable hydrogel for toxic metal adsorption from water, Polym. Int. 68 (2019) 964–971. https://doi.org/10.1002/pi.5787.

[185] Y. Li, T. Gao, Z. Yang, C. Chen, W. Luo, J. Song, E. Hitz, 3D-printed , all-in-one evaporator for high-efficiency solar steam generation under 1 sun illumination, Adv. Mater. 29 (2017) 1700981. https://doi.org/10.1002/adma.201700981.

[186] F. Guo, Y. Jiang, Z. Xu, H. Wang, C. Gao, Y. Xiao, B. Fang, Y. Liu, W. Gao, P. Zhao, Highly stretchable carbon aerogels, Nat. Commun. 9 (2018) 1–9. https://doi.org/10.1038/s41467-018-03268-y.

[187] S. Guo, K. Qiu, F. Meng, S.H. Park, M.C. Mcalpine, 3D printed stretchable tactile sensors, Adv. Mater. 29 (2017) 1701218. https://doi.org/10.1002/adma.201701218.

[188] Y. Kim, H. Yuk, R. Zhao, S.A. Chester, X. Zhao, Printing ferromagnetic domains for untethered fast-transforming soft materials, Nature 558 (2018) 274–279. https://doi.org/10.1038/s41586-018-0185-0

CHAPTER 2

MATERIALS AND METHODS

2. MATERIALS AND METHODS

2.1 Objective

In this chapter, the reactants employed for the synthesis of the different WBPUU, WBPUU/CNC and WBPUU/CNC/plant extract systems are described. Additionally, the characterization techniques carried out to analyse the different dispersions, films, inks and printed pieces are also specified. Finally, the DIW 3D-printing equipment used in this work is displayed.

2.2 Reactants

Waterborne polyurethane urea hydrogels were synthesized using a difunctional polycaprolactone diol (PCL) and a difunctional polyethylenglycol (PEG) (molecular mass in number from the supplier Mn=2000 and 1000 g mol^{-1} respectively) as soft segment (SS), both provided by Sigma-Aldrich. 2,2-Bis (hydroxymethyl) propionic acid (DMPA, 98% purity) and ethylene diamine (EDA, 99% purity), used as internal emulsifier and chain extender respectively, provided also by Sigma-Aldrich, and isophorone diisocyanate (IPDI, 99.5% purity), kindly supplied from Covestro, were used as hard segment (HS). Dibutyl tin dilaurate (DBTDL), provided by Sigma-Aldrich, was used as catalyst. The polyols and the DMPA were dried under vacuum at 60 °C for 4 h prior to their use. Triethylamine (TEA, 99.5% purity) was used as neutralizer of the carboxylic groups of DMPA (provided by Fluka) whereas butanone (supplied by Panreac) was used to transfer the neutralized DMPA into the reaction medium and also adjust viscosity. For the study of the variation of the molecular weight of the PEG, difunctional polyethylenglycol of 400 and 1500 g mol^{-1} were also used, all provided by Sigma Aldrich.

For the preparation of the composites, cellulose nanocrystals (CNC) provided by the University of Maine (USA) were used (2018-FPL-CNC-117 with a sulphur content of 1.0

wt% from the supplier) and for obtaining the plant extract, *Salvia officinalis L.* from Soria Natural were employed as dry material obtained in a herbalist.

Finally, methylene blue (MB) (82% purity) provided by Panreac has been used for the dye absorption process.

2.3 Characterization techniques

2.3.1 Dispersions characterization

2.3.1.1 Dynamic light scattering

The particle size of the polyurethane urea dispersions was measured by dynamic light scattering (DLS). This technique allows to measure the diffusion speed of particles by means of the dispersed light in the system, leading to the determination of the particle size distribution profile by the hydrodynamic radio. The measurements were carried out using a BI-200SM goniometer, from Brookhaven. The intensity of dispersed light was measured using a luminous source of He–Ne laser (Mini L-30, wavelength = 637 nm, 400 mW) and a detector (BI–APD) placed on a rotary arm which allows measuring the intensity at 90°. Samples were prepared mixing a small amount of the synthesized WBPUU aqueous dispersion with ultrapure water. Six measurements were performed per system and the mean is calculated as well as the standard deviation.

2.3.1.2 Zeta potential

The stability of the WBPUU dispersions was analysed by zeta potential (Z potential) using a ZetaSizer Nano Series ZEN3600, from Malvern Instruments. This technique measures the Z potential of the dispersion by applying an electric field across the dispersion. Particles within the dispersion with a Z potential will migrate toward the electrode of opposite charge with a velocity proportional to the magnitude of the Z potential, allowing to determine the stability of the dispersion. Samples were prepared diluting the WBPUU dispersions with ultrapure water.

2.3.1.3 Solid content

Solid content of different dispersions and WBPUU and WBPUU/CNC inks was calculated by drying 2 mL of each one in an oven at 100 °C for 8 h. The solid content, calculated by duplicate, was taken as the ratio between the weight of the dispersion and the weight of the dried sample following **Equation 2.1**.

$$\text{Solid content (\%)} = \frac{\text{dried sample weight}}{\text{weight of dispersion}} \text{ X100} \qquad \textbf{(2.1)}$$

2.3.1.4 Transmission electron microscopy

In order to study the morphology of the dispersion and inks particles, transmission electron microscopy (TEM) measurements were performed on a TECNAI G2 20 TWIN operated at 80 kV and equipped with LaB6 filament. Samples were diluted in water. A drop of suspension was spread into a TEM cooper grid (300 Mesh) covered by a pure carbon film and dried at room temperature. The grid was glow discharged before put the drop of suspension.

So as to obtain clear images of the particles for both the WBPUU dispersions and WBPUU/CNC inks, the studied systems were diluted in a 1 wt% of solid content in deionized water.

2.3.1.5 pH

The pH of the dispersions was measured using a pH meter GLP22 of Crison, which was calibrated with pH 4 and 7 buffer solutions standards. Measurements have been carried out per triplicate.

2.3.2 Physicochemical characterization

2.3.2.1 Gel permeation chromatography

Molar masses in weight (Mw) and dispersity index (Đ) of the prepared polyurethane urea films were determined by gel permeation chromatography (GPC) using a Thermo Scientific chromatograph, equipped with an isocratic Dionex UltiMate 3000 pump and a RefractoMax 521 refractive index detector. A mobile phase carries the sample thought a stationary phase packed in a column, which consist on a microporous packaged gel. Depending on the size of the different molecules, the retention time of the macromolecules, on in other words, the time that the macromolecule requires to complete the whole column will be different. The smaller macromolecules will result in bigger retention times becoming entrapped in the pores whereas the bigger ones will complete the column more rapidly. By this way, the macromolecules of the sample will be separated according to their sizes due to the different retention times. The separation was carried out at 30 °C within four Phenogel GPC columns from Phenomenex with 5 μm particle size and 10^5, 10^3, 100, and 50 Å porosities, respectively, located in an UltiMate 3000 thermostated column compartment. Tetrahydrofuran (THF) was used as mobile phase at a flow rate of 1 mL min^{-1}. Samples were prepared dissolving in

THF at 1 wt% the obtained films of the WBPUU dispersions and filtering the obtained solutions with nylon filters with 2 μm pore size. Mw and Đ were reported as weight average polystyrene standards.

2.3.2.2 Proton nuclear magnetic resonance

The chemical structure of WBPUUs was analysed by proton nuclear magnetic resonance (^{1}H NMR). This technique is based on the application of an electromagnetic field and posterior analysis of the frequencies of proton resonance which depend on the surrounding atoms of each proton nucleus. The measurements were carried out in a Bruker Avance 500 spectrometer, equipped with a BBO probe with gradient in z axis and using a resonant frequency of 125.77 MHz. Acquisition times were established at 3 s averaging 64 K scans, using an interpulse delay of 2 s. A time domain of 64 K was used in a spectral width of 10000 Hz. The solvent employed in all cases was deuterated DMSO.

2.3.2.3 Carbon nuclear magnetic resonance

Carbon nuclear magnetic resonance (^{13}C NMR) spectra of CNC were recorded with an Advance Bruker equipped with BBO z-gradient probe. Experimental conditions were as follows: 125.5 MHz, number of scans 14000, spectral window 25000 Hz and recovery delay 2 s. The solvent employed in all cases was deuterated DMSO.

2.3.2.4 Fourier transform infrared spectroscopy

The characteristic functional groups of the different WBPUUs and WBPUU/CNC prepared systems as well as the hydrogen bonding interactions were analysed by Fourier transform infrared spectroscopy (FTIR). This technique consists on the irradiation of the sample with an infrared light source. This absorbed light is reflected in the spectrum at different wavenumbers, which correspond to the different functional group, allowing to recognise them. For this purpose, the FTIR measurements were carried out using a Nicolet Nexus spectrometer provided with a MKII Golden Gate accessory (Specac) with a diamond crystal at a nominal incidence angle of 45° and ZnSe lens. Spectra were recorder in attenuated total reflection (ATR) mode between 4000 and 650 cm^{-1} averaging 64 scans with a resolution of 8 cm^{-1}.

2.3.2.5 X-ray diffraction

X-ray powder diffraction pattern of the CNC and WBPUU films was collected by using a Philips X'pert PRO automatic diffractometer operating at 40 kV and 40 mA, in theta-theta

configuration, secondary monochromator with Cu-Kα radiation (λ = 1.5418 Å) and a PIXcel solid state detector (active length in 2θ 3.347°). Data were collected from 5 to 75° 2θ (step size 0.026 and time per step = 80 s) at room temperature. A fixed divergence and antiscattering slit giving a constant volume of sample illumination were used.

2.3.2.6 Density measurements

The density of the printed and freeze dried scaffolds was obtained as the ratio between the weight and volume of a cylindrical specimen (12 mm diameter x 5 mm height), and values were averaged for five specimens.

2.3.3 Thermal characterization

2.3.3.1 Thermogravimetric analysis

The thermal stability of the WBPUU films and the WBPUU/CNC printed pieces was determined by thermogravimetric analysis (TGA) using a Mettler Toledo TGA/DSC 3+ equipment. This technique consists on controlling the degradation process of the sample by measuring the weight of the sample in a microbalance during a heating scan. Between 5 and 10 mg of samples were introduced in ceramic pans. The samples were heated from 25 to 800 °C in nitrogen atmosphere at a scanning rate of 10 °C min^{-1}. From the weight loss and its derivative curves, the initial degradation temperature (T_0) as the loss of 5% of the initial weight, and the maximum degradation temperature (T_d) as the minimum of the degradation peak in the derivative thermogravimetric curve were determined.

2.3.3.2 Differential scanning calorimetry

The thermal properties of the WBPUU films and different WBPUU/CNC printed pieces were determined by differential scanning calorimetry (DSC) using a Mettler Toledo DSC 3+ equipment provided with a robotic arm and an electric intracooler as refrigerator unit. This technique is based on the heat provided to the analysing sample and a reference, and consist on the comparison of both thermograms. When the sample undergoes a thermal transition, the required heat will be different between the sample part and the reference one reflecting in the thermograms. Between 5 and 10 mg of the samples was encapsulated in aluminium pans and heated from −50 to 200 °C at a scanning rate of 10 °C min^{-1} in nitrogen atmosphere. The inflection point of the heat capacity change observed was chosen as glass transition temperature (T_g). Moreover, melting temperature of both soft and hard segment (T_mSS and T_mHS) was settled as the maximum of endothermic peaks taking the area under the peak as melting enthalpy (ΔH_m).

2.3.4 Mechanical characterization

2.3.4.1 Tensile tests

Tensile analysis was performed for the WBPUU films and the different WBPUU/CNC printed pieces in an Instron 5967 universal testing machine provided with a 500 N load cell and pneumatic grips to hold the samples. This technique consists on applying a constant elongation rate of the samples until failure. By this, the equipment is able to record the force and elongation strain values of the sample in order to build a stress-strain curve, where the different mechanical properties of the material can be determined. For the WBPUU films, samples were cut in strips of 2.8 mm in width and 0.5 μm in thickness, whereas in the case of the printed WBPUU/CNC composites, strips were printed with 2.8 mm in width and 0.5 mm in thickness before drying, decreasing the thickness up to 0.4 μm after the drying process. All samples were tested at a constant elongation rate of 20 mm min^{-1} at room temperature with an initial distance between clamps of 10 mm. Young modulus (E), stress at break (σb), and strain at break (εb) were averaged from stress–strain curves of at least five specimens of each series.

2.3.4.2 Compression tests

For the compression testing of prepared WBPUU/CNC scaffolds, cylindrical specimens of 25 mm diameter x 30 mm height were prepared by freeze drying technique, and tested at room temperature in an Instron 5967 universal testing machine. The compression force was applied in the layer by layer printing direction. Samples were compressed at a fixed length of 22 mm at a crosshead speed of 10 mm min^{-1}. The average value of compression modulus was calculated as the slope of the stress-strain curve at low deformations. The compressive strength was taken as the stress reached at the compressive yield point that occurred below 10% deformation for all samples and the densification strain was taken as the strain at the intersection point between the stress plateau and a line extrapolated from the densification line. Compression values were averaged for three specimens.

2.3.5 Rheology

2.3.5.1 Thermomechanical characterization

The thermomechanical behaviour of the WBPUU films and printed WBPUU/CNC nanocomposites was determined by using an Eplexor 100 N analyser Gabo equipment. This analysis, which was performed in order to analyse the viscoelastic properties of films and the printed pieces, consists on the application of a sinusoidal stress as the strain response is

measured while the temperature is linearly varying. By this way, the phase difference between the stimulus and the response can be used to determine the storage modulus (E') and the loss modulus (E"), and the tangent of phase angle (tan δ). The variation of tan δ with the temperature allows to determine the glass transition temperature (Tg) of the sample manifested with a maximum in tan δ curve, which also can be observed as a drop in the curve related to E'. The measurements were carried out in tensile mode from −100 to 150 °C at a constant scanning rate of 2 °C min^{-1} and a fixed frequency equal to 1 Hz. The constant strain was established at 0.05% to keep the linear viscoelastic behaviour whatever the temperature.

2.3.5.2 Spectromechanical analysis

Rheological characterization was performed using a R101 model rheometer (Antoon Paar), provided by a temperature chamber and solvent trap. Flow test were performed at 22.5 °C using a plate-plate geometry of 50 mm as a shear rate sweep from 0.01 to 120 s^{-1}. Regarding the yield point determination dynamic oscillatory test were performed in a shear stress range of 0.09-1500 Pa at 22.5 °C in a plate-plate geometry of 25 mm. Strain sweep test were performed at 22.5 °C in a plate-plate geometry of 25 mm at a fixed frequency of 1 Hz varying the strain from 0.01 to 200%. Moreover, frequency sweep test was performed at 22.5 °C at a fixed strain, corresponding to the linear domain of 1%, in a plate-plate geometry of 25 mm varying the frequency from 0.01 to 10 Hz. Finally, structure recovery tests were performed at 22.5 °C in a three stage test in a plate-plate geometry of 25 mm, i) in the first one the viscosity is measured at 1 s^{-1} during 10 s, ii) in the second the shear rate is fixed at 100 s^{-1} and the viscosity is measured during 10 s, iii) in the last stage, the shear rate is fixed again at 1 s^{-1} and the viscosity is measured during 3 min.

2.3.6 Morphological characterization

2.3.6.1 Scanning electron microscopy

So as to study the morphology of prepared WBPUU/CNC *in situ* scaffolds, scanning electron microscopy (SEM) measurements were performed by a Field Emission Gun Scanning Electron Microscopy (FEG-SEM) Hitachi S-4800N, at a voltage of 5 kV.

Prior to the test, and in order to analyse the cross section of prepared scaffolds, the samples were cryofractured in liquid nitrogen so as to avoid the deformation of the scaffolds during the cutting process and sputter coated with a thin layer of gold (~ 10 nm) in a Emitech K550X ion sputter.

In addition, energy dispersive X-ray spectroscopy (EDS) was carried out by means of a ULTRAplus scanning electron microscope (SEM) from Zeiss Company equipped with a Gemini column and with an energy dispersive X-ray spectrometer from OXFORD INCA Synergy microanalysis system. The EDS microanalysis permits to evaluate the elemental composition of materials.

2.3.6.2 Atomic force microscopy

The morphology of the different WBPUU films and CNC was analysed by atomic force microscopy (AFM). This microscopy technique is based in the interactions between the nanometric tip of the microscope and the sample. The attractive-repulsion forces created a deflection in the tip depending on the morphology and the images are created by mapping those deflections in each point of the sample in tapping mode, using a Nanoscope IIIa scanning probe microscope (MultimodeTM Digital Instruments) with an integrated force generated by cantilever/silicon probes, applying a resonance frequency of about 180 kHz. The cantilevers were 125 μm long and had a tip radius of 5–10 nm. Samples were prepared by drying a drop of WPUU dispersion on glass supports via spin coating (Spincoater P6700) at 200 rpm for 130 s. Height and phase images were taken simultaneously.

In the case of CNC the height and diameter of the nanoentities were also determined. The average dimensions of the CNC were obtained after measuring 50 samples. The samples were prepared following the same methodology detailed previously for the WBPUU dispersions.

2.3.7 Superficial characterization

2.3.7.1 Static water contact angle

Static water contact angle (WCA) of the surface of the film was measured using a Phoenix-300 goniometer of SEO. This technique is based on the deposition of a deionized water drop into the surface of the film so as to study the water contact angle value at the equilibrium in the system air-water-film. For the measurement, drops of deionized water of 0.1 μL have been used. Ten measurements were performed per sample.

2.3.7.2 Water absorption

The evolution of the water absorption of the prepared WBPUU and WBUU/CNC scaffolds was carried out by weight difference measurements in order to analyse the capacity of the scaffolds for absorbing water. For this study, samples of around of 10-15 mg were immersed

in 5 mL of deionized water at 25 °C. Samples were weighted at different times for one week. In order to study the influence of the pH in the absorption capacity of the scaffolds, different pH values of 1, 7 and 12 were used. For this purpose, hydroclorydric acid (HCl 0.1 M) and sodium hydroxide (NaOH) were used to adjust the pH to 1 and 12 respectively. The water absorption percentage was determined from weight increase by means of the **Equation 2.2**:

$$\text{Swelling } (\%) = \frac{W_t - W_0}{W_0} \times 100 \qquad \textbf{(2.2)}$$

where W_t is assigned to the weight at time t, whereas W_0 is referred to the initial weight of the sample. Three measurements were averaged for each sample.

2.3.9 Study of the methylene blue absorption capacity by UV-vis spectroscopy

Quantitative analysis of the adsorption capacity of methylene blue (MB) was measured by UV-vis spectroscopy. Before the absorption test samples of 10 mm of diameter and 5 mm of height were printed and subsequently freeze dried. Furthermore, a solution of 500 mg L^{-1} of MB in deionized water was prepared. The samples were immersed in the solution for 24 h, and the remaining concentration of MB in the solution was tracked by UV-vis in order to determine the adsorption capacity of the scaffolds by studying the intensity of the peak located at 655 nm. This peak is the one characteristic of MB and used in the literature to study its presence [1].

The UV-vis measurements have been carried out in a UV-3600/3100 spectrometer from Shimadzu, in the range of 250-800 nm. Standards of known MB concentrations were prepared in order to perform the calibration curve. For this purpose, the initial solution of 500 mg L^{-1} was diluted in deionized water to give 0.5, 2, 5, 10, 15, 20, 25 and 30 mg L^{-1} solutions. The calibration curve of MB is displayed in **Figure 2.1**.

The removal efficiency (R) was calculated from **Equation 2.3**

$$R = \frac{C_0 - C_{24}}{C_0} \times 100 \qquad \textbf{(2.3)}$$

where C_0 and C_{24} are the initial concentration and the concentration of MB in the solution after 24 h expressed in mg L^{-1}, respectively.

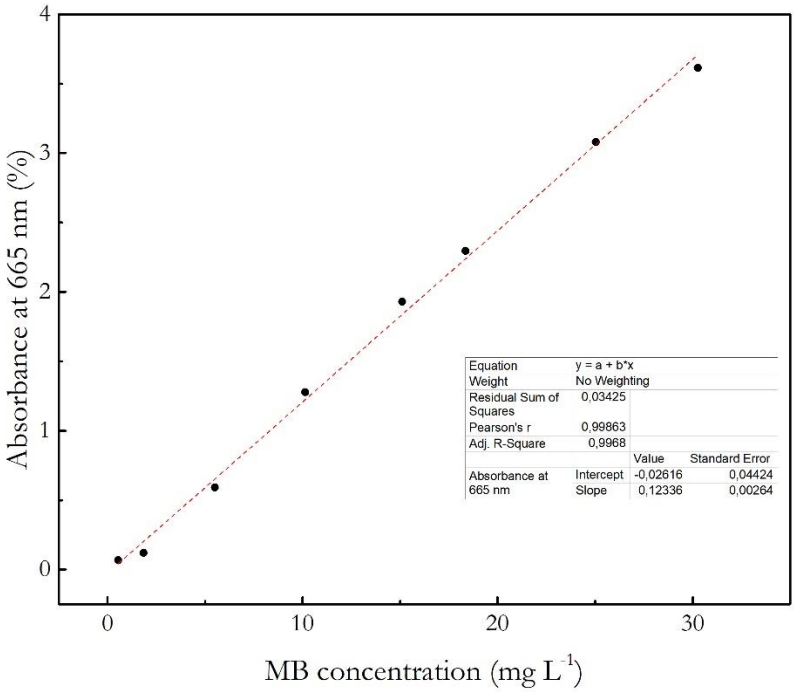

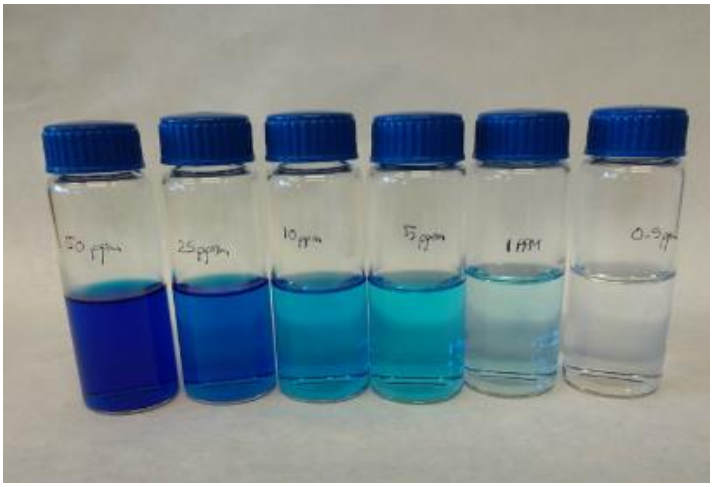

Figure 2.1 Calibration curve of MB (up), standards of different concentration of MB used for the construction of the calibration curve (down)

2.3.10 Antibiotic disc-plate antibacterial test

The testing of the micro biocidal activity of the systems was carried out by means of the antibiotic disc-plate technique, also known as disk diffusion test. This technique consists on the deposition, onto an agar surface of a Petri plaque, previously inoculated with the microorganism which is going to be the object of the study, of paper discs impregnated with the different antibiotic of biocide agents. As soon as the impregnated disc with the biocide

agent is putted into contact with the wet agar surface, the filter absorbs the water and the biocide agent spread through the Agar. Then, the biocide agent spreads radially through the thickness of the Agar forming a concentration gradient. In this case, the impregnated disc is substituted by a printed disc which contains the biocide agent. After depositing the disc with the biocide agent on the plaque, previously inoculated with the microorganism, the samples were incubated at 37 ºC for 24 h. The prepared pieces with potential antibacterial properties, the antibacterial extracts as well as a control piece without the biocide agent were tested against *Escherichia coli* (CECT 405) and *Staphylococcus aureus* (CECT 239). All the performed tests were carried out by duplicate so as to confirm the results.

2.4 3D-printing equipment

The DIW 3D-printing process used in this work concerns a modified conventional FDM 3-printing machine. This machine, which has been provided by Tumaker (Spain), has been modified by the addition of a piston and a motor in substitution of the extruder and the "hot end" so as to be able by using a syringe with a nozzle to extrude inks. By this way, the inks are loaded into a disposable syringe and are extruded through the nozzle as a result of the pressure applied by the piston. An image of the 3D-printing equipment used in this work is displayed in **Figure 2.2**.

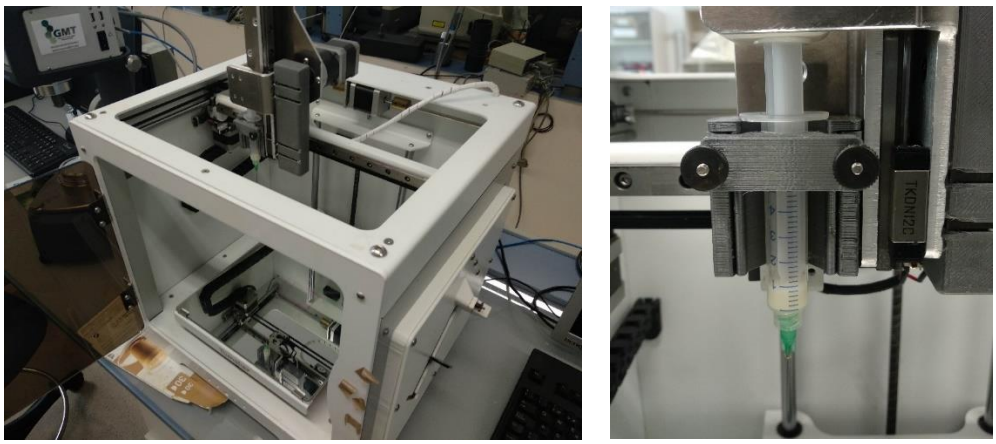

Figure 2.2 General overview of the DIW 3D-printing equipment (left), modified head of the printer for DIW 3D-printing (right)

2.5 References

[1] T. Whang, H. Huang, M. Hsieh, J. Chen, Laser-induced silver nanoparticles on titanium oxide for photocatalytic degradation of methylene blue, Int. J. Mol. Sci. 10 (2009) 4707–4718. https://doi.org/10.3390/ijms10114707.

CHAPTER 3

SYNTHESIS OF WATERBORNE POLYURETHANE UREA. STUDY OF THE INFLUENCE OF THE SOFT SEGMENT COMPOSITION

3. SYNTHESIS OF WATERBORNE POLYURETHANE UREA. STUDY OF THE INFLUENCE OF THE SOFT SEGMENT COMPOSITION

3.1 Objective

The objective of this chapter is to study the influence of the variation of the ratio of a hydrophobic diol like PCL and a hydrophilic diol like PEG in the properties of waterborne polyurethane urea dispersions, as well as in the films prepared from the synthesized dispersions by doing a comprehensive analysis of the influence of low PEG content (from 0.05 to 0.20 molar ratio). It is expected that the addition of PEG will increase the hydrophilicity of the film, as well as modify its morphology and thus its mechanical, thermomechanical and thermal properties due to the different nature of PEG compared to the more hydrophobic PCL. However, it is important to determine at which PEG content the effect in the properties of the systems are modified. The properties of the colloidal dispersions as well as the physicochemical, thermal, mechanical, and thermomechanical properties, morphology, and hydrophilicity of the films were evaluated and compared to the properties of similar materials reported in the literature. Additionally, in a second part of the chapter, the influence of the PEG molecular mass in the properties of the synthesized dispersions and films prepared from the dispersions were studied.

3.2 Effect of the PCL/PEG ratio in the properties of WBPUU dispersions and films

3.2.1 Experimental part

3.2.1.1 Synthesis of waterborne polyurethane urea dispersions

The synthesis of the WBPUU has been carried out using a 250 mL four-necked flask equipped with a mechanical stirrer, thermometer, condenser, and nitrogen inlet within a

controlled temperature bath. The synthesis consists on a two-step process where in the former the formation of the prepolymer is carried out, whereas the latter consists on the phase inversion and the chain extension. In the first step of the reaction, PCL, PEG, and IPDI were reacted in bulk at 80 °C for 3 h using a 0.1 wt% of DBTL, and then, the reaction is cooled until 50 °C where DMPA previously neutralized with TEA diluted in 5 mL of butanone was added. After 1 h, the system is cooled until room temperature, where the phase inversion step was carried out by adding deionized water drop by drop, under vigorous stirring. The decrease of the temperature before the phase inversion leads to avoid the reaction of the isocyanate with water. Finally, the chain extender (EDA) dissolved previously in deionized water was added drop by drop at 35 °C at which the chain extension reaction between the isocyanate groups of the nanoparticles and the diamine type chain extender is promoted, and left to react for 2 h to form the final WBPUU. Each step reaction progress was evaluated by dibutylamine back titration method according to ASTM D 2572-97. Once the reaction was completed, the remaining solvent was removed by vacuum distillation at 60 °C. The pH of the dispersion was measured after the synthesis, obtaining values in the range of 7–8 for all samples. Additionally, ionic strength has been calculated for all systems, obtaining values in the range of 0.075–0.078 mol L^{-1}.

Systems with different soft segments (SS) compositions were prepared varying the molar ratio of PEG from 0.05 to 0.2. The theoretical solid content was fixed at 25 wt% in order to guarantee stable dispersions. All systems were prepared maintaining constant the molar ratio of polyol/diisocyanate/emulsifier/chain extender of 1/3.5/1/1.5. The hard segment (HS) content, which is calculated as the percentage of the diisocyanate, emulsifier and chain extender, and the emulsifier percentage remain almost the same for all the synthesized WBPUU.

The scheme of the reaction is displayed in **Figure 3.1**, whereas the composition of the synthesized WBPUUs in terms of molar ratio of reactants and content (in wt%) of PEG, hard segment, carboxylic group and emulsifier is displayed in **Table 3.1**. The dispersions were stored at room temperature and no presence nor of aggregates nor of deposited material have been observed during time.

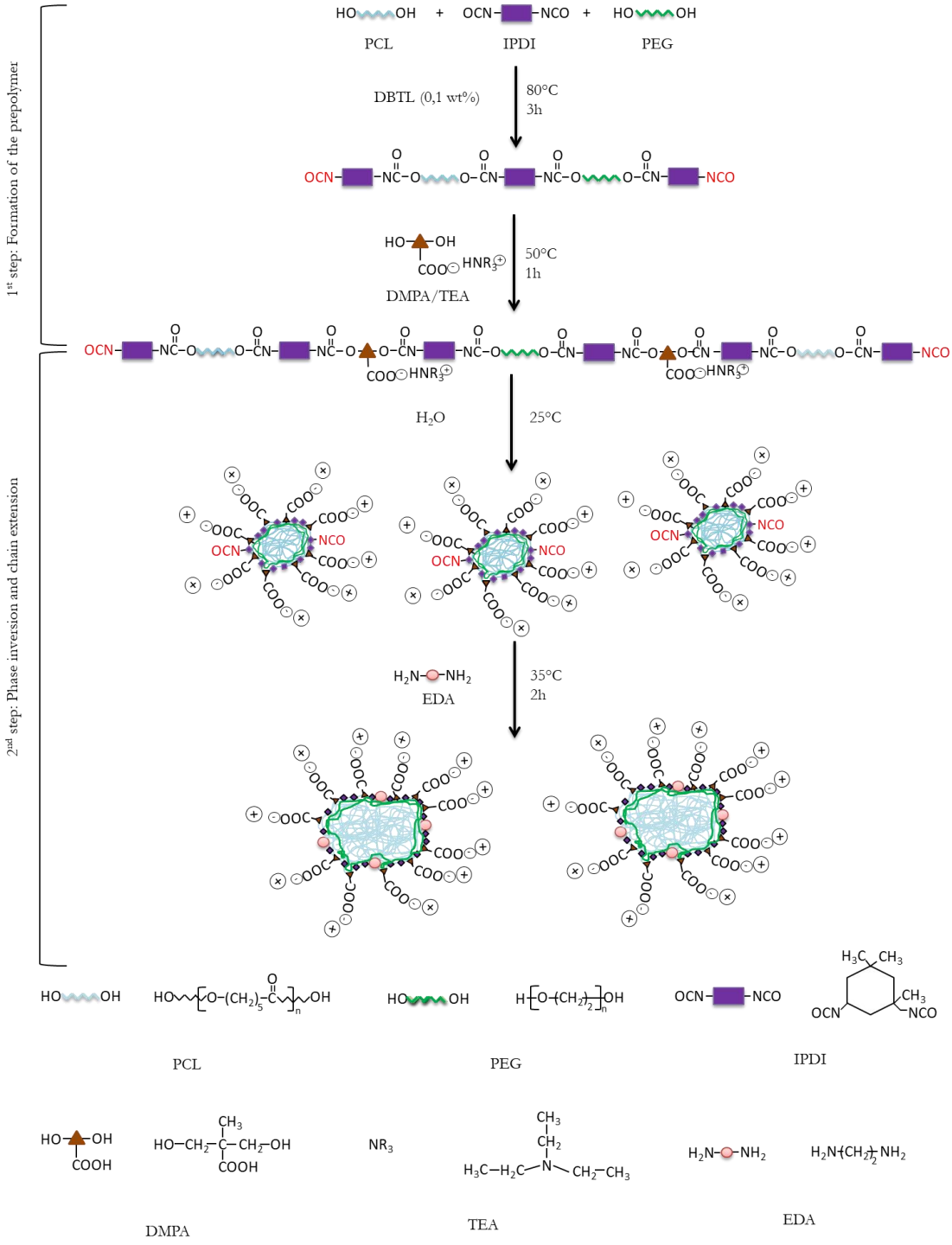

Figure 3.1 Scheme of the waterborne polyurethane urea synthesis, synthesis condition and chemical structure of the reagents

Table 3.1 Molar ratio of reactants and contents (in wt%) of PEG, hard segment carboxylic group and emulsifier

	System	PCL100	PCL95PEG5	PCL90PEG10	PCL85PEG15	PCL80PEG20
Molar ratio	**PCL**	1	0.95	0.90	0.85	0.80
	PEG	0	0.05	0.10	0.15	0.20
	IPDI	3.5	3.5	3.5	3.5	3.5
	DMPA	1	1	1	1	1
	EDA	1.5	1.5	1.5	1.5	1.5
PEG (wt%)		0	1.7	3.4	5.2	7.1
Hard segment (wt%)		36.5	37.1	37.7	38.3	39.0
$COOH_{tot}$ (wt%)		1.5	1.5	1.6	1.6	1.6
$Emulsifier_{tot}$ (wt%)		4.5	4.6	4.7	4.8	4.9

3.2.1.2 Films preparation

The dispersions were cast in Teflon molds, dried in a climatic chamber at 25 °C with a 50% of relative humidity for 1 week and followed by 3 days in a vacuum oven at 25 °C (400–420 mbar). After this time, polyurethane urea films with a thickness of about 0.5 mm were obtained from WBPUU dispersions. In **Figure 3.2** an image of the obtained PCL/PEG based WBPUU films is displayed.

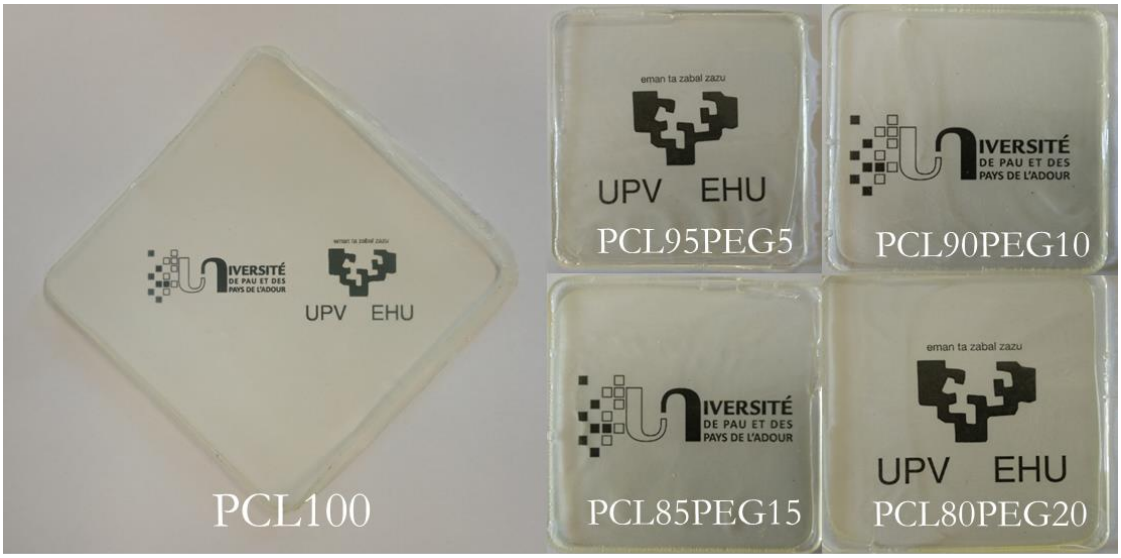

Figure 3.2 Digital image of the prepared PCL/PEG based WBPUU films

The solid content of the prepared dispersion and film size have been taken into account in order to ensure the desirable thickness of the film. The prepared films are homogeneous and showed a high transparency as can be observed in **Figure 3.2**. The films have been storage at room temperature in a desiccator in order to keep them away from humidity.

3.2.2 Results and discussion

3.2.2.1 Dispersion characterization

Table 3.2 summarizes the particle size of the synthesized WBPUU dispersions and polydispersity measured by DLS, the Z potential values as well as the real solid content.

Table 3.2 Characterization of the WBPUU dispersions. Particle size, polydispersity, Z potential and solid content

System	Particle size (nm)	Polydispersity	Zeta potential (mV)	Solid content (wt%)
PCL100	86±1	0.05±0.02	-44.2±0.3	25.0
PCL95PEG5	97±1	0.16±0.01	-48.7±0.9	23.3
PCL90PEG10	115±2	0.26±0.03	-41.6±0.2	25.2
PCL85PEG15	105±5	0.23±0.03	-44.1±0.9	24.5
PCL80PEG20	112±15	0.13±0.05	-42.7±0.6	26.2

DLS reveals a particle size of 86±0.1 nm for the PCL100 system, with a polydispersity equal to 0.05±0.02. These results are similar to those reported by other authors, which reported values in the range between 70 and 100 nm [1]. Comparing this obtained particle size with those of the dispersions containing PEG, an increase of both particle size and polydispersity can be observed. The hydrophilic nature of PEG allows the swelling of the particles by interactions with water. Thus, the particles present not only higher particle size, but also higher polydispersity with all systems presenting monomodal distributions with the absence of aggregates. This increase of the particle size leads to the reduction of the specific surface area [2–4], which can affect to the stability of the dispersion. However, in this case, no modification of the stability was observed as the particle size increased.

As far as the stability of the dispersions is concerned, all the systems present Z potentials below −30 mV. Hence, the stability of the prepared dispersions is proved since stable dispersions have a Z potential above +30 mV and below −30 mV [5]. The solid content was also determined by the aforementioned method. The synthesized WBPUUs showed a solid content close to the theoretical, suggesting that all the reagents were adequately integrated in

the stable nanoparticles. The WBPUU dispersions were stored under room temperature and no presence nor of aggregates nor of sedimented material has been observed during time. Despite all samples presented solid content values under a 27 wt%, samples containing higher PEG content presented higher viscosities, resulting in a physical gelation with solid contents above ~30%. This phenomenon, which was not been observed for PCL100 system, will represent an advantage as far as its potential use as 3D-printing inks, thus, will be taken into consideration in the choice of the WBPUU formulation.

The dispersions were also analysed by TEM. Images of the WBPUUs with different PEG contents are shown in **Figure 3.3**. The obtained images confirm the higher particle size of the WBPUUs containing PCL/PEG in their SS compared with the WBPUU based on just PCL. Additionally, the hydrophilic PEG in the SS tends to arrange at the nanoparticle shell. As can be observed in the inset of each image, at the intermediate PEG content the core and the shell start begin to differentiate and at the highest PEG content, a more defined core–shell structure seems to be observed in PCL80PEG20 system, suggesting that the addition of PEG promotes structural changes into the nanoparticle.

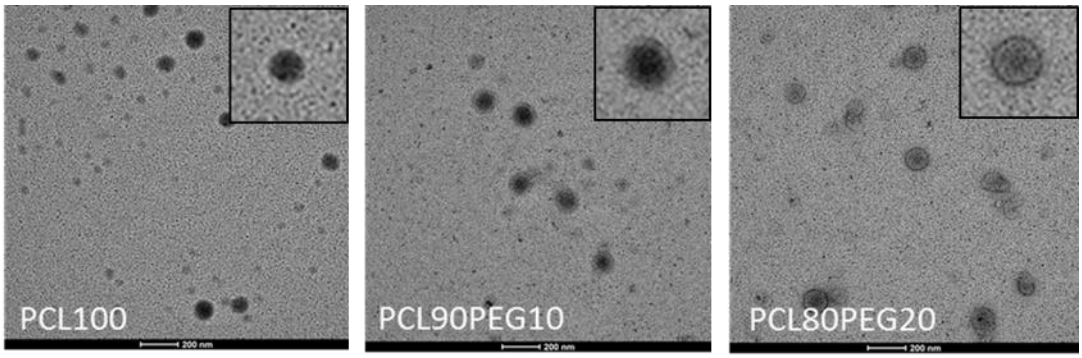

Figure 3.3 TEM images of different WBPUU systems. ×2500 magnification. Evolution of particle size and structure with the PEG content

3.2.2.2 Film characterization

The molecular mass of the synthesized polyurethane urea was determined by gel permeation chromatography. Films obtained by casting of the obtained dispersions were used for that purpose The obtained results are displayed in **Table 3.3**. Results showed that PCL100 is the WBPUU with the higher molecular mass. The addition of PEG results in lower molecular mass, probably owing to the lower molecular mass of PEG polyol (992 g mol^{-1}) compared with PCL polyol (1957 g mol^{-1}). This decrease of molecular mass is noticeable and greater in systems with higher amounts of PEG. Similar molecular mass values are reported in the literature for waterborne polyurethanes containing PEG in their SS, obtaining values

between 25000 and 15000 g mol^{-1} with different contents of PEG [6]. Despite this decrease, the aforementioned measured pH range of 7–8, confirmed that the reaction has been performed successfully. Regarding dispersity index, all system present similar values with the addition of PEG but higher compared with systems only containing PCL.

Additionally, the hydrophilic–hydrophobic nature of the surface of the prepared films has been determined by WCA measurement (**Table 3.3**). Analysing the obtained values, the addition of hydrophilic PEG to the WBPUUs resulted in a decrease of the contact angle as expected from the hydrophilic PEG shell observed for the particles. In films with higher amount of PEG it tends to arrange in the shell of the particle, showing more affinity with water compared with systems based only on PCL or with small amounts of PEG.

Table 3.3 Weight average molecular mass and dispersity index of synthesized WBPUU with different ratios of PEG/PCL and WCAs of the films

System	$\bar{M}_w$ (g mol^{-1})	Dispersity index ($\bar{M}_w/\bar{M}_n$)	Contact angle (°)
PCL100	35240	1.3	90±3
PCL95PEG5	25795	1.5	83±3
PCL90PEG10	24314	1.7	78±3
PCL85PEG15	23196	1.7	76±2
PCL80PEG20	21813	1.8	72±4

The characteristics functional groups of PUs were studied by FTIR. **Figure 3.4** shows the FTIR spectra of the WBPUU synthesized with only PCL in the SS (PCL100) and the WBPUU synthesized with the highest content of PEG (PCL80PEG20). Both spectra showed a band in the 3350–3320 cm^{-1} interval, where hydrogen bonded and non-hydrogen bonded N─H of urethane and urea groups appear [7]. In this case, the observed signal, situated at 3330 cm^{-1} suggests that most of the N─H groups are involved in hydrogen bonds. The peak around 1735 cm^{-1} corresponds to the C=O vibration of PCL and of urethane group [8], whereas a signal situated at 1640 cm^{-1} is attributed to hydrogen bonded C=O of urea groups [9]. The band situated at 1550 cm^{-1} in Amide II region is assigned to the C─N stretching vibration and N─H bending of urethane groups. The band located around 1460 cm^{-1} corresponds to ─CH_2─ bending band and the signal situated at 1024 cm^{-1} is assigned to C─O stretching vibration.

Additionally, the absence of bands in the 2260–2280 cm^{-1} interval (─NCO group) confirmed that the diisocyanate had completely reacted during the synthesis, and thus, means that the

polymerization reaction has happened successfully [10]. Comparing both spectra, no differences were observed, neither shifting of existing bands nor apparitions of new signals have been observed despite of their different SS compositions.

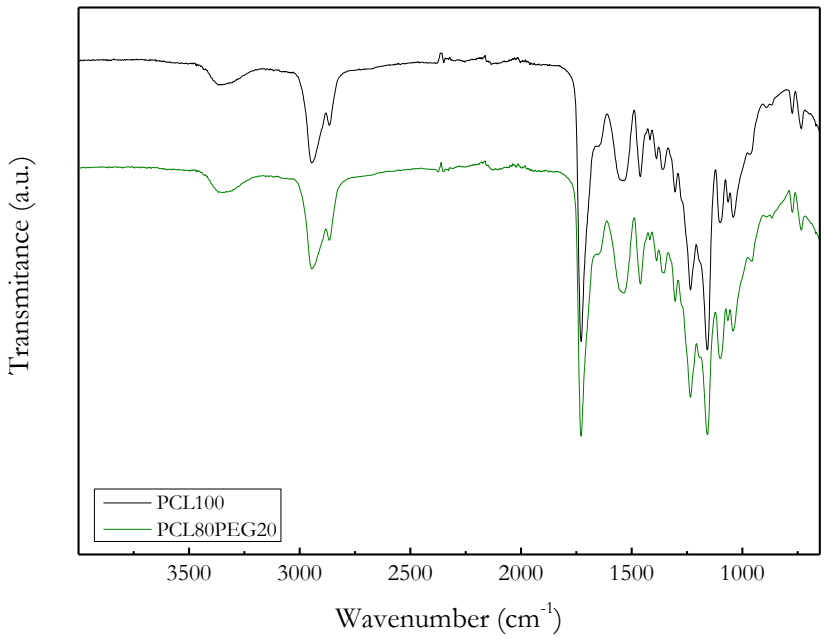

Figure 3.4 ATR-FTIR spectra of PCL100 and PCL80PEG20

The chemical structure of the prepared WBPUUs was also analysed by ^{1}H NMR. Spectra displayed in **Figure 3.5** showed differences between PCL100 and PCL80PEG20 WBPUUs. Spectrum of PCL100 showed typical chemical shifts related to the different protons of PCL polyol at 4.06 (Ha), 2.4 (Hb), 1.67 (Hc), and 1.36 (Hd) ppm. The spectrum of PCL80PEG20, in addition to peaks of PCL, showed a peak at 3.6 ppm, which is assigned to the methylene protons of the backbone of PEG (He). The presence of this new signal confirms the incorporation of the PEG. A peak related with methylene protons of DMPA at 3.9 ppm (Hf) is also observed in both spectra.

Taking into account the molecular mass of both polyols and the areas of Ha peak of PCL and He peak of PEG, the PEG content in PCL80PEG20 WBPUU is determined, obtaining a value of 0.22 (22 wt%) which is similar to the theoretical value of 20 wt%.

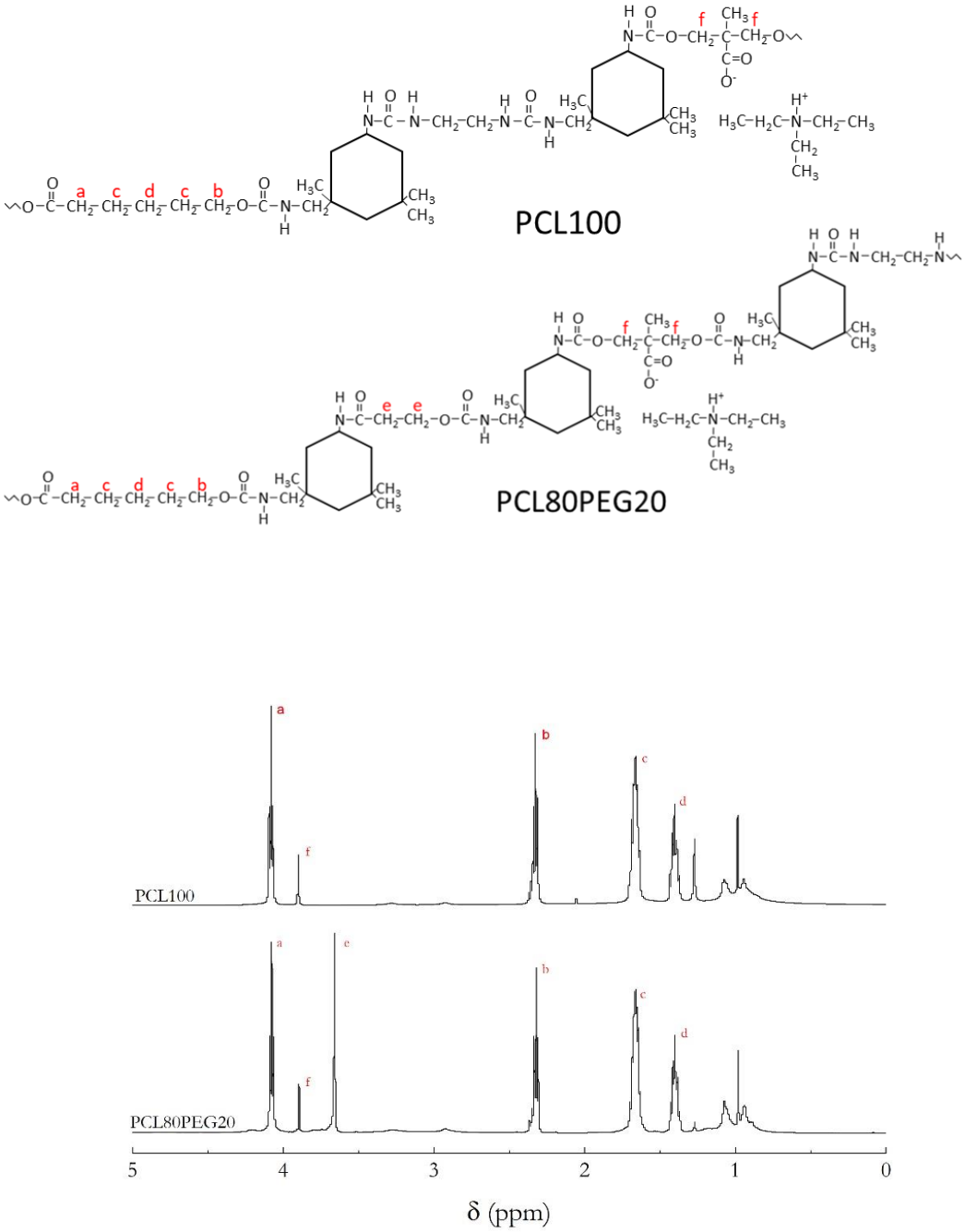

Figure 3.5 ^{1}H MNR spectra of PCL100 and PCL80PEG20

Thermal behaviour of the films has been studied by DSC. The thermograms of synthesized WBPUUs and neat polyols for comparison purposes are displayed in **Figure 3.6** and the values of the measured transitions are displayed in **Table 3.4**.

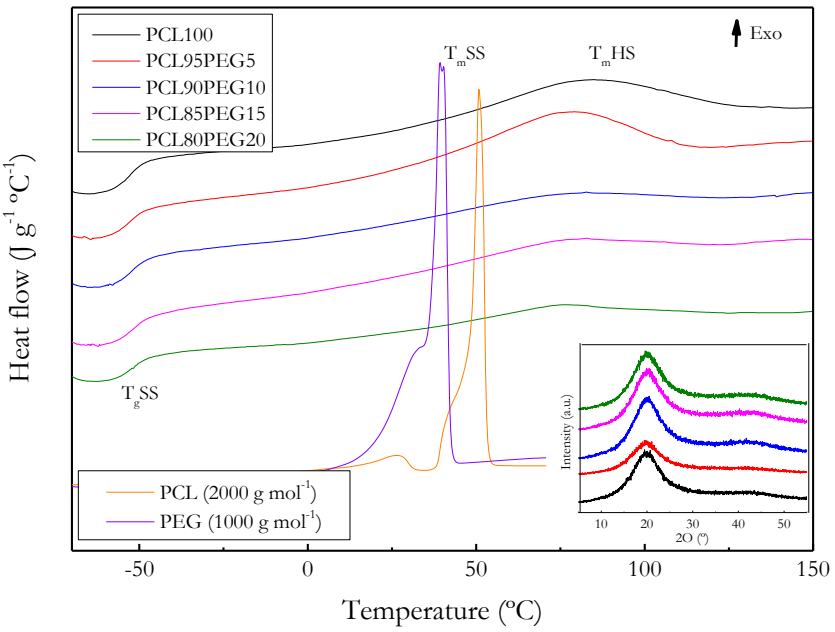

Figure 3.6 DSC thermograms of synthesized WPUU films and pure polyols. Inset: X-ray diffractograms of WBPUUs

Table 3.4 Measured thermal transitions of WBPUU films

System	T_gSS (°C)	T_mHS (°C)	ΔH_m (J g^{-1})
PCL100	-55.9	79.5	16.5
PCL95PEG5	-56.8	78.0	15.8
PCL90PEG10	-56.5	74.2	6.1
PCL85PEG15	-55.6	73.5	5.5
PCL80PEG20	-55.1	72.8	3.4

A transition was observed in all samples around −55 °C, which is related with the glass transition of the SS (T_gSS). Comparing to the glass transition temperature of pure polyols, an increase was observed respect to PCL T_g situated at −66.7 °C (no T_g was observed for PEG in this interval), due to mobility restrictions when they were integrated in the PU structure. In addition, no melting peaks of SS were observed, which indicates that this integration prevents PCL or PEG rich domains crystallization. Neat PEG and PCL showed a melting peak at 42.7 and 46.7 °C, respectively. X-ray diffraction analysis has been performed in order to confirm the lack of SS crystallization. The obtained results that are displayed in the inset of **Figure 3.6** did not show any sign of crystallization in all studied

WBPUUs agreeing with DSC results, showing all diffractograms wide diffraction peaks presenting low intensity. The two diffraction peaks observed at 18º and 43º are the characteristic peaks of the SS in segmented polyurethanes [11].

Regarding the HS, an endothermic transition can be observed in all samples in the 70–80 °C interval attributed to the short range ordered HS domains (T_mHS) [12]. This endothermic transition temperature measured for PCL100 is in the range of the values reported previously for other WBPUUs containing only PCL in the SS [13]. The temperature of this transition seems to decrease with the addition of PEG. Additionally, the enthalpy assigned to this phenomenon also seems to be lower with the addition of PEG. The tendency of PEG to arrange in the shell of nanoparticles as observed by TEM could hinder the ability of interactions between urethane and urea groups in the HS, thus resulting in a decrease of both melting temperature and enthalpy. This decrease is more appreciable starting from a 3.4 wt% of PEG (PCL90PEG10).

The thermal stability of WBPUU has been studied by TGA. The thermal degradation of polyurethane ureas is considered as a depolycondensation process which starts above 200 °C with the degradation of HS, and finished with the degradation of the SS [14]. In general, it consists on a first two degradations corresponding to urea and urethane linkages around 250 and 300 °C, respectively, and a third one around 350–400 °C assigned to the SS [15]. However, the temperature of the different degradation steps can be modified since the thermal stability of the polyurethane ureas is highly depending on the composition of the HS and SS, the type of diisocyanate, the ionic group content, as well as the microphase separation and crystallinity of the phases [16]. The TGA and DGT curves of the WBPUUs and polyols are displayed in **Figure 3.7**. The degradation temperatures taken from the curves are gattered in **Table 3.5**.

Analysing the obtained results, PCL based WBPUU showed one degradation step around 300 °C, whereas WBPUUs containing PEG also showed a second degradation step around 375 °C. Comparing with the TGA and DTG curves of neat PCL and PEG, a higher degradation temperature of PEG compared with PCL was observed, so, the second degradation appeared in PCL/PEG containing WBPUUs seems to correspond to the PEG. The obtained behaviour did not correspond with the aforementioned general behaviour, since the steps assigned to urea and urethane linkages and PCL polyol are overlapped in a single degradation process.

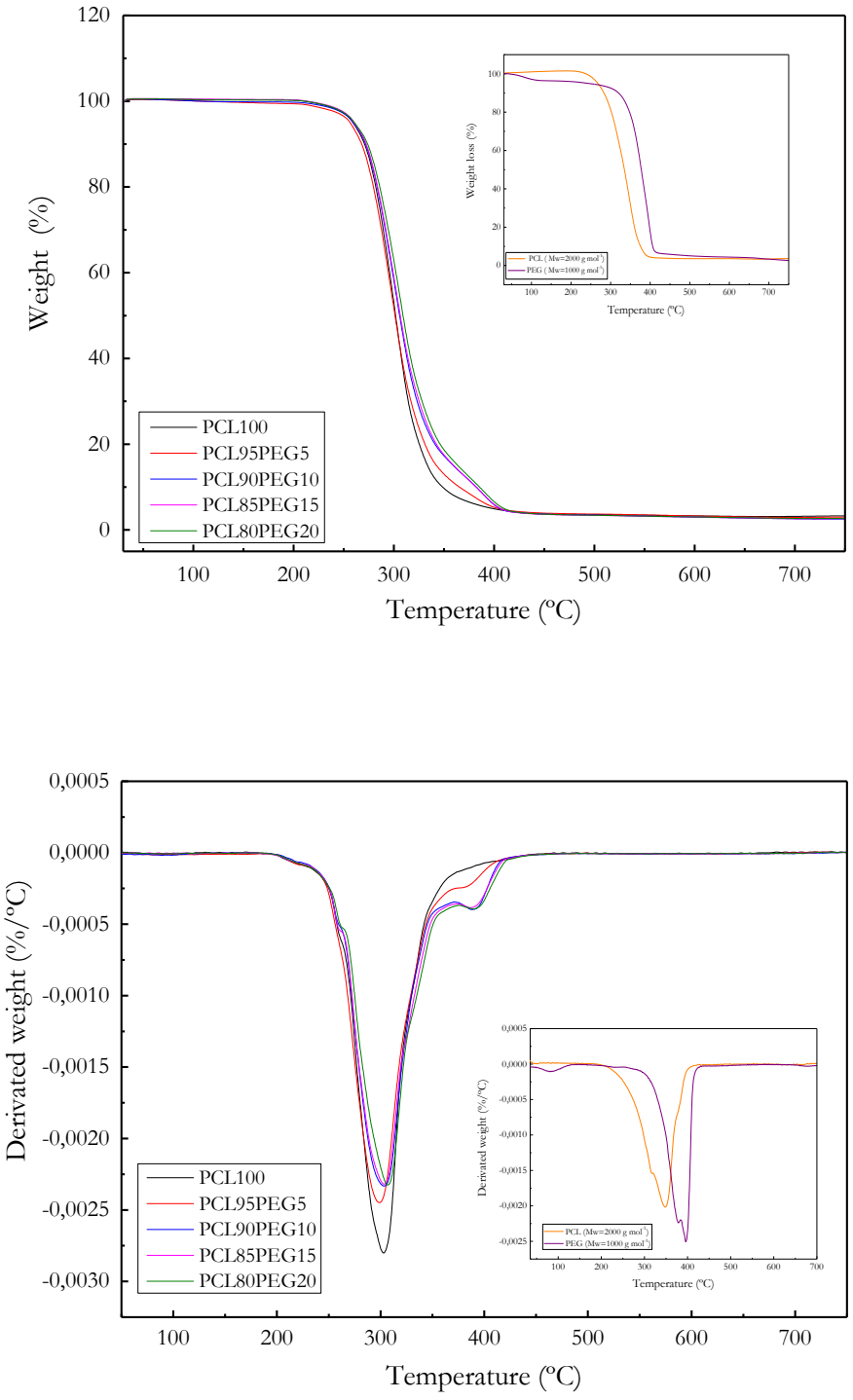

Figure 3.7 Variation of the weight (up) and the derivated weight (down) of the WBPUU as a function of the temperature. Weight of polyols (inside up) and derivated weight of polyols (inside down) have been included for comparative purposes

Table 3.5 Initial degradation and maximum degradation temperatures of system prepared from PEG with different PCL/PEG ratio

System	T_0 (°C)	T_d (°C)
PCL100	257	301
PCL95PEG5	257	300
PCL90PEG10	259	303
PCL85PEG15	260	303
PCL80PEG20	260	307

Studying the influence of the increase of the PEG content into the polymer backbone, a slight increase of the initial degradation temperature (T0) and the main degradation temperature (Td) were observed (**Table 3.5**). This slight increase of the thermal stability can be attributed to the increase of the PEG content in the WBPUU film as observed in **Table 3.1**. The higher thermal stability observed in **Figure 3.7** of the PEG diol compared with the PCL one provides to the WBPUU systems with higher content of the former higher thermal stability. Thermal stability of this WBPUU films is an important parameter in order to determine the potential applications of this material. All systems were stable until 250 °C where the first degradation process happens. However, the endothermic transition observed at 70–80 °C in the DSC thermograms for all systems, limits clearly the operational stability below this temperature. The prepared materials could be reuse by reprocessing the films above their melting temperature.

Regarding the thermomechanical properties, the evolution of storage modulus (E'), loss modulus (E") and tan δ with temperature of the different WBPUUs are presented in **Figure 3.8**. The PCL100 WBPUU showed the higher storage modulus at glassy state. The decrease in E' and the maximum of tan δ and E" observed at low temperatures are related to the glass transition temperature of the SS. For all the synthesized WBPUUs, the addition of PEG did not significantly change the T_gSS as also observed by DSC. Notwithstanding, a flattening and broadening of the tan δ peak is observed at the highest PEG content, owing to the restrictions in the molecular mobility from PEG chains assembled in the nanoparticles shell. Above T_gSS all systems showed a decreasing tendency of the E', presenting PCL100 and PCL95PEG5 higher modulus at room temperature. Similar behaviours were observed in the literature with maximum tan δ values, which is related with the T_gSS, in the same interval [13,17,18].

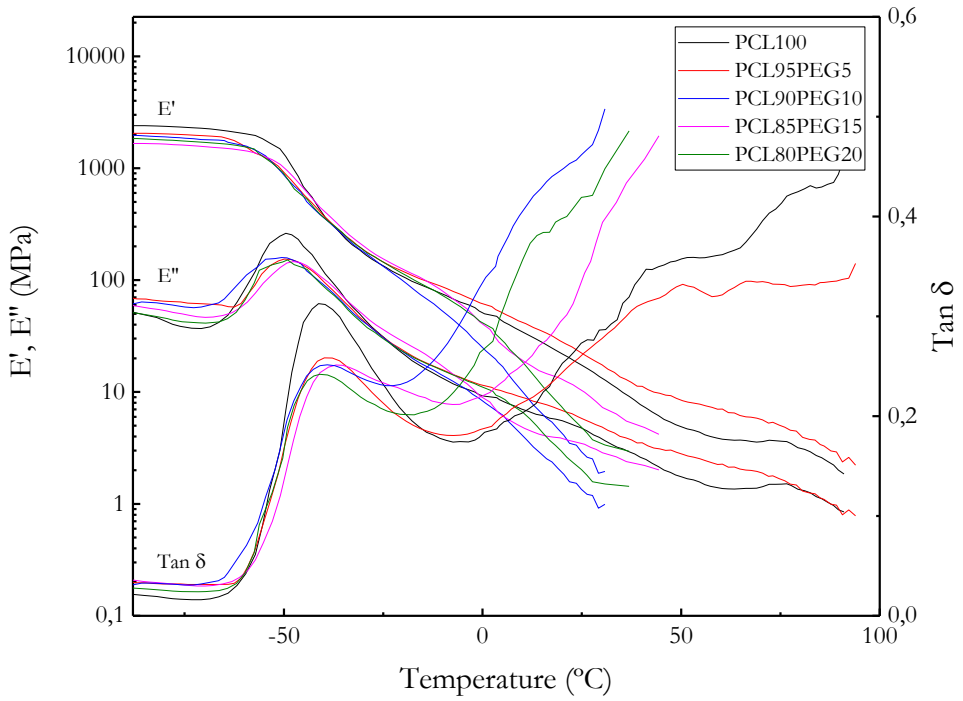

Figure 3.8 Storage and loss moduli (left axis) and tan δ (right axis) as a function of temperature for PCL/PEG WBPUU systems. Frequency = 1 Hz and scanning rate = 2°C min^{-1}

As far as the thermomechanical stability is concerned, the addition of PEG seems to decrease the thermomechanical stability compared to the PCL based polymer (PCL100). Both PCL100 and PCL95PEG5 showed higher stabilities whereas the other systems containing more amount of PEG experienced a significant decrease, showing a progressive drop of their E' and E" at lower temperatures. The assembly of the PEG into the shell of the particles seems to hamper the formation of short range interactions between urethane–urea groups, thus, decreasing their thermal stability.

Mechanical properties of the WBPUUs were evaluated by tensile testing. **Figure 3.9** shows the stress–strain curves of the different systems, whereas mechanical parameters such as Young modulus, tensile stress, and elongation at break are summarized in **Table 3.6**.

The behaviour of the different systems agreed with previous DSC and thermomechanical analysis results. A decrease of the urethane and urea short range ordering in the HS with the addition of PEG resulted in lower tensile modulus and stress at break, but higher strain at break. Similar thermal and mechanical behaviours were found for PCL100 and PCL95PEG5

WBPUUs. Comparing these values with those reported in previous works, one can notice higher values of Young modulus (23±2 MPa against 6.4±0.4 MPa), as well as similar strain at breaks (842±102% vs. 891±51%) [19]. The other systems presenting higher amount of PEG, exhibited similar Young modulus values as well as similar strain at break suggesting that the addition of only 3.4 wt% is enough to modify the behaviour of the WBPUU. Moreover, it is important to indicate that no remarkable differences were observed at higher PEG content.

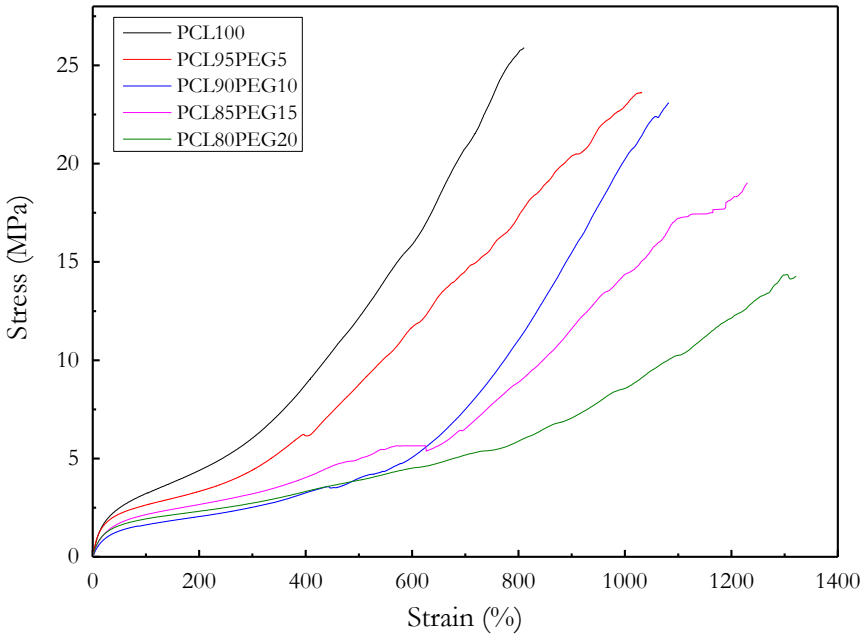

Figure 3.9 Stress–strain curves of WBPUUs at room temperature. Elongation rate = 20 mm min^{-1}

Table 3.6 Mechanical properties of WBPUU films

System	Young modulus (E) (MPa)	Stress at break (σ_b) (MPa)	Strain at break (ε_b) (%)
PCL100	21±2	29±8	842±102
PCL95PEG5	19±2	25±3	1063±114
PCL90PEG10	14±2	24±8	1080±41
PCL85PEG15	14±2	15±5	1106±122
PCL80PEG20	14±2	12±5	1312±84

AFM analysis was carried out in order to analyse the morphology of films formed from the dispersions. **Figure 3.10** shows the phase and three dimensional representation of height images of different WBPUU systems. High dissipating soft domains give dark contrast while stiffer phases appear brighter due to the different energy dissipation by the cantilever, enabling the possibility of differentiate the different domains [20].

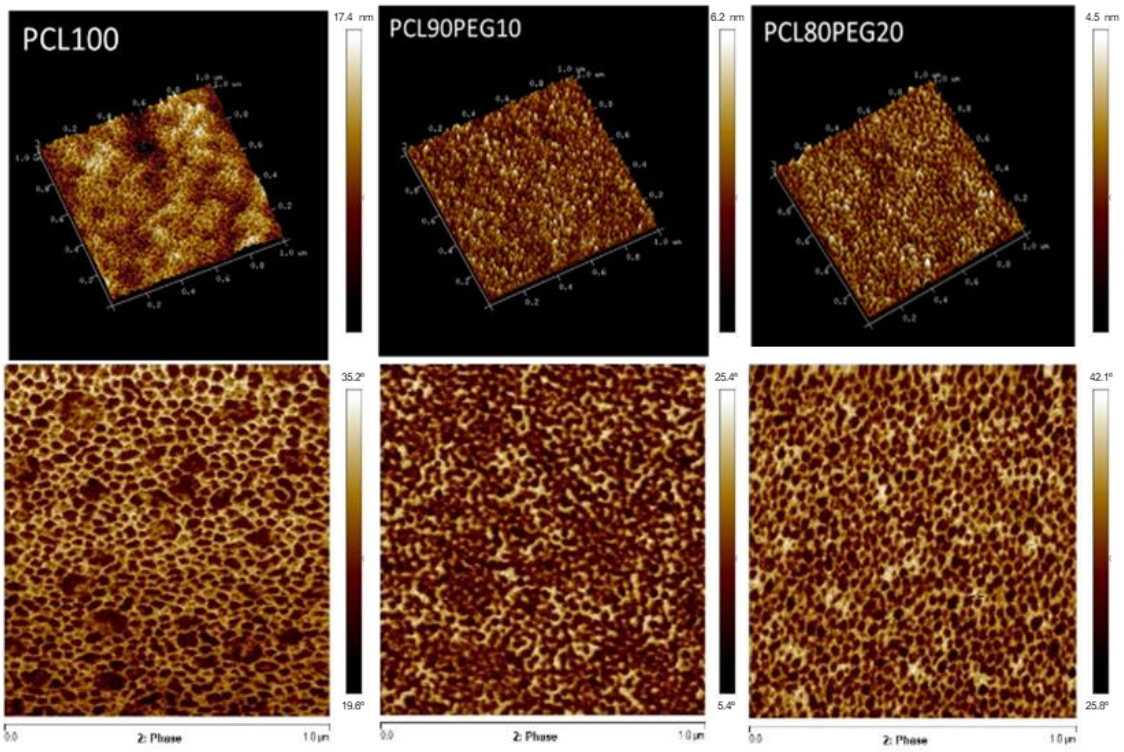

Figure 3.10 AFM 3D height reconstruction and phase images of PCL100, PCL90PEG10, and PCL80PEG20 WBPUUs

Analysing the obtained images, separated microphase segregation can be observed in PCL100 system. These phases, which are formed by the coalescence of the nanoparticles and presenting a spherical microstructure, are formed by dark domains corresponding to the core PCL and lighter zones, which are composed by the HS and represent the shell of the particles. The formation of these microdomains leads to better mechanical properties as well as higher thermomechanical stability as was obtained in mechanical testing and DMA. The addition of PEG to the WBPUU, however, seems to result in a modification of the morphology which can be observed with the addition of very small quantities of PEG (3.4 wt%). Above this quantity, no remarkable differences are observed in the morphology confirming the mechanical behaviour described previously. Due to its hydrophilic nature, the PEG tends to arrange at the shell of the particle, becoming slightly thicker, as was also observed by TEM.

As can be observed for the WBPUU with the highest amount of PEG, the thick of the particles shell increases whereas the dark domains corresponding to the PCL decrease their size, leading to the formation of a slightly different microstructure to that observed in PCL100. Hence, PCL90PEG10 and PCL80PEG20 present similar morphology as was also observed by TEM, both due to the arrangement of PEG in the shell of the particles. The analysed microstructures corroborate that hydrophilic PEG act as non-ionic emulsifier facilitating the formation of the nanoparticles.

It can conclude that the morphology changes observed by AFM as well as the core–shell morphology highlighted by TEM both confirm the assembly of PEG in the shell of the particle. This result in a hamper of the formation of short range ordering between urea and urethanes, which leads to systems with different mechanical, thermal, and thermomechanical properties. Above this modification of the properties, it was observed that when increasing the solid content of PCL100 system it maintains as a stable sol like dispersion, whereas PCL80PEG20 system tends to form a gel.

3.2.1.3 Conclusions

In this chapter, stable WBPUU dispersions varying PCL/PEG molar ratio in the SS were successfully synthesized. The increase of the PEG content in the WBPUU resulted in an increase of the particle size and polydispersity, obtaining values of 112±15 for PCL80PEG20 compared with the 86±1 of PLC100. Moreover, Z potential measurements confirmed the stability of all dispersions. The particle morphology analysed by TEM revealed that the addition of PEG led to a more segregated core–shell structure which is not observed in PCL100 particles.

Regarding film properties, PCL100 system showed higher Young modulus, thermomechanical stability, and higher enthalpy assigned to the short range ordering of hard domains due to the microstructure observed in that system. Systems containing PEG in their SS, however, showed higher elongation at break owing to the observed microstructure where PEG hampers the formation of short-range ordered domains between urea and urethanes. Concretely, the elongation at break increased 500% comparing the PCL100 system with the one containing the higher amount of PEG. Additionally, films containing hydrophilic PEG present also higher affinity with water obtaining decreasing WCAs when PEG is added, from 90±3 of PCL100 to 72±4 of PCL80PEG20. Finally, a low amount of 3.4 wt% of PEG is enough to modify the properties and higher PEG content does not result in a noticeable variation of the properties of films. Taking into consideration the observed physical gelation

for system containing PEG at high solid contents, PCL80PEG20 was selected so as to be the composition of the WBPUU ink, presenting the other systems more difficulties to form a physical network.

3.3 Effect of the molecular mass of PEG into the WBPUU dispersions and films

3.3.1 Experimental part

Based on the previously prepared PCL80PEG20, new WBPUUs were synthesized using PEG with different molecular mass in order to study its influence in the dispersions but also in films prepared from the dispersions. All systems were prepared following the same stoichiometry that was used for PCL80PEG20, that is 0.8/0.2/3.5/1/1.5 of PCL/PEG/IPDI/DMPA/EDA but using PEGs with different weight molecular mass of 400, 1000 and 1500 g mol^{-1}. In the **Table 3.7** the composition of the different prepared WBPUUs is displayed.

Table 3.7 Composition of the different prepared WBPUUs with different PEG molecular mass

System	Mw_{PEG} (g mol^{-1})	PEG (wt%)	Hard segment (wt%)	COOH (wt%)	Emulsifier (wt%)
PCLPEG400	400	2.8	40.6	1.6	5.1
PCLPEG1000	1000	6.7	38.9	1.6	4.8
PCLPEG1500	1500	9.8	37.7	1.5	4.7

Films were also prepared by casting the dispersions in Teflon molds and drying in a climatic chamber at 25 °C with a 50% of relative humidity for 1 week, followed by 3 days in a vacuum oven at 25 °C (400–420 mbar). After this time, polyurethane urea films with a thickness of about 0.5 mm were obtained from WBPUU dispersions. The solid content of the prepared dispersion has been taken into account in order to ensure the desirable thickness of the film. The films have been storage at room temperature in a desiccator in order to keep them away from humidity. In the **Figure 3.11** an image of the different films prepared from the aforementioned WBPUU is displayed. Despite PCLPEG400 and PCLPEG1000 presented a homogeneous appearance showing high transparency, the film prepared from PCLPEG1500 showed a non-homogeneous appearance, presenting multiple bubbles as well as non-homogeneous thickness of the film.

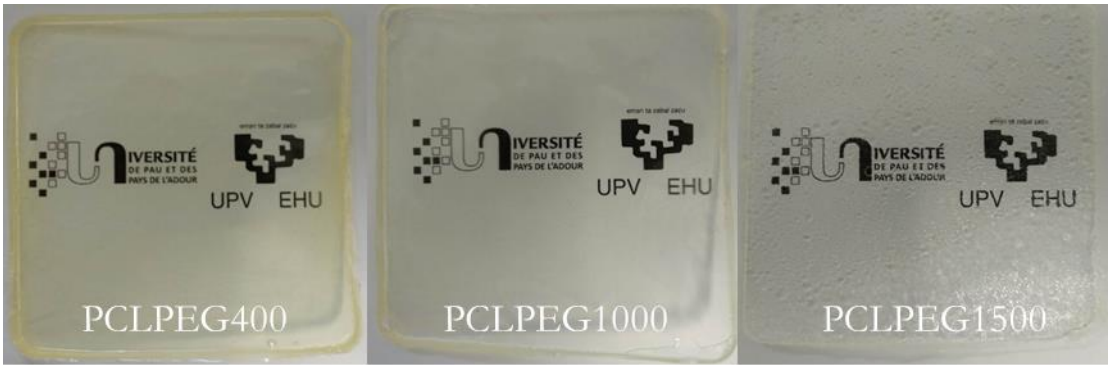

Figure 3.11 WBPUU films containing PEG with different molecular mass

3.3.2. Results and discussion

3.3.2.1 Dispersion characterization

Just as in the previous part, the particle size of the synthesized WBPUU dispersions and their average diameter measured by DLS, the Z potential measurements as well as the real solid content are summarized in **Table 3.8**.

Table 3.8 Characterization of the WBPUU dispersions synthesized with PEG of different molecular mass. Particle size, polydispersity, Z potential and solid content

System	Particle size (nm)	Polydispersity	Z potential (mV)	Solid content (%)
PCLPEG400	42±5	0.13±0.02	-46.3±0.8	23.2
PCLPEG1000	112±15	0.13±0.05	-42.7±0.6	26.2
PCLPEG1500	308±29	0.22±0.03	-34.9±0.9	24.8

Analysing the obtained results, an increase of the particle size was observed as the molecular mass of the PEG did. The PCLPEG400 presented the lowest particle size, around a 50% lower than the PCLPEG1000, whereas the system containing the higher molecular mass of PEG showed almost three times higher particle size than PCLPEG1000. This particle size increase matches with the higher PEG content. Regarding the polydispersity, both PCLPEG400 and PCLPEG1000 showed similar values despite their different particle size. Contrary, PCLPEG1500 presented higher polydispersity, resulting in a wider distribution of particle sizes. The stability of the dispersions, which was studied by Z potential, showed values in the range of the stability (above +30 mV and below −30 mV) [5], presenting values below -30 mV for all systems. However, the values obtained for the PCLPEG1500 are very close to the limit of the range, and would present stability problems. This decrease of the

stability was observed in the dispersion where deposited material at the bottom of the bottle after 24 h as well as the presence of agglomerates was seen. The presence of this agglomerates can explain the aforementioned inhomogeneous appearance of the PCLPEG1500 film. Additionally, it was observed that for an 80/20 ratio of PCL/PEG, the increase of the molecular mass of PEG (or in other words, the increase of the PEG content) favours the physical gelation of the WBPUU.

3.3.2.2 Films characterization

The measurements of molecular masses are reported in **Table 3.9** and showed similar Mw comparing PCLPEG1000 and PCLPEG1500 despite the lower molecular mass of the PEG diol in the former. The PCLPEG400 contrary, presenting much lower values of molecular mass due to the lower molecular mass of its PEG diol. Both PCLPEG400 and PCLPEG1000 presented similar dispersity, whereas PCLPEG1500 presented higher values, confirming a higher distribution of the molecular mass of the molecules. Additionally, the hydrophobic or hydrophilic behaviour was estimated by water contact angle. The water contact angle values displayed in **Table 3.9** showed a decrease of the contact angle as the molecular mass of the used PEG increased. As the molecular mass of the PEG increased the same does the PEG content resulting in a decrease of the contact angle due to the hydrophilic nature of the PEG as was previously observed in **Table 3.3**.

Table 3.9 Weight average molecular mass and dispersity of synthesized WBPUU with PEGs with different molecular mass and water contact angle of the films

System	$\bar{M}_w$ (g mol^{-1})	Dispersity ($\bar{M}_w/\bar{M}_n$)	Contact angle (°)
PCLPEG400	13904	1.8	77±2
PCLPEG1000	21813	1.8	72±4
PCLPEG1500	21928	2.4	66±1

The characteristics functional groups of polyurethane ureas were studied by FTIR. The results, which are displayed in **Figure 3.12** showed similar spectra compared with the ones observed for the variation of PCL/PEG ratio. All systems presented the aforementioned characteristic bands of the polyurethane ureas but nor apparition of new ones nor displacement of the existing ones are reported with the variation of the PEG molecular mass. The inset of the **Figure 3.12** confirmed the absence of displacement of the bands related to the characteristics C=O stretching vibrations of the urethane and urea groups. The absence

of the absorption peak related to the –NCO at 2260-2280 cm^{-1} corroborated that isocyanate reacted completely [21].

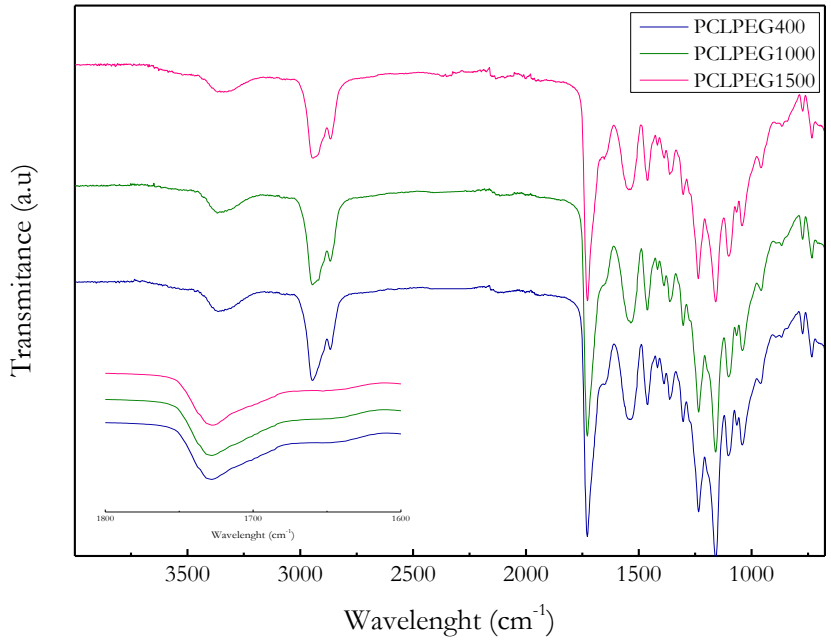

Figure 3.12 ATR-FTIR spectra of systems containing PEG with different molecular mass. Inset: magnification of the 1800-1600 cm^{-1} region

The thermograms of synthesized WBPUUs are shown in **Figure 3.13**, whereas the measured thermal transitions are displayed in **Table 3.10.** As happened previously for the study of variation of the PCL/ PEG ratio, all systems presented a transition around -55 ºC, which is assigned to the glass transition of the SS (T_gSS) and did not show any remarkable variation with the modification of the molecular mass of the PEG. Regarding the melting of the SS, PCLPEG400 and PCLPEG1000 did not show any melting peaks of SS, despite both neat PEG400 and PEG1000 presented a melting peak (T_mSS) at 1.7 and 42.7 °C, respectively. In this case, as was suggested for the variation of the PCL/PEG ratio, the incorporation of this polyols to the polymer backbone result in a restriction of the mobility of the chains avoiding the crystallization of the SS. The X-ray spectra of both PCLPEG400 and PCLPEG1000 displayed in **Figure 3.14** confirmed the lack of crystallization on the films. Contrary, PCLPEG1500 presented a melting peak at 51.4 °C, which is situated at the same temperature as the melting transition of neat PEG1500 diol and can be assigned to the melting transition of the SS. In this case, the X-ray spectra of PCLPEG1500 displayed in **Figure 3.14** showed

crystallization peaks confirming the crystallization of the SS for the film containing the PEG with the higher molecular mass. The higher molecular mass and amount of PEG of the PCLPEG1500 compared with the other WBPUUs allowed to the arrangement of rich PEG domains which crystalized. Hard segment wise, all systems presented an endothermic transition situated in the 70-80 ºC interval which is assigned to the short-range ordered HS domains and are situated in the same interval as was observed previously for the WBPUUs with different PCL/PEG ratios. Despite the temperature of this transition did not show any important variation with the increase of the molecular mass, and the corresponding enthalpy assigned to this phenomenon seems to be lower as the molecular mass of PEG increase.

As can be observed in the **Table 3.6**, the PCLPEG1500 presented higher PEG content in the polymer backbone, which in accordance to the results obtained for the systems with different PCL/PEG ratio, can lead to hinder the ability of interactions between urethane–urea groups in the HS, resulting in a decrease of both melting temperature and enthalpy. In addition, the HS content decreases as the PEG molecular mass increases.

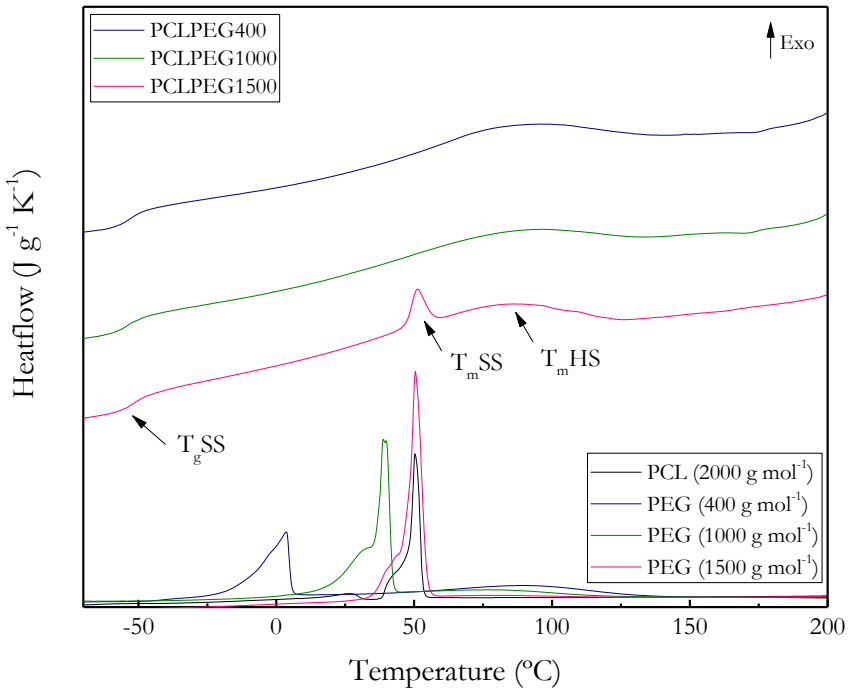

Figure 3.13 DSC thermograms of synthesized WPUU films containing PEG with different molecular mass and pure polyols

Table 3.10 Calculated thermal transitions of WBPU films containing PEG with different molecular mass

System	T_gSS (°C)	T_mSS (°C)	T_mHS (°C)	ΔH_m (J g^{-1})
PCLPEG400	-55.6	-	73.1	3.8
PCLPEG1000	-55.1	-	72.8	3.4
PCLPEG1500	-55.4	51.4	71.2	3.1

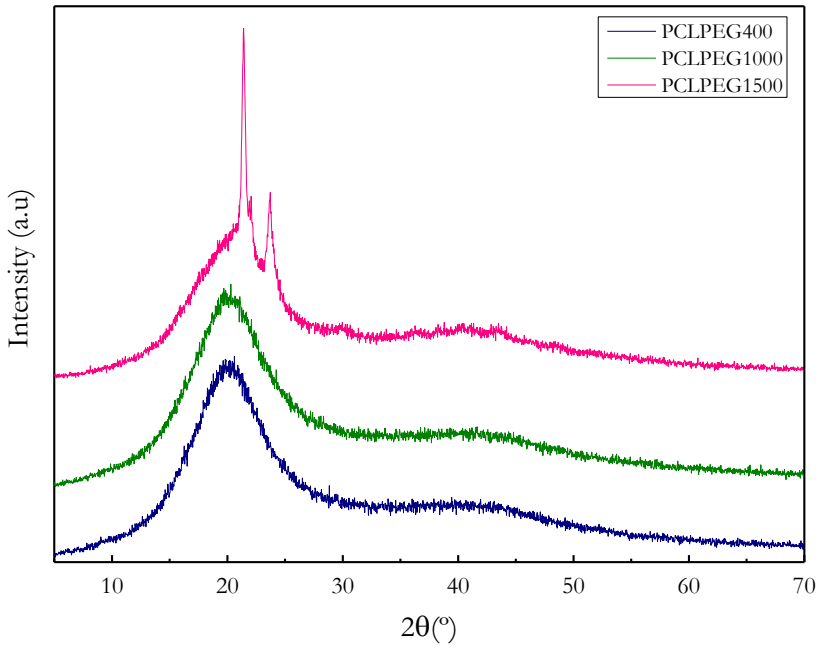

Figure 3.14 X-ray patterns of the WBPUUs prepared with PEG of different molecular mass

Additionally, the thermal degradation of the systems prepared varying the molecular mass of PEG was studied so as to evaluate the influence of the molecular mass of the PEG. The degradation curves are shown in **Figure 3.15** whereas the derivated weight curves are displayed in the inset of the figure**.** Analysing the obtained results, an increase of the thermal stability was observed as the molecular mass of the PEG increased. Presenting the main degradation peak higher temperature values for PCLPEG1500 system than PCLPEG1000 and PCLPEG400, which presented slightly lower values as can be observed in **Table 3.11**, where the degradation temperature of the 5% of the weight and the temperature of the main degradation peak in the derivate is displayed. The increase of the thermal stability of the films as the molecular mass of the PEG increased can be attributed to the higher PEG content contained in PCLPEG1500. As was observed in the insets of **Figure 3.7**, the degradation

curve of the PEG polyol, presented higher degradation temperature compared with the PCL one. Thus, the higher PEG content observed as the molecular mass of the used PEG increased explained this increase of the thermal stability of the films. Moreover, the intensity of the peak observed at 375 ºC related with the degradation of PEG increased as PEG content did.

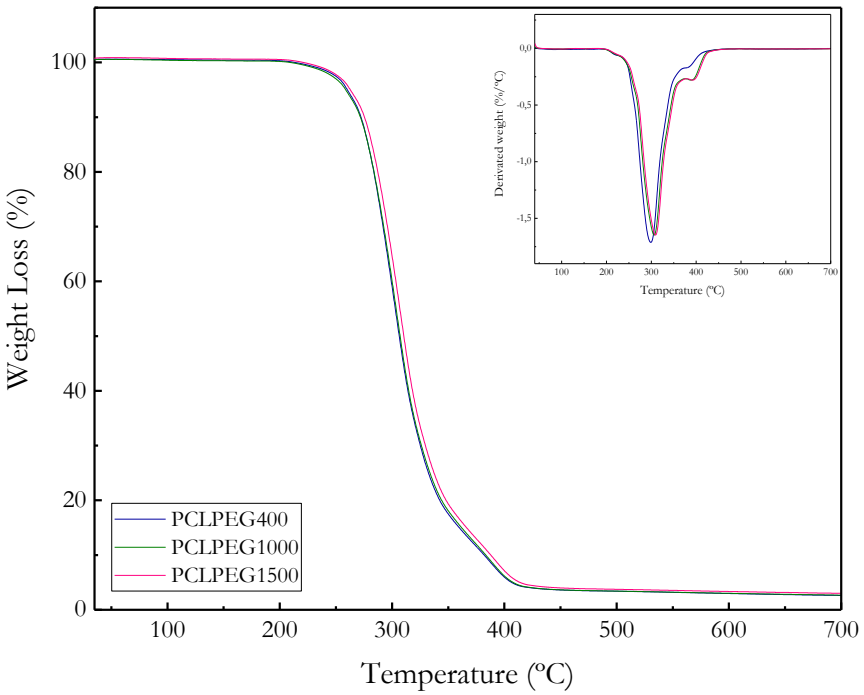

Figure 3.15 Variation of the weight and the derivated weight (inset) of the WBPUU containing PEG with different molecular mass as a function of the temperature

Table 3.11 Initial degradation and maximum degradation temperatures of WBPUU system prepared from PEG with different molecular mass

System	T_0 (°C)	T_d (°C)
PCLPEG400	259	299
PCLPEG1000	260	307
PCLPEG1500	263	309

Regarding the mechanical properties, the films of WBPUU containing different PEG molecular masses were evaluated by tensile testing. **Figure 3.16** shows the stress–strain

curves of the different systems, whereas the calculated mechanical parameters such as Young modulus, tensile stress, and elongation at break are summarized in **Table 3.12.**

A decrease of the Young modulus was observed as the molecular mass of the PEG increased resulting in a decrease of the stiffness of the films. In this case, maintaining the PCL/PEG ratio fixed, the increase of the molecular mass of the used PEG resulted in an increase of the PEG content in the WBPUU as can be observed in **Table 3.6**. This increase of the PEG content as far as mechanical properties is concerned leads to the obtaining of films with lower Young modulus. Contrary, the elongation at break showed an increase when the PEG molecular mass, and thus the PEG content, increased resulting in films with deformation ratio at break around 2000%. This behaviour is in line with the one observed for the variation of PCL/PEG ratio as well as with the observed one in the literature [22]. The increase of the PEG content in the WBPUUs particles lead to decrease of the urethane and urea short range ordering in the HS, resulting in lower tensile modulus and stress at break, but higher strain at break.

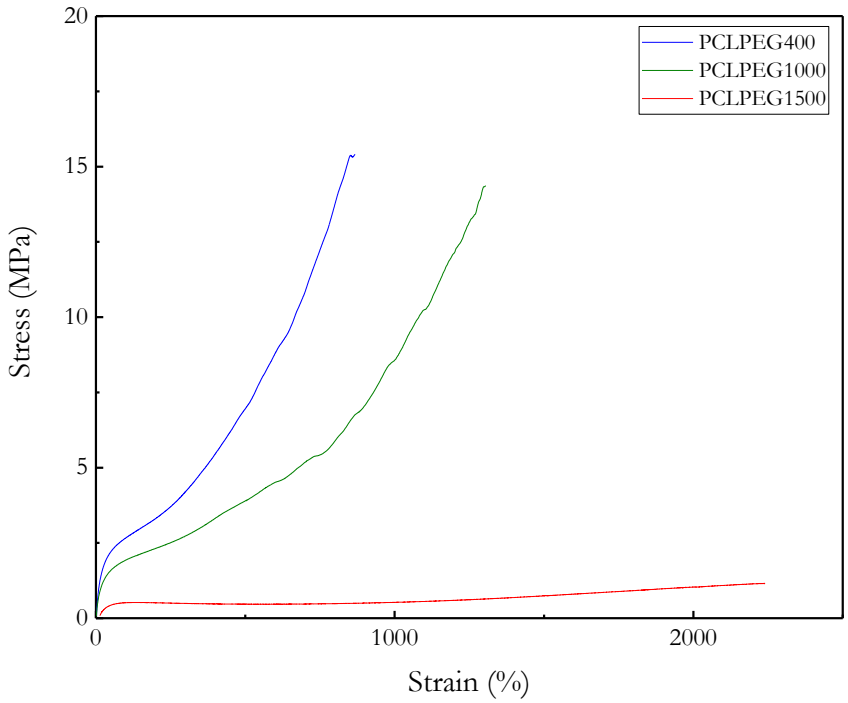

Figure 3.16 Stress-strain curves of WBPUU containing PEG with different molecular mass at room temperature. Elongation rate = 20 mm min^{-1}

Table 3.12 Mechanical properties of WBPUUs films containing PEG with different molecular mass

System	Young modulus (E) (MPa)	Stress at break (σ_b) (MPa)	Strain at break (ε_b) (%)
PCLPEG400	18±3	13±2	851±31
PCLPEG1000	14±2	12±5	1312±84
PCLPEG1500	3±2	2±1	2061±241

3.3.3 Conclusions

In this subsection, the influence of the molecular mass of the PEG into the previously prepared PCL/PEG based waterborne polyurethane urea was studied. For this purpose, different WBPUU dispersions were prepared, maintaining the PCL/PEG ratio to 0.8/0.2 and modifying the molecular mass of the used PEG to 400, 1000 and 1500 g mol^{-1}. The dispersions were subsequently used so as to prepare films by casting in order to study the influence of the molecular mass of the PEG in the films.

Regarding the dispersions, the increase of the molecular mass of the used PEG resulted in an increase of the particle size obtaining also a higher polydispersity, which also affects to the dispersion stability, obtaining Z potential values near to -30 mV, illustrating a decrease of the stability of the system, which was confirmed visually in the PCLPEG1500 system. This decrease of the stability leads to ease the physical gelation of the WBPUU at a solid content ~25 wt%.

Despite the film of the system containing a PEG with 400 g mol^{-1} presented a higher Young modulus compared with the other systems due to its lower PEG content, the dispersion presented a very high stability as well as a lower particle size, which can result in posterior problems to obtain the physical gelation which is required for the obtain of printable inks. The WBPUU prepared with a PEG of 1500 g mol^{-1} contrary, presented a higher particle size and lower stability, which can ease the physical gelation. However, the obtained film from this system presented a low homogeneity and very poor mechanical properties. Taking the aforementioned into account, the system synthesized using a PEG of 1000 g mol^{-1}, that is PCLPEG1000, which is the previously studied PCL80PEG20, represented the most accurate choice, obtaining a stable dispersion but with high particle size compared with PCLPEG400 but also a better mechanical properties of the film than the PCLPEG1500.

3.5 References

[1] M. Fuensanta, J.A. Jofre-Reche, F. Rodríguez-Llansola, V. Costa, J.I. Iglesias, J.M. Martín-Martínez, Structural characterization of polyurethane ureas and waterborne polyurethane urea dispersions made with mixtures of polyester polyol and polycarbonate diol, Prog. Org. Coatings. 112 (2017) 141–152. https://doi.org/10.1016/j.porgcoat.2017.07.009.

[2] M.R. Bezerra, D.. Andrade Neto, W.S. Galvão, N.S. Rios, A.C. de M. Carvalho, M.A. Correa, F. Bohn, R. Fernandez-Lafuente, P.B.A. Fechine, M.C. de Mattos, J.C.S. dos Santos, L.R.B. Goncalves, Design of a lipase-nano particle biocatalysts and its use in the kinetic resolution of medicament precursors, Biochem. Eng. J. (2017). https://doi.org/10.1016/j.bej.2017.05.024.

[3] D.B. Kittelson, Engines and nanoparticles: a review, J. Aerosol Sci. 29 (1998) 575–588.

[4] H. Honarkar, Waterborne polyurethanes: A review, J. Dispers. Sci. Technol. 39 (2018) 507. https://doi.org/10.1080/01932691.2017.1327818.

[5] J. Lee, M. Kim, C.K. Hong, S.E. Shim, Measurement of the dispersion stability of pristine and surface-modified multiwalled carbon nanotubes in various nonpolar and polar solvents, Meas. Sci. Technol. 18 (2007) 3707–3712. https://doi.org/10.1088/0957-0233/18/12/005.

[6] I. Díez-García, A. Santamaria-Echart, A. Eceiza, A. Tercjak, Triblock copolymers containing hydrophilic PEO blocks as effective polyols for organic solvent-free waterborne poly(urethane-urea)s, React. Funct. Polym. 131 (2018) 1–11. https://doi.org/10.1016/j.reactfunctpolym.2018.07.003.

[7] I. Yilgör, E. Yilgör, G.L. Wilkes, Critical parameters in designing segmented polyurethanes and their effect on morphology and properties: A comprehensive review, Polymer 58 (2015) A1–A36. https://doi.org/10.1016/j.polymer.2014.12.014.

[8] A.E. L. Ugarte, B. Fernandez-d'Arlas, A. Valea, M. L. Gonzalez, M.A. Corcuera, Morphology–properties relationship in high-renewable content polyurethanes, Polym. Eng. Sci. 54 (2014) 2282–2291. https://doi.org/https://doi.org/10.1002/pen.23777.

[9] P. Król, B. Król, Surface free energy of polyurethane coatings with improved hydrophobicity, Colloid Polym. Sci. 290 (2012) 879–893. https://doi.org/10.1007/s00396-012-2598-x.

[10] M.A. Pérez-Limiñana, F. Arán-Aís, A.M. Torró-Palau, A.C. Orgilés-Barceló, J.M. Martín-Martínez, Characterization of waterborne polyurethane adhesives containing different amounts of ionic groups, Int. J. Adhes. Adhes. 25 (2005) 507–517. https://doi.org/10.1016/j.ijadhadh.2005.02.002.

[11] C. Fang, S. Pan, Z. Wang, X. Zhou, W. Lei, Y. Cheng, Synthesis of waterborne polyurethane using snow as dispersant: Structures and properties controlled by polyols utilization, J. Mater. Sci. Technol. 35 (2019) 1491–1498. https://doi.org/10.1016/j.jmst.2019.03.017.

[12] C. Fang, X. Zhou, Q. Yu, S. Liu, D. Guo, R. Yu, J. Hu, Synthesis and characterization of low crystalline waterborne polyurethane for potential application in water-based ink binder, Prog. Org. Coatings. 77 (2014) 61–71. https://doi.org/10.1016/j.porgcoat.2013.08.004.

[13] A. Santamaria-Echart, I. Fernandes, A. Saralegi, M.R.P.F.N. Costa, F. Barreiro, M.A. Corcuera, A. Eceiza, Synthesis of waterborne polyurethane-urea dispersions with chain extension step in homogeneous and heterogeneous media, J. Colloid Interface Sci. 476 (2016) 184–192. https://doi.org/10.1016/j.jcis.2016.05.016.

[14] S.M. Cakić, I.S. Ristić, O.Z. Ristić, Thermal analysis of polyurethane dispersions based on different polyols, in: F. Zafar, E. Sharmin (Eds.), Polyurethane, IntechOpen, London, (2012) 79–100. https://doi.org/10.5772/35800.

[15] C.C. Santos, M.C. Delpech, F.M.B. Coutinho, Thermal and mechanical profile of cast films from waterborne polyurethanes based on polyether block copolymers, J. Mater. Sci. 44 (2009) 1317–1323. https://doi.org/10.1007/s10853-009-3272-7.

[16] Y. Zhihui, W. Guangfeng, Z. Huixuan, Effects of the reagent molar ratio on the phase separation and properties of waterborne polyurethane for application in a water-based ink binder, J. Appl. Polym. Sci. 134 (2017) 1–11. https://doi.org/10.1002/app.45406.

[17] I. Díez-García, A. Santamaría-Echart, A. Eceiza, A. Tercjak, Synthesis and characterization of environmentally-friendly waterborne poly(urethane-urea)s, Eur.

Polym. J. 99 (2018) 240–249. https://doi.org/10.1016/j.eurpolymj.2017.12.026.

[18] S.M. Cakić, I.S. Ristić, I. Krakovský, D.T. Stojiljković, P. Bělský, L. Kollová, Crystallization and thermal properties in waterborne polyurethane elastomers: Influence of mixed soft segment block, Mater. Chem. Phys. 144 (2014) 31–40. https://doi.org/10.1016/j.matchemphys.2013.12.008.

[19] A. Santamaria-Echart, I. Fernandes, F. Barreiro, A. Retegi, Development of waterborne polyurethane-ureas added with plant extracts: Study of different incorporation routes and their influence on particle size, thermal, mechanical and antibacterial properties, Prog. Org. Coatings. 117 (2018) 76–90. https://doi.org/10.1016/j.porgcoat.2018.01.006.

[20] C. Prisacariu, E. Scortanu, A. Airinei, B. Agapie, M. Iurzhenko, Y.P. Mamunya, New developments in thermoplastic polyurethanes of variable crystallinity: Sensitivity of cyclic stress-strain response to chemical structure, Procedia Eng. 10 (2011) 446–454. https://doi.org/10.1016/j.proeng.2011.04.076.

[21] S. Li, Z. Liu, L. Hou, Y. Chen, T. Xu, Effect of polyether/polyester polyol ratio on properties of waterborne two-component polyurethane coatings, Prog. Org. Coatings. 141 (2020) 105545. https://doi.org/10.1016/j.porgcoat.2020.105545.

[22] R. Li, Z. Shan, Enhancement of thermal conductivity of PEG-PPG-based waterborne polyurethane coating by incorporating ordered polyethylene glycol fragment, Polym. Test. 69 (2018) 125–132. https://doi.org/10.1016/j.polymertesting.2018.05.024.

CHAPTER 4

INFLUENCE OF THE SOLID CONTENT ON THE RHEOLOGY AND PRINTING PERFORMANCE OF WBPUU INKS

4. INFLUENCE OF THE SOLID CONTENT ON THE RHEOLOGY AND PRINTING PERFORMANCE OF WBPUU INKS

4.1 Objective

Based on previous results, increasing the solid content of PCL80PEG20 system or increasing the molecular mass of PEG with a PCL/PEG of 0.8/0.2 favours the gelation of the system. Therefore, the aim of this chapter is to study the influence of the variation of the solid content on the printing performance of the aforementioned PCL/PEG based WBPUU. The different systems were studied from the rheological viewpoint and subsequently used in the printing by DIW 3D-printing of different pieces in order to demonstrate the relationship between the rheological properties of the inks and their printing viability, stablishing an optimal window of compositions of the inks.

For that purpose, different WBPUUs with a solid content from 27 to 46 wt% were prepared maintaining a PCL/PEG ratio of 0.8/0.2. By studying the obtained rheological parameters for all inks and analysing their corresponding printing performance, a correlation between the former and the latter can be made, leading to the establishment of designing criteria as far as solid content of the WBPUU is concerned. These criteria may help to optimize the ideal solid content of the synthesized WBPUU in order to achieve the best possible printing performance.

4.2 Experimental part

WBPUUs with different solid contents and with a PCL/PEG ratio of 0.8/0.2 have been synthesized according to the methodology displayed in the Chapter 3. The synthesis consists on a two-step reaction where the former consist on the formation of the prepolymer from PCL, PEG, DMPA and IPDI, whereas the latter involves the chain extension with EDA in heterogeneous media, once the phase inversion was carried out. The molar ratio of

PCL/PEG/DMPA/IPDI/EDA reagents was 0.8/0.2/1/3.5/1.5. The solid content of the prepared WBPUU was varied from 27 to 46 wt% by adding different contents of water during the phase inversion step. During the chain extension step and with solid contents above 27 wt% it was observed that the WBPUU formed a gel by means of a physically crosslinked network.

The different prepared systems are enlisted in **Table 4.1** whereas in **Figure 4.1** the influence of the increase of the solid content on the final synthesized inks is shown. Systems presenting low solid content result in liquid dispersions as was observed in the Chapter 3, or viscous inks, which still flow but presented higher structuration. Contrary, an increase of the solid content result in elastic gels, and in the case of solid contents above 36 wt% one can observe a solid behaviour.

All the synthesized inks were printed by direct ink writing 3D-printing technology using a Voladora 3D-printing machine, provided by Tumaker (Spain) and modified in order to allow the use of extrusion based DIW technology. Samples were loaded in a syringe of 6 mL and printed at a printing speed of 6 mm s^{-1} using a needle of 0.8 mm of diameter. Prior to the printing, all samples, loaded into the syringes, were centrifuged for 3 min at 3000 rpm to remove the existing bubbles. The maximum shear rate on the needle wall is calculated from the equation 4.1, and is equal to 19 s^{-1} [1].

$$\dot{\gamma}_{max} = \frac{4\,\dot{Q}}{\pi\, r^3} \qquad (4.1)$$

where r is the needle internal radium and $\dot{Q}$ the flow rate calculated as $\dot{Q}=Sr^2$ with S as the printing speed in mm s^{-1}. All samples were printed in dog bone shape according to ISO 527.

Table 4.1 Designation and calculated solid content of prepared WBPUU

System	Calculated solid content (%)
WBPUU27	27
WBPUU29	29
WBPUU32	32
WBPUU36	36
WBPUU46	46

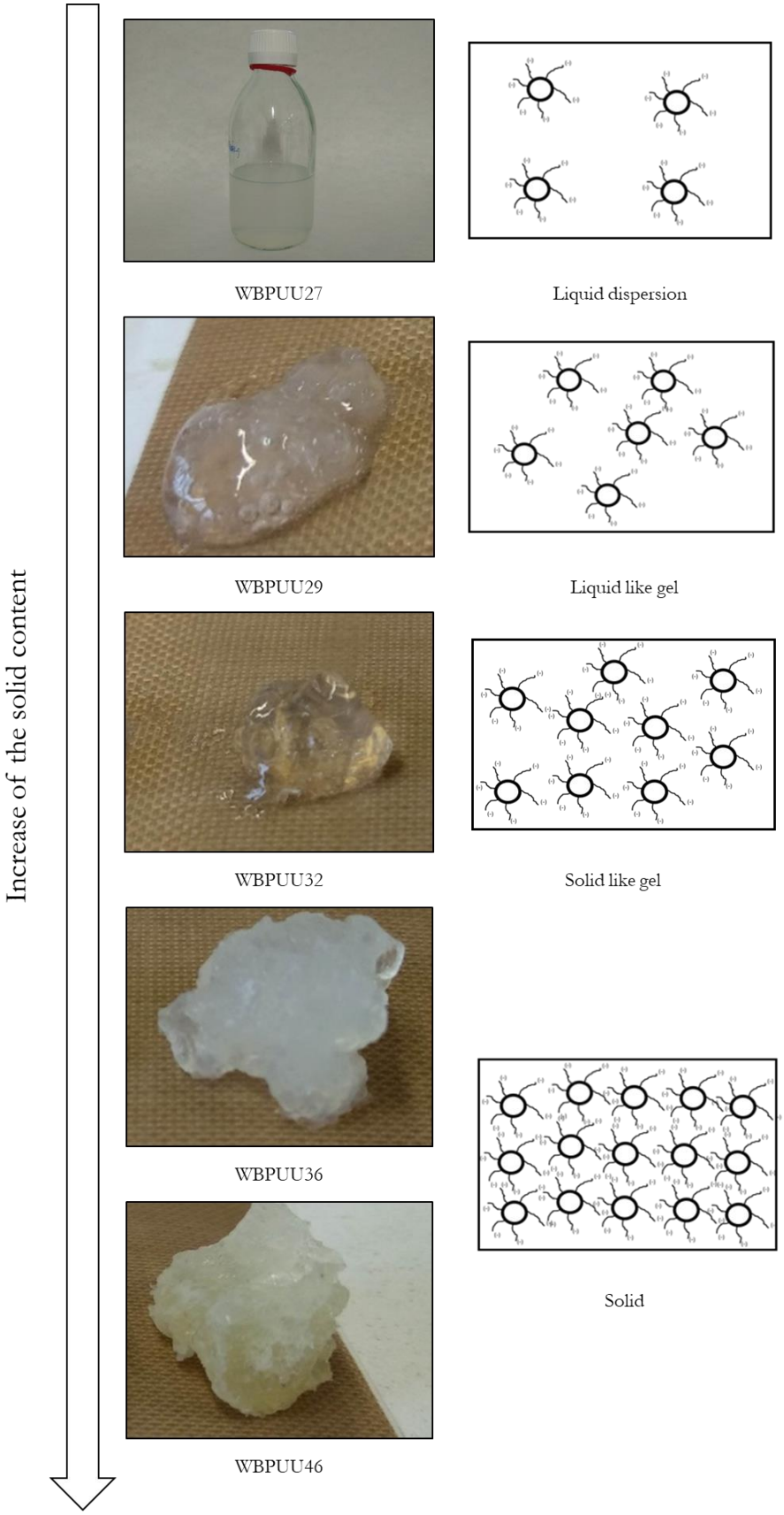

Figure 4.1 Illustration of the effect of the variation of the solid content of the WBPUU in the behaviour of the final material

4.3 Results and discussion

4.3.1 Rheological characterization of inks

Flow tests were performed for the different prepared WBPUUs. The obtained viscosity curves are displayed in **Figure 4.2**, whereas the calculated viscosity values at different shear rates for the different systems are summarized in **Table 4.2**. As can be observed, all the prepared systems showed shear thinning behaviour in the range between 0.01-100 s^{-1}. It is assumed that as the shear rate increased, the network of the hydrogel weakens leading to the decrease of the viscosity. This important property to obtain a printable materials was also observed for similar systems in the literature [2–6]. Comparing systems with different solid contents, it can conclude that despite all systems presented the aforementioned shear thinning behaviour, the viscosity measured at low rates (0.01 s^{-1}) is higher as the solid content of the ink increases. The same behaviour was observed in the viscosity calculated at the maximum shear rate value during the printing (19 s^{-1}) and at the maximum shear rate of 100 s^{-1}. This results are in agreement with the observed ones in the literature for the increase of the solid content in other systems [7].

Comparing the viscosity values at the different shear rates displayed in **Table 4.2**, a higher viscosity difference was observed at low rates compared with the ones obtained at higher rates.

Additionally, WBPUUs with low solid content present a Newtonian plateau at very low shear rates (between 0.01 and 0.1 s^{-1} for WBPUU27 and 0.01-0.03 s^{-1} for WBPUU29), which is reduced and suddenly disappeared completely with the increase of the solid content (see **Figure 4.2**).

Table 4.2 Viscosity values measured at different shear rates for the synthesized WBPUU with different solid content

System	Viscosity (Pa s)		
	η at 0.01 s^{-1}	η at 19 s^{-1}	η at 100 s^{-1}
WBPUU27	569	5	2
WBPUU29	3851	12	4
WBPUU32	7274	18	9
WBPUU36	18777	52	13
WBPUU46	74515	158	45

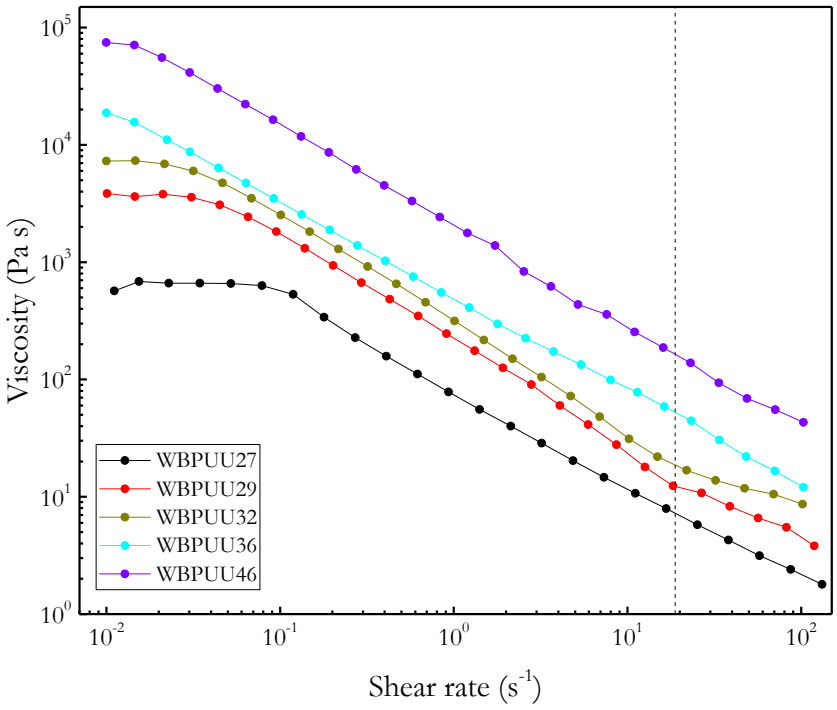

Figure 4.2 Viscosity as a function of shear rate (T = 22.5 °C) of WBPUUs with different solid contents. (----) Printing shear rate (19 s^{-1})

In order to determine the yield point of the inks, spectromechanical analysis was performed with increasing shear stress (**Figure 4.3**). Even if it is not the ideal method, the yield point was determined according the method proposed by *Cyriac et al.*, where the yield point is calculated as the stress at which the storage modulus is deviated from the linearity [8]. Additionally, the flow point of the inks was calculated as the crossover between G' and G" in order to study the behaviour of the material during its breakdown. For that purpose, "flow transition index" (FTI) was determined as the ratio between flow point and yield point [9]. Analysing the results, which are displayed in **Table 4.3**, an increase of both yield point and flow point as the solid content increases was observed. As explained by *Ketel et al.* [10], the yield point of a colloidal system arises from the interparticle strength, exhibiting a power law dependence on particle spacing and resulting in a scaling of the yield point with the decrease of the water content [11,12]. As the particle concentration increased, the interparticle space decreased, leading to a reduction in the interaction volume between the particles and thus, to an increase of the yield point [13]. This increase of the yield point with the particle concentration has been observed in the literature [14,15], and will result in printability

problems if the high yield point values difficult a smooth and continuous flow through the nozzle [10], obtaining a discontinuous extrusion [16].

Regarding the FTI index, there was a decrease when the solid content was increased, suggesting a transition from a weak network to a stiffer material presenting a brittle behaviour with the increase of solid content [9]. This parameter is indicative of the ability of the structure to yield, breakdown and similarly to rebuild during the printing process. Additionally, the yield point also has influence on the shape fidelity of the printed piece as was explained in the introduction. Concretely, low values of yield point, as was observed for WBPUU27 and WBPUU29 could result in systems which flowed easily after being printed, losing the given shape and collapsing due to the weight of the upper layers. Systems presenting higher yield points, contrary, would not flow after being printed, due to their higher yield points, allowing to maintain the given shape as well as supporting the weight of the multi-layered 3D construct without collapsing.

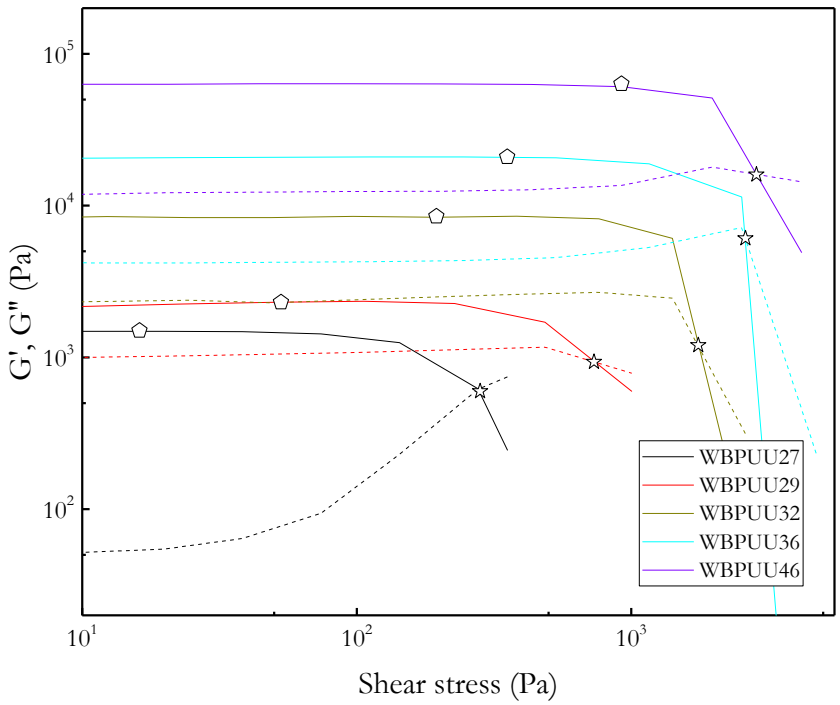

Figure 4.3 (—) Storage and (----) loss moduli as a function of shear stress. Yield point and flow point determination of WBPUU inks with different solid contents (T = 22.5 °C). (⬠) Yield point and (☆) flow point

The experimental data of the flow curves were adjusted to the Herschel Bulkley model so as to determine "K" and "n" index (**Figure 4.4**). The selection of this model to adjust the experimental data, which will be also used in the following chapters, has been carried out in Appendix A (pages 245-258), where the suitability of the Herschel Bulkley model has been tested in opposition of other rheological models typically used to describe the behaviour of non-Newtonian fluids.

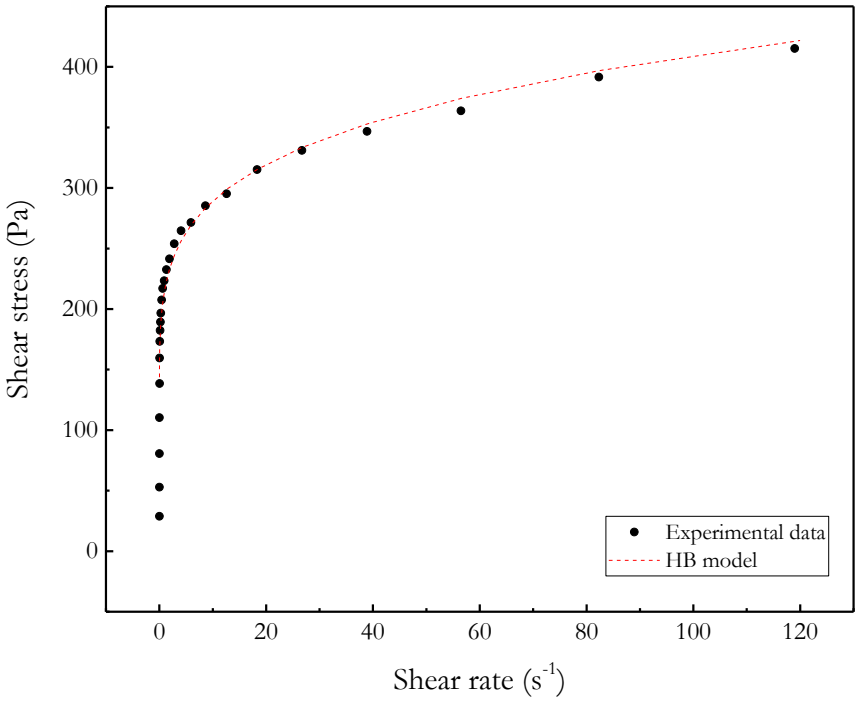

Figure 4.4 Adjustment to the Herschel Bulkley (HB) model of WBPUU29 flow curve

Comparing the experimental data with the predicted model, a good correlation was observed for all systems obtaining R^2 values above 0.84. The results, which are also displayed in **Table 4.3**, showed an increasing value of the "K" index with the increase of the solid content, meaning higher consistency of the material for systems presenting higher solid content, which could difficult the extrusion of the material during 3D-printing or result in poor extrudability [17,18]. Regarding "n" index, all system showed values under 1, which confirms the aforementioned non-Newtonian shear thinning behaviour [19] and is desirable for 3D-printing. According to some authors, an increase of the yield point and values of the "n" index under 1 indicates stronger mechanic strength and better ability of shape retention [20].

Table 4.3 Yield point, flow point, flow transition index and parameters obtained from the adjustment to Herschel Bulkley model ($\sigma-\sigma_y=k\dot{\gamma}^n$) of WBPUU inks with increasing solid content

System	Yield point (Pa)	Flow point (Pa)	FTI	Herschel Bulkley model		
				K index (Pa s n^{-1})	n index	R^2
WBPUU27	17	282	16	72	0.24	0.97
WBPUU29	44	562	11	115	0.21	0.92
WBPUU32	195	1755	9	238	0.14	0.84
WBPUU36	354	2608	7	303	0.37	0.98
WBPUU46	921	2857	3	1032	0.20	0.94

Oscillatory strain sweep tests were performed for the different WBPUUs in order to determine the linear viscoelastic region (LVR) of the prepared gels (**Figure 4.5**).

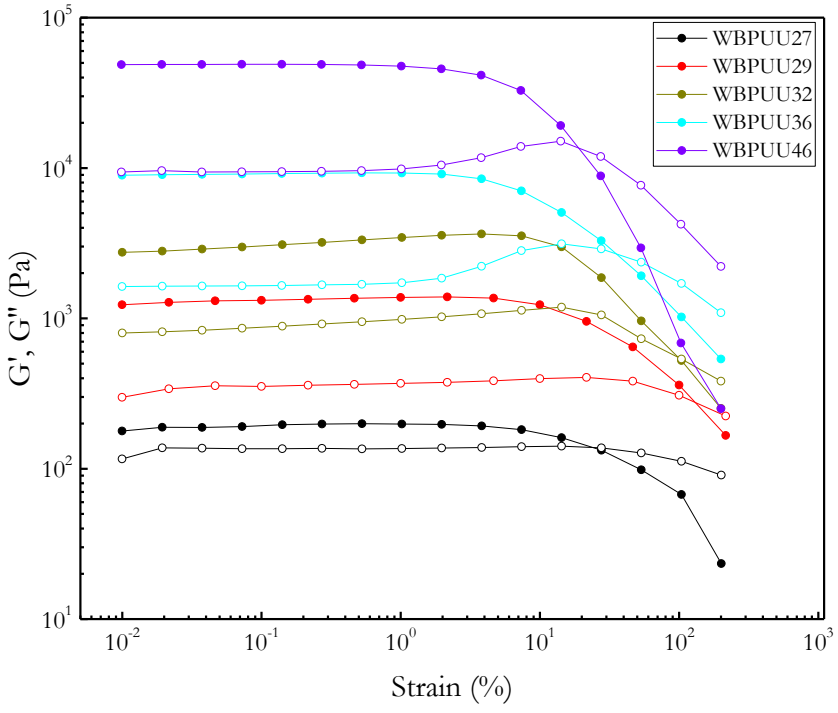

Figure 4.5 G' (●) and G" (○) as a function of strain (T = 22.5 °C) of WBPUU inks with different solid content at 1 Hz

Analysing the obtained results, it was noticed that at low strain values both the storage and the loss moduli were independent of the strain. In all samples, G' remains higher than G", confirming that the material is highly structured [21]. However, the smaller difference between G' and G" at LVR for WBPUU27 suggests a weaker structure for this gel, despite the low G' values also justify this weaker structuration of the ink. At strains above 2%, all systems presented a drop of their G' as a result of the structural deformation of the gel, leading to the transition from elastic to viscous behaviour when G" overpass G' and due to the complex phenomena linked to the non-linear rheological behaviour. These phenomena are not explored in the present work.

Frequency sweeps were also performed in the LVR to analyse the structural integrity of the inks during the process. The measured G' and G" and tan δ as a function of the frequency are displayed in **Figure 4.6** whereas values measured at 1 Hz of G', G" and tan δ are displayed in **Table 4.4**.

Analysing the obtained results, systems containing higher solid content presented higher values of both storage and loss moduli as was observed in the literature [22], showing a more structured network. All systems showed G' over G" in all the studied range, indicating a predominant elastic behaviour or gel like structure [23]. It has been showed that inks with higher G' facilitate stronger shape retention for the deposited layers [24]. According to the literature, empirically, a storage modulus above 10^3 Pa is necessary to support high stable 3D structure of multiple layers [25], so, except WBPUU27, all the systems are good candidate for printing. Regarding tan δ, all systems with the exception of WBPUU27 presented values in the range between 0.1 and 0.3, showing a more elastic behaviour compared with WBPUU27. This system, which presented a tan δ of 0.52 at 1 Hz, showed a less elastic behaviour, which could lead to problems retaining the shape since, the material could flow after printing as will be observed later. The tan δ experienced a decrease as the solid content increased, which could lead to systems presenting a better shape fidelity.

For comparative purposes of the shape fidelity with the systems analysed in the next chapters, the storage modulus and tan δ of WBPUU27, WBPUU29, WBPUU32, WBPUU36 and WBPUU46 are represented in the supplementary material (Appendix C, **Figures SC.6-SC.7**, pages 273-274). From the aforementioned systems only WBPUU29 and WBPUU32 are situated in the area delimited by the printable systems observed in the literature. Contrary, WBPUU27, WBPUU36 and WBPUU46 are located out of this area.

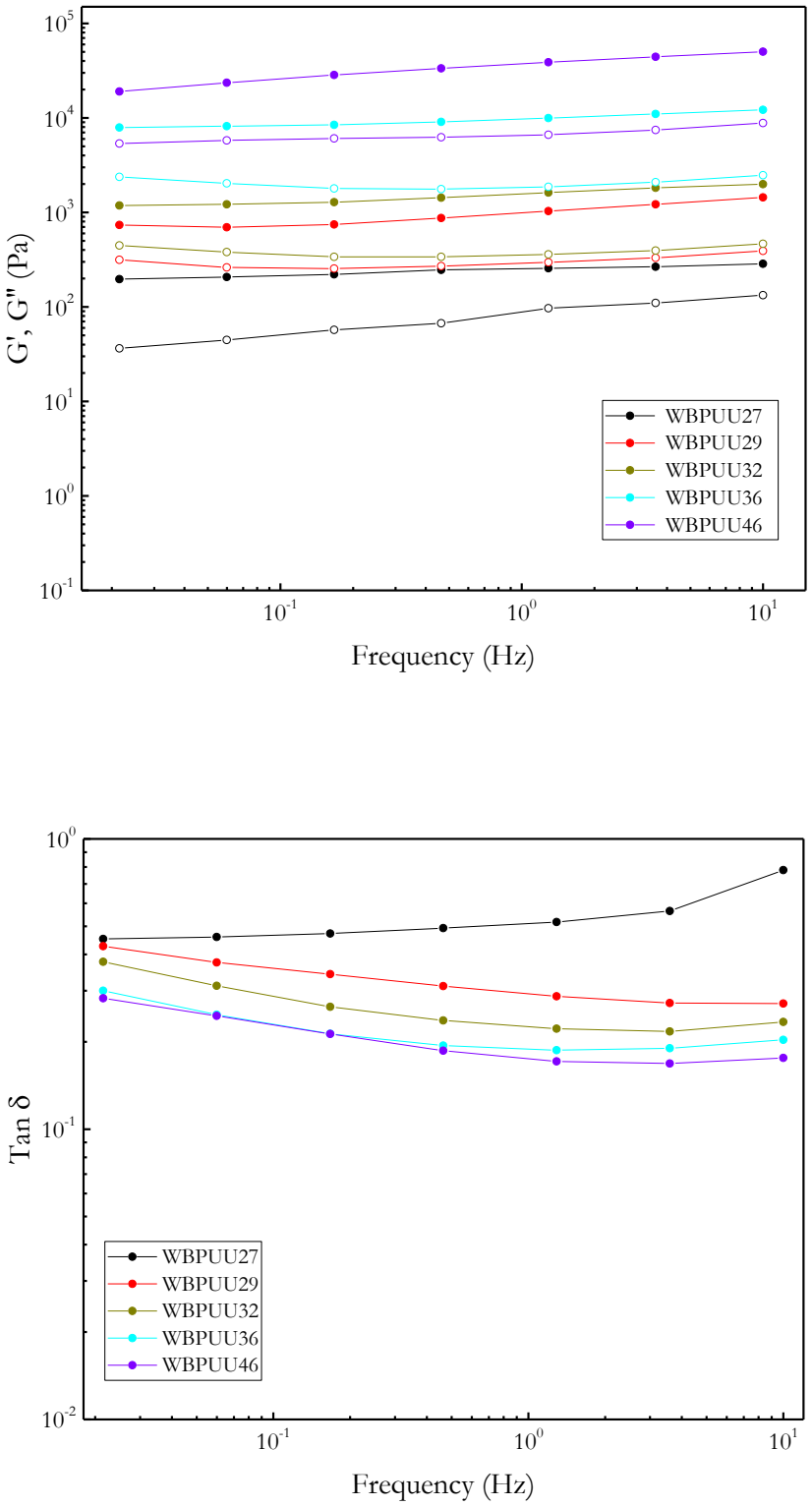

Figure 4.6 G' (●) and G" (○) as a function of frequency of WBPUU inks with different solid contents (up) and tan δ as a function of frequency (down) (T = 22.5 °C)

Table 4.4 Storage modulus, loss modulus and tan δ values at 1 Hz, and structure recovery percentage of inks with different solid content

System	Storage modulus (Pa)	Loss modulus (Pa)	Tan δ	Structure recovery (%)
WBPUU27	206	106	0.52	63
WBPUU29	1033	296	0.29	84
WBPUU32	1618	359	0.22	83
WBPUU36	9966	1865	0.19	40
WBPUU46	38738	6630	0.17	-

The structural integrity and shape fidelity of the printable inks were tested by determining their recovery capacity in order to predict their performance during printing. It was not possible to study the behaviour of WBPUU46 system due to its high elastic behaviour. The obtained curves are displayed in **Figure 4.7**.

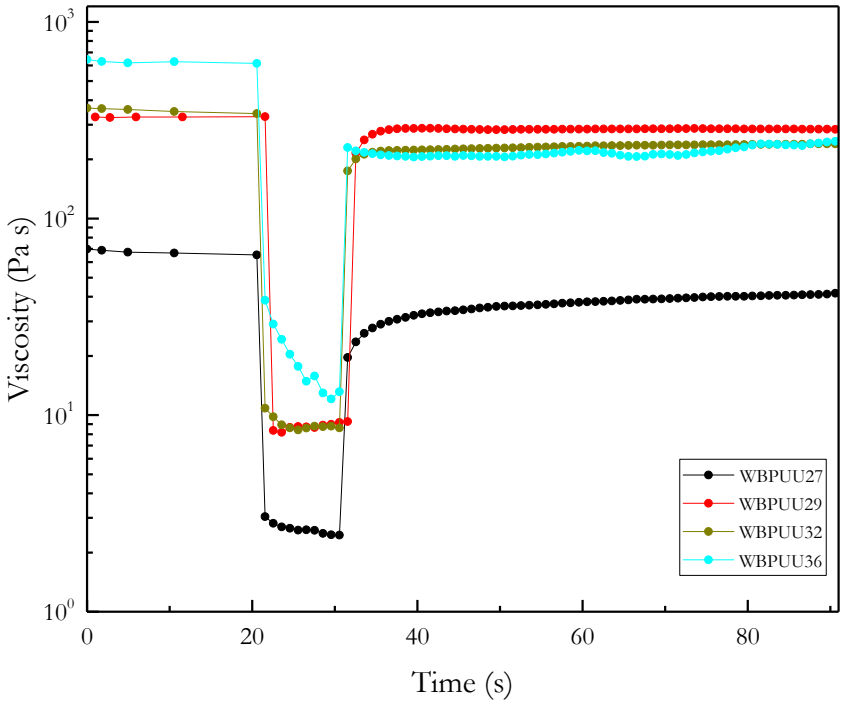

Figure 4.7 Structure recovery test of WBPUU based inks with different solid contents (T = 22.5 °C)

Analysing the obtained results, the WBPUU29 and WBPUU32 showed recovery values of 84 and 83% respectively, showing and increase compared with WBPUU27 (63%). *Peak et al.* reported that an initial viscosity recovery of 80% is significant for 3D-printing [26], confirming the viability of these inks for DIW 3D-printing. However, systems containing solid content above 32 wt% experienced a decrease of the recovery obtaining values of 40%. This decrease happened due to a slip of the material during the high shear rate period, which can be noticed by the observed decrease of the viscosity measured at 100 s^{-1}. The calculated recovery values are displayed in **Table 4.4**.

Analysing the evolution of the rheological parameters with the increase of the solid content (**Figure 4.8**) a clear tendency was observed in all studied parameters. All ones linked to the printability of the material (viscosity, yield point and consistency index) increased as the solid content of the ink did. The values measured for high solid content inks resulted in systems that required more pressure to be extruded and which can show uniformity problems during printing or even lead to systems that cannot be extruded due to the small inner diameter of the nozzle.

Regarding the other parameters, which are linked to the shape fidelity, the increase of the solid content resulted in an increase of the storage modulus but also in a decrease of the tan δ, meaning a more structured elastic behaviour, obtaining systems with more structured gel network. In this case, systems presenting higher solid content should present better shape fidelity, according with the rheological analysis. The structure recovery percentage, seems to maintain over a desirable 80% for WBPUU29 and WBPUU32, however, at solid contents of 36 wt%, there was a decrease of the recovery due to the highly elastic behaviour of the inks. In this case, the ink flips from the plates of the rheometer instead of absorb the applied shear which is reflected in a lower capacity to recover when the applied shear rate is removed.

For comparative purposes with systems studied in other chapters, the rheological properties of WBPUU29 and WBPUU32 system are represented with the other systems which presented the best printing performances for every chapter (Appendix C, **Figures SC.1-SC.5**, pages 268-272).

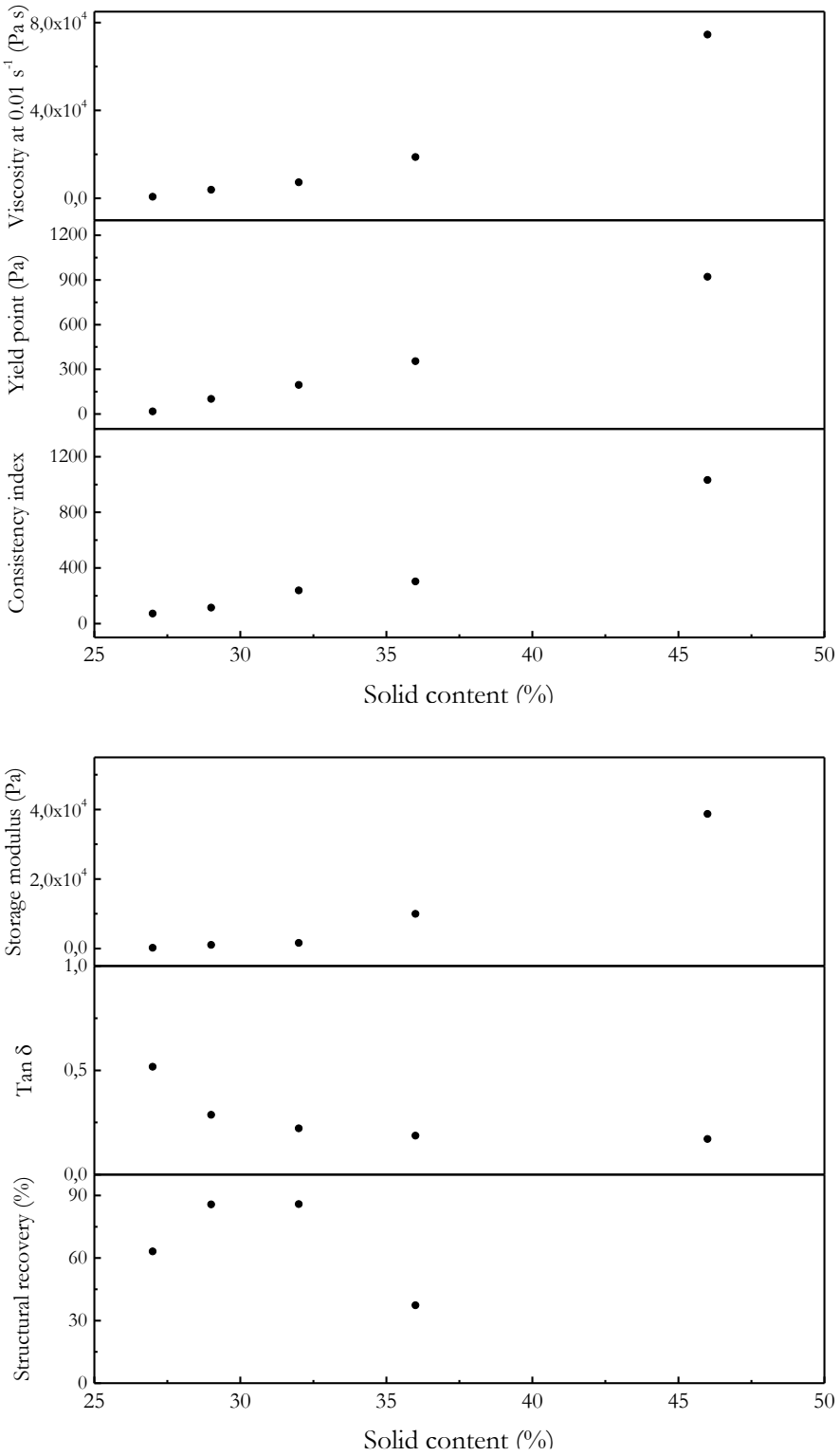

Figure 4.8 Evolution of the rheological parameters with the increase of the solid content of the inks. Parameters related to the printability (up) and to the shape fidelity (down)

4.3.2 DIW 3D-printing of WBPUU systems

All systems were printed by DIW 3D-printing in order to correlate rheological parameters and printing performance. The digital images of the printed pieces are displayed in **Figure 4.9**. Systems presenting low yield points were printed successfully, forming the ink a continuous and homogeneous thread when were extruded, whereas the ones with high yield point values, as well as storage modulus, were unable to be printed (WBPUU36 and WBPUU46). Regarding the shape fidelity, from among the printable systems, WBPUU32 presented clearly the best results. Moreover, this ink has shown the highest storage modulus and lower tan δ of all printable systems, confirming the results predicted by the rheology. The high recovery value of this ink after applying a stress confirmed the building of a strong structure that can support multiple layers, as well as maintain the shape designed by the software. However, the WBPUU32 system presented not good enough surface finish as was expected. Taking this issue into account, the inclusion of nanoentities could be an option so as to improve the final appearance of the printed piece.

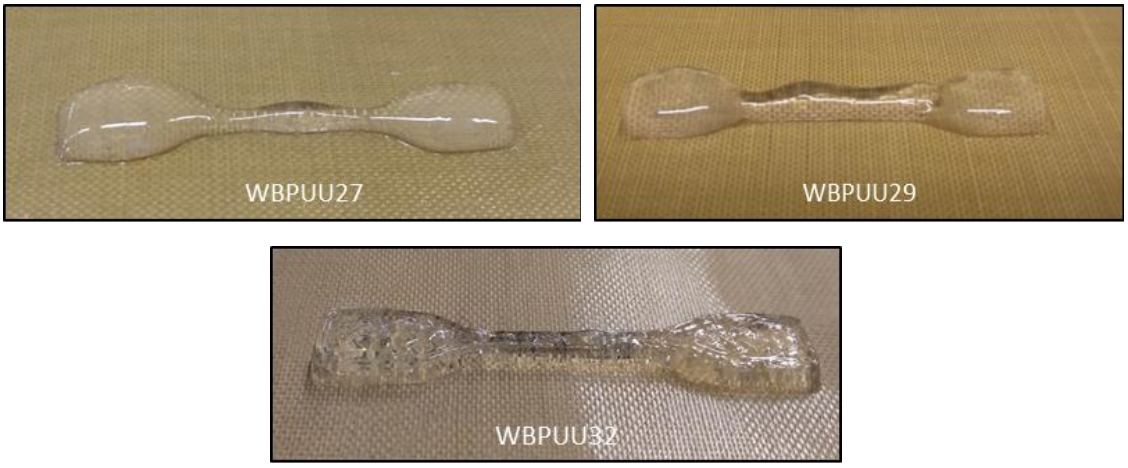

Figure 4.9 Printed pieces of WBPUU gels with different solid contents

4.4 Conclusions

In this chapter, the influence of the variation of the solid content on the printing performance of a novel waterborne polyurethane urea based ink synthesized with a combination of hydrophobic PCL and hydrophilic PEG in the soft segment was studied. In order to establish the optimal conditions for the printing performance, an extensive rheological analysis was performed for the different inks formulations, which were subsequently used to print different pieces so as to study their final appearance and shape

fidelity and hence, the correlation between the rheological analysis and the printing performance.

All the studied inks showed a shear thinning behaviour, confirming their suitability for DIW 3D-printing. The increase of the solid content of the ink resulted in an increase of both yield point and viscosity, which resulted in printability limitations for inks presenting high solid contents. Regarding the shape fidelity, the storage modulus increased and the tan δ decreased as the solid content of the systems increased, leading to more structured and elastic inks, which can maintain better the shape and support multiple layers. Finally, the structure recovery test showed that the increase of the solid content lead to the obtaining of inks with better capacity of recovering their initial stage. However, systems presenting solid contents of 36 wt% presented a decrease of the recovery percentage due to their so solid behaviour which difficult the recovery capacity. In this case, the WBPUU32 showed the best printing performance. However, their poor surface appearance requires more adjustment of WBPUU based ink formulation.

4.5 References

[1] W.S. Janna, Introduction to fluid mechanics, 4th ed., CRC Press, Boston, 2010.

[2] G. Siqueira, D. Kokkinis, R. Libanori, M.K. Hausmann, A.S. Gladman, A. Neels, P. Tingaut, T. Zimmermann, J.A. Lewis, A.R. Studart, Cellulose nanocrystal inks for 3D printing of textured cellular architectures, Adv. Funct. Mater. 27 (2017) 1604619. https://doi.org/10.1002/adfm.201604619.

[3] K. Markstedt, A. Mantas, I. Tournier, D. Hägg, P. Gatenholm, 3D bioprinting human chondrocytes with nanocellulose − alginate bioink for cartilage tissue engineering applications, Biomacromolecules 16 (2015) 1489–1496. https://doi.org/10.1021/acs.biomac.5b00188.

[4] M. Guvendiren, H.D. Lu, J.A. Burdick, Shear-thinning hydrogels for biomedical applications, Soft Matter. 8 (2012) 260–272. https://doi.org/10.1039/c1sm06513k.

[5] A. Ribeiro, M.. Blokzijl, R. Levato, C.. Visser, M. Castilho, W.. Hennink, T. Vermonden, J. Malda, Assessing bioink shape fidelity to aid material development in 3D bioprinting, Biofabrication 10 (2017) 0–21. https:// doi.org/10.1088/1758-5090/aa90e2.

[6] L. Liu, O.N. Ciftci, Effects of high oil compositions and printing parameters on

food paste properties and printability in a 3D printing food processing model, J. Food Eng. 288 (2021) 110135. https://doi.org/10.1016/j.jfoodeng.2020.110135.

[7] S.S.L. Chan, R.M. Pennings, L. Edwards, G. V Franks, 3D printing of clay for decorative architectural applications: Effect of solids volume fraction on rheology and printability, Addit. Manuf. 35 (2020) 101335. https://doi.org/10.1016/j.addma.2020.101335.

[8] F. Cyriac, P.M. Lugt, R. Bosman, On a new method to determine the yield stress in lubricating grease, Tribol. Trans. 58 (2015) 1021–1030. https://doi.org/10.1080/10402004.2015.1035414.

[9] A. Corker, H.C. Ng, E. Garcı, R.J. Poole, 3D printing with 2D colloids: designing rheology protocols to predict printability of sof-materials, Soft Matter. 15 (2019) 1444–1456. https://doi.org/10.1039/c8sm01936c.

[10] S. Ketel, G. Falzone, B. Wang, N. Washburn, G. Sant, A printability index for linking slurry rheology to the geometrical attributes of 3D-printed components, Cem. Concr. Compos. 101 (2018) 32–43. https://doi.org/10.1016/j.cemconcomp.2018.03.022.

[11] J.A. Lewis, Colloidal processing of ceramics, J. Am. Ceram. Soc. 83 (2000) 2341–2359. https://doi.org/10.1111/j.1151-2916.2000.tb01560.x.

[12] H. Jin, D. Jia, Z. Yang, Y. Zhou, Mechanical and dielectric properties of direct ink writting Si2N2O composites, J. Eur. Ceram. Soc. (2020). https://doi.org/10.1016/j.jeurceramsoc.2020.08.063.

[13] V.L. Wiesner, L.M. Rueschhoff, A.I. Diaz-cano, R.W. Trice, J.P. Youngblood, Producing dense zirconium diboride components by room-temperature injection molding of aqueous ceramic suspensions, Ceram. Int. 42 (2016) 2750–2760. https://doi.org/10.1016/j.ceramint.2015.11.005.

[14] X. Zhang, W. Huo, J. Liu, Y. Zhang, S. Zhang, J. Yang, 3D printing boehmite gel foams into lightweight porous ceramics with hierarchical pore structure, J. Eur. Ceram. Soc. 40 (2020) 930–934. https://doi.org/10.1016/j.jeurceramsoc.2019.10.032.

[15] C. Minas, D. Carnelli, E. Tervoort, A.R. Studart, 3D printing of emulsions and foams into hierarchical porous ceramics, Adv. Mater. 28 (2016) 9993–9999.

https://doi.org/10.1002/adma.201603390.

[16] C. Sun, J. Xiang, M. Xu, Y. He, Z. Tong, 3D extrusion free forming of geopolymer composites : Materials modification and processing optimization, J. Clean. Prod. 258 (2020) 120986. https://doi.org/10.1016/j.jclepro.2020.120986.

[17] Z. Liu, M. Zhang, B. Bhandari, C. Yang, Impact of rheological properties of mashed potatoes on 3D printing, J. Food Eng. 220 (2017) 76–82. https://doi.org/10.1016/j.jfoodeng.2017.04.017.

[18] Z. Liu, M. Zhang, Y. Ye, Indirect prediction of 3D printability of mashed potatoes based on LF-NMR measurements, J. Food Eng. 287 (2020) 110137. https://doi.org/10.1016/j.jfoodeng.2020.110137.

[19] T.F. Tadros, Rheology of dispersions: principles and applications, John Wiley & Sons, 2010.

[20] W.J. Costakis Jr, L.M. Rueschhoff, A.I. Diaz-cano, J.P. Youngblood, R.W. Trice, Additive manufacturing of boron carbide via continuous filament direct ink writing of aqueous ceramic suspensions, J. Eur. Ceram. Soc. 36 (2016) 3249–3256. https://doi.org/10.1016/j.jeurceramsoc.2016.06.002.

[21] R.E. Abouzeid, R. Khiari, D. Beneventi, A. Dufresne, Biomimetic mineralization of three-dimensional printed alginate/TEMPO-oxidized cellulose nanofibril scaffolds for bone tissue engineering, Biomacromolecules 19 (2018) 4442–4452. https://doi.org/10.1021/acs.biomac.8b01325.

[22] C. Kuo, H. Qin, Y. Cheng, X. Jiang, X. Shi, An integrated manufacturing strategy to fabricate delivery system using gelatin / alginate hybrid hydrogels: 3D printing and freeze-drying, Food Hydrocoll. 111 (2021) 106262. https://doi.org/10.1016/j.foodhyd.2020.106262.

[23] F. Yang, M. Zhang, B. Bhandari, Y. Liu, Investigation on lemon juice gel as food material for 3D printing and optimization of printing parameters, LWT - Food Sci. Technol. 87 (2018) 67–76. https://doi.org/10.1016/j.lwt.2017.08.054.

[24] J.A. Lewis, J.E. Smay, Direct ink writing of three-dimensional ceramic structures, J. Am. Ceram. Soc. 89 (2006) 3599–3609. https://doi.org/10.1111/j.1551-2916.2006.01382.x.

[25] L. Li, Q. Lin, M. Tang, A.J.E. Duncan, C. Ke, Advanced polymer designs for direct-ink-write 3D printing, Chem. Eur. J. (2019) 1–15. https://doi.org/10.1002/chem.201900975.

[26] C.W. Peak, J. Stein, K.A. Gold, A.K. Gaharwar, Nanoengineered colloidal inks for 3D bioprinting, Langmuir 34 (3) (2017) 917–925. https://doi.org/10.1021/acs.langmuir.7b02540.

CHAPTER 5

IN SITU ADDITION OF CELLULOSE NANOCRYSTALS TO ENHANCE THE PRINTING PERFORMANCE OF WBPUU BASED INKS

5. *IN SITU* ADDITION OF CELLULOSE NANOCRYSTALS TO ENHANCE THE PRINTING PERFORMANCE OF WBPUU BASED INKS

5.1 Objective

The objective of this chapter is to study the influence of the addition of cellulose nanocrystals on the printing performance of the aforementioned PCL/PEG based WBPUU. As was observed in the literature, the addition of nanoentities can pilot the rheological behaviour of the ink [1–3], so it is expected that the addition of the CNC modify these rheological properties and hence the printing performance. For this aim, the CNC was added in different amounts to the WBPUU, previously dispersed in deionized water during the phase inversion step, taking into advantage of the hydrophilic nature and water dispersability of the CNC. The different gels were studied from the rheological viewpoint and subsequently printed by DIW 3D-printing.

Different WBPUU/CNC_{is} nanocomposites with a CNC content from 0 to 2 wt% were prepared maintaining a PCL/PEG ratio of 0.8/0.2, and the solid content on 29 wt%. By studying the obtained rheological parameters for all inks and the corresponding printing performance, a correlation between the former and the latter can be made, leading to the establishment of design criteria. These criteria may help to optimize the ideal CNC content of the WBPUU/CNC_{is} nanocomposites in order to achieve the best possible printing performance, as well as to study the influence of the addition of nanoentities on both the rheological properties and the printing performance.

Additionally, as was observed in the literature, nanoentities have been extensively used as mechanical reinforcement and it is expected that the CNC can enhance the mechanical properties of the final printed piece [4–6]. The printed pieces from WBPUU based inks with different amounts of CNC were also characterized from the physicochemical, thermal,

mechanical and thermomechanical viewpoints in order to study the influence of CNC as reinforcement, apart from in the rheology as viscosity modulator.

5.2 Experimental part

A WBPUU with a PCL/PEG ratio of 0.8/0.2 has been synthesized according to the methodology proposed in Chapter 3. The molar ratio of PCL, PEG, DMPA, IPDI and EDA was 0.8:0.2:1:3.5:1.5 and the solid content of the prepared WBPUU was fixed to 29 wt%. Different amounts of CNC previously dispersed in water, were added during the phase inversion step, so as to obtain WBPUU/CNC nanocomposites *in situ*. Taking into account that CNC were added during the WBPUU synthesis, it is expected the reaction between some –OH groups of CNC and –NCO of the prepolymer. In the **Table 5.1** the different prepared WBPUU/CNC_{is} nanocomposites are enlisted as well as their CNC content. Concretely they were named as $WBPUUX_{is}$, where X is the added CNC content.

Table 5.1 Designation and CNC content of prepared WBPUU/CNC_{is} nanocomposites

System	CNC (wt%)
WBPUU	0
WBPUU0.25$_{is}$	0.25
WBPUU0.5$_{is}$	0.5
WBPUU1$_{is}$	1
WBPUU2$_{is}$	2

All the synthesized inks were printed by DIW 3D-printing technology using the equipment described in Chapter 2. Regarding the printing conditions, the samples were printed following the conditions used in Chapter 4. As in Chapter 4, all samples were printed in dog bone shape according to ISO 527 so as to study the printing performance of the different inks. Additionally, in order to perform the mechanical and thermomechanical analysis, strips were also printed with 2.8 mm in width, 0.5 mm in thickness and 50 mm in length. Printed pieces were dried at room temperature for 48 hours before physicochemical, thermal, thermomechanical and mechanical characterization. As a result, all samples showed a decrease of their height due to the water removal.

Regarding the addition method, as was explained in the introduction, the *in situ* method will result in a different disposition of the CNC in the matrix comparing to other methods like the *ex situ* one, which will be studied in following chapters. Concretely, as was proposed by

Chen et al. [7] the addition of CNC during the phase inversion step, prior to the chain extension will lead to the reaction between some free -NCO groups, preserved for the posterior reaction with the diamine leading the urea, and the -OH groups of the CNC. An illustration of the CNC integration mechanism is displayed in **Figure 5.1**.

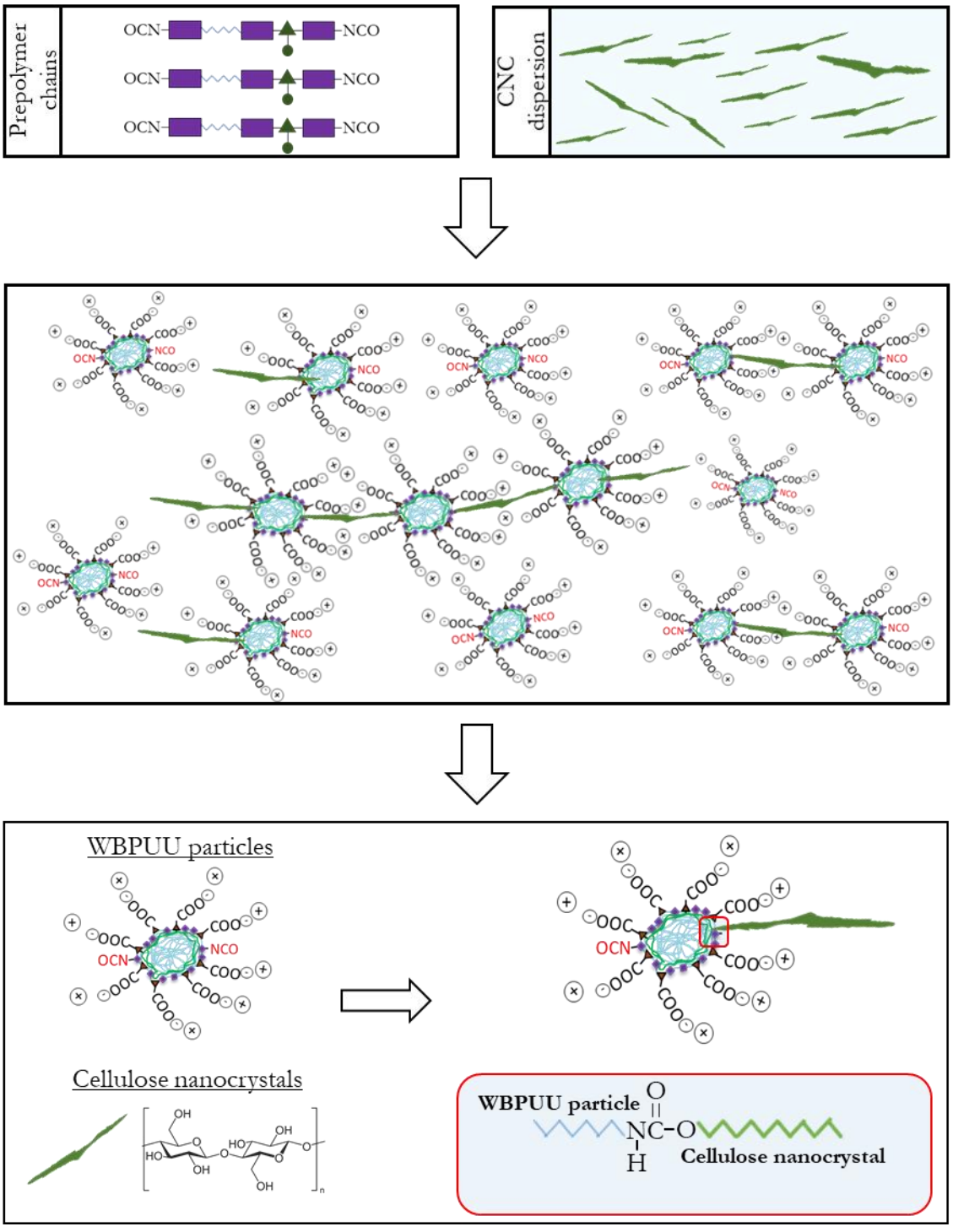

Figure 5.1 Illustration of the proposed CNC integration mechanism in the WBPUU/CNC_{is} nanocomposites produced by *in situ* addition method

This inclusion of the CNC into the WBPUU backbone can lead to a different disposition of the particles in the ink, leading to a variation of the rheological parameters, but also of the mechanical and thermomechanical properties of the printed pieces.

5.3 Results and discussion

5.3.1 Physicochemical characterization of CNC, WBPUU and WBPUU/CNC$_{is}$ nanocomposites

The WBPUU, CNC and WBPUU/CNC$_{is}$ nanocomposites were characterized in order to study the effect of the CNC into the matrix. CNC physicochemical properties and morphology were analysed in order to understand their effect over the nanocomposites performance. The crystallinity of the CNC was analysed by X-ray diffraction.

Figure 5.2 shows the obtained diffractogram, where CNC presented the classical crystallography pattern for cellulose I [8], with characteristic diffraction peaks at 14.6, 16.8, 20.2, 22.7 and 34.7 °, related to $(1\bar{1}0)$, (110), (102), (200) and (004) crystallographic planes [9–11]. The crystallinity index (CI%) of the nanocrystals was calculated following the equation 5.1 proposed by *Segal et al.* [12]

$$CI\ (\%) = \frac{(I_{200} - I_{am})}{I_{200}} X\ 100 \qquad (5.1)$$

where I_{200} is the intensity corresponding to the (200) plane, whereas I_{am} is the amorphous contribution and was obtained from the broad peak observed around 18° [10]. For the CNC, a crystallinity index of 82% was obtained, which agrees with the values reported for sulphuric acid isolated CNC [13]. Additionally, the crystallite size (β) was measured from the diffractogram using the Scherer's equation (equation 5.2) [14]

$$\beta = \frac{\varkappa\, \lambda}{\tau \cos\theta} x100 \qquad (5.2)$$

where $\varkappa$ represents a dimensionless shape factor of 0.9, λ is the wavelength, τ is the line broadening at half of the maximum intensity, and θ the Bragg angle. The crystallite size was calculated as 6.4 nm for CNC. This result is in agreement with the observed values in the literature for native cellulose [15].

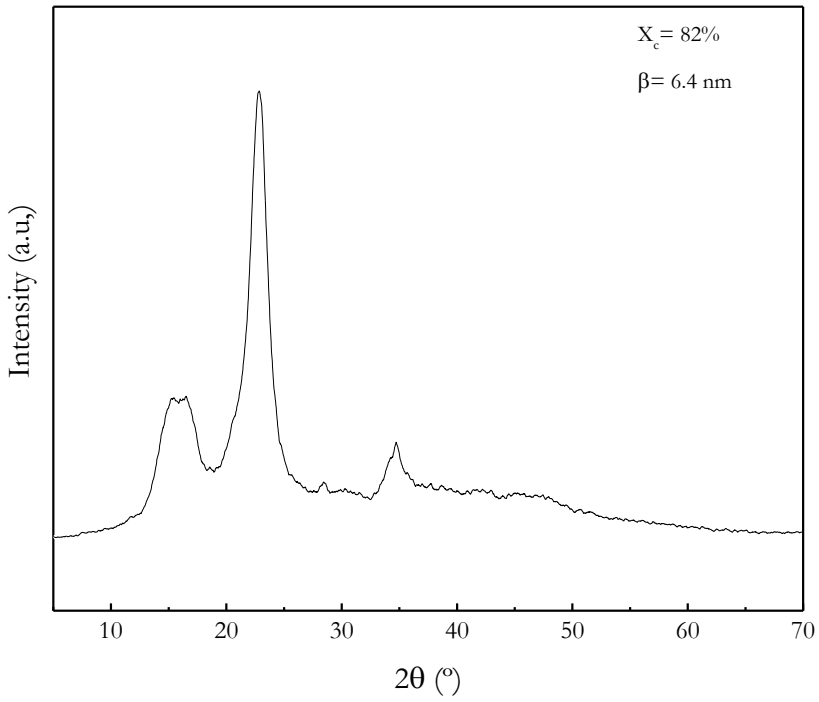

Figure 5.2 X-ray pattern of the CNC

The morphology of CNC was analysed by AFM. The height AFM image of CNC is displayed in **Figure 5.3**

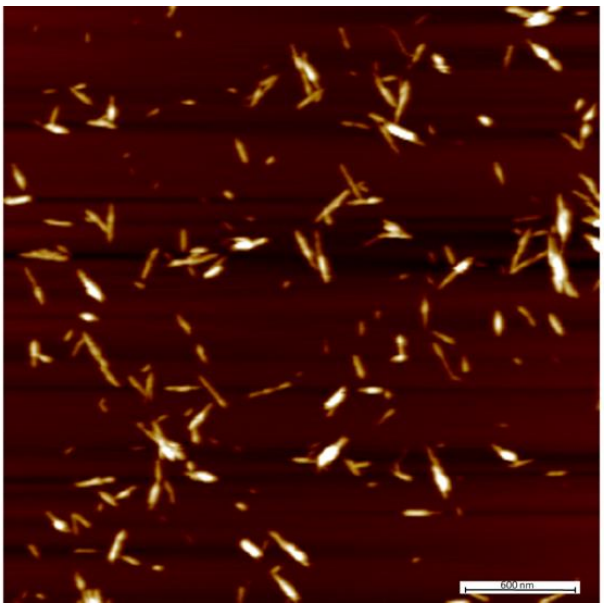

Figure 5.3 Height AFM image of CNC

The results confirmed the nanometric dimensions of the crystals, obtaining length values from height image and diameter values from height profile of 215±37 nm and 5±1 nm respectively. The average dimensions were obtained from 50 measurements of the total CNC population.

The chemical structure of the CNC was also analysed by ^{13}C MNR. Spectra displayed in **Figure 5.4** showed typical chemical shifts related to the different carbons of CNC. The peak observed between 60 and 70 ppm is assigned to C_6 of the primary alcohol group. Regarding the broad peak appeared between 70 and 80 ppm, it is attributed to the carbons C_2, C_3 and C_5. Finally, the C_4 signal appeared at as peak located between 80 and 95 ppm, whereas the signal around 100 ppm correspond to the anomeric carbon C_1. The obtained result corresponded to the ones observed in the literature obtaining similar values for all carbons [16].

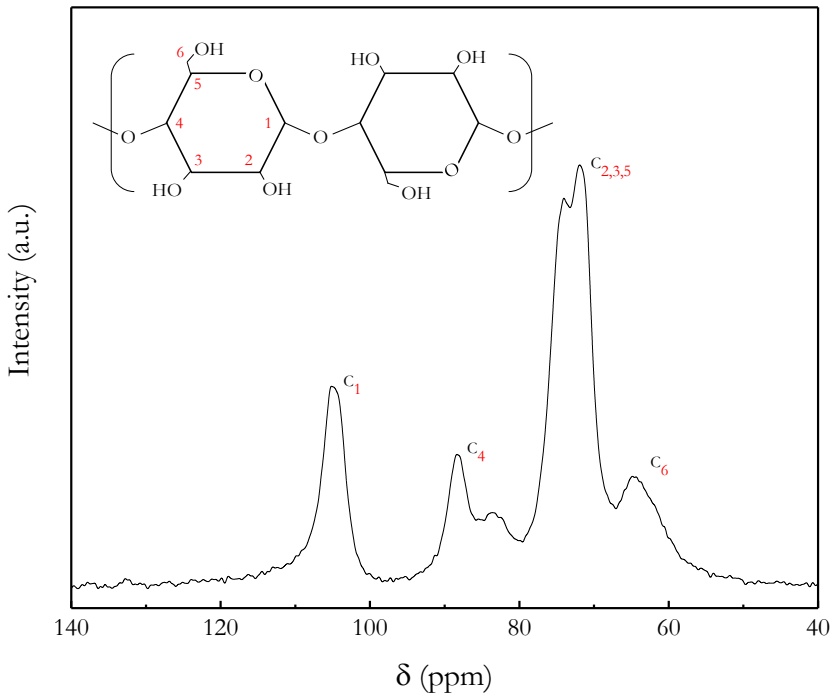

Figure 5.4 ^{13}C MNR spectra of CNC

The main functional groups of neat components and the hydrogen bonding interactions between CNC and WBPUU matrix in the nanocomposites were studied by FTIR. **Figure 5.5** shows the spectra of nanocomposites and neat components. In the nanocomposites, a

single band was observed in the 3600-3100 cm^{-1} interval, which is also observed in the WBPUU matrix and is assigned to the N-H stretching vibration of urethane group [17]. This band also englobes the observed one for the CNC, which is attributed to O-H stretching vibration. Regarding the carbonyl region, which is situated between 1800-1600 cm^{-1} and is shown in the inset of **Figure 5.5**, a displacement towards lower wavenumber in the stretching vibration of C=O group can be observed. In the case of the WBPUU matrix the C=O band appeared at 1735 cm^{-1}, but in the WBPUU/CNC_{is} nanocomposites this band is displaced towards lower wavenumbers as the CNC content increased, suggesting the existence of hydrogen bonding interactions between WBPUU and CNC [18].

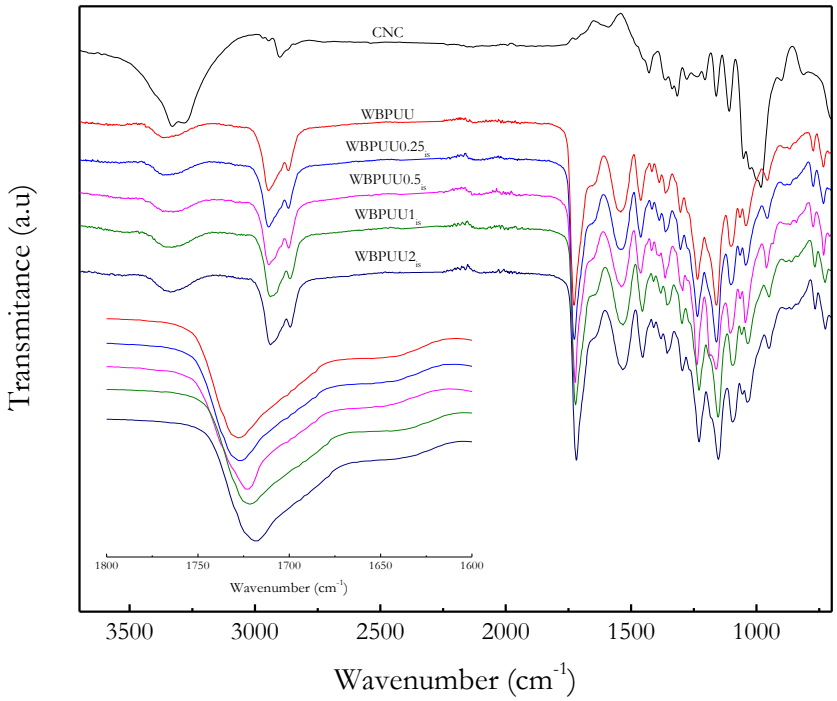

Figure 5.5 FTIR spectra of WBPUU, CNC and WBPUU/CNC_{is} nanocomposites. Inset: magnification of the 1800-1600 cm^{-1} region

The thermal stability of the CNC, WBPUU and WBPUU/CNC_{is} nanocomposites was studied by TGA. The thermogravimetric weight as well as the derivative weight curves are displayed in **Figure 5.6**.

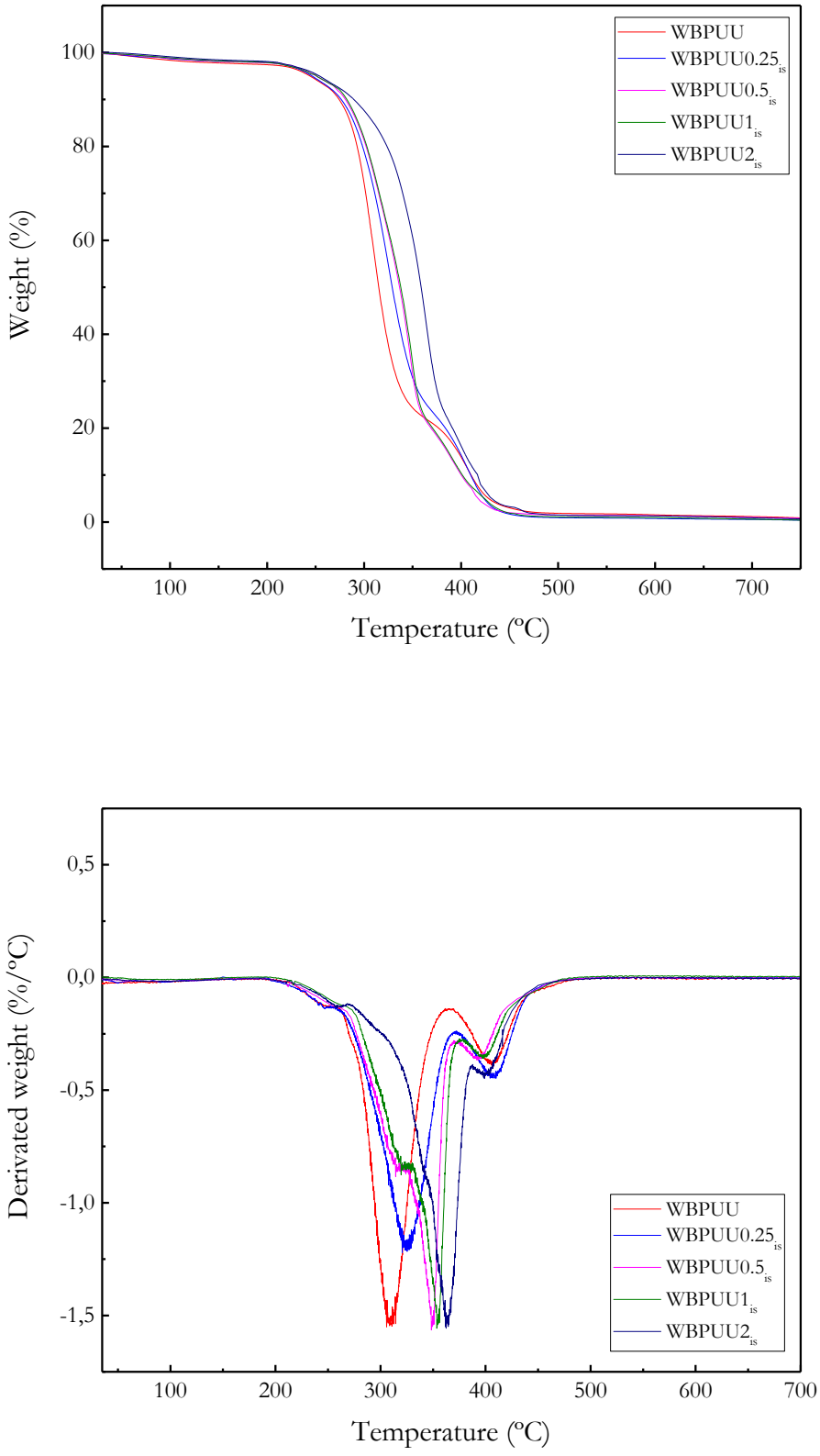

Figure 5.6 Variation of the weight (up) and derivated weight curves (down) of WBPUU and WBPUU/CNC_{is} nanocomposites

The WBPUU matrix showed a two-step degradation process, as was observed in the Chapter 3 for the films with the same composition, which can be observed also in all the WBPUU/CNC_{is} nanocomposites. Studying the initial degradation and the maximum degradation temperatures, which are displayed in **Table 5.2**, a significant increase of both values was observed in the nanocomposites, attributed to the increase of thermal stability with CNC addition, due to the stabilization of urethane groups by interactions of the WBPUU matrix and the CNC, as also observed by FTIR.

Table 5.2 Initial degradation and maximum degradation temperatures of WBPUU matrix and nanocomposites

System	T_0 (°C)	T_d (°C)
WBPUU	250	312
WBPUU0.25$_{is}$	256	320
WBPUU0.5$_{is}$	264	339
WBPUU1$_{is}$	277	361
WBPUU2$_{is}$	281	364

5.3.2 TEM analysis of the WBPUU and WBPUU/CNC_{is} inks

In order to study the integration of the CNC reinforcement in the WBPUU particles, as well as to understand the resulting interactions, the WBPUU/CNC_{is} composites were analysed by TEM. Images of the WBPUU and WBPUU2$_{is}$ are shown in **Figure 5.7**. The presence of agglomerates of particles in the case of the WBPUU2$_{is}$ system as well as the absence of free cellulose nanocrystals could suggest that the nanoentities are embedded into the particles (for a clearer observation see TEM image of WBPUU2$_{es}$ in **Figure 6.4** at page 164 where CNC were added *ex situ*). WBPUU matrix contrary showed a homogeneous distribution of particles, with no presence of agglomerates. This observation could confirm the proposed integration of cellulose nanocrystals into the polyurethane particles, where the CNC reacts with the polyurethane prepolymer in an early stage of the synthesis, concretely during the phase inversion, resulting in a chemical bonding between the aforementioned CNC and the polymer backbone. This inclusion of the nanoentities in the polyurethane particles will modify the rheological properties of the WBPUU/CNC_{is} inks in a different way to the addition carried out after the synthesis (studied in Chapter 6), resulting as well in the obtaining of a final material with different thermal, mechanical and thermomechanical properties.

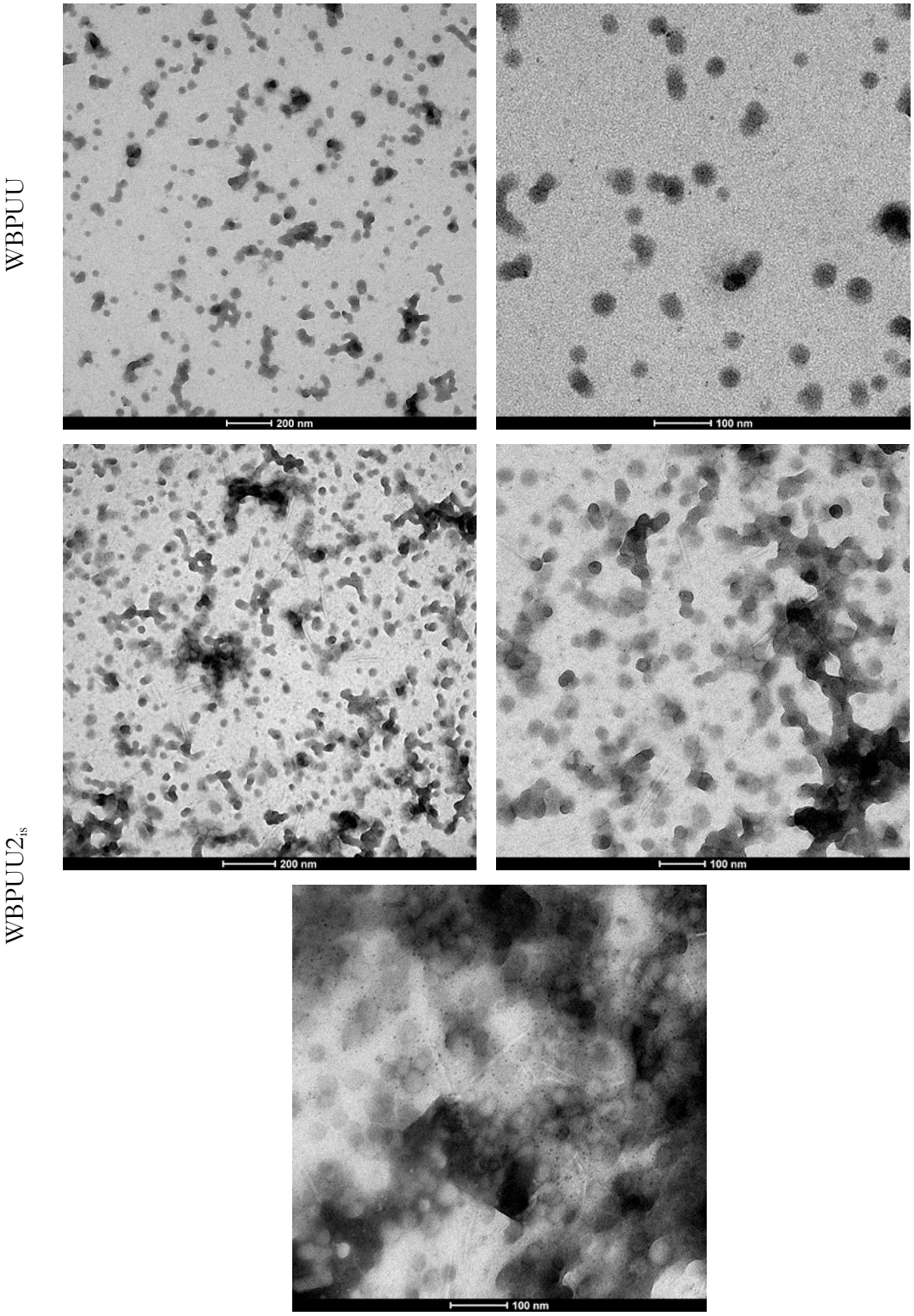

Figure 5.7 TEM images of WBPUU (up) WBPUU2$_{is}$ (down) inks. The images where taken in a 1% dilution of the original inks

5.3.3 Rheological characterization of inks with different CNC contents

In order to study the viscosity of the prepared WBPUU/CNC_{is} based inks, flow test was performed at increasing shear rate. The obtained curves are displayed in **Figure 5.8**, whereas in **Table 5.3** the measured viscosity values of the inks at different shear rates are enlisted.

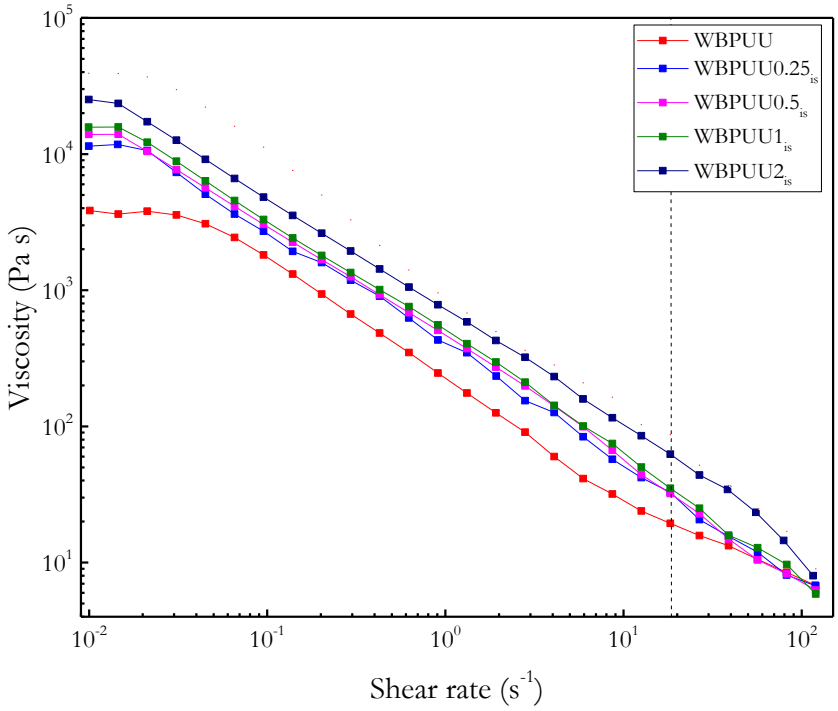

Figure 5.8 Viscosity as a function of shear rate and the printing shear rate (19 s^{-1}) (---) of prepared WBPUU and WBPUU/CNC_{is} nanocomposite inks (T = 22.5 °C)

Table 5.3 Viscosity values measured at different shear rates for the synthesized WBPUU with different CNC content

System	Viscosity (Pa s)		
	η at 0.01 s^{-1}	η at 19 s^{-1}	η at 100 s^{-1}
WBPUU	3851	12	4
WBPUU0.25$_{is}$	11434	32	7
WBPUU0.5$_{is}$	13939	32	7
WBPUU1$_{is}$	15737	35	7
WBPUU2$_{is}$	25101	62	10

As can be observed, the incorporation of CNC resulted in an increase of the viscosity as the CNC content increased. However, a more gradual variation of viscosity was observed with

the addition of CNC, compared with the observed behaviour in Chapter 4 for the variation of the solid content. WBPUU/CNC_{is} inks presented a viscosity range of 11434-25101 Pa s at 0.01 s^{-1} in contrast with the 3851 Pa s obtained for WBPUU matrix. Contrary, at the shear rate corresponding to the printing performance (19 s^{-1}) the composite inks showed a viscosity in the range of 32.2-62.4 Pa s whereas the matrix presented a 19.3 Pa s showing smaller differences between the WBPUU matrix and the WBPUU/CNC_{is} nanocomposites compared with the ones observed at 0.01 s^{-1}. The smaller increase of the viscosity of the composites with the addition of CNC compared with the obtained with the variation of the solid content lead to a more accurate modification of the viscosity compared with the one observed for the variation of the solid content analysed in Chapter 4. Additionally, the addition of CNC resulted in a decrease of the Newtonian plateau which was observed on the matrix at low shear rates, which is progressively decreasing as the CNC content increases until to its completely disappearance at CNC contents above 1 wt%.

Inks containing CNC also showed a decrease of the viscosity as the shear rate increase, or in other words, a shear thinning behaviour, which was observed also in Chapter 4 for the WBPUU inks with different solid contents. Taking into account the similar obtained flow curves of the WBPUU matrix and WBPUU/CNC_{is} nanocomposites, it can conclude that the inclusion of CNC did not influence the shear thinning behaviour previously showed by the WBPUU inks, that is, according to the literature, desirable for a successful printing performance [19,20].

In order to study the influence of the CNC in the printability of the inks, the yield point and flow point of the different systems were calculated using the same methodology used in Chapter 4. The determination of both yield and flow point is displayed in **Figure 5.9** by analysing the variation of the storage and loss modulus as a function of the shear stress.

Analysing the obtained results, which are displayed in **Table 5.4**, an increase of both yield and flow points with the increase of the CNC content was observed. The yield point presented a constant increase as more amount of CNC was added to the composite, however, above 1 wt% of CNC the inks showed a higher increase of the yield point compared with other composites presenting lower quantities of CNCs. This greater increase of the yield point produced by the addition of higher quantity of CNCs can lead posteriorly to problems of extrudability of the ink. Nevertheless, as was explained in the introduction, the yield point is not the only parameter who rules the printability of the system, so it is possible to present bad printability even if the yield point appears to be in the printable range. Despite high

values of yield point can difficult the extrusion process of the inks, also played an important role as far as shape fidelity is concerned. Systems presenting very low values of yield point, as in the case of WBPUU, flow easily when are extruded, but also after being printed, losing their given shape and collapsing due to the weight of the 3D multi-layered construct as observed in Chapter 4. WBPUU/CNC_{is} composites contrary, presented higher yield point values, which resulted in higher difficulties to extrude but at the same time retain better the given shape, being able to support successfully the 3D design without collapsing. Regarding the FTI index, no difference between different contents of cellulose was observed, and comparing with the matrix a small decrease is observed, suggesting that the addition of CNC did not has a strong influence in the brittleness of the ink, at least with low CNC content.

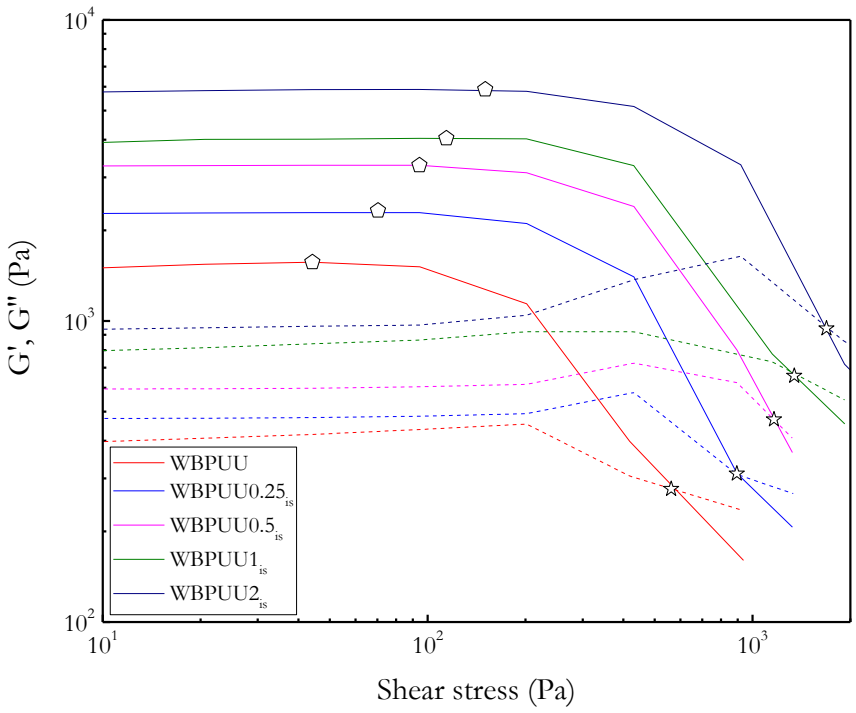

Figure 5.9 G' (—) and G" (----) as a function of shear stress of WBPUU and WBPUU/CNC_{is} nanocomposites and the measured yield point (⬠) and flow point (☆) (T = 22.5 °C)

The experimental data of the obtained WBPUU/CNC_{is} nanocomposites were adjusted to the Herschel Bulkley model so as to describe the experimental data and study the influence of the CNC in the inks. An example of the adjustment of the experimental flow curve to the

proposed model is displayed in **Figure 5.10**, whereas the obtained values from the adjustment are enlisted in **Table 5.4.**

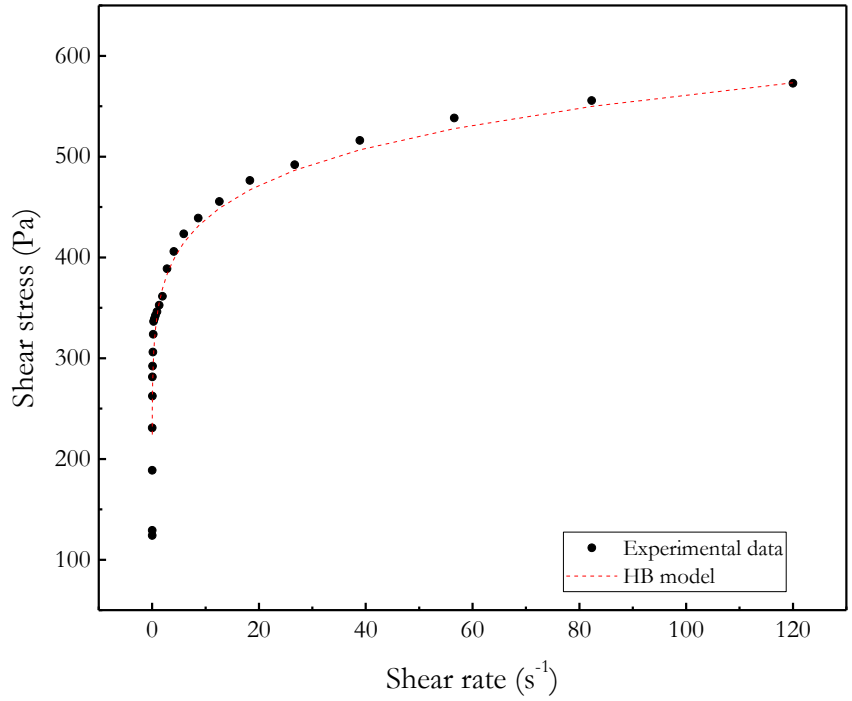

Figure 5.10 Adjustment to the Herschel Bulkley (HB) model of WBPUU0.5$_{is}$ flow curve

Regarding the adjustment of the experimental data to the Herschel Bulkley model, the flow curves of both matrix and WBPUU/CNC$_{is}$ nanocomposites showed a good correlation with the model obtaining R^2 values above 0.9 for all systems, with a maximum of 0.97 for WBPUU2$_{is}$.

The result showed a similar tendency to the observed in Chapter 4 for the variation of the solid content, obtaining an increase of the consistency index as the CNC content was increased, leading to higher consistency of the material for systems presenting higher CNC content, which can hence, result in extrusion problems of the material during 3D-printing or result in a poor printing performance [21].

In addition, the flow index kept similar for all systems with values between 0.1-0.2, but lower in general if compared to the observed ones for the solid content variation, confirming a more accused shear thinning behaviour [22].

Table 5.4 Determination of yield point, flow point, FTI index and parameters obtained from the adjustment to Herschel Bulkley model ($\sigma-\sigma_y=K\dot{\gamma}^n$) of WBPUU inks containing CNC

System	Yield point (Pa)	Flow point (Pa)	FTI	Herschel Bulkley model		
				K index (Pa s n^{-1})	n index	R^2
WBPUU	44	562	13	177	0.15	0.92
WBPUU0.25$_{is}$	70	1056	12	277	0.12	0.94
WBPUU0.5$_{is}$	94	1061	11	335	0.18	0.90
WBPUU1$_{is}$	114	1344	12	369	0.17	0.91
WBPUU2$_{is}$	150	1689	11	606	0.19	0.97

Oscillatory tests of the inks with different CNC content were also performed in order to study the shape fidelity of the synthesized WBPUU/CNC$_{is}$ inks. Initially, the variation of both the storage and loss moduli were studied as a function of the strain at a fixed frequency of 1 Hz (**Figure 5.11**) so as to determine the linear viscoelastic region (LVR).

The results showed that all systems presented a similar behaviour. The moduli were independent of the strain amplitude, being G' higher than G", suggesting a highly structured gel network [23]. At strains above 8% for all system, a decrease, and finally a crossover between G' and G" illustrate the end of the LVR resulting in the disruption of the structured network leading to the transition from elastic to a viscous behaviour. Studying the addition of CNC, an increase of both G' and G" was observed as the CNC content increases. Concretely, the WBPUU/CNC$_{is}$ nanocomposites presented a bigger difference between G' and G" compared with the matrix which showed a smaller one, reflecting the lower structuration of the matrix compared with the nanocomposites.

Additionally, a phenomenon called "weak strain overshoot" can be clearly observed in systems containing higher CNC content. In those systems, the structure of the gels resists against deformation up to a certain strain where G" increases when G' starts decreasing. Then, at higher strains the complex structure is destroyed over the critical strain and G" start decreasing [24]. This phenomenon, which did not appear on the WBPUU matrix, is observed in the nanocomposite with the smaller quantity of CNC (0.25 wt%) and results more remarkable as the CNC content increased. This type of behaviour is classically observed in filled rubber material and linked to the Payne effect [25–28].

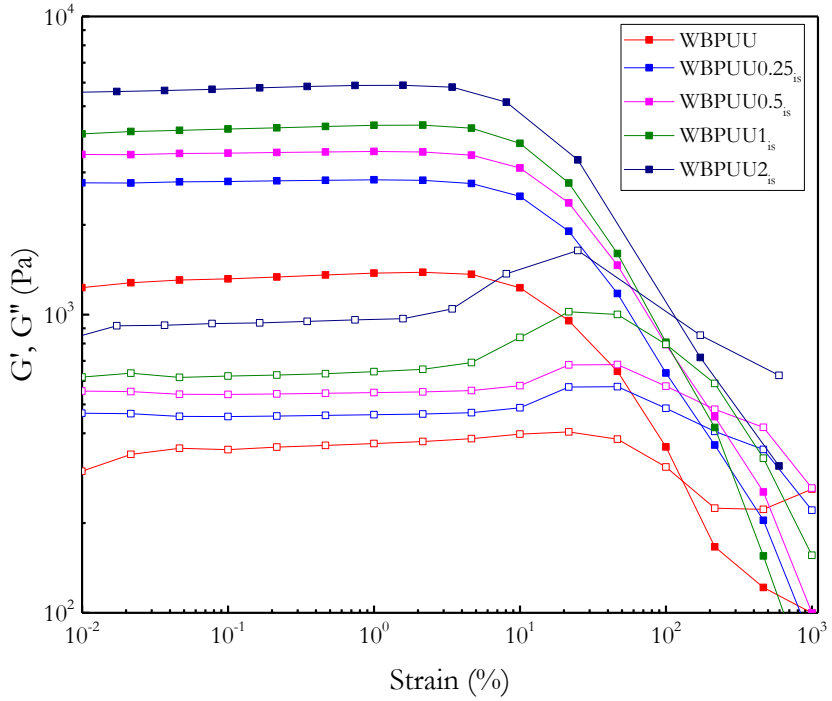

Figure 5.11 G' (■) and G" (□) as a function of strain (T = 22.5 °C) of WBPUU and WBPUU/CNC_{is} inks with different CNC contents at 1 Hz (T = 22.5 °C)

Moreover, the variation of both storage and loss moduli as a function of the frequency was studied by fixing the strain value to 1%, which was determine in **Figure 5.11** as part of the LVR for WBPUU and WBPUU/CNC_{is} based inks. The representation of both G', G" and tan δ as a function of the frequency is displayed in **Figure 5.12**, whereas the measured values for comparative purpose at 1 Hz are enlisted in **Table 5.5**.

Analysing the obtained results, an increase of both G' and G" was observed as the CNC content of the ink increased, presenting all studied systems G' over G", which according to the literature is desirable for DIW 3D-printing since viscous inks cannot be shaped by using this additive manufacturing technique [29,30]. This increase of the storage modulus leads to a more structured network for systems containing higher amount of CNC as was observed in oscillatory strain test. As was previously indicated, according to the literature, empirically, a storage modulus above 10^3 Pa is necessary to support high stable 3D structure of multiple layers [31], highlighting the requirement of suitable G' values to promote an adequate shape retention [32]. Additionally, *Álvarez-Castillo et al.* presented a printability map for a plasma protein based doughs where systems having both viscoelastic moduli below 10^3 Pa and over

10^5 Pa would be too weak to keep the shape or too stiff to be properly extruded, respectively [33]. Taking this values as a reference, all system presents an appropriate storage modulus for their use as inks for DIW 3D-printing. Regarding the loss modulus, however, all studied systems presented G" values under 10^3 Pa, which according to *Álvarez-Castillo et al.* could present problems to promote an adequate shape maintaining.

The inclusion of CNC in the WBPUU based ink resulted in a decrease of the tan δ from 0.29 to 0.20 at 1 Hz, illustrating a turn towards a more elastic behaviour for the composites. However, comparing the different prepared WBPUU/CNC_{is} compositions, the addition of higher amounts of CNC do not affect considerably the tan δ, obtaining for all systems tan δ values between 0.17-0.2. Despite the behaviour with the addition of CNC follows the same tendency as the one observed in Chapter 4 for the modification of the solid content (an increase of the modulus and a decrease of the tan δ with the solid content), the modification produced by the addition of CNC seems more accurate compared with the one produced with the increase of the solid content.

Additionally, the WBPUU, WBPUU0.25_{is}, WBPUU0.5_{is} and WBPUU2_{is} systems were mapped in **Figure SC.6** and **SC.7** at pages 273-274 of the supplementary material facing their storage modulus with the tan δ. The results showed that WBPUU0.25_{is} and WBPUU0.5_{is} are situated in the area of successful printing performance, whereas WBPUU is located under the lower limit, illustrating a bad shape fidelity. This observation indicates that the solid content is not the once parameter to consider but the structure of the solid part within the matrix is the key factor. Moreover, WBPUU2_{is} is mapped over the aforementioned area suggesting cohesion problems due to a too elastic behaviour.

Table 5.5 Storage modulus, loss modulus and tan δ values at 1 Hz and structure recovery percentage of inks with different CNC added *in situ*

System	Storage modulus (Pa)	Loss modulus (Pa)	Tan δ	Structure recovery (%)
WBPUU	1033	296	0.29	84
WBPUU0.25_{is}	2073	339	0.20	91
WBPUU0.5_{is}	2218	409	0.18	88
WBPUU1_{is}	2710	468	0.17	85
WBPUU2_{is}	4663	681	0.18	74

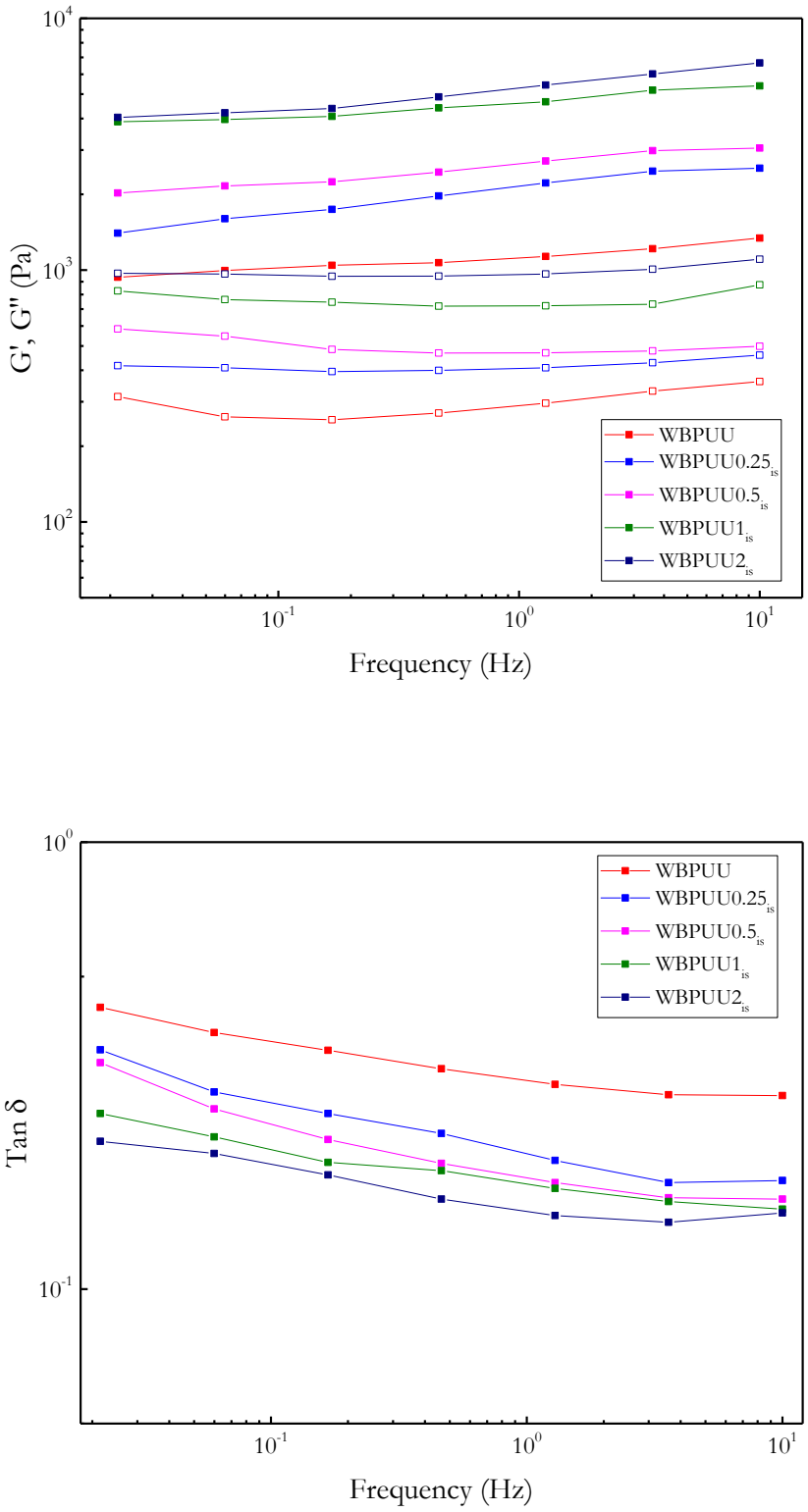

Figure 5.12 G' (■) and G" (□) as a function of frequency of WBPUU and WBPUU/CNC_{is} nanocomposites (up) and tan δ as a function of frequency (down) (T = 22.5 °C)

Finally, the recovery of the prepared inks was studied by a structure recovery test which have been presented in the Chapter 2. The results of the tests are reported in **Fig 5.13**, whereas the recovery values are displayed in **Table 5.6**. The evolution of the recovery followed the same tendency as the study of the variation of the solid content studied in Chapter 4. At low content of CNC, values around 90% of recovery were obtained, presenting the WBPUU0.25is a maximum value of 91%, which resulted in higher values compared with the 84% of recovery of the WBPUU matrix. According to the literature, an 80% of recovery is desirable for 3D-printing [34], so both the matrix and all composites with CNC content under 1 wt% present a theoretical adequate recovery for their application of DIW 3D-printing. Regarding the composites presenting CNC contents above 1 wt%, contrary to the behaviour observed for nanocomposites with lower CNC content, a drastic decrease of the recovery is observed, up to 74% due to the slipping of the material out of the geometry of the rheometer during the test because of its so elastic behaviour.

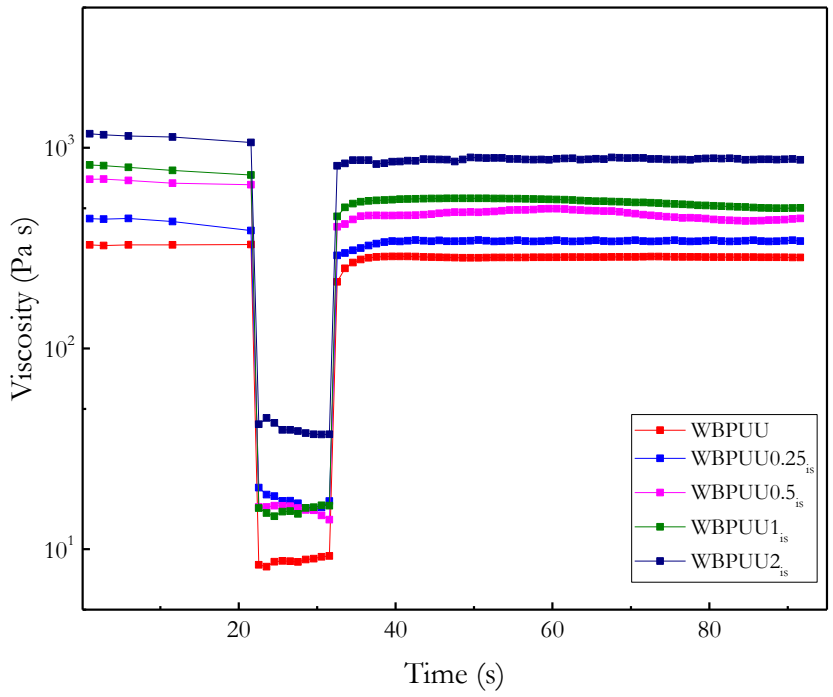

Figure 5.13 Evolution of viscosity with time at different shear rates of WBPUU and WBPUU/CNC_{is} nanocomposites. (T = 22.5 °C)

Finally, in **Fig 5.14** the variation of the previously studied rheological parameters as a function of the CNC content is displayed for comparative purposes.

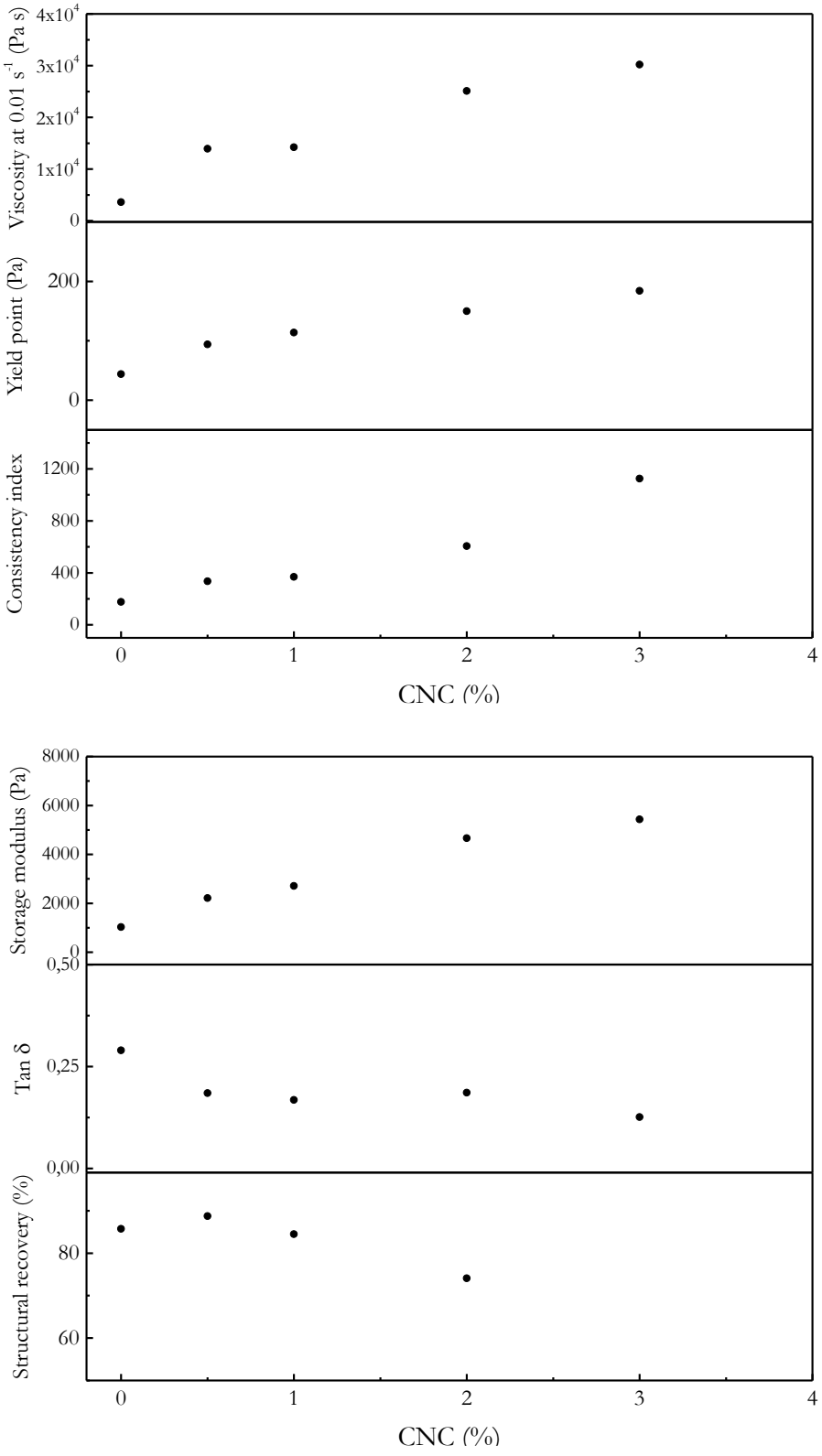

Figure 5.14 Variation of the studied rheological parameters with the addition of CNC *in situ*. Parameters related to the printability (up) and to the shape fidelity (down)

Analysing the evolution of the studied rheological parameters with the inclusion of CNC *in situ*, a clear tendency was observed. The results showed a similar behaviour if we compare this evolution with the observed one for the increase of the solid content studied in the Chapter 4. All parameters related to the printability increased as the CNC content did. The increase of the yield point and initial viscosity could result in extruding problems such as discontinuous extrusion, lack of homogeneity, or even impossibility to print the ink through the nozzle. Thus, it will be important to work with systems that may allow a continuous and homogeneous flow of the thread.

The dependence of the yield point with the increase of CNC content can be explained by power law $\tau_y = k\,\Phi^p$, where τ_y is the yield point, Φ the volume fraction of CNC, k is a constant that depends on the interparticles interaction and particle size, whereas p exponent depends on the microstructure of the particle network. The observed power law ($\tau_y = 122.16\,\phi^{0.316}$) is often interpreted in terms of the underlying microstructure of the load bearing particle network [35]. In the case of spherical like particles, the network is normally formed by fractal like agglomerates which connect with each other to fill up the volume of the suspension [36].

Regarding the other parameters, which are assigned to the shape fidelity, an increase of the storage modulus was observed as the CNC content increased. The inclusion of the nanocrystals acted as a reinforcement of the gel network, leading to systems that can maintain better the shape. The addition of CNC to the WBPUU based ink, decreased the tan δ leading to a more elastic structures. The evolution of the tan δ with an increasing amount of CNC, however, was different if compared with solid content, since no big differences were observed for the different systems containing CNC, presenting all of them a highly elastic behaviour. This low tan δ which is correlated with highly elastic behaviour can lead in cohesion problems between layers resulting in a poor printing performance. Finally, the percentage of recovery followed a similar behaviour compared to the evolution of the solid content, showing an increase of the recovery above 80% in all systems. Moreover, the system WBPUU0.25$_{is}$ showed recovery values up to 92% showing a better recovery capacity compared with the WBPUU matrix.

Analysing this results, the addition of small amounts of CNC to the ink seems to improve the shape fidelity of the systems, increasing its recovery capacity as well as decreasing the tan δ slightly increasing the parameters related to the printability (viscosity, yield point and consistency index). Nevertheless, the addition of bigger amounts of CNC (above 1 wt%) seems to increase considerably the parameters related to printability such as the yield point

and viscosity, which can lead to printability problems. So, taking this analysis into account, the addition of very low quantities of CNC to the WBPUU based ink will help to improve the printing performance, but probably higher amounts of CNC could be counterproductive due to the decrease of the printability.

For comparative purposes the rheological properties, WBPUU0.5$_{is}$ system is included in **Figures SC.1-SC.5** of the Appendix C of the supplementary material at pages 268-272 represented with systems studied in other chapters.

Additionally, with the aim of ease the comparison between the influence of the *in situ* method and the ex situ one studied in the Chapter 6, the evolution of the rheological properties as a function of the CNC content obtained from both addition methods are displayed simultaneously in Appendix B (pages 245-258).

5.3.4 DIW 3D-printing of inks with different in situ added CNC contents

WBPUU matrix as well as WBPUU/CNC$_{is}$ nanocomposites have been printed by DIW 3D-printing, obtaining dog bone shaped pieces for all the systems until 1 wt% of CNC (**Figure 5.15**). Systems containing more amount of CNC presented so high storage modulus that were not able to be printed with the printer, despite presenting yield point values in the range of reported to printing. WBPUU1$_{is}$ was printed, but presented homogeneity problems in the printed thread, due to its so elastic behaviour, showing also a poor cohesion capacity as was also observed in the literature for very low values of tan δ [37]. However, WBPUU0.25$_{is}$ and WBPUU0.5$_{is}$ presented good printability and better appearance if compared with the WBPUU matrix, especially as far as shape fidelity is concerned. Despite the matrix presented good printability, the shape fidelity was not still acceptable, concretely in the borders of the piece. The addition of CNC strongly participates keeping the given shape. The increase of the rheological parameters such as viscosity and storage modulus resulted higher compared to the values observed in the literature for WBPU/CNC systems prepared *ex situ* for such a small amount of CNC. In this case, the early addition of CNC, could lead, as was proposed by *Chen et al.* [7], to the formation of a chemical bonding between the CNC and the WBPUU prepolymer, through some of the -NCO free groups of the prepolymer which were formulated for the posterior extension by EDA. Notwithstanding, the temperature during the phase inversion is reduced in order to avoid side reactions with water, and hence, also with the -OH of CNC. However, with high amounts of CNC this reaction could happened easier, leading to a greater increase of rheological parameters such as viscosity and storage modulus than was expected.

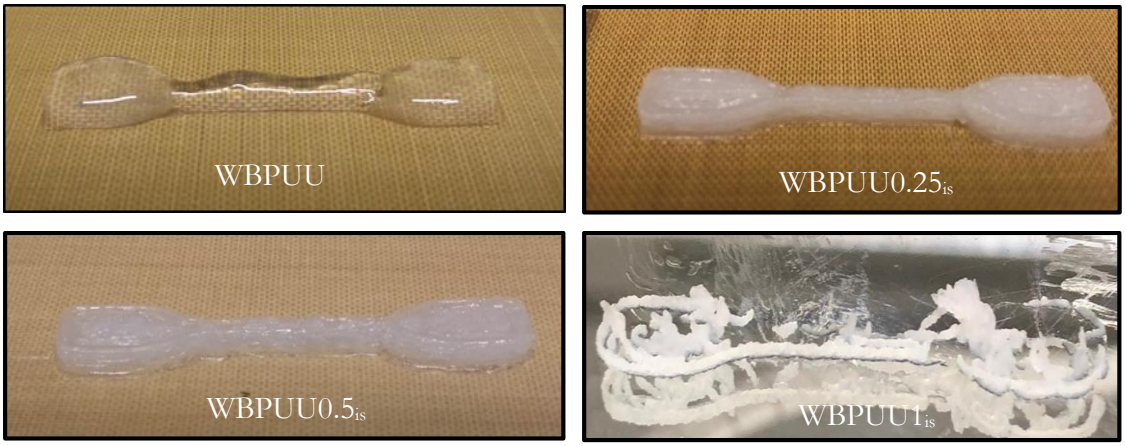

Figure 5.15 Printed pieces of WBPUU and WBPUU with different CNC contents added *in situ*

5.3.5 Mechanical and thermomechanical characterization of printed pieces

The influence of the cellulose nanocrystals on the mechanical properties of the printed pieces was studied by tensile test. Strip shape printed pieces of WBPUU, WBPUU0.25$_{is}$ and WBPUU0.5$_{is}$ were analysed. Young modulus and stress and strain at break determined from stress-strain curves are reported in **Table 5.6**. Systems with CNC content higher than 0.5 wt% did not result in recognizable strip pieces.

Table 5.6 Mechanical properties of WBPUU and WBPUU/CNC$_{is}$ printed pieces

System	Young Modulus (MPa)	Stress at break (MPa)	Strain at break (%)
WBPUU	14±1	16±2	1303±35
WBPUU0.25$_{is}$	17±1	15±1	1120±49
WBPUU0.5$_{is}$	120±6	10±1	979±40

The results showed that the incorporation of CNC in the WBPUU matrix contributed to increase the stiffness of the printed pieces. The Young modulus of the final material increased up to almost ten times when 0.5 wt% of CNC is added to the ink, concretely from 14 to 120 MPa. Contrary, the elongation at break decreased with the increase of CNC content, more noticeably for the system containing 0.5 wt% of CNC, which experienced a decrease of the elongation at break from 1303 to 979%. Comparing these results with the ones observed in the literature for *ex situ* prepared similar WBPU/CNC systems, to obtain a similar increase of the Young modulus, *Liu et al.* reported a CNC content of 5 wt% [38],

whereas other authors obtained a smaller increase of the Young modulus with similar quantities of cellulose derivated reinforcements [7,18,39].

Regarding the thermomechanical properties, the evolution of storage modulus and tan δ with temperature of the different WBPUU/CNC_{is} nanocomposites are reported in **Figure 5.16**.

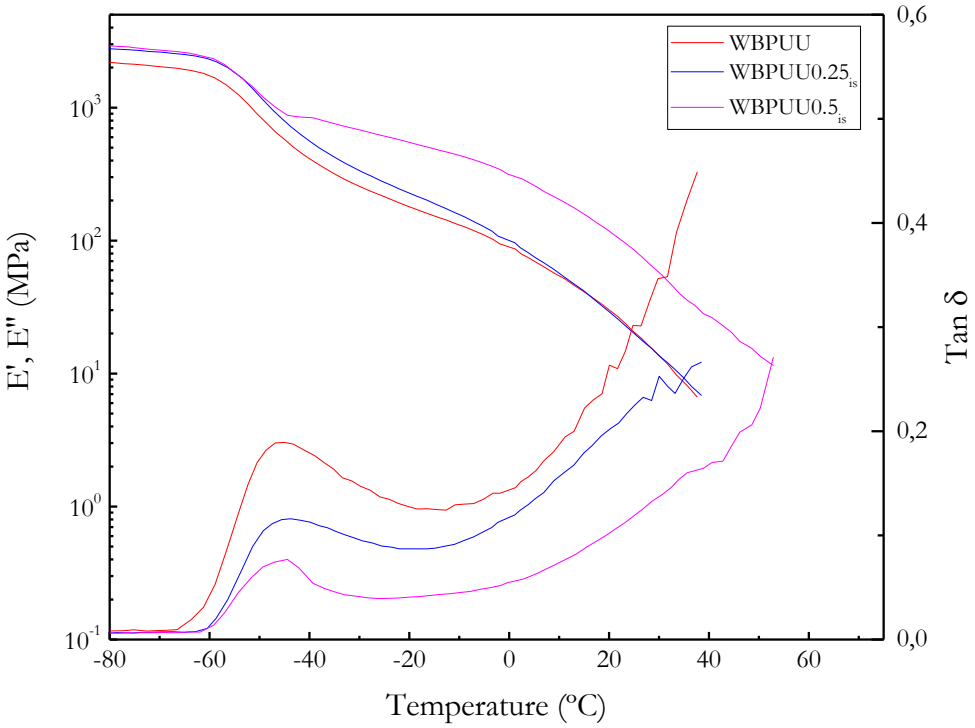

Figure 5.16 Storage modulus and tan δ as a function of temperature for WBPUU and WBPUU/CNC_{is} nanocomposites. Frequency = 1 Hz and scanning rate = 2 °C min^{-1}

As can be observed, the addition of CNC resulted in an increase of the E' in the whole temperature interval owing to the reinforcement effect of the nanocrystals [40]. In the glassy state, between -80 and -60 °C, E' modulus exhibits higher values, around 2600-2800 MPa for nanocomposites whereas for WBPUU is 2100 MPa, and maintained almost constant, due to the reinforcing effect of CNC. At higher temperatures, a decrease for E' was observed, usually reflected by a peak in tan δ curve, which is related with the material's Tg [41]. Tan δ peak shifted slightly to higher temperature and decreased in intensity with the increase of CNC content, indicative of the effective interactions between matrix and CNC, as were also observed by FTIR, which hinder chain mobility [42]. At higher temperatures,

nanocomposites, especially the WBPUU0.5$_{is}$, showed higher E' and its decrease, associated with the disruption of intermolecular associations and starting of the flow [7], shifted clearly to higher temperatures, reflecting an enhancement of the thermomechanical stability. This reinforcing effects and chain mobility restrictions corroborate that CNC interacts effectively with the matrix in agreement with FTIR, TGA and mechanical properties results.

5.4 Conclusions

In this chapter, a series of nanocomposites based on WBPUU loaded with different contents of CNCs (from 0.25 to 2 wt%) were prepared by adding the nanoentities during the synthesis of the WBPUU matrix, concretely during the phase inversion step, previously dispersed in deionized water. The different prepared WBPUU/CNC$_{is}$ nanocomposites were studied from the rheological viewpoint and subsequently printed so as to study the influence of the CNC in the printing performance as well as to study the viability of this inks for DIW 3D-printing. Moreover, the different WBPUU/CNC$_{is}$ nanocomposites were also analysed mechanically, thermomechanicaly and chemically in order to study the influence of the CNC reinforcement into the properties of the matrix. Additionally, so as to analyse the interaction of the CNC added during the synthesis with the matrix, TEM microscopy was used to study the prepared inks.

The TEM showed the interaction mechanism between CNC and the WBPUU matrix, where the early addition of the CNC reinforcement favoured the formation of a chemical bonding between the prepolymer and the CNC which resulted in the inclusion of the CNC into the particles. This was confirmed by the absence of free CNC in the TEM images and the presence of agglomerates at 2 wt% of CNC, suggesting that the CNC were embedded into the particles, resulting in a different disposition of the reinforcement in the ink and thus, obtaining a different rheological, mechanical and thermomechanical properties than if the reinforcement were free in the ink.

The rheological analysis of the WBPUU/CNC$_{is}$ nanocomposites showed that all prepared system presented a shear thinning behaviour, confirming their suitability for DIW 3D-printing. The increase of the CNC content of the ink resulted in an increase of both yield point and viscosity, which resulted in printability limitations for inks presenting higher CNC contents. The storage modulus increased and the tan δ decreased as the CNC content of the systems increased, leading to more structured and elastic inks, which can maintain better the shape and support multiple layers. This behaviour is similar to the one observed in Chapter

4 for the increase of the solid content, however, in this case, the modification of the studied rheological parameters resulted to be more accurate.

Regarding the influence of the CNC in the properties of the matrix, the addition of those nanoentities resulted in a remarkable increase of the stiffness and thermomechanical stability of the final printed pieces, acting as a reinforcement of the final material. This increase is higher compared with the one obtained in the literature for *ex situ* added reinforcements, requiring in those cases much more quantity of CNC to obtain similar increases. Hence, this remarkable increase of both stiffness and thermomechanical stability compared with the ones observed in the literature can be justified due to the aforementioned chemical bonding between the CNC and the WBPUU backbone.

5.5 References

[1] H. Li, S. Liu, L. Li, Rheological study on 3D printability of alginate hydrogel and effect of graphene oxide, Int. J. Bioprinting. 2 (2016) 54–66. https://doi.org/10.18063/IJB.2016.02.007.

[2] Y. Guo, Y. Liu, J. Liu, J. Zhao, H. Zhang, Z. Zhang, Shape memory epoxy composites with high mechanical performance manufactured by multi-material direct ink writing, Compos. Part A. 135 (2020) 105903. https://doi.org/10.1016/j.compositesa.2020.105903.

[3] K. Markstedt, A. Mantas, I. Tournier, D. Hägg, P. Gatenholm, 3D bioprinting human chondrocytes with nanocellulose − alginate bioink for cartilage tissue engineering applications, Biomacromolecules 16 (2015) 1489–1496. https://doi.org/10.1021/acs.biomac.5b00188.

[4] J.A. Lewis, Direct ink writing of 3D functional materials, Adv. Funct. Mater. 16 (2006) 2193–2204. https://doi.org/10.1002/adfm.200600434.

[5] G. Siqueira, D. Kokkinis, R. Libanori, M.K. Hausmann, A.S. Gladman, A. Neels, P. Tingaut, T. Zimmermann, J.A. Lewis, A.R. Studart, Cellulose nanocrystal inks for 3D printing of textured cellular architectures, Adv. Funct. Mater. 27 (2017) 1604619. https://doi.org/10.1002/adfm.201604619.

[6] E. Feilden, C. Ferraro, Q. Zhang, E. García-tuñón, E.D. Elia, F. Giuliani, L. Vandeperre, E. Saiz, 3D printing bioinspired ceramic composites, Sci. Rep. 7 (2017) 1–9. https://doi.org/10.1038/s41598-017-14236-9.

[7] R. Chen, C. Huang, S. Hsu, Composites of waterborne polyurethane and cellulose nanofibers for 3D printing and bioapplications, Carbohydr. Polym. 212 (2019) 75–88. https://doi.org/10.1016/j.carbpol.2019.02.025.

[8] Y. Liu, H. Hu, X-ray Diffraction study of bamboo fibers treated with NaOH, Fibers Polym. 9 (2008) 735–739. https://doi.org/10.1007/s12221-008-0115-0.

[9] A.D. French, Idealized powder diffraction patterns for cellulose polymorphs, Cellulose 21 (2014) 885–896. https://doi.org/10.1007/s10570-013-0030-4.

[10] S. Park, J.O. Baker, M.E. Himmel, P.A. Parilla, D.K. Johnson, Cellulose crystallinity index: measurement techniques and their impact on interpreting cellulase performance, Biotechnol. Biofuels 3 (2010) 1–10. https://doi.org/10.1186/1754-6834-3-10.

[11] Y.M. Zhou, S.Y. Fu, L.M. Zheng, H.Y. Zhan, Effect of nanocellulose isolation techniques on the formation of reinforced poly (vinyl alcohol) nanocomposite films, Express Polym. Lett. 6 (2012) 794–804. https://doi.org/10.3144/expresspolymlett.2012.85.

[12] L. Segal, J.J. Creely, A. Martin, M. Conrad, Empirical method for estimating the degree of crystallinity of native cellulose using the X-ray diffractometer, Text. Res. J. (1958) 786–794. https://doi.org/10.1177/004051755902901003.

[13] H. Kargarzadeh, I. Ahmad, I. Abdullah, A. Dufresne, S.Y. Zainudin, R.M. Sheltami, Effects of hydrolysis conditions on the morphology , crystallinity , and thermal stability of cellulose nanocrystals, Cellulose 19 (2012) 855–866. https://doi.org/10.1007/s10570-012-9684-6.

[14] B.D. Cullity, Elements of x-ray diffraction, 1978.

[15] S. Elazzouzi-hafraoui, Y. Nishiyama, J. Putaux, L. Heux, F. Dubreuil, C. Rochas, The shape and size distribution of crystalline nanoparticles prepared by acid hydrolysis of native cellulose, Biomacromolecules (2008) 57–65. https://doi.org/10.1021/bm700769p.

[16] R.H. Atalla, J.C. Gast, D.W. Sindorf, V.J. Bartuska, G.E. Maciel, Carbon-13 NMR spectra of cellulose polymorphs, J. Am. Chem. Soc. 102 (1980) 3249–3251. https://doi.org/https://doi.org/10.1021/ja00529a063.

[17] Z. Gao, J. Peng, T. Zhong, J. Sun, X. Wang, C. Yue, Biocompatible elastomer of waterborne polyurethane based on castor oil and polyethylene glycol with cellulose nanocrystals, Carbohydr. Polym. 87 (2012) 2068–2075. https://doi.org/10.1016/j.carbpol.2011.10.027.

[18] A. Santamaria-Echart, L. Ugarte, A. Arbelaiz, N. Gabilondo, M.A. Corcuera, A. Eceiza, Two different incorporation routes of cellulose nanocrystals in waterborne polyurethane nanocomposites, Eur. Polym. J. 76 (2016) 99–109. https://doi.org/10.1016/j.eurpolymj.2016.01.035.

[19] C. Thibaut, A. Denneulin, S. Rolland, D. Beneventi, L. Orgéas, D. Chaussy, A fibrous cellulose paste formulation to manufacture structural parts using 3D printing by extrusion, Carbohydr. Polym. 212 (2019) 119–128. https://doi.org/10.1016/j.carbpol.2019.01.076.

[20] X. Zhang, W. Huo, J. Liu, Y. Zhang, S. Zhang, J. Yang, 3D printing boehmite gel foams into lightweight porous ceramics with hierarchical pore structure, J. Eur. Ceram. Soc. 40 (2020) 930–934. https://doi.org/10.1016/j.jeurceramsoc.2019.10.032.

[21] Z. Liu, M. Zhang, B. Bhandari, C. Yang, Impact of rheological properties of mashed potatoes on 3D printing, J. Food Eng. 220 (2017) 76–82. https://doi.org/10.1016/j.jfoodeng.2017.04.017.

[22] C. Jeon, B.R. Hodges, Comparing thixotropic and Herschel – Bulkley parameterizations for continuum models of avalanches and subaqueous debris flows, Nat. Hazards Earth Syst. Sci. 18 (2018) 303–319. https://doi.org/ 10.5194/nhess-18-303-2018.

[23] R.E. Abouzeid, R. Khiari, D. Beneventi, A. Dufresne, Biomimetic mineralization of three-dimensional printed alginate/TEMPO-oxidized cellulose nanofibril scaffolds for bone tissue engineering, Biomacromolecules 19 (2018) 4442–4452. https://doi.org/10.1021/acs.biomac.8b01325.77.

[24] K. Hyun, S.H. Kim, K.H. Ahn, S.J. Lee, Large amplitude oscillatory shear as a way to classify the complex fluids, J. Nonnewton. Fluid Mech. 107 (2002) 51–65. https://doi.org/ 10.1016/S0377-0257(02)00141-6.

[25] A.R. Payne, The dynamic properties of carbon black loaded natural rubber

vulcanizates. Part II, J. Appl. Polym. Sci. 6 (1962) 368–372. https://doi.org/10.1002/app.1962.070062115.

[26] F. Clement, Etude des mécanismes de renforcement dans les réseaux polymdiméthylsiloxane chargés avec de la silice, Université Paris VI, 1999.

[27] L. Chazeau, J.D. Brown, L.C. Yany, Modulus recovery kinetics and other insights into the Payne effect for filled elastomers, Polym. Compos. 21 (2000) 202–222. https://doi.org/10.1002/pc.10178.

[28] A.R. Payne, Reinforcement of elastomers, in: G. Krauss (Ed.), Interscience, 1965.

[29] E. Pulatsu, J. Su, J. Lin, M. Lin, Factors affecting 3D printing and post-processing capacity of cookie dough, Innov. Food Sci. Emerg. Technol. 61 (2020) 102316. https://doi.org/10.1016/j.ifset.2020.102316.

[30] J. Su, W. Gao, K. Trinh, S.M. Kenderes, T. Pulatsu, C. Zhang, A. Whittington, M. Lin, J. Lin, 4D printing of polyurethane paint-based composites, Int. J. Smart Nano Mater. 10 (2019) 237–248. https://doi.org/10.1080/19475411.2019.1618409.

[31] L. Li, Q. Lin, M. Tang, A.J.E. Duncan, C. Ke, Advanced polymer designs for direct-Ink-write 3D printing, Chem. Eur. J. (2019) 1–15. https://doi.org/10.1002/chem.201900975.

[32] Y. Liu, D. Liu, G. Wei, Y. Ma, B. Bhandari, P. Zhou, 3D printed milk protein food simulant: Improving the printing performance of milk protein concentration by incorporating whey protein isolate, Innov. Food Sci. Emerg. Technol. 49 (2018) 116–126. https://doi.org/10.1016/j.ifset.2018.07.018.

[33] E. Alvarez-castillo, S. Oliveira, C. Bengoechea, I. Sousa, A rheological approach to 3D printing of plasma protein based doughs, J. Food Eng. 288 (2021). https://doi.org/10.1016/j.jfoodeng.2020.110255.

[34] C.W. Peak, J. Stein, K.A. Gold, A.K. Gaharwar, Nanoengineered colloidal inks for 3D bioprinting, Langmuir 34 (3) (2017) 917–925. https://doi.org/10.1021/acs.langmuir.7b02540.

[35] A.R. Studart, E. Amstad, L.J. Gauckler, Yielding of weakly attractive nanoparticle networks, Soft Matter. 7 (2011) 6408–6412. https://doi.org/10.1039/c1sm05598d.

[36] M.K. Hausmann, P.A. Ru, G. Siqueira, J. Läuger, R. Libanori, T. Zimmermann, A.R.

Studart, Dynamics of cellulose nanocrystal alignment, ACS Nano. 12 (2018) 6926–6937. https://doi.org/10.1021/acsnano.8b02366.

[37] V. Perez, M. Felix, A. Romero, A. Guerrero, Characterization of pea protein-based bioplastics processed by injection moulding, Food Bioprod. Process. 97 (2015) 100–108. https://doi.org/10.1016/j.fbp.2015.12.004.

[38] H. Liu, S. Cui, S. Shang, D. Wang, J. Song, Properties of rosin-based waterborne polyurethanes/cellulose nanocrystals composites, Carbohydr. Polym. 96 (2013) 510–515. https://doi.org/10.1016/j.carbpol.2013.04.010.

[39] G. Mondragon, A. Santamaria-Echart, M.E. V. Hormaiztegui, A. Arbelaiz, C. Peña-Rodriguez, V. Mucci, M. Corcuera, M.I. Aranguren, A. Eceiza, Nanocomposites of waterborne polyurethane reinforced with cellulose nanocrystals from sisal fibres, J. Polym. Environ. 26 (2017) 1869–1880. https://doi.org/10.1007/s10924-017-1089-z.

[40] L. Rueda, A. Saralegui, B. Fernández, Q. Zhou, L.A. Berglund, M.A. Corcuera, I. Mondragon, A. Eceiza, Cellulose nanocrystals/polyurethane nanocomposites . Study from the viewpoint of microphase separated structure, Carbohydr. Polym. 92 (2013) 751–757. https://doi.org/10.1016/j.carbpol.2012.09.093.

[41] S.M. Cakić, I.S. Ristić, I. Krakovský, D.T. Stojiljković, P. Bělský, L. Kollová, Crystallization and thermal properties in waterborne polyurethane elastomers: Influence of mixed soft segment block, Mater. Chem. Phys. 144 (2014) 31–40. https://doi.org/10.1016/j.matchemphys.2013.12.008.

[42] Q. Wu, M. Henriksson, X. Liu, L.A. Berglund, A high strength nanocomposite based on microcrystalline cellulose and polyurethane, Biomacromolecules 8 (2007) 3687–3692. https://doi.org/https://doi.org/10.1021/bm701061t.

CHAPTER 6

EX SITU ADDITION OF CELLULOSE NANOCRYSTALS TO ENHANCE THE PRINTING PERFORMANCE OF WBPUU BASED INKS

6. *EX SITU* ADDITION OF CELLULOSE NANOCRYSTALS TO ENHANCE THE PRINTING PERFORMANCE OF WBPUU BASED INKS

6.1 Objective

This chapter focused on the study of the influence of the addition of CNC after the synthesis of the WBPUU, which is known as *ex situ* method, in contrast with the *in situ* method studied in the previous chapter. In this context, cellulose nanocrystals were used to reinforce and to improve the printing performance of a novel PCL/PEG based polyurethane urea ink. For that, different amounts of CNC were added to a previously synthesized WBPUU by vigorous mechanical stirring. The different prepared WBPUU/CNC_{es} nanocomposites inks have been analysed from the rheological viewpoint and subsequently printed to evaluate the effect of the CNC in the printing process as well as in the printed pieces. Additionally, the mechanical and thermomechanical properties as well as the thermal stability of the printed pieces were analysed in order to study the influence of the CNC reinforcement. It is expected that the *ex situ* addition of CNC will not only improve the shape fidelity of the ink, which leads to a better printing performance, but also acts as a reinforcement which can enhance the mechanical properties of the printed pieces. Although some works in the literature have compared the properties of nanocomposites prepared from *in situ* and *ex situ* methods [1], few research is done in the comparison of both methods rheological wise, and hence as far as printing performance is concerned. In the present chapter the obtained rheological analysis results of *ex situ* method of CNC incorporation have been compared with the ones obtained in the previous chapter for *in situ* method in order to determine the advantages and drawbacks of every method. Additionally, the mechanical and thermomechanical properties obtained from both CNC addition methods were compared to study the influence of the CNC integration route in the properties of the printed pieces.

6.2 Experimental part

A WBPUU with a PCL and PEG ratio of 0.8/0.2 has been synthesized according to the methodology described in Chapter 3. The ratio of PCL/PEG/IPDI/DMPA/EDA was 1/3.5/1/1/1.5 and the solid content of the inks was fixed to 29 wt%.

The WBPUU/CNC_{es} nanocomposites were prepared by mixing different amounts of CNC with the synthesized WBPUU. The mixing has been carried out by vigorous mechanical stirring, using an ultraturrax stirrer at 12000 rpm during 5 minutes. As a result, homogeneous white coloured inks were obtained. WBPUU/CNC_{es} nanocomposites with 0.5, 1 and 2 wt% of CNC were prepared. The different systems were named as $WBPUUX_{es}$, where X is the added CNC content. In **Table 6.1** the different synthesized WBPUU/CNC_{es} composites are enlisted. As a result of the vigorous stirring, the CNC was successfully dispersed in the WBPUU dispersion. The **Figure 6.1** illustrated the formation process of the WBPUU/CNC_{es} nanocomposites.

Table 6.1 Designation and CNC content of prepared WBPUU/CNC_{es} nanocomposites

System	CNC (wt%)
WBPUU	0
$WBPUU0.5_{es}$	0.5
$WBPUU1_{es}$	1
$WBPUU2_{es}$	2

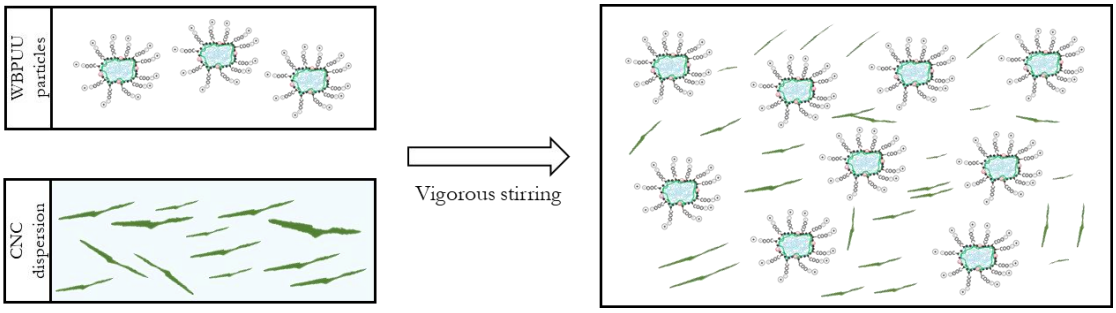

Figure 6.1 Illustration of the formation process of the WBPUU/CNC_{es} nanocomposites by *ex situ* method

The different prepared WBPUU/CNC_{es} inks were printed using the equipment displayed in Chapter 2, following the printing conditions explained in Chapter 5.

6.3 Results and discussion

6.3.1 Physicochemical characterization of WBPUU and WBPUU/CNC$_{es}$ nanocomposites

The interactions between the WBPUU and CNC of the printed pieces were studied by FTIR. **Figure 6.2** showed the spectra of both WBPUU and WBPUU/CNC$_{es}$ nanocomposites. Analysing the obtained results, both matrix and composites showed similar spectra with no apparition of new bands in the case of nanocomposites. Regarding the carbonyl region in the range 1800-1600 cm^{-1}, a shift towards lower wavenumbers is observed in the band situated at 1735 cm^{-1} for the matrix as the CNC content increased, which can be observed in the inset of **Figure 6.2**.

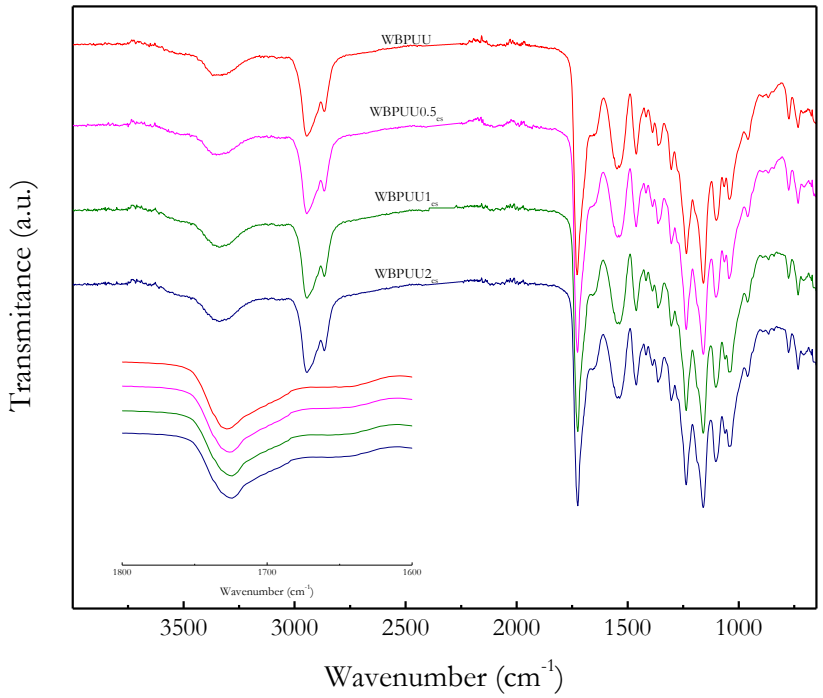

Figure 6.2 FTIR spectra of WBPUU and WBPUU/CNC$_{es}$ nanocomposites. Inset: magnification of the carbonyl region 1800-1600 cm^{-1}

The displacement of this band, which is related to C=O of PCL and urethane in WBPUU, can be attributed to the hydrogen bonding interaction between WBPUU and CNC, suggesting a successful interaction between the CNC and the WBPUU [2]. This shift of the carbonyl band, resulted smaller comparing to the one observed in Chapter 5 for *in situ*

addition of CNC, confirming a less strong interaction between the polymer and the nanoentities in the *ex situ* method.

The thermal stability of the matrix and WBPUU/CNC_{es} nanocomposites prepared by *ex situ* method have been studied by TGA. The different TGA and DTG curves of WBPUU and WBPUU/CNC_{es} nanocomposites are displayed in **Figure 6.3**.

Analysing the obtained degradation curves, a two-step degradation can be observed for the WBPUU matrix, in accordance to the degradation of PCL80PEG20 based system observed previously (Chapter 3). The addition of *ex situ* incorporated CNC seems to decrease the second degradation step as was observed also for *in situ* reinforced WBPUU/CNC_{is} nanocomposites (Chapter 5). Studying the initial degradation and the maximum degradation temperatures, which are displayed in **Table 6.2**, a significant increase of both values was observed in the nanocomposites, resulting in systems with higher thermal stability as a result of the CNC reinforcement.

Table 6.2 Initial degradation and maximum degradation temperatures of WBPUU and WBPUU/CNC_{es} nanocomposites

System	T_0 (°C)	T_d (°C)
WBPUU	250	312
WBPUU0.5$_{es}$	252	335
WBPUU1$_{es}$	258	339
WBPUU2$_{es}$	262	348

However, comparing this increase of the thermal stability with the observed one in the previous chapter for the *in situ* addition of CNC, a lower increase of both T_0 and T_d is observed, requiring more amount of CNC reinforcement added by *ex situ* method so as to reach the values obtained for nanocomposites containing small amounts of *in situ* added CNC. In fact, WBPUU0.5_{is} presented higher T_0, and thus higher thermal stability than WBPUU2_{es}, confirming the weaker interactions between WBPUU and CNC when the nanoentities are added after the synthesis of the ink.

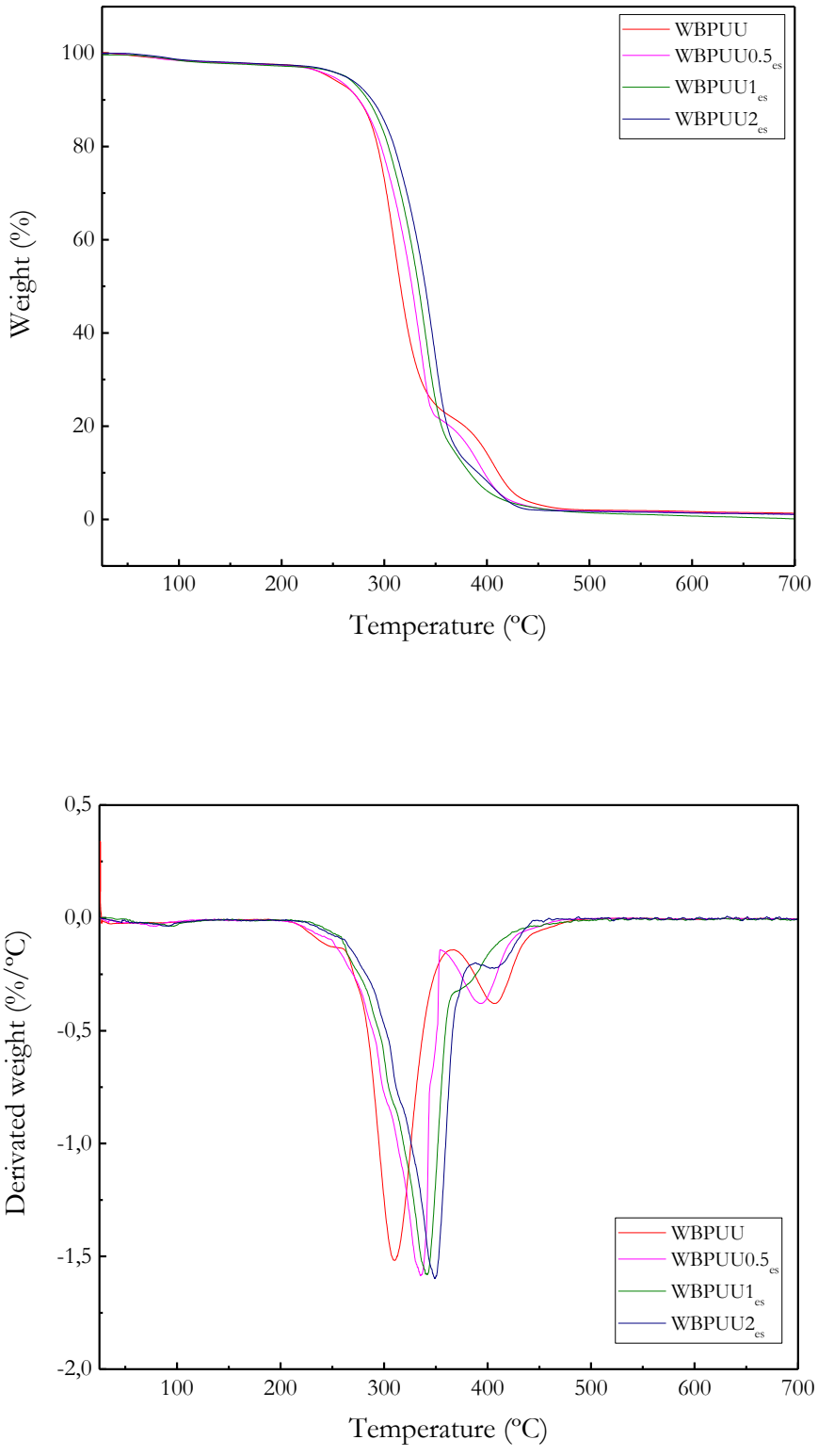

Figure 6.3 Variation of the weight (up) and derivated weight curves (down) of WBPUU and WBPUU/CNC_{es} nanocomposites obtained by *ex situ* method

6.3.2 TEM analysis of the WBPUU/CNC$_{es}$ inks

In order to study the interactions between the WBPUU particles and the CNC reinforcement, the WBPUU/CNC$_{es}$ nanocomposites obtained via *ex situ* method were studied by TEM. Images of the WBPUU (shown in Chapter 5) and WBPUU2$_{es}$ are shown in **Figure 6.4**.

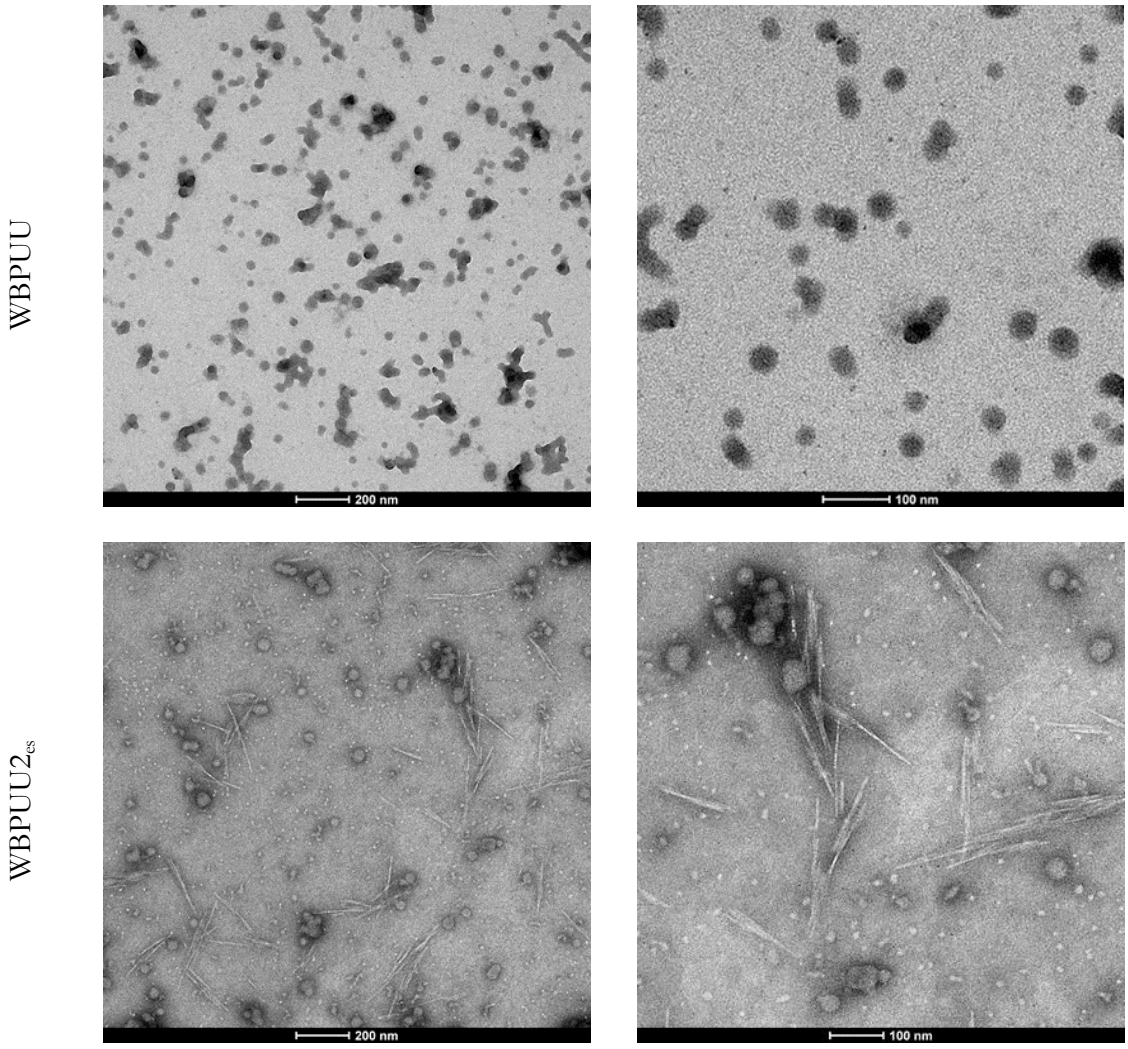

Figure 6.4 TEM images of WBPUU (up) and WBPUU2$_{es}$ (down) inks. The images where taken in a 1% dilution of the original inks

The images showed that the cellulosic reinforcement has been successfully incorporated to the WBPUU based ink showing a good dispersion of the CNC. Despite the images presented few agglomerates, the results confirmed the viability of the mechanical stirring as the dispersing mechanism for the addition of CNC to the aqueous based inks. The WBPUU matrix contrary, only showed particles in its corresponding images, presenting similar particle sizes than WBPUU2$_{es}$ but with the absence of the aforementioned CNC reinforcement. The

presence of some CNC agglomerates in the dispersion can be justified due to the big amount of reinforcement incorporated to the ink. Regarding the interaction between the WBPUU particles and the CNC, as can be observed in the images, despite some nanoentities are in contact with the particles, the CNC did not appear embedded in the particles as was the case of the *in situ* prepared nanocomposites in Chapter 5 (**Figure 5.7**, page 136). Indeed, the CNC were observed in their complete dimension. This results, confirmed the ones obtained by other authors for *ex situ* addition of nanoentities into a WBPU matrix [1,2].

Comparing the obtained image with the one observed in Chapter 5 for the *in situ* addition of the CNC, it can be observed a good particle dispersion and the presence of free CNC. In this case the addition of the CNC after the formation of the WBPUU particles for the *ex situ* method, promote different interactions between the particles and the nanoentities observed in *in situ* method. Additionally, these physical interactions are removed more easily when the inks are diluted resulting in an effective separation between particles and reinforcement, whereas the chemical bonding produced in the *in situ* method resulted in the apparition of agglomerates even with a 1% of dilution.

6.3.3 Rheological characterization of WBPUU/CNC$_{es}$ inks

Flow test were also performed to the *ex situ* obtained WBPUU/CNC$_{es}$ nanocomposites. The viscosity curves, which are in **Figure 6.5**, showed a shear thinning behaviour desirable for DIW 3D-printing [3–5]. According to the literature, a shear thinning behaviour is beneficial in printing to allow a rapid structural recovery [6] The viscosity values of the inks at different shear rates are enlisted in **Table 6.3**. and showed a decrease of the viscosity from 3000-9000 Pa s at 0.01 s^{-1} to 10-50 Pa s at the printing rate of 19 s^{-1}. Comparing the viscosity of the prepared systems with the increasing *ex situ* added CNC content, an increase of the viscosity values is observed in all shear rates when CNC content increases. However, comparing these results with the ones obtained for the same system but *in situ* method, a much lower increase of the viscosity was observed, presenting WBPUU0.25$_{is}$ nanocomposite higher values at 0.01s^{-1} rate than WBPUU2$_{es}$ ink. For comparative purposes between *in situ* and *ex situ* method, the variation of the viscosity at 0.01 and 19 s^{-1} as a function of the CNC content of both methods are represented in the supplementary material (Appendix B, **Figures SB.1** and **SB.2** at pages 260-261).

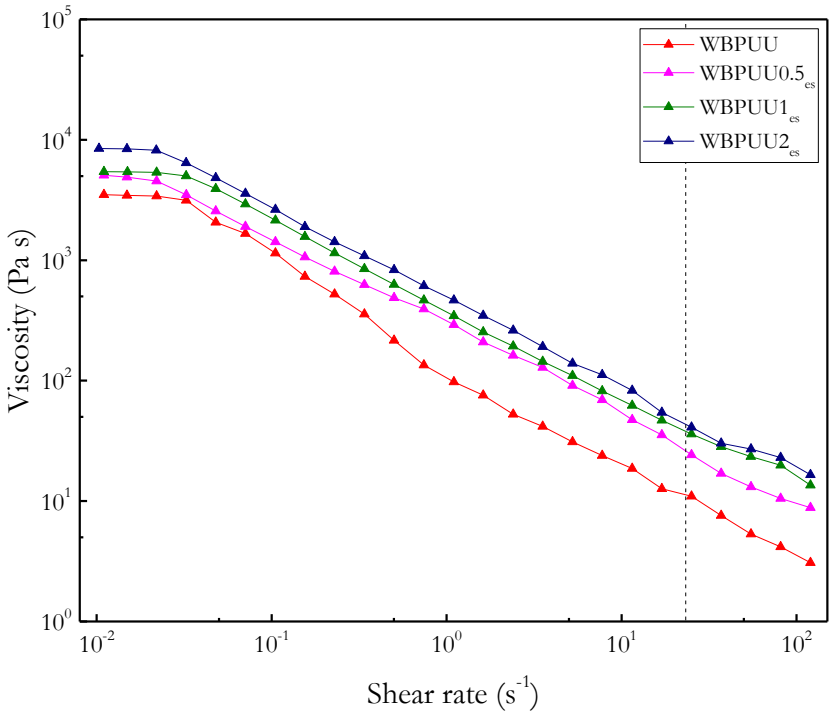

Figure 6.5 Viscosity as a function of the shear rate of WBPUU and WBPUU/CNC_{es} nanocomposites. (---) Printing shear rate 19 s^{-1} (T = 22.5 °C)

Table 6.3 Viscosity values measured at different shear rates for the synthesized WBPUU and WBPUU/CNC_{es} nanocomposites

System	Viscosity (Pa s)		
	η at 0.01 s^{-1}	η at 19 s^{-1}	η at 100 s^{-1}
WBPUU	3851	12	4
WBPUU0.5$_{es}$	5074	26	10
WBPUU1$_{es}$	5438	37	16
WBPUU2$_{es}$	8453	44	19

Additionally, contrarily to that observed for the increase of the solid content in Chapter 4 and the *in situ* addition of CNC in Chapter 5, the Newtonian plateau at low rates in WBPUU seems to stay similar with the *ex situ* addition of CNC, presenting a zone of constant viscosity, which is related to the zero shear viscosity from 0.01 to 0.02 s^{-1}.

The influence of the CNC on the printability of the inks was studied trough the yield point and flow point of the different systems using the same methodology as used in Chapter 4

and 5. The determination of both yield and flow point is displayed in **Figure 6.6** by analysing the variation of the storage and loss moduli as a function of the shear stress.

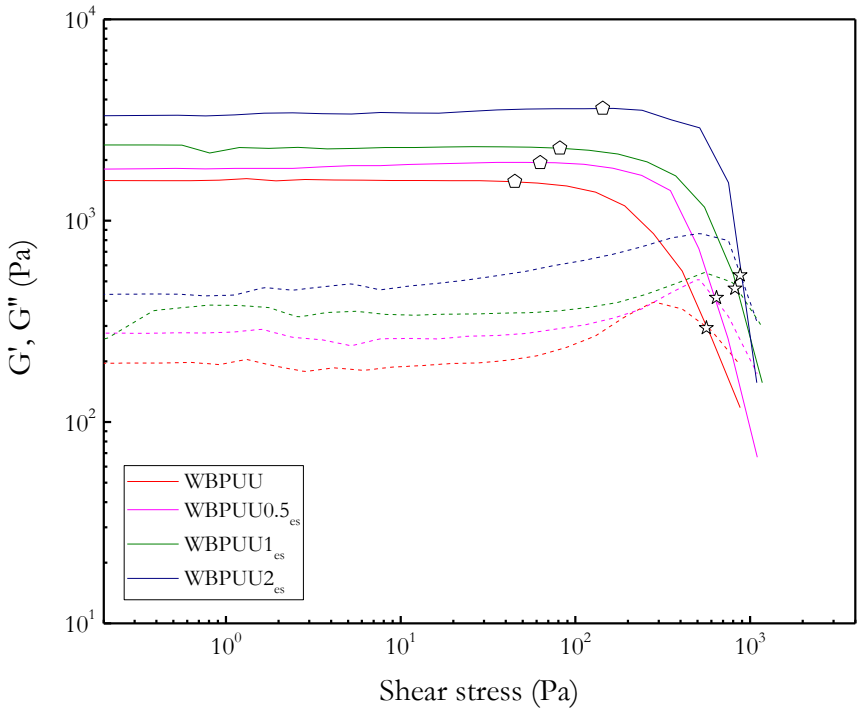

Figure 6.6. (—) G' and (---) G" as a function of shear stress of WBPUU and WBPUU/CNC_{es} nanocomposites (T = 22.5 °C). Determination of (⬠) yield point and (☆) flow point

Results are displayed in **Table 6.4**. An increase of both yield and flow point with the increase of the CNC content was observed, presenting all systems at low shear stress much higher G' than G", illustrating the ability for the inks to maintain the shape at rest state [7]. The yield point presented a constant increase as more amount of CNC was added to the nanocomposite. However, above 1 wt% of CNC the inks showed a higher increase of the yield point compared with other composites presenting lower quantities of CNCs. Anyway, the obtained low yield point values should not make ink extrusion more difficult since in the literature materials presenting similar values are usually printed easily [8–10]. Finally, regarding the FTI, the decreasing observed values as the CNC content increase suggests a more brittle behaviour for nanocomposites compared with the matrix, as well as with prepared *in situ* systems in Chapter 5.

Regarding the comparison between *in situ* and *ex situ* method, the variation of the yield point as a function of the CNC content are represented in **Figure SB.3** at page 262 of Appendix B for comparative purposes. In this case, as observed with the viscosity, the *ex situ* addition of CNC resulted in a lower increase of the yield point compared with the *in situ* method, presenting the WBPUU1$_{es}$ lower yield point values than WBPUU0.5$_{is}$.

The flow curves of the matrix and different WBPUU/CNC$_{es}$ compositions were adjusted to the Herschel Bulkley model using the previously calculated yield point values. The proposed model fitted with the experimental data obtaining high R^2 values. The parameters obtained from this adjustment can be observed in **Table 6.4**, whereas an example of the adjustment of the experimental flow curve is displayed in **Figure 6.7**.

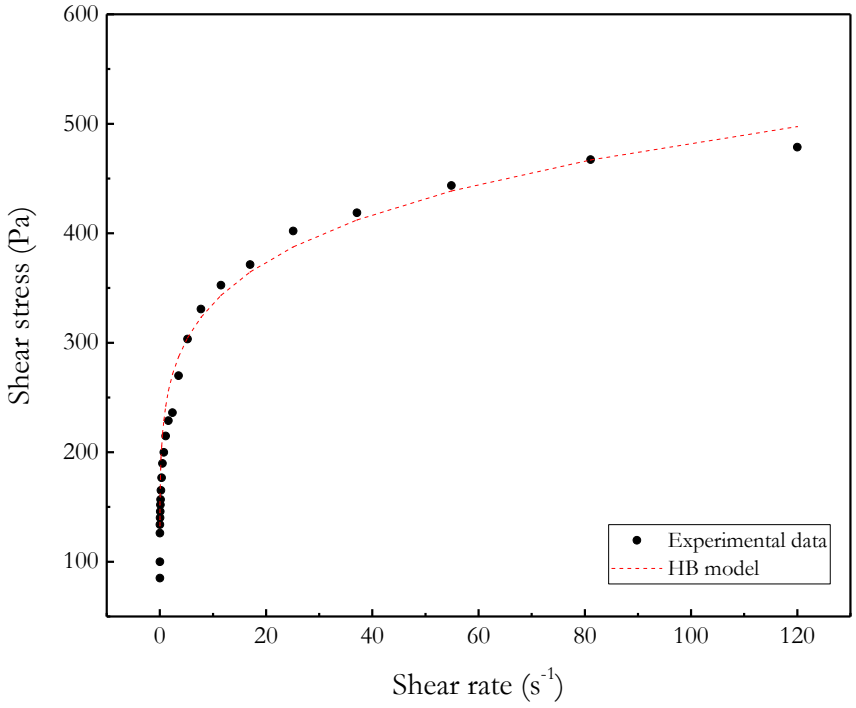

Figure 6.7 Adjustment to the Herschel Bulkley (HB) model of WBPUU0.5$_{es}$ flow curve

Regarding the consistency index, higher values as the CNC content increased were observed. Nevertheless, comparing this values with the obtained ones with the in situ prepared inks, a smaller increase was observed, meaning a lower influence of the ex situ added CNC in the consistency of the ink than the in situ ones. The increase of the K index is usually related to a decrease of the printability, obtaining in some cases of very high values an inhomogeneous

and very poor extrusion of the ink. Contrary, the flow index (n), remained in similar values in both addition methods, obtaining in all systems values under 1 which confirms the shear thinning behaviour of the systems [11,12].

Table 6.4 Determination of yield point, flow point, FTI index and parameters obtained from the adjustment to Herschel Bulkley model ($\sigma-\sigma_y=K\dot{\gamma}^n$) of WBPUU and WBPUU/$CNC_{es}$ nanocomposites

System	Yield point (Pa)	Flow point (Pa)	FTI	Herschel Bulkley model		
				K index (Pa s n^{-1})	n index	R^2
WBPUU	44	562	13	194	0.19	0.95
WBPUU0.5$_{es}$	63	643	10	197	0.17	0.99
WBPUU1$_{es}$	82	820	10	203	0.18	0.98
WBPUU2$_{es}$	123	877	7	211	0.18	0.98

The variation of both storage and loss moduli as a function of the frequency have been studied so as to analyse the influence of the WBPUU/CNC_{es} obtained inks in the printing shape fidelity. The strain has been fixed to 1% as a result of a previous test were both storage and loss moduli were plotted as a function of strain in order to determine the linear viscoelastic region (LVR) (**Figure 6.8**).

The obtained curves showed a LVR presenting a plateau of both storage and loss moduli, with G' over G" illustrating an elastic behaviour for all systems [13]. At higher strain values, the network is destroyed as a result of the increasing strain resulting in a decrease of both G' and G" up to the crossover of both moduli, illustrating the sweep to a predominant viscous behaviour and the flow of the ink [14]. The lower difference between G' and G" observed for WBPUU represents a less structured network, as was observed previously, compared with the nanocomposites, which as a result of the CNC addition resulted in more structured inks.

Additionally, as described in the previous chapters, at the end of the LVR region, a phenomena called "weak strain overshoot" can be observed in systems containing higher CNC content, where the loss modulus experienced an increase and a local maximum prior to the drop of both G' and G" as a result of the destroy of the structured network [15].

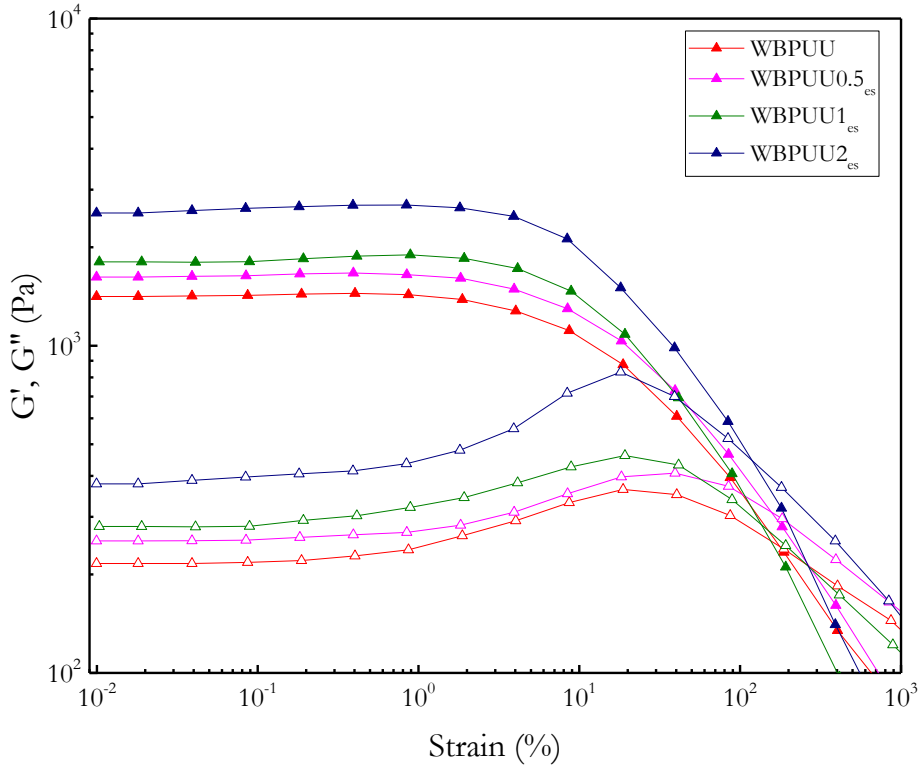

Figure 6.8 G' (▲) and G" (Δ) as a function of strain (T = 22.5 °C) of WBPUU and WBPUU/CNC_{es} nanocomposites with different CNC contents at 1 Hz

Once the LVR region was determined, the variation of both storage and loss moduli as a function of the frequency has been studied so as to analyse the influence of the WBPUU/CNC_{es} inks in the printing shape fidelity. The results are shown in the **Figure 6.9**, whereas, the measured values of storage modulus, loss modulus and tan δ at a fixed frequency of 1 Hz are displayed in **Table 6.5**.

Table 6.5 Storage modulus, loss modulus and tan δ values at 1 Hz and structure recovery percentage of WBPUU and WBPUU/CNC_{es} nanocomposites

System	Storage modulus (Pa)	Loss modulus (Pa)	Tan δ	Structure recovery (%)
WBPUU	1033	296	0.29	84
WBPUU0.5$_{es}$	1776	330	0.19	83
WBPUU1$_{es}$	2313	334	0.14	84
WBPUU2$_{es}$	2736	395	0.13	85

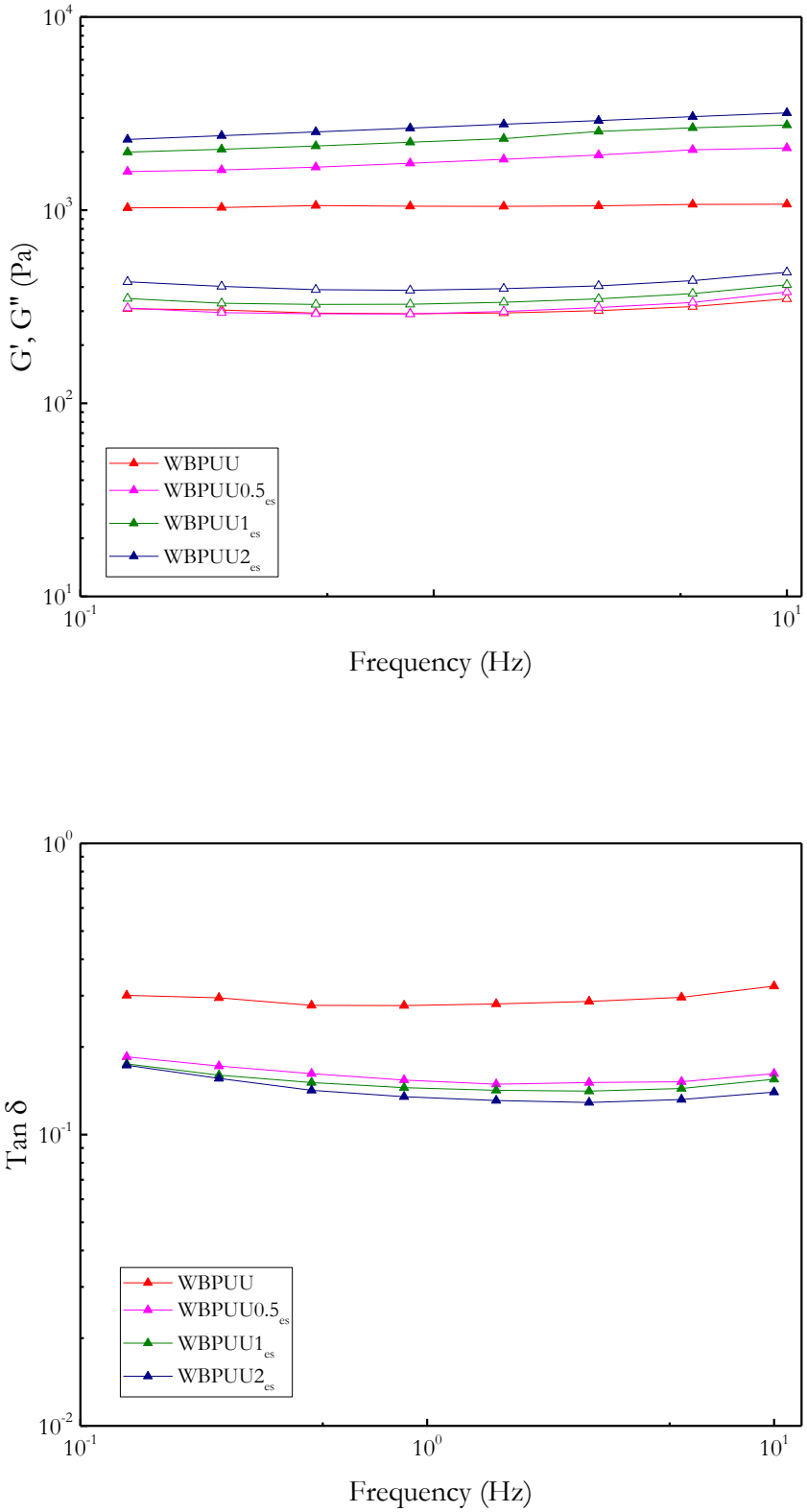

Figure 6.9 G' (▲) and G" (Δ) of WBPUU and WBPUU/CNC_{es} nanocomposites (up) and tan δ (down) as a function of the frequency (T = 22.5 °C)

The results showed an increase of both storage and loss moduli as the CNC content increased, leading to more structured materials which probably will present better shape fidelity properties. Both matrix and WBPUU/CNC_{es} nanocomposites presented G' over G" in all the frequency range which according to the literature represented an elastic gel or gel like structure [16]. Regarding the storage modulus values, which determines the mechanical strength of the inks [17,18], all nanocomposites presented higher values compared with the matrix, presenting an increase from 1033 Pa for WBPUU to 2736 Pa for $WBPUU2_{es}$ at 1 Hz. Higher values of G' indicates that the ink exhibits stronger mechanical strength and could self-support better its own weight after printing [19]. All systems presented G' values higher than the 10^3 Pa, which are, as already discussed, the lower limit proposed in the literature in order to achieve the capacity of supporting multi-layered constructs without collapsing.

Analysing the tan δ, a decrease can be noticed comparing the values of the *ex situ* prepared WBPUU/CNC_{es} nanocomposites with the one of the WBPUU, illustrating the higher elastic behaviour of the inks containing CNC, and thus resulting in a higher capacity of retaining the given shape. The increase of the reinforcement content led to the obtaining of lower tan δ, which is correlated to a more pronounced elastic behaviour and hence, lead to the obtaining of more strong and structured inks [20,21].

As observed with other rheological parameters, the increase of both G' and G" is lower compared with the one observed in the systems with CNC added *in situ*, obtaining similar values with 0.5 wt% *in situ* and 2 wt% *ex situ*. The tan δ values of *ex situ* systems were also lower compared with the ones observed for *in situ* method. For comparative purposes, the evolution of both storage modulus and tan δ of *in situ* and *ex situ* method as a function of the CNC content are represented in **Figures SB.5** and **SB.6** at pages 264-265.

For comparative purposes with systems proposed in other chapters, the storage and loss moduli as well as the tan δ of $WBPUU2_{es}$ as a function of frequency is represented in **Figure SC.3** and **SC.4** at pages 270-271 of the Appendix C of the supplementary material.

Additionally, $WBPUU1_{es}$ and $WBPUU2_{es}$ are mapped as a function of their storage modulus and tan δ in **Figure SC.6** and **SC.7** at pages 273-274, situating both systems containing CNC in the area delimited by the literature for systems presenting good shape fidelity.

The structure recovery capacity of the inks was tested in order to analyse the capacity of the inks of recovering their initial viscosity after a high shear rate appliance, which can be correlated with the printing performance where high shear rates are applied during the

extrusion. As happened in Chapter 4, all systems presented a rapid and reversible viscosity response making this inks suitable for 3D-printing as they could be easily extruded out while rapidly recovered enough mechanical strength necessary to support the next extruded layer [22]. The recovery curves are shown at **Figure 6.10** whereas recovery values are displayed in **Table 6.5**.

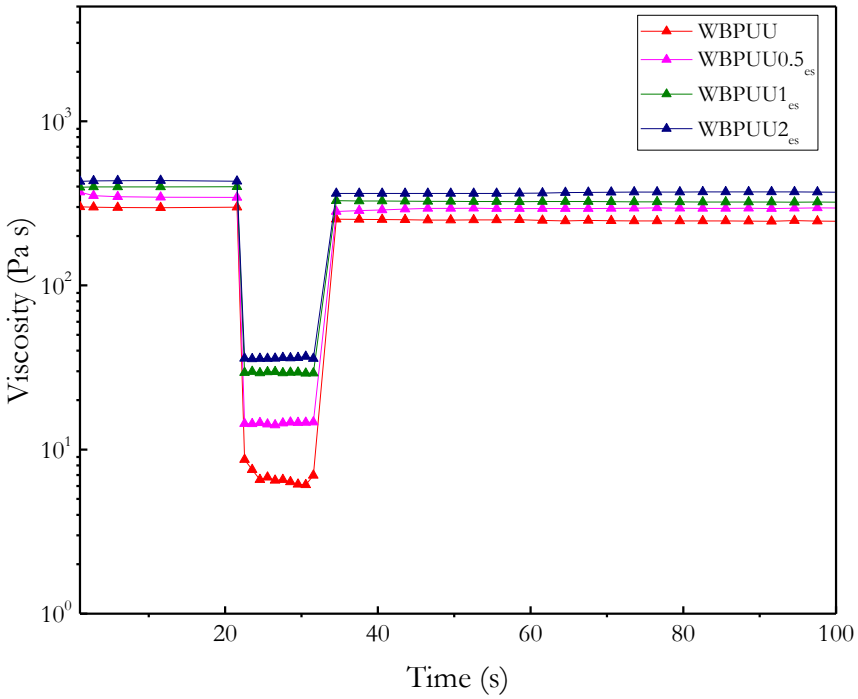

Figure 6.10 Structure recovery test of WBPUU and WBPUU/CNC_{es} nanocomposites as a function of time (T = 22.5 °C)

The results showed similar values of recovery for both matrix and nanocomposites, obtaining values above 80% for all system, which is recommendable for 3D-printing applications according to the literature [23]. The comparison of the recovery values of *in situ* and *ex situ* method as a function of the CNC content are represented in **Figure SB.7** at page 266 for comparative purposes. Comparing the structure recovery results obtained from both *in situ* and *ex situ* methods, the recovery capacity is different depending the CNC content, presenting at lower CNC contents a better recovery for *in situ* method. Contrary, at higher CNC content, systems prepared by *ex situ* method presented better recovery values, observing an inversion of the behaviour at 1 wt% of CNC.

The variation of the previously studied rheological parameters as a function of the *ex situ* added CNC content is displayed in **Figure 6.11**

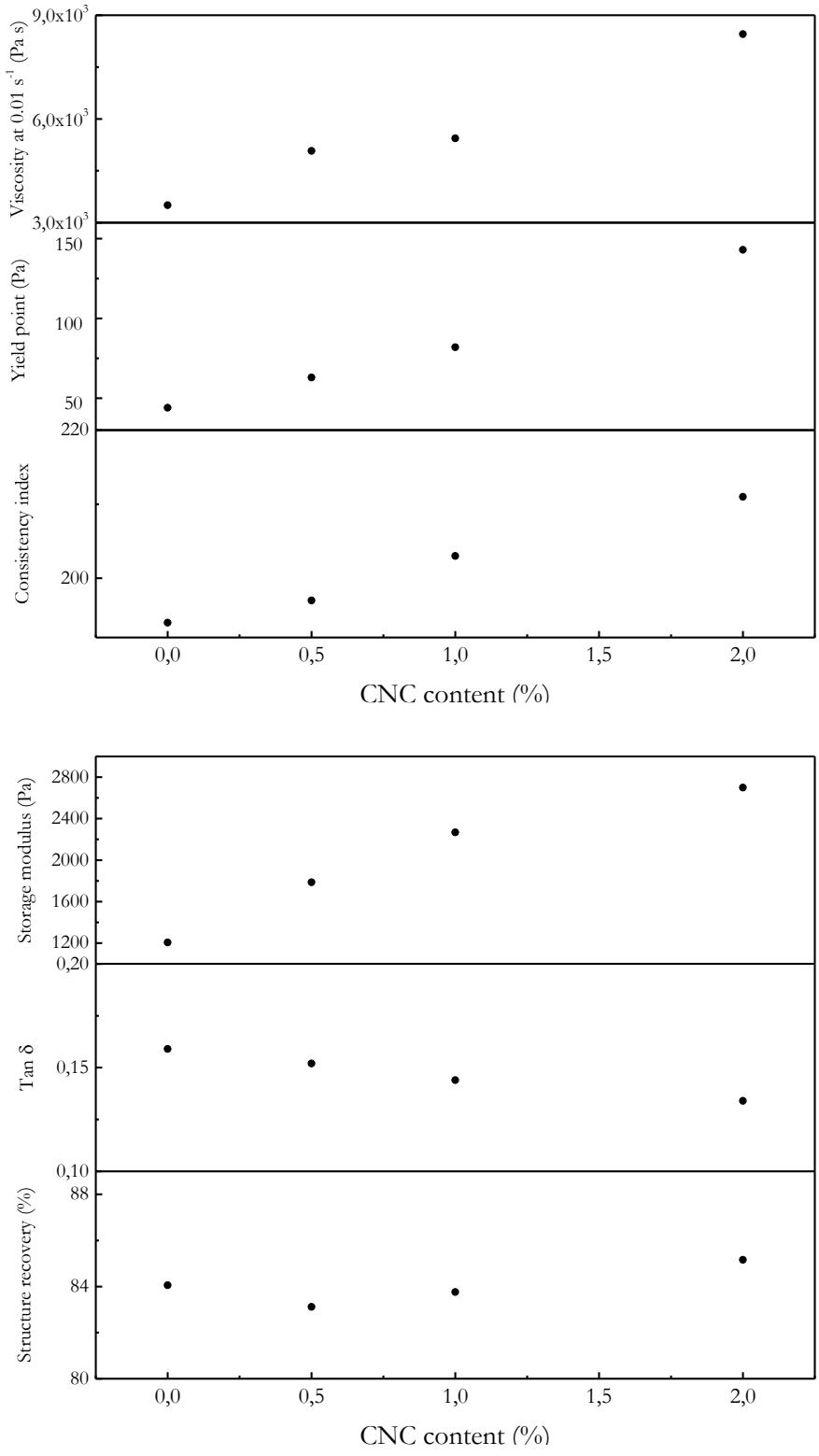

Figure 6.11 Variation of the studied rheological parameters with the addition of CNC *ex situ* related to the printability (up) and to the shape fidelity (down)

Observing the evolution of the parameters related to the printability of the inks, the addition of CNC by *ex situ* method resulted in an increase of all parameters. However, in this case, the *ex situ* prepared inks presented a lower increase of the viscosity, yield point and consistency index compared with the prepared ones via *in situ*, as can be observed in **Figures SB.1-SB.4** at Appendix B (pages 260-263). This lower modification of these parameters suggest a successful extrusion of all inks prepared via *ex situ* (until a 2 wt% of CNC content), in opposition to the *in situ* prepared inks that presented extrusion problems for systems containing CNC contents above 0.5 wt%. Regarding the parameters linked to the shape fidelity, the addition of CNC by *ex situ* method increased the storage modulus and decreased the tan δ maintaining the structure recovery in similar values for all CNC added quantities. This results illustrated the increase of the structuration of the inks, swiping from a viscous dispersion towards more elastic inks, which are able to maintain successfully the given 3D construct and to support the weight of the uppers layers of the multi-layered construct without collapsing.

6.3.4 DIW 3D-printing of inks with different ex situ CNC contents

Finally, the different *ex situ* prepared nanocomposites have been printed by DIW 3D-printing in order to confirm the result observed in the rheological analysis. The digital images of the different printed pieces are displayed in **Figure 6.12**. Regarding the printability, all prepared systems were successfully printed. The lower viscosity and yield point values compared with the *in situ* systems allowed to process inks with higher CNC content. Indeed, the ink containing 2 wt% of CNC_{es} was successfully printed in contrast with WBPUU/CNC_{is} inks were only up to a 0.5 wt% of reinforcement resulted in printable systems. Conversely, as far as shape fidelity is concerned, the lower variation of storage modulus compared with the matrix observed in *ex situ* method resulted in less structured inks compared with the ones obtained by *in situ* methods, which resulted in a worse shape fidelity even having similar values of tan δ. In this case, the lower observed yield point values compared with the ones obtained in Chapter 5 for the *in situ* addition of CNC leads to a lower capacity to retain the given shape. This decrease of the shape fidelity resulted in printed pieces which collapse owing its own weight leading to the ink spreading and hence, to the loose of the given 3D form. As happened for the *in situ* addition of CNC, the increase of the CNC content resulted in printed pieces which better shape fidelity presenting a better appearance after being printed. Nevertheless, the good printability observed in $WBPUU2_{es}$ suggests the possibility

to increase more the CNC content to enhance more the shape fidelity without compromising the extrudability of the ink.

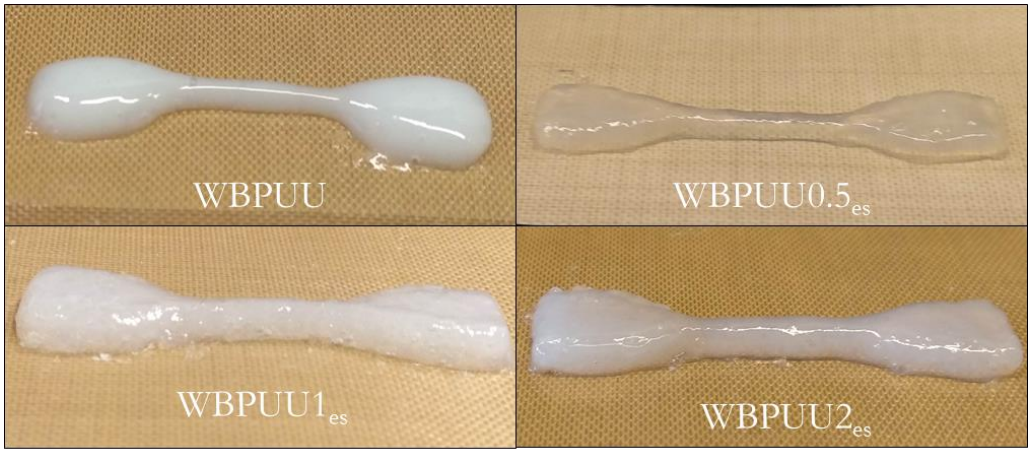

Figure 6.12 Printed pieces from WBPUU and WBPUU/CNC_{es} nanocomposites

6.3.5 Mechanical and thermomechanical characterization of printed pieces

The influence of the CNC on the mechanical properties of the WBPUU has been studied by testing printed strips from the different prepared samples. The results, which are displayed in **Table 6.6** showed the Young modulus, strain at break and stress at break and of different prepared systems.

Analysing the obtained results, an increase of the Young modulus was observed as the CNC content did, resulting also in an increase of the stress at break. This behaviour is related with the effective CNC reinforcement effect which results in stiffer pieces [24]. As a result of this reinforcement, the WBPUU/CNC_{es} nanocomposites showed decreasing strain at break as the CNC content increases, owing to the restrictions of the WBPUU chains mobility due to the CNC addition [25]. Comparing these values with the observed ones for similar *ex situ* systems in the literature, lower increases of Young modulus are observed compared with the ones measured in this work but a higher decrease of strain at break as well [1,2]. However, this increase of the stiffness of the pieces result lower compared with the one observed in Chapter 5 for WBPUU/CNC_{is} system. In this case the increase of the Young modulus for $WBPUU2_{es}$ resulted much lower compared to the 0.5 wt% of CNC reinforcement done by *in situ* method, confirming that the different addition methods resulted in different arrangements between WBPUU and CNC which leads to different mechanical properties of the printed pieces.

Table 6.6 Mechanical properties of WBPUU and WBPUU/CNC_{es} nanocomposites

System	Young modulus (MPa)	Strain at break (%)	Stress at break (MPa)
WBPUU	18±2	1036±34	9±1
WBPUU0.5$_{es}$	30±3	827±64	10±3
WBPUU1$_{es}$	41±3	747±38	12±3
WBPUU2$_{es}$	55±2	672±39	13±2

Finally, the thermomechanical stability of the printed WBPUU and WBPUU/CNC_{es} based inks has been studied by DMA. The evolution of the storage modulus and tan δ as a function of the temperature is displayed in **Figure 6.13**. An increase of the E' in all the temperature range as the CNC content of the composites increased was noticed, confirming the successful reinforcement of the WBPUU ink by the nanoentities [26]. In the glassy state, at low temperatures, the properties of the polyurethane systems are ruled by the soft phase showing a slight but constant decrease of the E' where the molecular motions were largely restricted to vibration and short range rotation. In this case the WBPUU2$_{es}$ presented an increase of the E' of around 10% compared with the WBPUU matrix. At higher temperatures, a decrease of the storage modulus was observed in all systems, presented also as a maximum peak in the tan δ value. This sweep represented the main relaxation process of the soft phase in both WBPUU and WBPUU/CNC_{es} nanocomposites, associated to the glass transition of the soft segment. The tan δ showed a maximum peak at -48 ºC in the case of the WBPUU matrix, representing the glass transition temperature (T_g), whereas the WBPUU/CNC_{es} nanocomposites presented a maximum at the same temperature but showing a smaller peak. The addition of CNC in this case leads to a limitation of the mobility of the amorphous macromolecular chains which are close of the reinforcement, as was suggested by other authors [27–29], resulting in the aforementioned reduction and widening of the peak of tan δ assigned to the T_g due to the lower quantity of free polymer chains.

Above the T_g, the storage modulus kept decreasing upon temperature in all systems, presenting the WBPUU matrix a lower E' compared with the WBPUU/CNC_{es} nanocomposites at room temperature, which showed higher storage modulus as the CNC content increased. This behaviour confirms the successful reinforcement of the CNC to the

matrix, where the presence of the cellulosic reinforcement provokes interactions between the filler and the matrix, hampering the molecular mobility and thus promoting the rigidity of the nanocomposite. Regarding the thermomechanical stability, the systems containing *ex situ* added CNC presented higher thermomechanical stability compared with the WBPUU matrix as a result of the successful addition of the CNC as was also observed by FTIR, TGA and mechanical properties results.

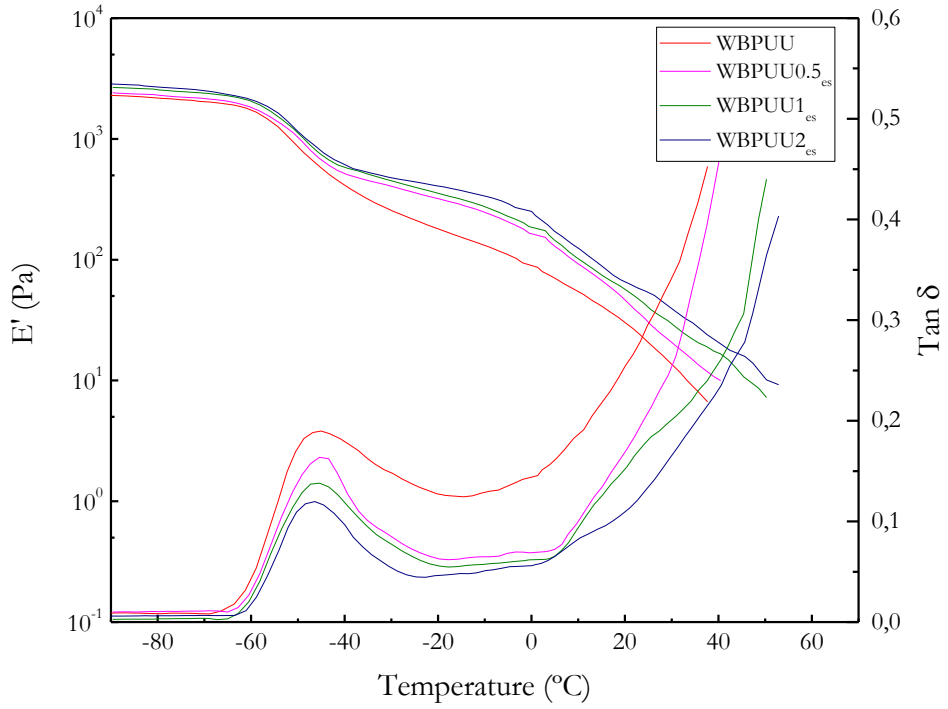

Figure 6.13 Storage modulus and tan δ as a function of temperature for WBPUU and WBPUU/CNC_{es} nanocomposites. Frequency = 1 Hz and scanning rate = 2 °C min^{-1}

Comparing the aforementioned results with the ones obtained by *in situ* reinforcement in Chapter 5, a slightly lower E' values are observed in *ex situ* systems. The weaker physical interactions produced by this addition method compared with the chemical bonding produced by the *in situ* incorporation of CNC, resulted in nanocomposites presenting lower thermomechanical stability and lower E' values in all the temperature range. Indeed, $WBPUU2_{es}$ presented lower E' values and lower thermomechanical stability compared with $WBPUU0.5_{is}$, which had much lower amount of CNC reinforcement.

6.4 Conclusions

In this chapter, a series of WBPUU/CNC_{es} nanocomposite based inks were prepared by mixing a previously synthesized PCL/PEG based waterborne polyurethane urea dispersion and cellulose nanocrystals by means of mechanical stirring. So as to study the influence of the added nanoentities in the printing performance of the inks, the prepared nanocomposites were studied from the rheological viewpoint and subsequently printed by DIW 3D-printing so as to confirm their viability for this technology. Additionally, the interaction mechanism between the WBPUU particles and the CNC reinforcement was studied as well as the thermal, mechanical and thermomechanical properties of the printed WBPUU/CNC_{es} pieces.

Regarding the interactions between the WBPUU and the CNC, the TEM images revealed that, contrary to what observed in the Chapter 5 for the *in situ* addition of CNC, the *ex situ* addition of the CNC did not resulted in a chemical interaction between the particles and the reinforcement, but forming a physical interaction which resulted in the modification of rheological properties of the ink, but also of the mechanical, thermal and thermomechanical properties of the printed piece.

The rheological analysis of the inks showed a similar tendency as was observed in Chapter 5, that is, showing an increase of the viscosity, yield point and storage modulus and a decrease of the tan δ as the CNC content of the inks increased. This results illustrates the obtaining of inks with better shape fidelity as the CNC content of the ink increased, being able to support 3D multi-layered constructs without collapsing. Despite the addition of CNC also lead to the apparition of limitations of the printability, presenting systems with very high viscosity, yield points and storage modulus problems to be extruded successfully through such a thin nozzle, in this case all systems were successfully printed, presenting all a continuous and homogeneous thread.

Comparing these rheological parameters with the ones observed in Chapter 5 for *in situ* addition of CNC, the post-synthesis addition of CNC resulted in a slighter modification of the aforementioned parameters, presenting a lower increase of both viscosity, yield point and storage modulus as can be observed in **Figures SB.1-SB.7** (pages 260-266 Appendix B). This lower influence in the rheological properties allowed to load more amount of CNC into the ink than the *in situ* method. However, in order to obtain similar rheological properties higher amount of CNC added *ex situ* is needed so as to reach a similar behaviour. In fact,

WBPUU2$_{es}$ presented lower rheological parameters compared with WBPUU0.5$_{is}$, presenting the *ex situ* system a worse printing performance than the *in situ* one.

Finally, regarding the study of the WBPUU/CNC$_{es}$ printed pieces, the displacement of the carbonyl band towards lower wavenumbers observed at the FTIR spectra, illustrates the hydrogen bonding interactions between WBPUU and CNC. The addition of the cellulosic reinforcement resulted in an increase of the thermal and thermomechanical stability, as well as in the obtaining of stiffer printed pieces with higher Young modulus and lower strain at breaks, confirming the successful reinforcement of the CNC. However, as happened with the rheology, this increase is slighter compared with the one observed for *in situ* addition of CNC. The different interaction between WBPUU and CNC of both methods leads to the obtaining of different types of materials as well as to the obtaining of different printing performances.

6.5 References

[1] R. Chen, C. Huang, S. Hsu, Composites of waterborne polyurethane and cellulose nanofibers for 3D printing and bioapplications, Carbohydr. Polym. 212 (2019) 75–88. https://doi.org/10.1016/j.carbpol.2019.02.025.

[2] A. Santamaria-Echart, L. Ugarte, A. Arbelaiz, N. Gabilondo, M.A. Corcuera, A. Eceiza, Two different incorporation routes of cellulose nanocrystals in waterborne polyurethane nanocomposites, Eur. Polym. J. 76 (2016) 99–109. https://doi.org/10.1016/j.eurpolymj.2016.01.035.

[3] Y. Liu, Y. Yu, C. Liu, J.M. Regenstein, X. Liu, P. Zhou, Rheological and mechanical behavior of milk protein composite gel for extrusion-based 3D food printing, LWT - Food Sci. Technol. 102 (2019) 338–346. https://doi.org/10.1016/j.lwt.2018.12.053.

[4] G. Zhang, D. Carloni, Y. Wu, 3D printing of transparent YAG ceramics using copolymer-assisted slurry, Ceram. Int. 46 (2020) 17130–17134. https://doi.org/10.1016/j.ceramint.2020.03.247.

[5] E. Courtial, C. Perrinet, A. Colly, D. Mariot, J.-M. Frances, R. Fulchiron, C. Marquette, Silicone rheological behavior modification for 3D printing: Evaluation of yield stress impact on printed object properties, Addit. Manuf. 28 (2019) 50–57. https://doi.org/10.1016/j.addma.2019.04.006.

[6] S. Shin, H. Kwak, J. Hyun, Transparent cellulose nanofiber based open cell culture platform using matrix-assisted 3D printing, Carbohydr. Polym. 225 (2019) 115235. https://doi.org/10.1016/j.carbpol.2019.115235.

[7] J. Zhang, B.J. Allardyce, R. Rajkhowa, S. Kalita, R.J. Dilley, X. Wang, X. Liu, Silk particles, microfibres and nanofibres: A comparative study of their functions in 3D printing hydrogel scaffolds, Mater. Sci. Eng. C. 103 (2019). https://doi.org/10.1016/j.msec.2019.109784.

[8] M. Lille, A. Nurmela, E. Nordlund, S. Metsa-Kortelainen, N. Sozer, Applicability of protein and fiber-rich food materials in extrusion-based 3D printing, J. Food Eng. 220 (2018) 20–27. https://doi.org/10.1016/j.jfoodeng.2017.04.034.

[9] Z. Liu, M. Zhang, B. Bhandari, C. Yang, Impact of rheological properties of mashed potatoes on 3D printing, J. Food Eng. 220 (2017) 76–82. https://doi.org/10.1016/j.jfoodeng.2017.04.017.

[10] C.A. Hamilton, G. Alici, M. Panhuis, 3D printing Vegemite and marmite: redefining "breadboards," J. Food Eng. 220 (2017) 83–88. https://doi.org/10.1016/j.jfoodeng.2017.01.008.

[11] Y. Yang, X. Wang, X. Lin, L. Xie, R. Ivone, J. Shen, A tunable extruded 3D printing platform using thermo-sensitive pastes, Int. J. Pharm. 583 (2020) 119360. https://doi.org/10.1016/j.ijpharm.2020.119360.

[12] S. Mantihal, S. Prakash, F.C. Godoi, B. Bhandari, Effect of additives on thermal, rheological and tribological properties of 3D printed dark chocolate, Food Res. Int. 119 (2019) 161–169. https://doi.org/10.1016/j.foodres.2019.01.056.

[13] Y. Jiang, J.A. De La, L. Ding, B. Wang, X. Feng, Z. Mao, H. Xu, X. Sui, Rheology of regenerated cellulose suspension and influence of sodium alginate, Int. J. Biol. Macromol. 148 (2020) 811–816. https://doi.org/10.1016/j.ijbiomac.2020.01.172.

[14] Y. Liu, D. Liu, G. Wei, Y. Ma, B. Bhandari, P. Zhou, 3D printed milk protein food simulant: Improving the printing performance of milk protein concentration by incorporating whey protein isolate, Innov. Food Sci. Emerg. Technol. 49 (2018) 116–126. https://doi.org/10.1016/j.ifset.2018.07.018.

[15] K. Hyun, S.H. Kim, K.H. Ahn, S.J. Lee, Large amplitude oscillatory shear as a way to classify the complex fluids, J. Nonnewton. Fluid Mech. 107 (2002) 51–65.

https://doi.org/10.1016/S0377-0257(02)00141-6.

[16] F. Yang, M. Zhang, B. Bhandari, Y. Liu, Investigation on lemon juice gel as food material for 3D printing and optimization of printing parameters, LWT - Food Sci. Technol. 87 (2018) 67–76. https://doi.org/10.1016/j.lwt.2017.08.054.

[17] S.M. Park, H.W. Kim, H.J. Park, Callus-based 3D printing for food exemplified with carrot tissues and its potential for innovative food production, J. Food Eng. 271 (2020) 109781. https://doi.org/10.1016/j.jfoodeng.2019.109781.

[18] J.J. Nijdam, D. Lecorre-bordes, A. Delvart, B.S. Schon, A rheological test to assess the ability of food inks to form dimensionally stable 3D food structures, J. Food Eng. 291 (2021) 110235. https://doi.org/10.1016/j.jfoodeng.2020.110235.

[19] L. Liu, O.N. Ciftci, Effects of high oil compositions and printing parameters on food paste properties and printability in a 3D printing food processing model, J. Food Eng. 288 (2021) 110135. https://doi.org/10.1016/j.jfoodeng.2020.110135.

[20] I.M. Cotabarren, S. Cruces, C.A. Palla, Extrusion 3D printing of nutraceutical oral dosage forms formulated with monoglycerides oleogels and phytosterols mixtures, Food Res. Int. 126 (2019) 108676. https://doi.org/10.1016/j.foodres.2019.108676.

[21] A. Vicente, P. Fuci, S.M. Oliveira, L.H. Fasolin, Printability , microstructure , and flow dynamics of phase-separated edible 3D inks, Food Hydrocoll. 109 (2020) 106120. https://doi.org/10.1016/j.foodhyd.2020.106120.

[22] Z. Liu, B. Bhandari, S. Prakash, S. Mantihal, M. Zhang, Linking rheology and printability of a multicomponent gel system of carrageenan-xanthan-starch in extrusion based additive manufacturing, Food Hydrocoll. 87 (2019) 413–424. https://doi.org/10.1016/j.foodhyd.2018.08.026.

[23] C.W. Peak, J. Stein, K.A. Gold, A.K. Gaharwar, Nanoengineered colloidal inks for 3D bioprinting, Langmuir 34 (3) (2017) 917–925. https://doi.org/10.1021/acs.langmuir.7b02540.

[24] X. Cao, H. Dong, C.M. Li, New nanocomposite materials reinforced with flax cellulose nanocrystals in waterborne polyurethane, Biomacromolecules 8 (2007) 899–904. https://doi.org/https://doi.org/10.1021/bm0610368.

[25] H. Liu, S. Cui, S. Shang, D. Wang, J. Song, Properties of rosin-based waterborne

polyurethanes/cellulose nanocrystals composites, Carbohydr. Polym. 96 (2013) 510–515. https://doi.org/10.1016/j.carbpol.2013.04.010.

[26] L. Rueda, A. Saralegui, B. Fernández, Q. Zhou, L.A. Berglund, M.A. Corcuera, I. Mondragon, A. Eceiza, Cellulose nanocrystals/polyurethane nanocomposites. Study from the viewpoint of microphase separated structure, Carbohydr. Polym. 92 (2013) 751–757. https://doi.org/10.1016/j.carbpol.2012.09.093.

[27] L.A. Berglund, Natural fibers, biopolymers and biocomposites, CRC Press, Boca Ratón, 2005.

[28] L. Chazeau, M. Paillet, J.Y. Cavaille, Plasticized PVC reinforced with cellulose whiskers. I. Linear viscoelastic behavior analyzed through the quasi-point defect theory, J. Poymer Sci. Part B Polym. Phys. 37 (1999) 2151–2164. https://doi.org/10.1002/(SICI)1099-0488(19990815)37:16<2151::AID-POLB17>3.0.CO;2-V

[29] A. Dufresne, Dynamic mechanical analysis of the interphase in bacterial polyester / cellulose whiskers natural composites, Compos. Interfaces 7 (2000) 53–67. https://doi.org/10.1163/156855400300183588

CHAPTER 7

APPLICATIONS OF THE PRINTED PIECES FROM PCL/PEG BASED WBPUU INKS VIA DIW 3D-PRINTING

7. APPLICATIONS OF THE PRINTED PIECES FROM PCL/PEG BASED WBPUU INKS VIA DIW 3D-PRINTING

7.1 Objective

In this chapter, two potential applications of the aforementioned PCL/PEG based WBPUU inks were proposed and studied in order to demonstrate their viability. By one hand, the preparation of WBPUU/CNC_{is} scaffolds so as to absorb cationic dyes such as methylene blue, and the second one, the synthesis of WBPUU containing plant extract based inks in order to obtain 3D constructs with antibacterial properties.

In a first part, scaffolds based on *in situ* WBPUU/CNC nanocomposites were prepared by the freeze drying technique of the printed pieces. As a result of this process, shape customized scaffolds were obtained with high porosity. In this context, the prepared scaffolds were studied as a potential substrate for absorption of cationic dyes. As was mentioned before, the use of polyurethane based scaffolds for water waste removal has been extensively studied in the literature. The capacity of this scaffolds to absorb heavy metals such as copper [1], lead, or different types of oils represents a cheap alternative compared to more expensive treatments. Nevertheless, one of the principal contamination sources that affects to the water is that of the dyes. Since the invention of the picric acid in 1771, which produced a bright yellow on silk, synthetic dyes represented one of the mayor issues as far as water treatment is concerned, with a production of over 10^5 different dyes with an annual production of over $7x10^5$ metric tons [2]. Their toxicity may give rise to eyes and skin irritation, weakness and dizziness, becoming an important issue for the human being [3].

In the literature, the use of polyurethane scaffolds has been extensively studied as sorption materials for dye absorption due to its advantages in terms of cost, flexibility, simplicity, ease and insensitivity to toxic pollutants compared with other techniques [4,5]. Polyurethanes

have been proved to be a successful remover of many synthetic dyes such as methylene blue [6,7], brilliant green [8,9], indigo carmine [10] or congo red [11] among others. Despite some works use the polyurethane scaffolds without any charged additive, obtaining good removal percentages [12], most of the works explored the use of an active substance, which is also known as "carrier" charged in opposition of the dye, to promote a ionic crosslinking between the anionic or cationic dye and the anionic or cationic carrier. A wide variety of "carriers" have been used in the literature for facilitating the removal of the dyes. *Baldez et al.* promote the absorption of cationic rhodamina B in a polyurethane by the inclusion of anionic sodium dodecysulfate [13], *Moraes et al.*, contrary, use chemically modified and unmodified cellulose in a polyurethane foam so as to absorb methylene blue and procion red HE-7B. In this last case, the addition of the modified and unmodified cellulose increased the absorption capacity of procion red HE-7B but did not modify the one corresponding to the methylene blue [6].

The absorption capacity of the prepared WBPUU/CNC_{is} nanocomposite scaffolds prepared by DIW 3D-printing and freeze drying was tested against cationic methylene blue (MB). MB is a cationic dye, which is used commonly for colouring paper and temporary hair colorant, and despite not strongly hazardous, it can cause some harmful effects, such as heartbeat increase, vomiting, shock, cyanosis, jaundice, quadriplegia, and tissue necrosis in humans, so its removal is of the major importance so as to avoid the contamination of the water with this pollutant [14]. It is expected that the anionic groups presented in the polymer backbone as a result of the addition of DMPA during the synthesis interacted with the cationic ones of the MB blue, leading to a successful removal of the dye. According to these elements, the synthesis and printing of a series of WBPUU/CNC_{is} nanocomposite based inks with different CNC content is proposed. Additionally, a number of the printed systems were immersed in a $CaCl_2$ dispersion of 1 M prior to the freeze drying process so as to promote a chemical crosslinking between the WBPUU and the Ca^{2+} ions, which will result in the formation of more rigid scaffolds.

In respect of the experimental method used in the present work, the prepared scaffolds have been analysed physicochemicallly, morphologically, and mechanically in order to study the influence of both CNC and the Ca^{2+} crosslinking. It is expected that the addition of the CNC to the ink will improve the shape fidelity of the printed samples, as was already observed in Chapter 5, as well as modify the morphology of the scaffold and increase their swelling capacity. The ionic crosslinking of WBPUU through Ca^{2+}, contrary, will result in a modification of the morphology of the printed scaffolds, leading to more rigid pieces as was observed by other authors [15]. Finally, the absorption capacity of the system which

presented the more interesting properties for the application has been tested against MB in order to study its viability as cationic dye absorption material.

In the second part of this chapter, the viability of a WBPUU/plant extract based system was analysed as a potential printable ink with antibacterial properties. As has been mentioned in the introduction, some plant extracts presented antibacterial, antimicrobial and anti-inflammatory properties as a result of the biologically active compounds [16,17]. In this context, the incorporation of plant extracts into waterborne polyurethane dispersions has been successfully performed in the literature, leading to the obtaining of WBPUU/plant extract films prepared from the dispersions, which presented antimicrobial activity [18].

In this sense, for this work *Salvia officinalis L.*, commonly known as sage has been selected as the bioactive plant extract. This extract has been obtained by infusion method and added by *in situ* method previously dispersed in deionized water during the phase inversion step, so as to obtain WBPUU/*Salvia* dispersions. In order to guarantee a good printing performance, different amounts of CNC were added by *ex situ* method with the aim to obtain printed pieces with good shape fidelity. The printed pieces were dried and freeze dried in order to obtain solid pieces and scaffolds respectively. The different prepared WBPUU/*Salvia*/CNC_{es} inks were studied from the rheological viewpoint with the aim to analyse the influence of the *Salvia* extract in the WBPUU and WBPUU/CNC_{es} inks. Finally, the prepared pieces were tested against some bacterial agents to demonstrate their viability as antibacterial materials.

7.2 WBPUU/CNC_{is} scaffolds for cationic dye absorption

7.2.1 Experimental part

7.2.1.1 Materials

The selected inks for the preparation of the scaffolds are the WBPUU/CNC_{is} nanocomposites synthesized in Chapter 5. The selection was made according to their good balance between printing performance and shape fidelity. WBPUU/CNC_{is} inks with 0.25 and 0.5 wt% of CNC were employed. WBPUU matrix was used for comparative purpose.

7.2.1.2 DIW 3D-printing of the inks and scaffold preparation by freeze drying

WBUU and WBPUU/CNC_{is} based inks were printed as cylinders of 12 mm of diameter and 5 mm of height by extrusion based 3D-printing using the DIW 3D-printing equipment displayed in Chapter 2. Regarding the printing conditions, the samples were printed following the conditions used in previous chapters. Prior to the freeze drying process, some of the

printed samples were immerse in a $CaCl_2$ solution of 0.1 M during 30 or 60 minutes in order to crosslink the printed piece. The systems were washed in deionized water so as to remove the remaining unreacted $CaCl_2$ from the piece prior to the freeze drying process. Finally, all samples were freeze dried at -60ºC and 0.1 Pa during 48 h. The characteristic, composition and preparation process of all prepared scaffolds are enlisted in **Table 7.1**. Additionally, an illustration of the preparation process of the shape customized scaffolds is displayed in **Figure 7.1.**

Table 7.1 Preparation conditions, denomination and density of the prepared WBPUU scaffolds

System	Time in $CaCl_2$ (min)	Density (g cm^{-3})
WBPUU	-	0.225±0.014
WBPUU0.25$_{is}$	-	0.414±0.003
WBPUU0.5$_{is}$	-	0.424±0.003
WBPUU30Ca	30	0.256±0.043
WBPUU60Ca	60	0.303±0.012
WBPUU30Ca0.25$_{is}$	30	0.484±0.010
WBPUU60Ca0.25$_{is}$	60	0.491±0.040
WBPUU30Ca0.5$_{is}$	30	0.525±0.010
WBPUU60Ca0.5$_{is}$	60	0.537±0.007

Figure 7.1 Process of preparation of WBPUU0.5$_{is}$ based shape customized scaffold. From left to the right: a) CAD design, b) printed piece and c) final piece after freeze drying process

The different prepared systems are denoted as WBPUUX$_{is}$, where X is the CNC content. Additionally, systems which where immersed in $CaCl_2$ are enlisted as WBPUUYCa or

WBPUUYCaX$_{is}$, where Y represented the immersion time of the printed piece into the $CaCl_2$ solution and X the CNC content. Regarding the measured densities of the prepared scaffolds which are displayed also in **Table 7.1**, systems containing CNC presented higher densities as the CNC content increased, due to the increase of the total concentration of the ink (WBPUU+CNC). Systems immersed in $CaCl_2$ presented even higher densities due to the shrinkage of the piece due to the formed shell at the surface of the piece as well as the loaded Ca^{2+} ions. The calculated density resulted to be higher as the immersion time in $CaCl_2$ was.

As the result of the aforementioned procedure, scaffolds with the form of cylinders were obtained with good reproducibility of the 3D design. However, samples which were previously immersed in $CaCl_2$ before the freeze drying procedure presented a loss of definition due to the aforementioned shrinkage of the piece compared with the ones which were not exposed to $CaCl_2$. The former presented as a result a rigid shell surrounding the core of the scaffold, which is able to support up to 50 g of weight prior to the freeze drying process, and is formed due to the chemical crosslink produced between the COO^- of WBPUU particles and the Ca^{2+}. In the **Figure 7.2**, images of prepared WBPUU, WBPUU0.5$_{is}$ and WBPUU30Ca0.5$_{is}$ scaffolds are displayed. Additionally, the capacity of the shell produced by Ca^{2+} crosslinking to support weight prior to the freeze drying process is illustrated for WBPUU30Ca0.5$_{is}$ system.

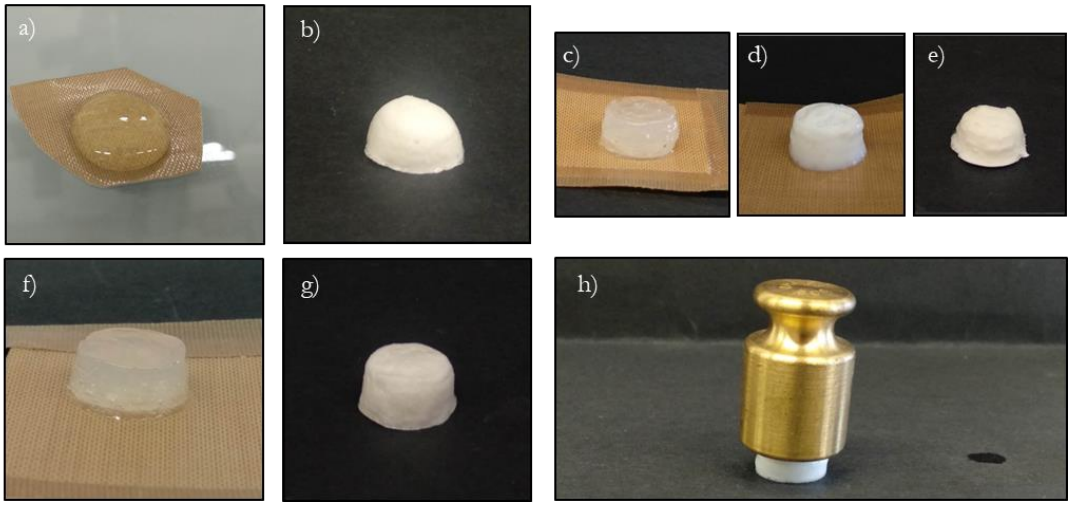

Figure 7.2 Images of the preparation of the scaffolds: a) printed piece and b) freeze dried sample from WBPUU ink, c) printed piece, d) post crosslinked sample and e) freeze dried sample from WBPUU30Ca0.5$_{is}$, f) printed piece and g) freeze dried sample from WBPUU0.5$_{is}$ and h) consistency of the Ca^{2+} shell on the printed piece prior to freeze drying (WBPUU30Ca0.5$_{is}$) supporting a load of 50g

In **Figure 7.3** a scheme of the crosslinking of the WBPUU particles and WBPUU/CNC_{is} system with the $CaCl_2$ is displayed.

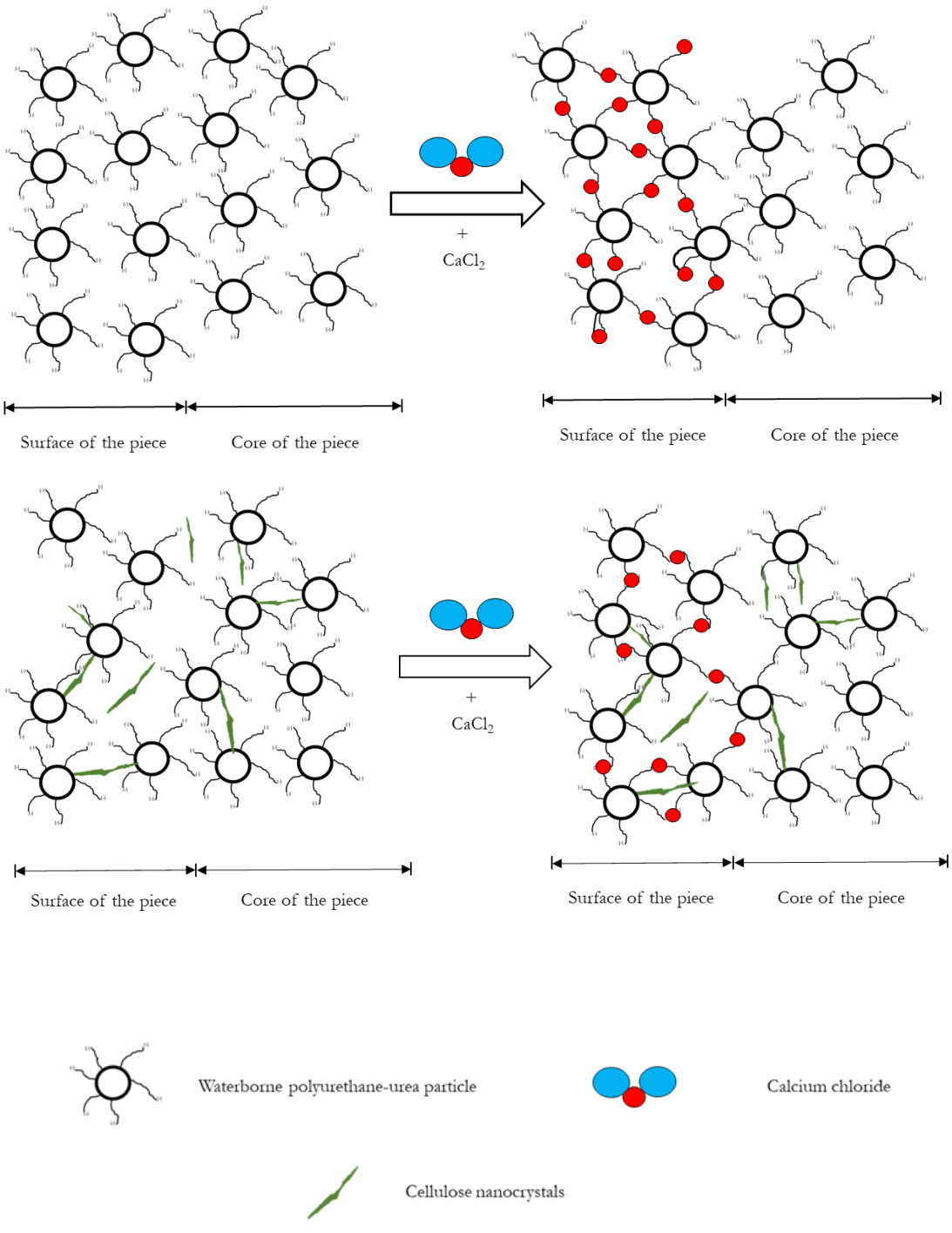

Figure 7.3 Crosslinking process of the WBPUU pieces immersed in $CaCl_2$ (up) and WBPUU/CNC_{is} pieces immersed in $CaCl_2$ (down)

As was mentioned before, the chemical crosslinking of WBPUU through Ca^{2+} is produced when the samples are immersed into $CaCl_2$ by the ionic interaction of the COO^- groups of the WBPUU particles and the Ca^{2+} ions of the $CaCl_2$. This interaction is produced in the surface of the printed piece and resulted in the formation of a rigid shell surrounding a non-crosslinked core. This shell presented high consistency, and as was observed in **Figure 7.2 h)** is able to support weight without collapsing prior to the freeze drying process.

7.2.2 Results and discussions

7.2.2.1 Influence of the $CaCl_2$ immersion time of the WBPUU based inks

The crosslinking process magnitude of the sample immersed in $CaCl_2$ solution was tested by performing a viscosity test at a fixed shear rate of 1 s^{-1} during 180 s to a WBPUU ink prior and after the immersion, in order to study the influence of the aforementioned crosslinking procedure in the structure of the inks. The results are displayed in **Figure 7.4**.

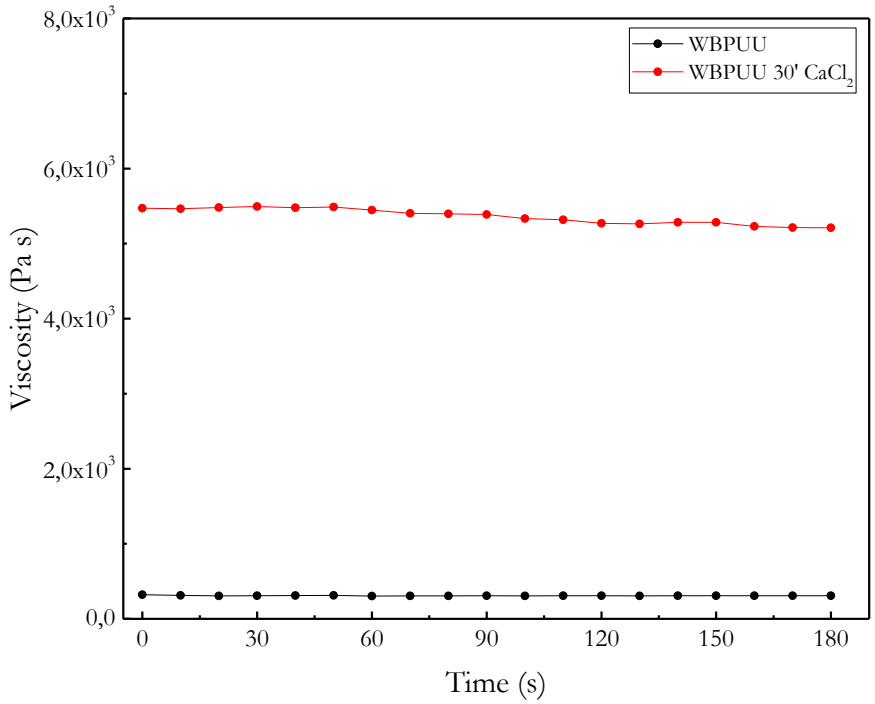

Figure 7.4 Viscosity as a function of time at a shear rate of 1 s^{-1} for WBPUU before (black) and after the immersion in $CaCl_2$ (red)

The results showed a clear increase of the viscosity of the crosslinked system, presenting a constant viscosity value of ~300 Pa s for the not crosslinked WBPUU ink in contrast with

the ~5200 Pa s of the ink immersed in $CaCl_2$. The crosslinking process produced between the Ca^{2+} and the COO^- groups of the WBPUU particles resulted in an increase of the viscosity as a result of the ionic network.

Moreover, oscillatory measurements were also performed in order to study the influence of the Ca^{2+} crosslinking in the structuration of the inks. The storage and loss moduli of both crosslinked and non-crosslinked WBPUUs as a function of the time are shown in **Figure 7.5.** The crosslinking with Ca^{2+} resulted in an increase of both storage and loss moduli, compared with the non-crosslinked system. The systems studied after the crosslinking process presented at 1 Hz an increase of 1897% and a 1360% of storage and loss moduli respectively. Additionally, the tan δ of the systems tested after the immersion in $CaCl_2$ solution presented lower values compared with the ones observed for the non-crosslinked WBPUU. This sweep towards lower values of tan δ illustrates the transition between an initially viscous behaviour of the non-crosslinked WBPUU and the more elastic behaviour observed in the WBPUU after the immersion in $CaCl_2$.

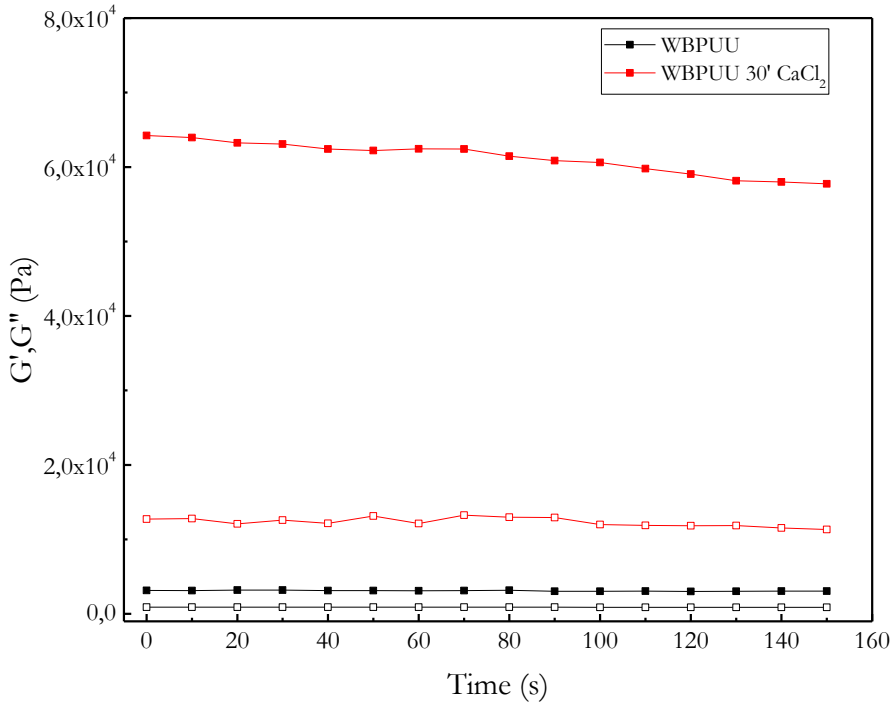

Figure 7.5 Storage (■) and loss (□) moduli as a function of time at 1 Hz of the WBPUU before (black) or after immersion in $CaCl_2$ (red)

7.2.2.2 Characterization of the WBPUU/CNC$_{is}$ prepared scaffolds

In order to study the morphology of the prepared scaffolds, electron scanning microscopy was used so as to obtain images of the structure of the printed scaffolds. The images of the obtained cross section images of the scaffolds with different CNC content are displayed in **Figure 7.6** whereas in **Figure 7.7** the corresponding ones to the WBPUU/CNC$_{is}$ scaffolds presenting different immersion times in $CaCl_2$ are displayed.

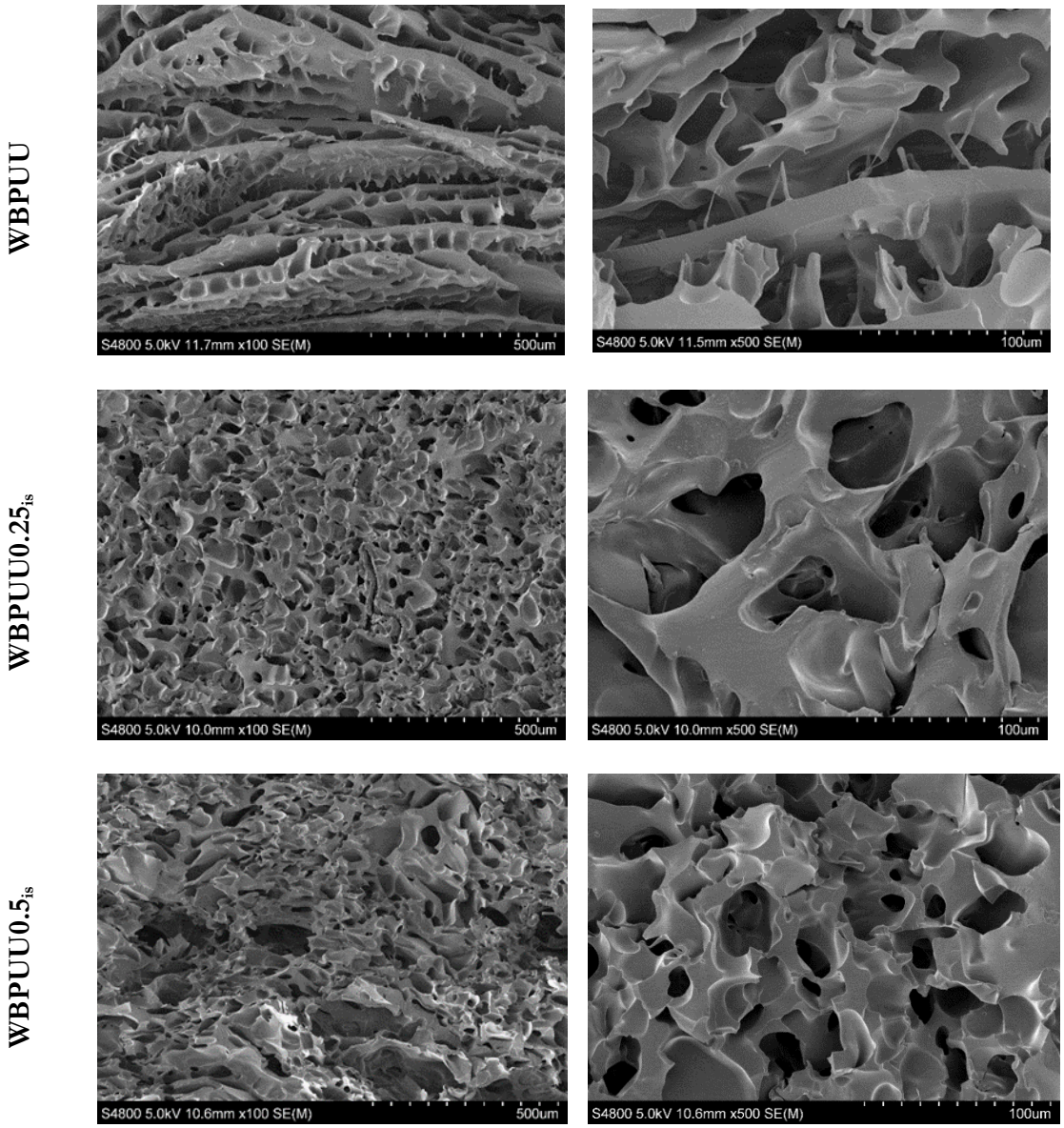

Figure 7.6 SEM images of the WBPUU/CNC$_{is}$ scaffolds with different CNC content

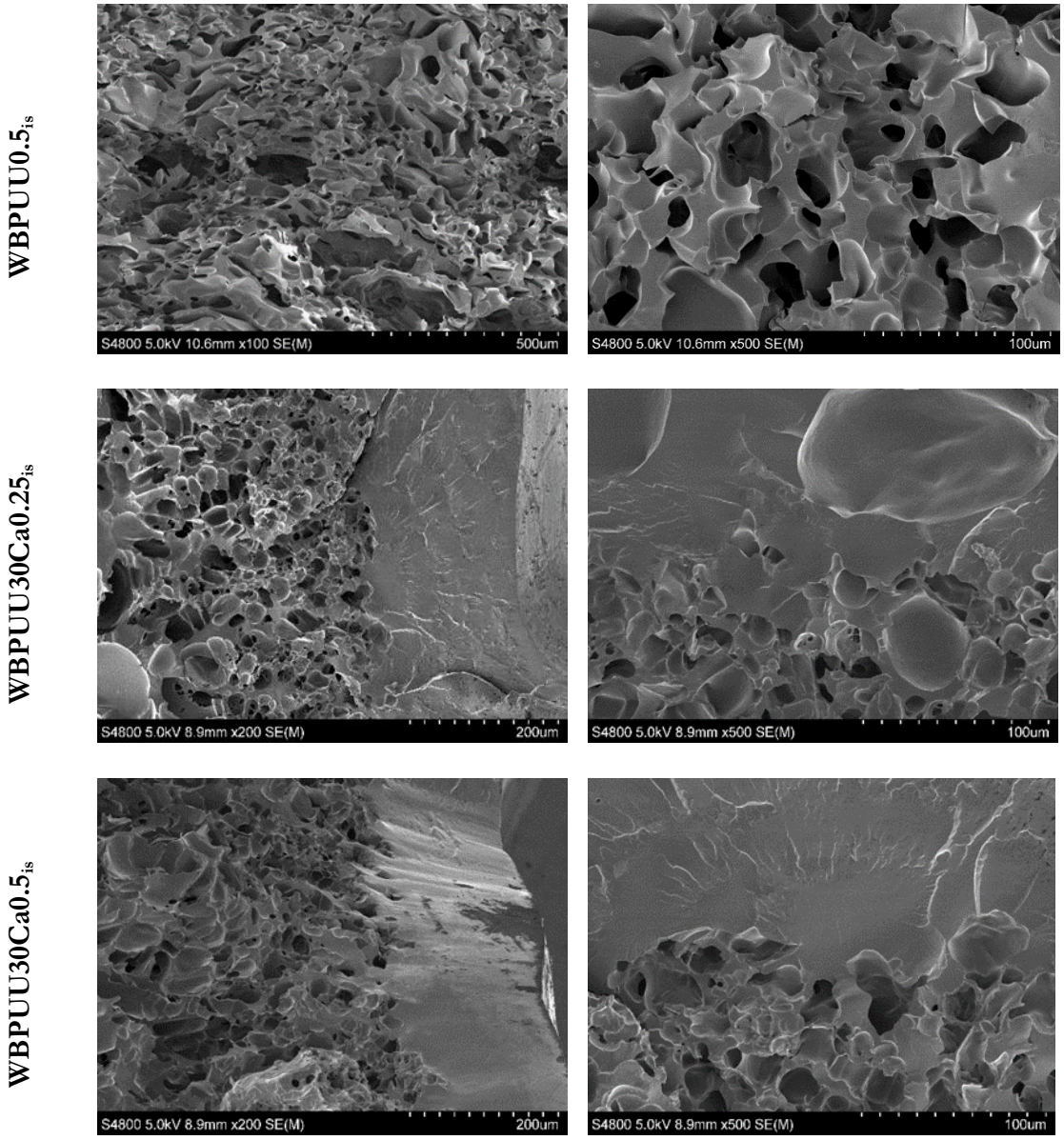

Figure 7.7 SEM images of the WBPUU/CNC_{is}/Ca scaffolds with different immersion times in $CaCl_2$

Heterogeneous morphology can be observed for the WBPUU based scaffold. The viscous behaviour of this ink is not able to support a multi-layered 3D construct, resulting in the collapse of the structure which result in the aforementioned heterogeneous morphology. Both WBPUU0.25$_{is}$ and WBPUU0.5$_{is}$, presented a homogeneous morphology. In this case, the printed inks are able to support the weight of the upper layers, allowing to obtain multi-layered ordered systems which resulted after the freeze drying in a homogenous morphology. Comparing the porosity of the scaffolds presenting different CNC content, the pore size seems to decrease as the CNC content increases, resulting in system presenting higher specific surface. These results are in accordance with the measured density, where the

systems containing the higher amount of CNC presented the higher density values. Contrary, the WBPUU matrix presented the lower ones. This decrease of the pore size and the increase of the density is produced due to the higher concentration of the inks containing higher CNC content. Presenting, hence, lower water content, which will result in lower pore size.

Moreover, the influence of the immersion time of the printed pieces in $CaCl_2$ in the morphology of the obtained scaffolds was also studied. According to the images, the immersion of the printed scaffolds into $CaCl_2$ prior to the freeze drying process, resulted in the formation of a solid compact shell of around 200 μm at the surface of the piece for both systems immersed 30' as a result of the chemical crosslinking of the Ca^{2+}. As a result of this crosslinking, the porosity observed for the non-crosslinked systems disappeared completely at the surface, increasing the rigidity of the scaffolds. Finally, due to the formed shell, the previously observed homogeneous morphology in systems containing CNC seems to disappear. In this case, the aforementioned shell will hamper the freeze drying process resulting in a more heterogeneous morphology. The observed shrinkage, the non-porous shell and the Ca^{2+} ions loaded resulted in an increase of the density of the scaffold, as was observed previously in **Table 7.1**.

Additionally, in order to confirm the presence of the aforementioned Ca^{2+} ions in the crosslinked scaffolds, EDS analysis has been performed to explore the presence of Ca in the composition of the scaffold. The results which are displayed in **Table 7.2** and **Figure 7.8** supported the presence of the Ca in the composition of the shell observed in scaffolds immersed in $CaCl_2$, confirming their incorporation by the ionic interaction between the Ca^{2+} and the WBPUU particles.

Table 7.2 Composition of the core and the shell of the WBPUU030Ca20.5$_{is}$ scaffold measured by EDS

Element	**Weight percent (%)**	
	WBPUU core	WBPUU shell
O	32.79	54.76
C	73.19	29.68
Ca	-	5.98
Cl	-	0.52

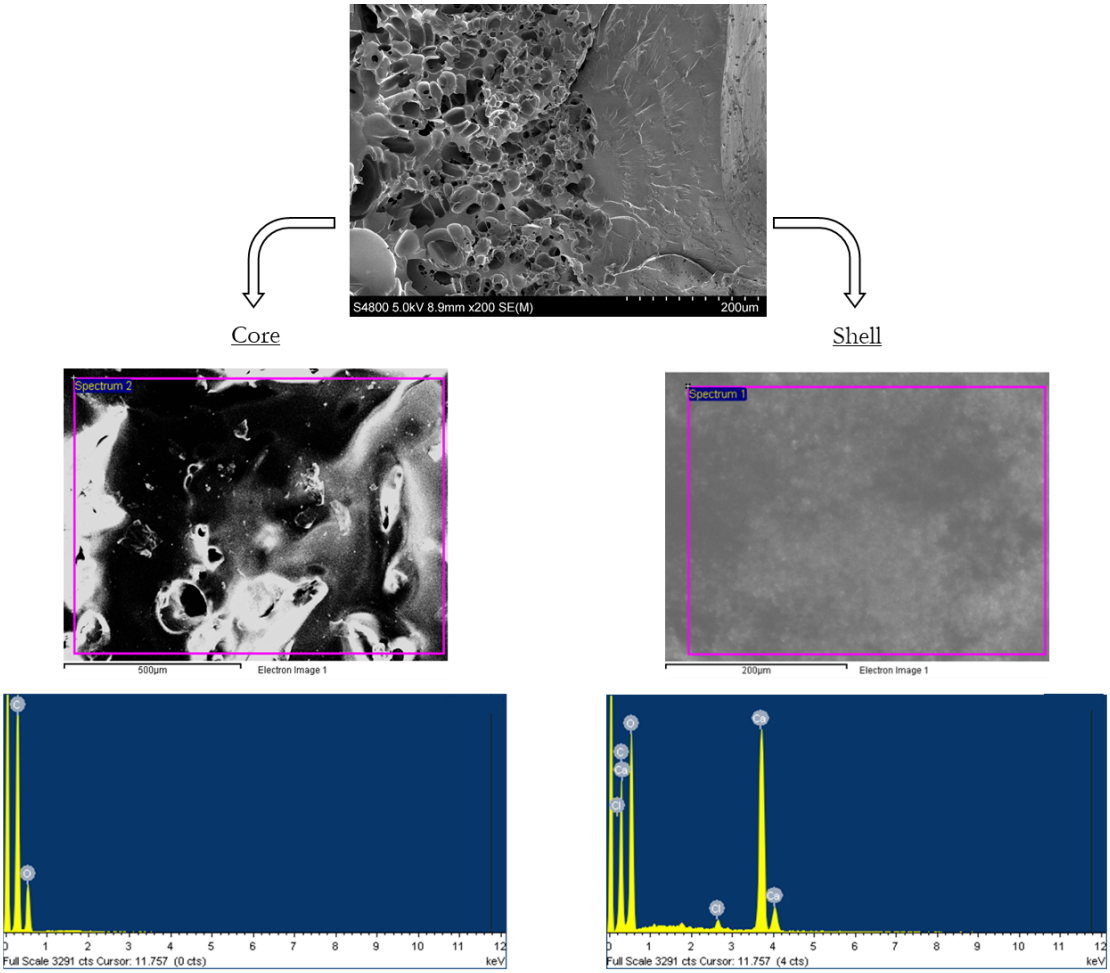

Figure 7.8 EDS analysis in the core and in the shell of the WBPUU030Ca20.5$_{is}$ scaffold obtained by freeze drying once the printed piece was immersed in $CaCl_2$

Concretely, as can be observed in **Table 7.2**, the shell formed after the immersion in $CaCl_2$ and theoretically as a result of the Ca^{2+} crosslinking, presented a weight percent of around a 6% of Ca, but also a residual Cl which has not been removed successfully when the samples were washed after the immersion process. The unreacted core contrary, did not present any sign of Ca, noticing only the presence of both oxygen and carbon.

With the aim of study the effect of the chemical crosslinking produced by the immersion of the sample in the $CaCl_2$, FTIR measurements were performed. The spectra of the prepared WBPUU/CNC$_{is}$ systems immersed in $CaCl_2$ are displayed in **Figure 7.9**. As far as the influence of the Ca^{2+} crosslinking is concerned, a displacement of the carbonyl band situated around 1699 cm^{-1} downwards when the carboxylated group was fully ionized by calcium was reported in the literature [19].

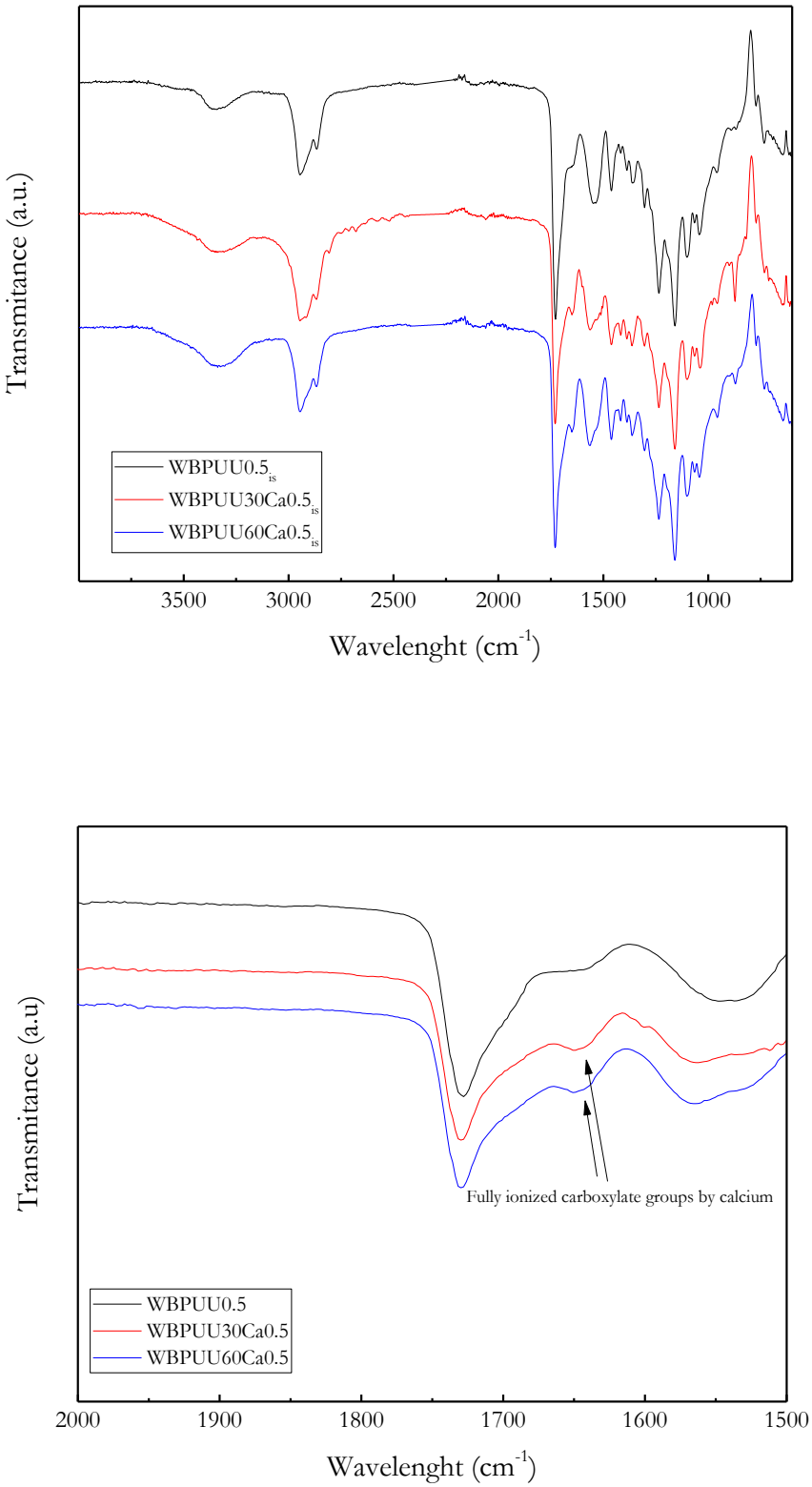

Figure 7.9 FTIR spectra of WBPUU/CNC_{is}/Ca scaffolds. Study of the influence of the immersion in $CaCl_2$ (up), magnification of the 2000-1500 cm^{-1} interval (down)

As can be observed in the magnification of the 2000-1500 cm^{-1} region at **Figure 7.9,** a new band is observed at 1648 cm^{-1} in WBPUU30Ca0.5$_{is}$ and WBPUU60Ca0.5$_{is}$ scaffolds. This band can be assigned to the fully ionized carboxylate groups by calcium ions, which appeared at similar wavelengths compared to the ones observed in the literature, confirming the successfully performed Ca^{2+} crosslinking process.

Furthermore, the influence of the Ca^{2+} crosslinking in the thermal degradation of the different WBPUU/CNC$_{is}$ based scaffolds was tested by TGA. The obtained weight curves are shown in **Figure 7.10** whereas their derivative are displayed in **Figure 7.11**.

Studying the influence of the formation of the Ca^{2+} crosslink in the thermal stability, the results showed similar degradation curves for all systems, however, an increase of the second degradation situated around 350 °C is produced as can be observed in the DTG of the curves when the immersion time in $CaCl_2$ was increased. Additionally, system immersed in $CaCl_2$ presented higher residual mass values after the degradation process compared with the unreacted ones, probably due to the presence of Ca in the printed scaffold.

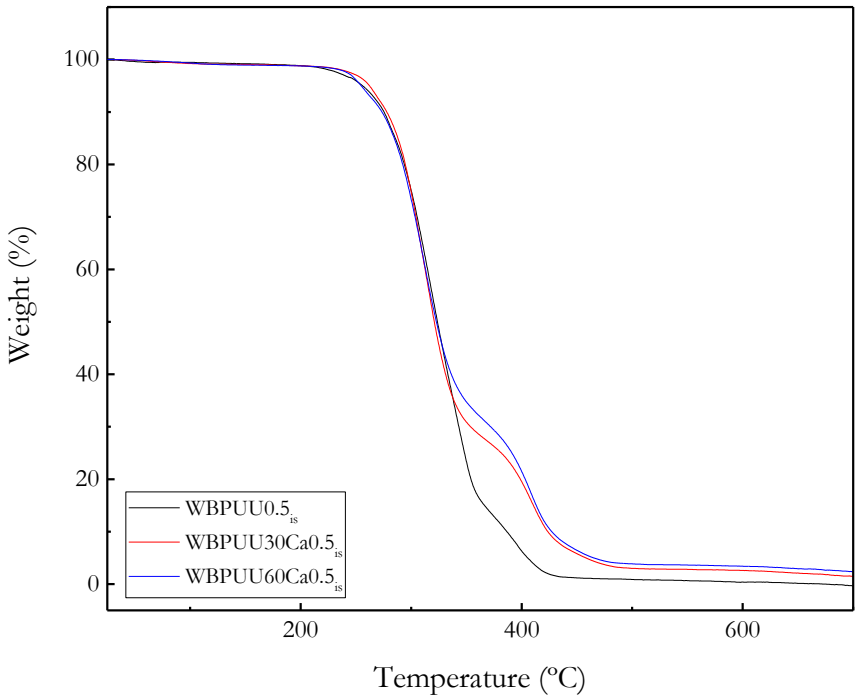

Figure 7.10 Variation of weight of WBPUU/CNC$_{is}$ with different immersion times in $CaCl_2$

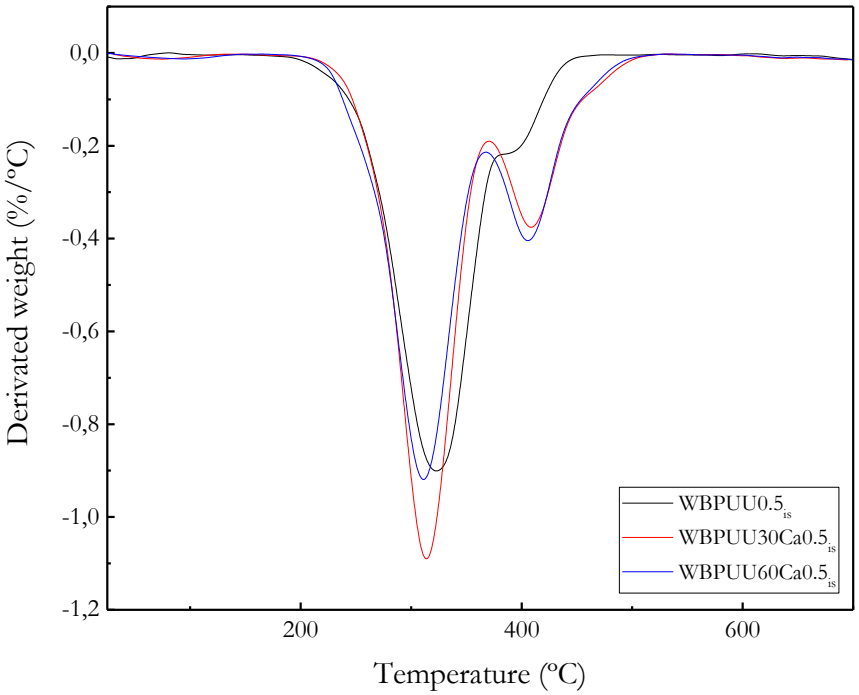

Figure 7.11 DTG curves of WBPUU/CNC_{is} with different immersion times in $CaCl_2$

In order to study the mechanical properties, compression test was performed to the different prepared WBPUU/CNC_{is} scaffolds (**Figure 7.12**). As can be observed, all systems presented typical compression behaviour, showing an initial linear elastic response of stress vs strain followed by an extended plateau and a final region of increasing the stress [20–22]. However, systems with a 60 min of immersion in $CaCl_2$ did not present the aforementioned plateau, presenting a continuous increase of the stress as a function of the strain. Initial bending and buckling happened on the walls of the scaffold as the compression force is applied, but some cracking initiates at the yield point and the plateau is the result of progressive brittle crushing of the cells under the compressive loads. In the final region, densification of the scaffold pilots the behaviour of the scaffold becoming closer to that of a non-foamed one. Comparing the obtained compression values of the different prepared scaffolds which are displayed in **Table 7.3** the addition of CNC in the scaffolds resulted in an increase of both the Young modulus and the stress at the plateau (σ_{yc}). The inclusion of the CNC in the scaffold led to the obtain of more rigid scaffolds due to the successful reinforcement effect observed in previous chapters for WBPUU/CNC_{is}. A slight decrease of the strain corresponding to the densification (ε densification) was also observed in scaffolds containing CNC.

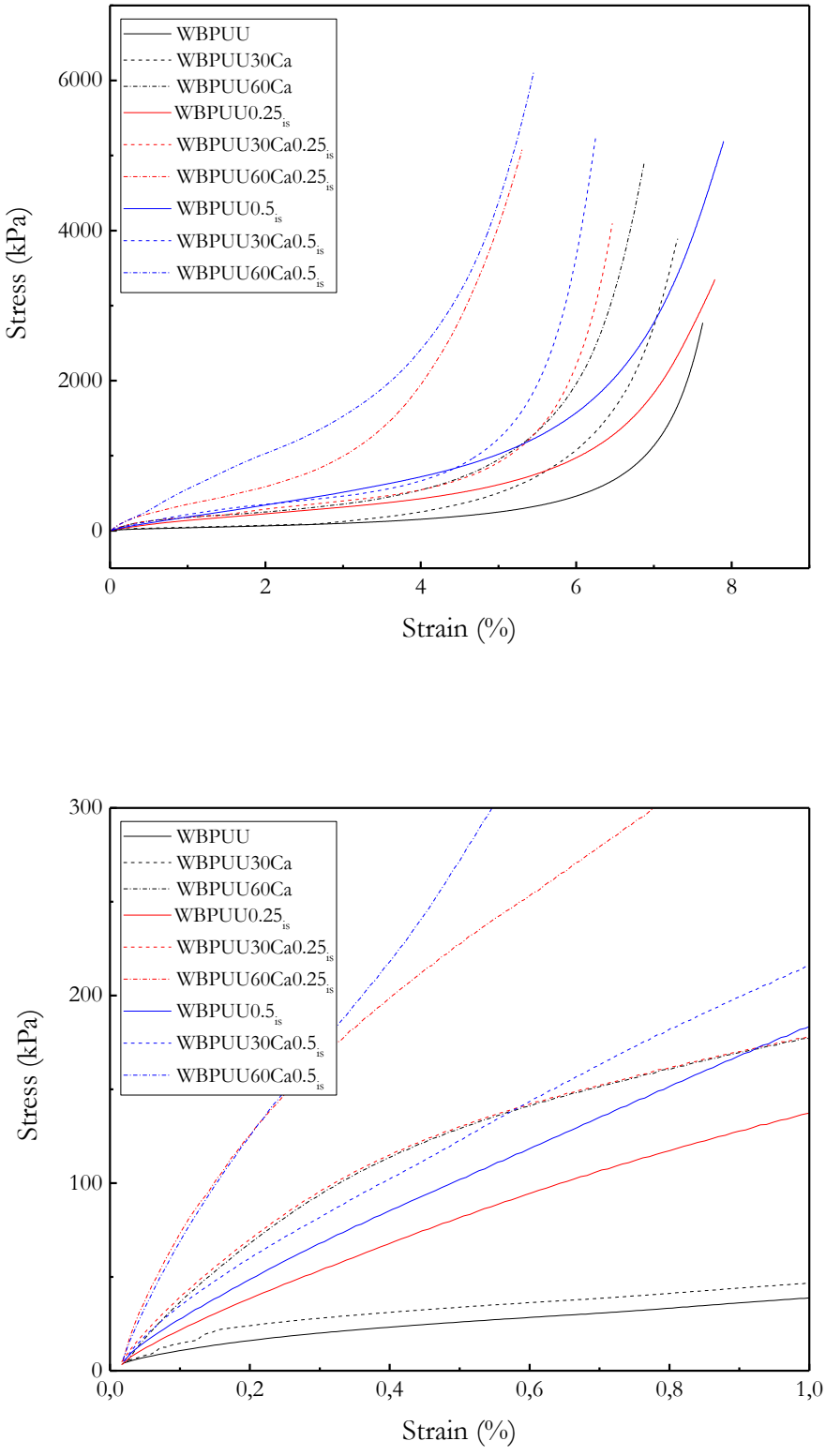

Figure 7.12 Stress-strain compression curves of WBPUU/CNC_{is} scaffolds (up), inset of the elastic zone (down)

Table 7.3 Compression properties of the WBPUU/CNC_{is} prepared scaffolds

System	E (MPa)	σ_{yc} (kPa)	$\varepsilon_{densification}$ (%)
WBPUU	3±1	70±10	6.5±0.5
WBPUU30Ca	12±3	120±30	6.3±0.2
WBPUU60Ca	31±2	-	5.8±0.8
WBPUU0.25	15±1	270±30	6.1±0.3
WBPUU30Ca0.25	32±3	330±20	5.8±0.7
WBPUU60Ca0.25	54±4	-	4.4±0.2
WBPUU0.5	20±2	320±10	6.3±0.2
WBPUU30Ca0.5	28±4	360±60	5.6±0.3
WBPUU60Ca0.5	50±6	-	4.3±0.3

Regarding the samples immersed in $CaCl_2$, the previously observed rigid and non-porous shell, resulted in a high increase of the Young modulus in all immersed samples compared with the same formulations without the exposure to $CaCl_2$. Indeed, an increase of even 260% comparing the Young modulus of $WBPUU0.25_{is}$ (15±1 MPa) with $WBPUU60Ca0.25_{is}$ (54±4 MPa) was observed. Additionally, as was previously mentioned, samples immersed 60 minutes into $CaCl_2$ did not presented the aforementioned plateau increasing the stress as the strain increased. In those systems, the rigid shell of the exterior of the scaffold rules the compression behaviour.

Studying the influence of the combination of CNC addition and the Ca^{2+} crosslinking in the mechanical properties, a lower influence was observed in the former compared with the latter. In the samples immersed in $CaCl_2$, the influence of the CNC reinforcement was overshadowed by the influence of the rigid shell. In fact, $WBPUU0.5_{is}$ presented an increase of Young modulus of 570% comparing with the one observed for WBPUU, while the Young modulus for the same systems immersed in $CaCl_2$ for 60 min (WBPUU60Ca and $WBPUU60Ca0.5_{is}$) presented a less noticeable increase of 61%. According to the literature, the density of the scaffolds seems to have a direct relationship with the densification phenomenon [24], where systems presenting higher densities implied lower densification values. Analysing the obtaining results, all systems presented densification strain percentages of 4-6%, with the lowest value occurring for the scaffolds which presented the highest

immersion times in $Cacl_2$, illustrating the rigid compact shell observed in those systems in the SEM images. Comparing this values with the observed ones in the literature for other polyurethane scaffolds systems, much lower values of $\varepsilon_{densification}$ were observed but also higher compression modulus [25] illustrating the obtaining of scaffolds with high rigidity, as the result of the enhancement by both the effect of the CNC reinforcement and the immersion in $CaCl_2$.

Furthermore, the water absorption capacity of the prepared scaffolds was tested during a week by weight difference and expressed as swelling (%) by exposing the scaffolds to water with different pH. The swelling as a function of the time of the WBPUU and WBPUU/CNC_{is} are shown in **Figure 7.13**.

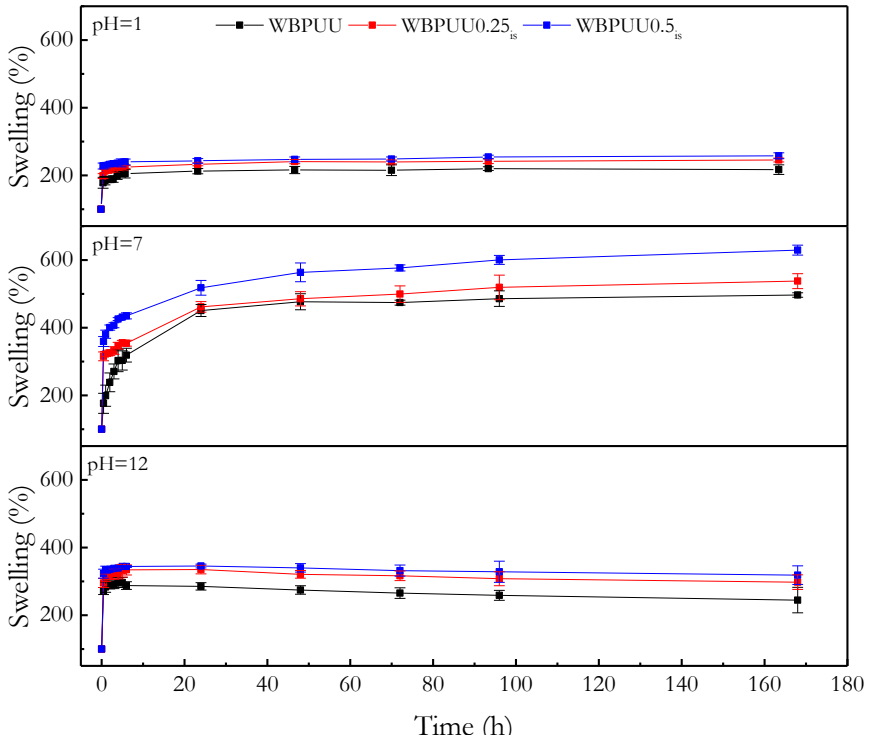

Figure 7.13 Water absorption capacity of prepared WBPUU/CNC_{is} at different pH

The results showed a variation of the absorption capacity depending on the CNC content and the pH of the medium. All the samples, independent on the CNC content and pH of the media reach the swelling equilibrium almost in one day. Comparing the CNC content, the addition of the CNC resulted in an increase of the swelling in all studied media as the CNC content increased, showing a maximum swelling for the WBPUU0.5_{is} system of 629% at pH = 7 after 1 week. The incorporation of CNC in the polyurethane contributed to a greater capacity of water absorption in the WBPUU/CNC_{is} nanocomposites, taking into

account that the water molecules could tend to diffuse where CNC nanoentities are located [26] owing to the hydrophilic character of CNC [27]. The hydrophilic nature of the CNC leads to an increase of the swelling, obtaining at pH = 7 and 1 week an increase of a 27%, from WBPUU to WBPUU0.5$_{is}$. Additionally, the 3D complex structure that samples containing CNC present, as can be observed by SEM, allowed to present a higher surface for absorption resulting in an increase of the swelling.

Regarding the samples immersed in $CaCl_2$, which are displayed in **Figure 7.14**, a similar behaviour compared with the observed ones for the CNC variation was observed, reaching the swelling equilibrium almost in one day. The results showed that the water absorption capacity decreased as the immersion time increased. The formed chemical bonding induced by the Ca^{2+} addition resulted in a rigid compact shell at the surface of the scaffold as was observed by SEM. This compactness justified the reduction of the swelling that was observed in all media. Indeed, the WBPUU60Ca0.25$_{is}$ presented a decrease of around 35% respect to the WBPUU0.25$_{is}$ at pH = 7.

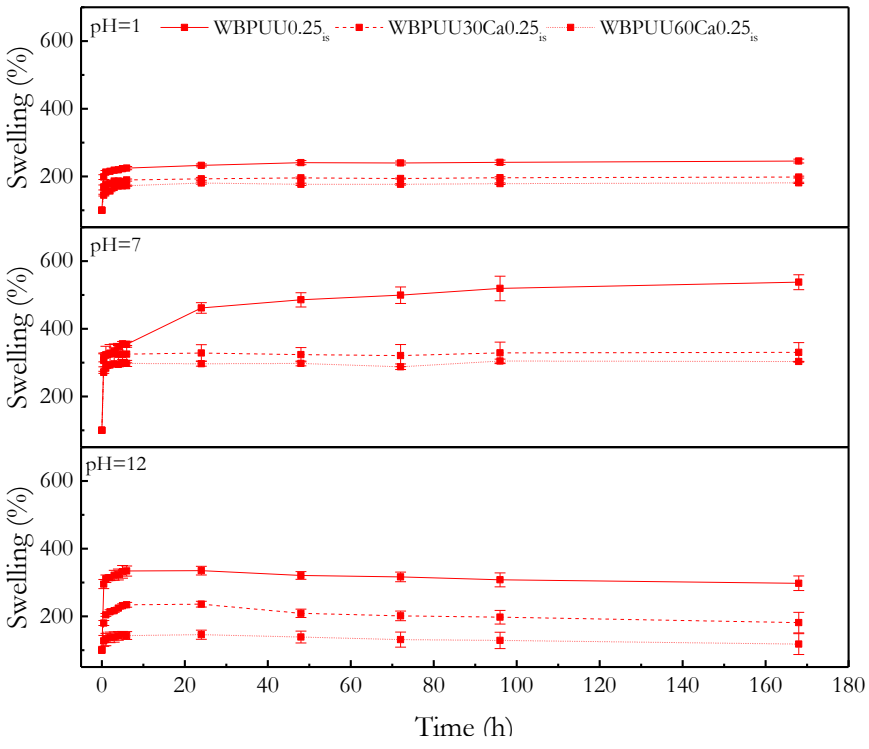

Figure 7.14 Water absorption capacity of prepared WBPUU/CNC$_{is}$/Ca at different pH

As far as the variation of the pH is concerned, it can be seen also variations water absorption capacity wise. The scaffolds immersed in pH = 7 presented the higher swelling compared with the ones obtained at other media. Indeed, in WBPUU0.25$_{is}$ system samples immersed

in acid and basic media showed a decrease of the swelling of around 59% and 49% at 1 week for pH = 1 and pH = 12 respectively compared with the swelling obtained a pH = 7. In the case of the basic medium, the decrease observed in the swelling after 2 days which was observed in all samples suggests a degradation of the scaffold due to the exposure of the basic medium. This degradation, confirmed by visual examination, is not observed for the samples exposed to both acid and neutral media.

Finally, the absorption capacity of the printed pieces for the cationic methylene blue (MB) was carried out. Taking into account the swelling results, WBPUU0.5$_{is}$ system was selected due to its higher adsorption capacity. The samples were immersed in deionized water at pH = 7 for 24 h prior to the absorption test so as to obtain swollen samples and posteriorly immersed in a methylene blue solution (12 ppm) during 24 h. The test has been carried out per triplicate. The absorption curves of the MB and the remaining concentration of MB are displayed in **Figure 7.15**.

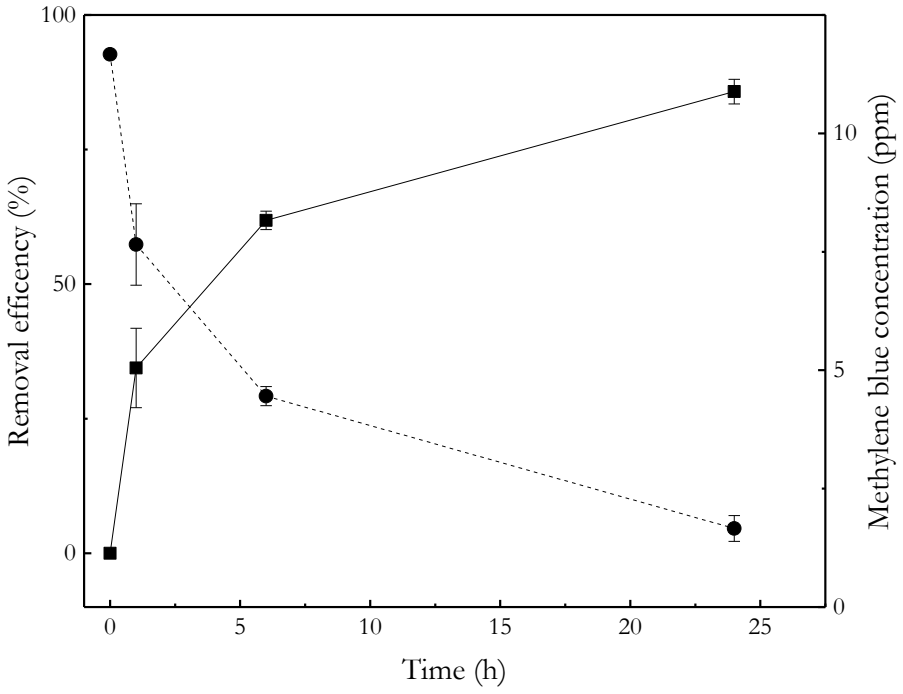

Figure 7.15 Removal efficiency of the WBPUU0.5$_{is}$ scaffold as a function of the time

Analysing the obtained results which are displayed in **Table 7.4**, a decrease of the MB concentration in the solution was observed, decreasing from an initial 12 ppm to 8 ppm after 1 h and finally to a 2 ppm after one day. Visually, as can be observed in **Figure 7.16**, the MB

dilution seems to be less blueish after 24 h compared with the initial dilution. Contrary, the swollen scaffold presents a bluing as a result of dye absorption, confirming the successful absorption of the methylene blue by the scaffold. According to the **Equation 2.3** a removal percentage of 34±7% after 1 h of exposure and of 86±2% after 24 h was obtained, confirming the high efficiency of the absorption capacity of the WBPUU/CNC_{is} scaffolds.

Table 7.4 Removal efficiency of the WBPUU0.5_{is} scaffold and the remaining methylene blue concentration of the dispersion

Time (h)	Removal efficiency (%)	Methylene blue concentration (ppm)
0	-	12±0.0
1	34±7	8±1.0
6	62±2	4±0.2
24	86±2	2±0.2

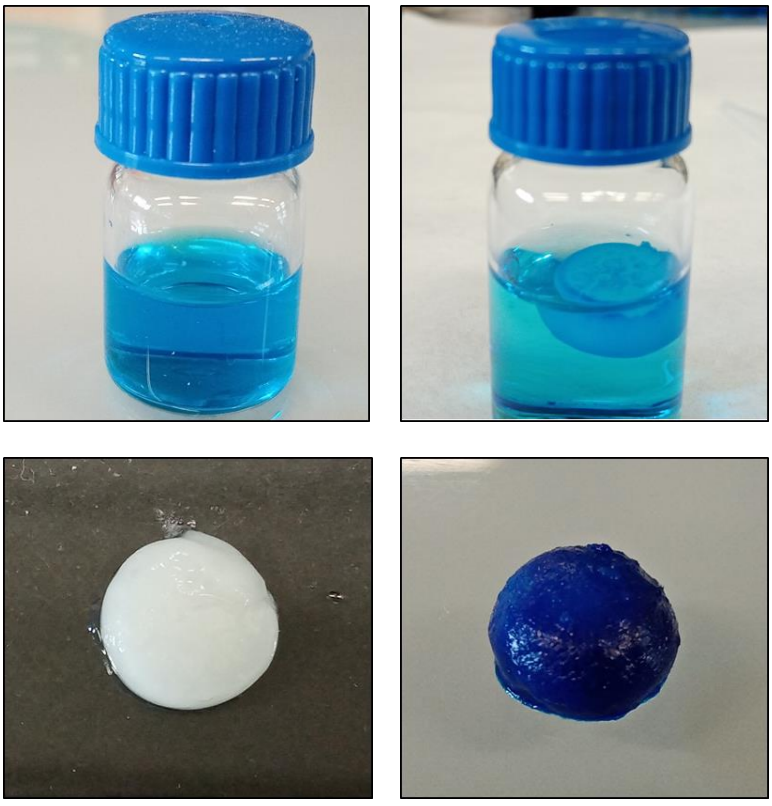

Figure 7.16 Dispersion of methylene blue (12 ppm) at t = 0 h (left) the same methylene blue dispersion at t = 24 h (right) (up) and aspect of the scaffold before the immersion in MB (left) and after 24 h of immersion in MB (right) (down)

7.2.3 Conclusions

Shape customized scaffolds based on WBPUU/CNC_{is} were prepared successfully with different CNC content by DIW 3D-printing and freeze drying technique. As a result, porous scaffolds with the desired shape were obtained. Additionally, some of the prepared scaffolds were immersed in $CaCl_2$ before freeze drying obtaining a compact rigid shell according to SEM images as a result of the ionic crosslinking between the Ca^{2+} and the WBPUU particles. All systems were characterized from the physicochemical, thermal, mechanical and morphological viewpoint. The capacity of absorbing dyes was also evaluated in order to propose a potential application of this material as absorbing material.

The results showed that the addition of CNC to the prepared scaffolds provide a more homogeneous porous structure, having a smaller pore size as the CNC content increased as was observed by SEM. Regarding the water absorption capacity of the WBPUU/CNC_{is} scaffolds, the aforementioned homogeneous porous structure provided by the addition of CNC as well as the hydrophilic nature of CNC resulted in an increase of the swelling as the CNC content increase.

The pieces immersed in $CaCl_2$, contrary, showed a compact rigid shell surrounding the porous scaffold as a result of the ionic crosslinking produced by the reaction of the Ca^{2+}. This shell resulted in scaffolds presenting much higher compression modulus and strength as well as lower densification strain compared with the non-crosslinked ones. However, this external shell hampers the water absorption capacity, showing lower absorption values compared with the non-crosslinked systems.

Finally, the dye absorption capacity of the prepared WBPUU/CNC_{is} scaffolds was tested against the methylene blue, a cationic dye. For that purpose, the WBPUU0.5_{is} system was selected due to its higher swelling. The results confirmed the efficiency of the prepared scaffolds to absorb a cationic dye, presenting a removal efficiency of 86±2 % in 24 h, and decreasing the MB concentration of the dissolution from an initial 12 ppm to a much lower 2 ppm after 24 h. These results confirmed the viability of using the prepared WBPUU/CNC_{is} scaffolds as potential materials for the absorption of cationic dyes such as MB.

7.3 WBPUU/plant extract based inks for the 3D-printing of antibacterial materials

7.3.1 Experimental part

7.3.1.1 Salvia extract

Plant extract was obtained from commercial *Salvia officinalis L.* plant by infusion method. This extract was chosen due to its recognized antimicrobial activity according to the literature [28] as well as for its proven capacity to be incorporated into WBPUU dispersion to prepare WBPUU/plant extract films with antibacterial properties [18]. The method consists initially in the addition of 20 g of ground plant to 800 mL of boiling distilled water. After 5 min, the suspension was filtered by vacuum filtration and freeze dried, obtaining as result extract rich in bioactive compounds in powder form. The different intermedia products obtained in each step of the infusion method are shown in **Figure 7.17**.

Raw material

Infusion process

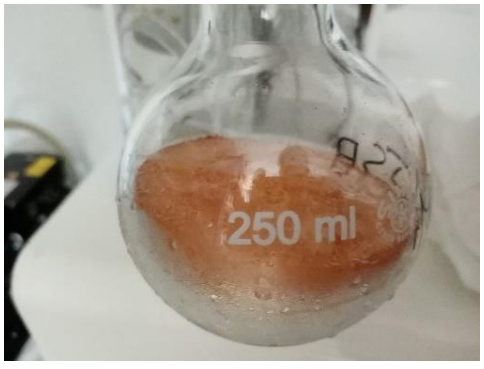

Freeze drying process

Freeze dried extract

Figure 7.17 Images of raw material, infusion process, freeze drying process and freeze dried extract of *Salvia*

In order to verify the extraction efficiency of the process, the **Equation 6.1** was used to establish the efficiency percentage.

$$\text{Efficency } (\%) = \frac{W_i - W_f}{W_i} \qquad \textbf{(6.1)}$$

where W_i and W_f are the initial weight of ground plants and the weight of the resultant extract, respectively. According to this equation, an efficiency of the process of 16±2% was obtained for the obtaining process of bioactive *Salvia* extract. These result are in accordance with the ones obtained in a previous work for the obtaining of *Salvia* extract by infusion method [29].

7.3.1.2 Synthesis of WBPUU/Salvia inks and preparation of the WBPUU/Salvia/CNC$_{es}$ nanocomposites

Waterborne polyurethane urea dispersion with a PCL/PEG ratio of 0.8/0.2 was synthesized following a two-step polymerization process as was previously described in Chapter 3. For the addition of the plant extract by the *in situ* method, the extract was dissolved in the deionized water employed in the phase inversion step. In this way, the extract was incorporated successfully to the dispersion during the formation of the particles. As a result, after the phase inversion step a liquid dispersion with high viscosity was obtained, presenting a solid content of 29 wt%.

Regarding the preparation of the WBPUU/*Salvia*/CNC$_{es}$ nanocomposite inks, the addition of the nanoentities has been carried out by *ex situ* method as was explained in Chapter 6. That is, by adding the cellulose nanocrystals to the previously synthesized WBPUU/*Salvia* dispersion. The nanoentities were successfully dispersed into the WBPUU/*Salvia* dispersion by vigorous mechanical stirring (Ultraturrax 12000 rpm) obtaining an increase of the viscosity of the dispersion due to the physical interactions between the CNC and the WBPUU/*Salvia* particles.

The *Salvia* extract content has been fixed to a 3 wt% for all systems, which according to the literature is enough to provide an antibacterial activity in the WBPUU films [18]. Contrary, regarding the addition of CNC *ex situ*, a 2 and 3 wt% were added in order to reach suitable printing performance of the WBPUU/*Salvia* inks. The samples were coded as WBPUU$_S$ for systems containing *Salvia* and WBPUU$_S$X$_{es}$ for the systems containing *Salvia* and *ex situ* added CNC, where X was referred to the CNC weight content in the polyurethane urea.

The different prepared systems are enlisted in **Table 7.5** whereas the appearance of neat $WBPUU_S$, $WBPUU_S2_{es}$ and $WBPUU_S3_{es}$ dispersions are shown in **Figure 7.18**.

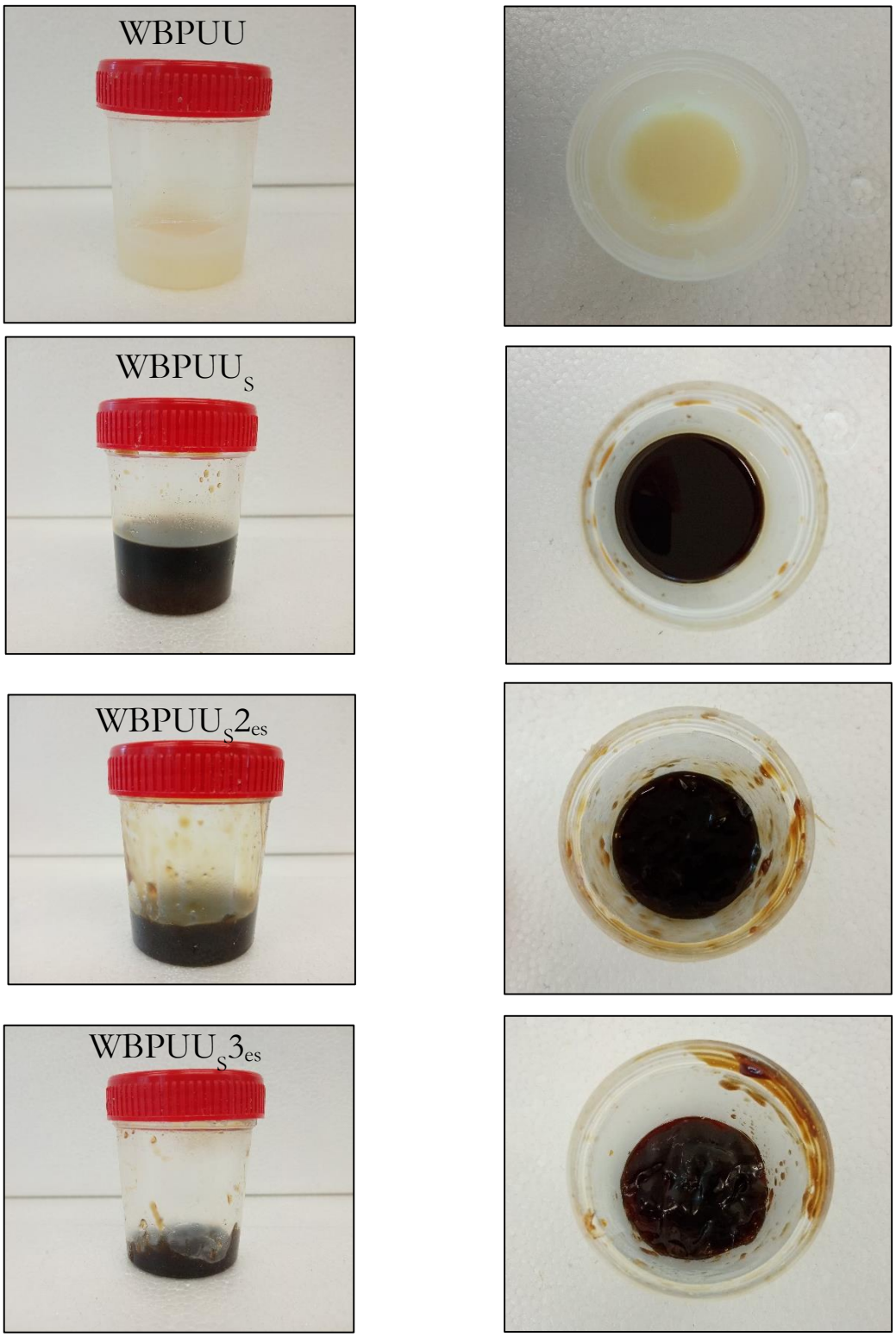

Figure 7.18 Appearance of the WBPUU, WBPUU/*Salvia* and WBPUU/*Salvia*/CNC_{es} inks

Table 7.5 Designation and composition of the WBPUU/*Salvia* based inks

System	*Salvia* content (%)	CNC content (%)
WBPUU$_S$	3	0
WBPUU$_S$2$_{es}$	3	2
WBPUU$_S$3$_{es}$	3	3

For comparative purpose, the WBPUU29 ink synthesized in Chapter 4 and denoted as WBPUU was analysed together with the inks containing *Salvia*. The WBPUU matrix presented a white and translucent appearance, whereas all systems containing *Salvia*, that is WBPUU/*Salvia* and WBPUU/*Salvia*/CNC$_{es}$ presented a browner like aspect. This aspect is in accordance with the used *Salvia* extract, presenting the systems containing the extract the same tonality than the extract itself.

Additionally, the WBPUU$_S$ systems seems to present visually lower viscosity compared with WBPUU matrix, despite presenting similar solid content percentage.

7.3.1.3 DIW 3D-printing of WBPUU/Salvia and WBPUU/Salvia/CNC$_{es}$ inks and preparation of the scaffolds

The different prepared inks were printed by DIW 3D-printing using the equipment shown in Chapter 2 and following the printing condition displayed in Chapter 4.

The samples were printed in a "coin" form, presenting 20 mm of diameter and 5 mm of height. After the printing some of the pieces were dried at room temperature, resulting in a decrease of the volume due to the solvent evaporation whereas the rest of the samples were freeze dried. The process, consist on a freezing process of the printed samples during 24 h followed by a freeze drying process (-60 ºC and 0.1 Pa during 24 h). As a result, porous scaffolds were obtained with the designed form. In **Figure 7.19** an illustration of the steps of both process is shown, that is, the drying in air of the printed sample and the freeze drying process respectively.

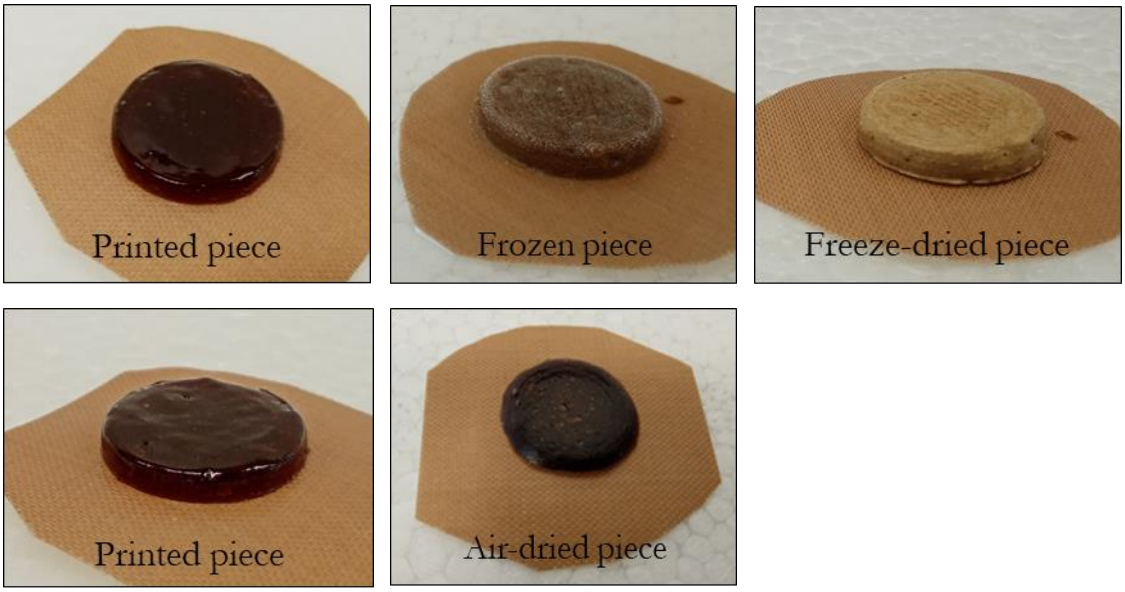

Figure 7.19 Freeze drying process and drying process (up) and air drying process (down) of $WBPUU_S2_{es}$ ink

7.3.2 Results and discussion

7.3.2.1 Characterization of the dispersion

Taking into account the visually observed decrease of viscosity for the system containing *Salvia* extract added *in situ* compared with the WBPUU matrix, both the particle size and the dispersion stability of the ink were studied by DLS and Z potential so as to analyse the influence of the extract into the particles and the dispersion itself. The obtained results of particle size and Z potential of both WBPUU and $WBPUU_S$ matrices are shown in **Table 7.6**. Analysing the obtained results, a decrease of the particle size was observed as the result of the addition of *Salvia* extract. As was explained before, due to the chemical structure of some of the bioactive compounds, some extracts can promote their activity as natural surfactants [30–32], facilitating the dispersion formation, and thus, contributing to the obtaining of smaller particles. These results agreed with the ones observed in previous works, where the addition of small amounts of *Salvia* extract during the phase inversion step resulted in a decrease of the particle size of the dispersion [29].

Regarding the stability of the dispersions, the Z potential of the system containing *Salvia* showed values of -41.45±0.9 mV, which represented an increase of the stability of the dispersion compared with the observed one for WBPUU matrix. The lower particle size obtained in $WBPUU_S$ allowed to a higher stability of the dispersion, however both systems showed Z potential values corresponding with stable dispersions [33].

Table 7.6 Characterization of the WBPUU and WBPUU$_S$ dispersions. Influence of the *in situ Salvia* addition

System	Particle size (nm)	Polydispersity	Zeta potential (mV)	Solid content (wt%)
WBPUU	113±12	0.16±0.01	-38.7±0.6	29
WBPUU$_S$	75±10	0.08±0.02	-41.45±0.9	29

Additionally, the influence of the *in situ* addition of *Salvia* in the morphology of the WBPUU was also studied by AFM. **Figure 7.20** shows the phase images of the WBPUU matrix and WBPUU$_S$ systems. Studying the obtained phase images, it can be observed that despite the inclusion of *Salvia* presented a notorious influence as far as the formation of the dispersion is concerned, in the case of the morphology, no noticeable differences were observed, obtaining similar phase images in the case of WBPUU and WBPUU$_S$.

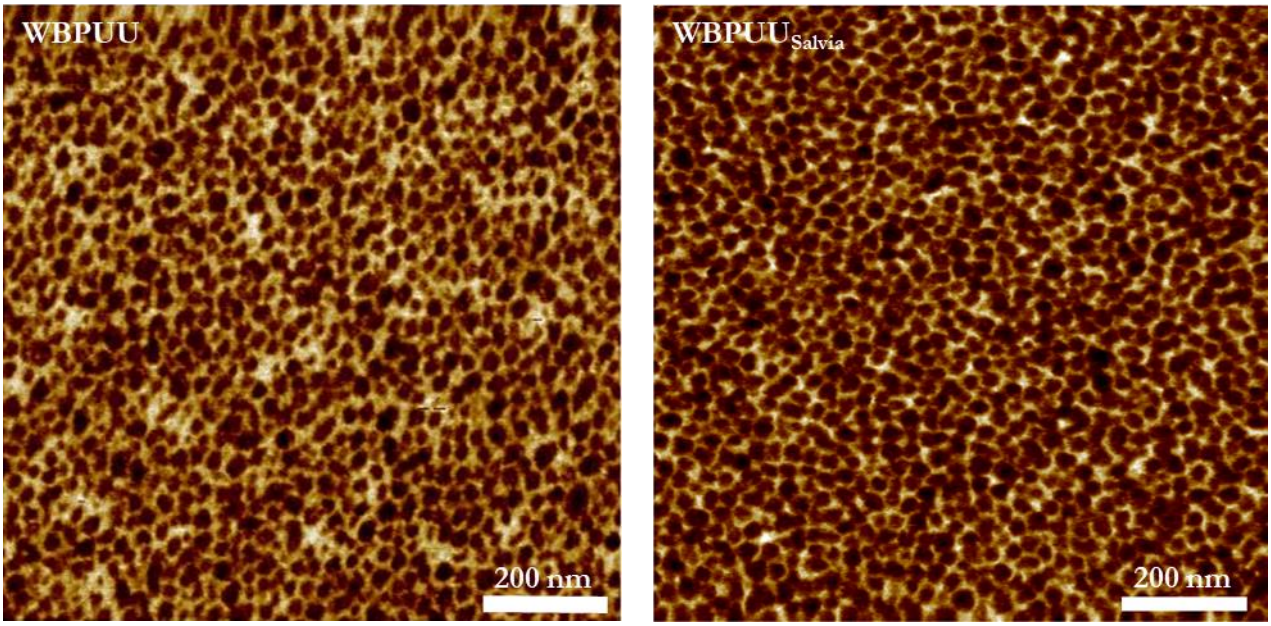

Figure 7.20 AFM phase images of WBPUU and WBPUU$_S$

7.3.2.2 Rheological characterization of the WBPUU/Salvia and WBPUU/Salvia/CNC$_{es}$ inks

So as to study the influence of the *Salvia* extract in the WBPUU based inks, flow test was performed to the different WBPUU/*Salvia* systems and compared with that without *Salvia* (WBPUU). The viscosity curves showed that the addition of plant extract modify the viscosity of the WBPUU based ink, showing lower values the WBPUU$_S$ comparing with WBPUU (**Figure 7.21**). This decrease of the viscosity can be attributed to the hydrophilic

groups of the phenolic compounds presented in the extract, promoting the dispersion formation and posterior stability of the WBPUU particles, acting as surfactant [34]. This slight decrease of the viscosity with the *in situ* addition of small amounts of *Salvia* into WBPUU dispersion was previously observed in a previous work, concretely for an *in situ* addition of 1 wt% of *Salvia* [29].

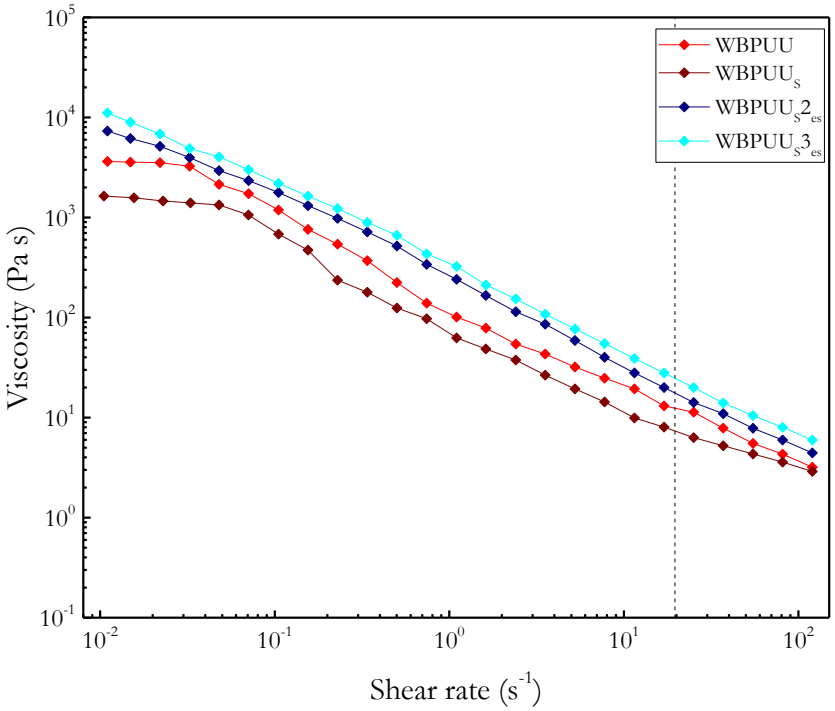

Figure 7.21 Viscosity curves of WBPUU, WBPUU/*Salvia* and WBPUU/*Salvia*/CNC$_{es}$ systems. Printing shear rate at 19 s^{-1} (----)

Regarding the addition of CNC by *ex situ* method, as was observed in Chapter 6, it resulted in an increase of the viscosity in all shear rate range. In this case, the addition of the *Salvia* extract also modifies the rheological behaviour, presenting WBPUU$_S$2$_{es}$ slightly lower values than WBPUU2$_{es}$ analysed in the Chapter 6 (7305 vs 8553 Pa s at 0.01 s^{-1}; 27 vs 44 Pa s at 19 s^{-1} and 5 vs 19 Pa s at 100 s^{-1}). Taking into account the lower values obtained for WBPUU$_S$ compared with WBPUU, the addition of CNC did not modify this behaviour. Finally, the addition of the extract did not modify the previously observed shear thinning behaviour of the WBPUU based inks, which is an important parameter so as to obtain a successful printing performance.

For comparative purposes with systems proposed in other chapters, viscosity of $WBPUU_S3_{es}$ as a function of the shear rate is represented in **Figure SC.1** at page 268 of the Appendix C.

The printability of the inks containing *Salvia* was studied by determining their yield point and flow point studying the variation of the storage and loss moduli as a function of the shear stress as in previous chapters. The obtained curves are represented in **Figure 7.22** whereas the calculated yield and flow point parameters are displayed in **Table 7.7**.

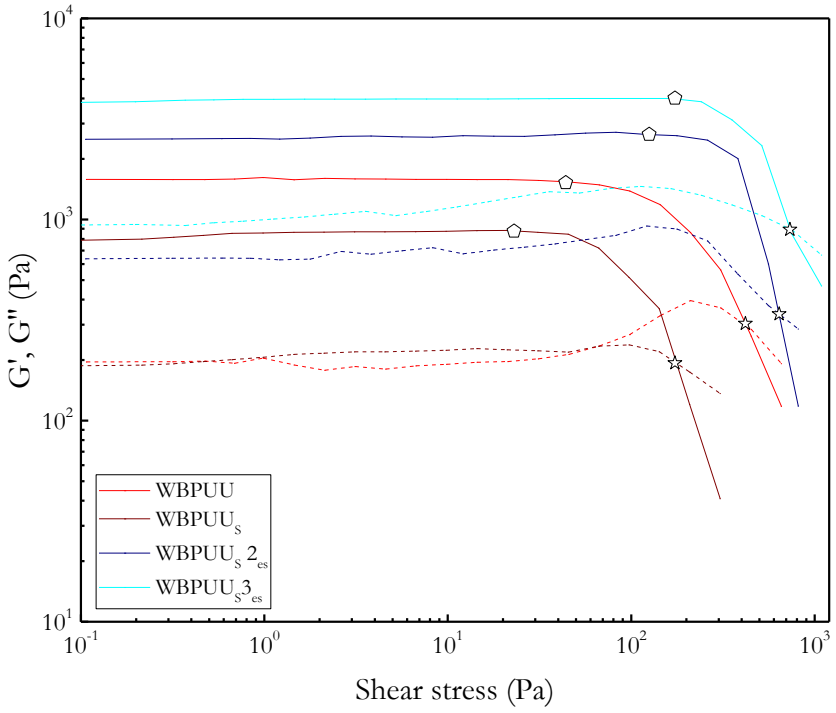

Figure 7.22 G' (—) and G" (----) as a function of shear stress (T = 22.5 °C). Determination of yield point (⬠) and flow point (☆) in WBPUU, WBPUU/*Salvia* and WBPUU/*Salvia*/CNC_{es} systems

Analysing the obtained results, lower yield point and flow points values were observed for $WBPUU_S$ comparing to the WBPUU confirming the influence of the *Salvia* extract in the rheological parameters. Regarding the addition of CNC, as happened in Chapter 6, the *ex situ* addition of the nanoentities resulted in an increase of both yield and flow point, presenting the $WBPUU_S2_{es}$ lower values than the same system without *Salvia*, that is $WBPUU2_{es}$. However, the addition of 3 wt% CNC results in an ink with yield point and flow point values

comparable to the WBPUU/CNC inks in Chapter 5 and 6, that showed the best printing performance.

Table 7.7 Determination of yield point, flow point, FTI and parameters obtained from the adjustment to Herschel Bulkley model ($\sigma-\sigma_y=K\dot{\gamma}^n$) of WBPUU inks containing CNC_{es} and *Salvia*

System	Yield point (Pa)	Flow point (Pa)	FTI	Herschel Bulkley model		
				K index (Pa s n^{-1})	n index	R^2
WBPUU	44	562	13	177	0.15	0.92
$WBPUU_S$	23	173	8	116	0.35	0.98
$WBPUU_S2_{es}$	104	640	6	208	0.34	0.91
$WBPUU_S3_{es}$	173	733	4	235	0.18	0.90

For comparative purposes with systems proposed in other chapters, yield point of $WBPUU_S3$ as a function of the shear stress is represented in **Figure SC.2** at page 269 of the Appendix C.

In order to analyse the behaviour of the inks as a function of the shear rate, the experimental data of the studied WBPUU, WBPUU/*Salvia* and WBPUU/*Salvia*/CNC_{es} inks were adjusted to the Herschel Bulkley model. The proposed model presents a good correlation with the experimental data, showing R^2 values over 0.9. From the adjustment of the theoretical model, K index, and n index were obtained for the different studied inks. All parameters, are reported in **Table 7.6.** The inclusion of *Salvia* extract resulted in a decrease of the K index, resulting in less structured inks. Additionally, the increase of the flow index illustrates a decrease of the shear thinning behaviour which is observed in all systems. Regarding the *ex situ* addition of CNC, as observed in Chapter 6, the inclusion of the nanoentities after the synthesis resulted in an increase of consistency of the ink as the CNC content increased. However, for the $WBPUU_S2_{es}$ ink, the obtained K index and n index, still are different to the ones without the plant extract displayed in Chapter 6. However, the addition of a 3 wt% CNC, results in an ink ($WBPUU_S3_{es}$) with K and n values comparable to $WBPUU2_{es}$ of Chapter 6 and $WBPUU0.5_{is}$ of Chapter 5, that showed the best printing performance.

Moreover, mechanical spectroscopy was performed with the prepared systems to analyse the shape fidelity of the potential inks. For that purpose, initially the storage and loss moduli where represented as a function of the strain, maintaining the frequency at 1 Hz, so as to

determine the LVR region where both moduli are independent of the strain. The results, which are represented in **Figure 7.23** showed G' over G" in all systems, presenting a plateau which correspond to the LVR region until 1%, and is followed by a decrease of both G' and G" until the crossover of both moduli, illustrating the destruction of the structured network. Regarding the influence of the *Salvia* extract, its incorporation modified the behaviour of the WBPUU matrix, presenting as expected lower values of both G' and G".

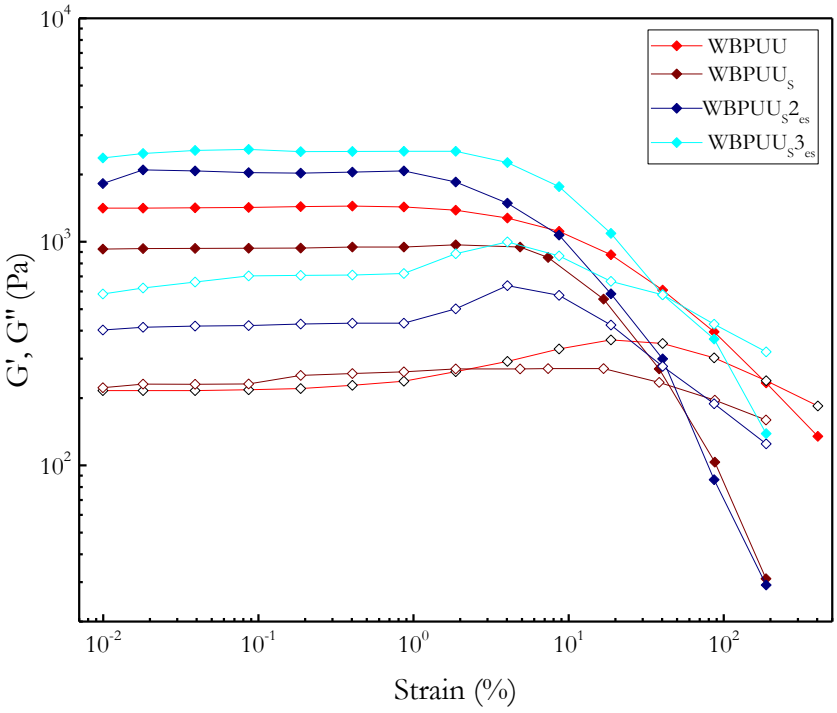

Figure 7.23 G' (♦) and G" (◊) as a function of strain (T = 22.5 °C) of WBPUU, WBPUU/*Salvia* and WBPUU/*Salvia*/CNC$_{es}$ systems at 1 Hz

Moreover, taking into account the LVR limit of 1% for all systems, the storage and loss moduli were represented as a function of the frequency with a fixed strain of 1%. The obtained G' and G" curves are displayed in **Figure 7.24**, whereas the measured values of G', G" and tan δ are displayed in **Table 7.8**.

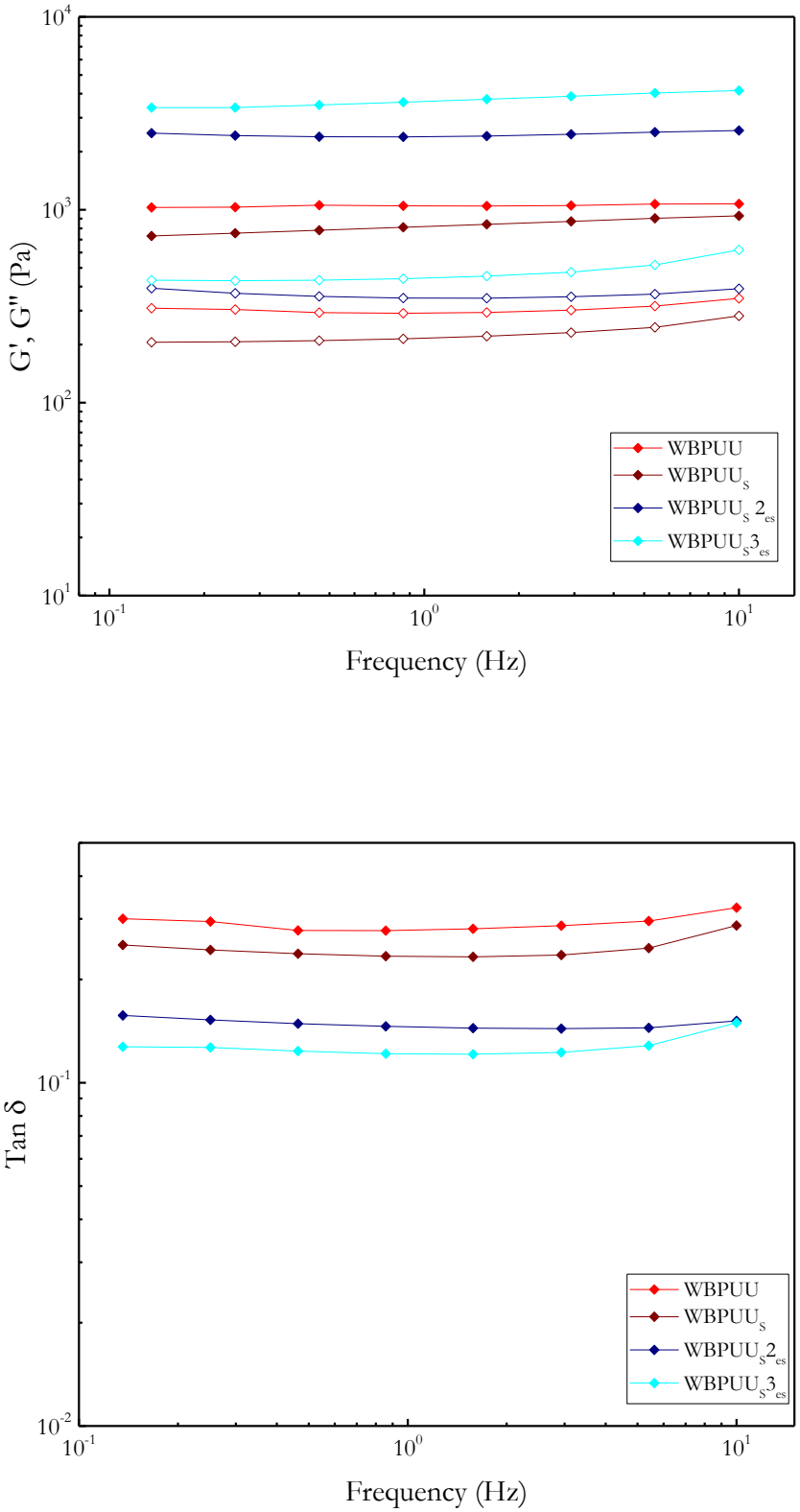

Figure 7.24 G' (♦) and G" (◊) of WBPUU, WBPUU/*Salvia* and WBPUU/*Salvia*/CNC$_{es}$ (up) and tan δ (down) as a function of the frequency (T = 22.5 °C)

Table 7.8 Storage modulus, loss modulus and tan δ values at 1 Hz and structure recovery percentage of inks with *Salvia* and *Salvia*/CNC_{es}

System	Storage modulus (Pa)	Loss modulus (Pa)	Tan δ	Structure recovery (%)
WBPUU	1033	296	0.29	84
$WBPUU_S$	824	390	0.23	70
$WBPUU_S2_{es}$	2373	349	0.15	86
$WBPUU_S3_{es}$	3633	441	0.12	88

Regarding the *in situ* addition of *Salvia*, as happened with the viscosity and the yield point, resulted in a decrease of both G' and G" illustrating a less structured network compared with the matrix, which will present problems to maintain the given shape. Regarding the *ex situ* addition of CNC to systems containing *Salvia*, as happened in Chapter 6 for the *ex situ* addition of CNC, resulted in an increase of both storage and loss moduli as the CNC content increased, leading to the obtaining of more structured inks, representing an improvement of the shape fidelity. However, this increase of G' and G" is lower comparing the same amount of CNC in systems with and without *Salvia*, presenting $WBPUU2_{es}$ system a storage modulus of 2736 Pa at 1 Hz in contrast with 2373 Pa observed in $WBPUU_S2_{es}$ at the same frequency, illustrating the surfactant effect of the plant extract which resulted in more liquid dispersions.

However, regarding the tan δ, $WBPUU_S$ presented slightly lower values compared with the WBPUU matrix, which can be correlated with a system with slightly higher elastic behaviour. In the case of the *ex situ* addition, the clear decrease of the tan δ illustrates an increase of the elastic behaviour compared with the matrix. This inks will show a highly cohesive thread when are extruded due to the aforementioned elastic behaviour which resulted in a recognizable patter when the DIW 3D-printing performance is carried out. According to the criteria proposed by *Li et al.* of a minimum storage modulus of 10^3 Pa to obtain inks with good shape fidelity [35], both systems containing CNC presented acceptable values, whereas regarding the WBPUU and $WBPUU_S$, the former presented values just over the minimum whereas the latter showed lower values, suggesting a poor shape fidelity.

For comparative purposes with systems proposed in previous chapters, the storage and loss moduli of $WBPUU_S3_{es}$ as well as the tan δ as a function of frequency is represented in **Figure SC.3 and SC.4** at pages 270-271 of the supplementary material. Finally, $WBPUU_S$, $WBPUU_S2_{es}$ and $WBPUU_S\,3_{es}$ were represented in **Figure SC.6 and SC.7** at pages 273-274

so as to compare their shape fidelity with other systems in a storage modulus vs tan δ plot. The results situated the $WBPUU_S2_{es}$ system in the area of appropriate shape fidelity delimited by the results observed in the literature, whereas $WBPUU_S3_{es}$ is mapped just above the upper limit. $WBPUU_S$ contrary, is situated under the lower limit, illustrating its poor shape fidelity due to its highly viscous behaviour.

The structure recovery of the *Salvia* containing inks was also studied, so as to analyse the influence of the plant extract addition in the capacity of the inks of recovering their initial stage after being printed. For that purpose, a structure recovery test was performed to the WBPUU, $WBPUU_S$ and $WBPUU_S/CNC_{es}$ inks using the procedure proposed in Chapter 2. The results of the structure recovery test of the inks are represented in **Figure 7.25**, whereas the calculated structure recovery percentages are displayed in **Table 7.8.**

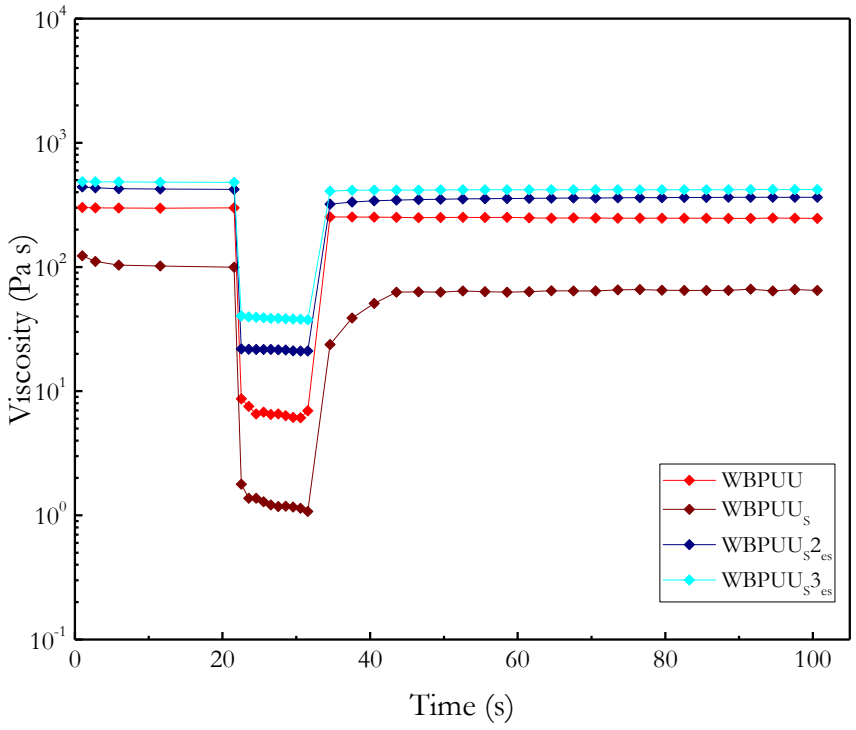

Figure 7.25 Structure recovery test of WBPUU, WBPUU/*Salvia* and WBPUU/*Salvia*/CNC_{es} based inks (T = 22.5 °C)

The results confirmed the influence of the *Salvia* extract observed previously on the rheological properties, presenting $WBPUU_S$ lower recovery than the WBPUU. The addition of CNC *ex situ*, as happened in Chapter 6 resulted in an increase of the percentage of recovery

obtaining values above 85%, which according to the literature is a recommendable value for the DIW 3D-printing application [36].

Finally, the different *Salvia* containing inks together with WBPUU were printed by DIW 3D-printing in a "coin" form. The results displayed in **Figure 7.26** showed the different pieces after being printed, prior to the drying process

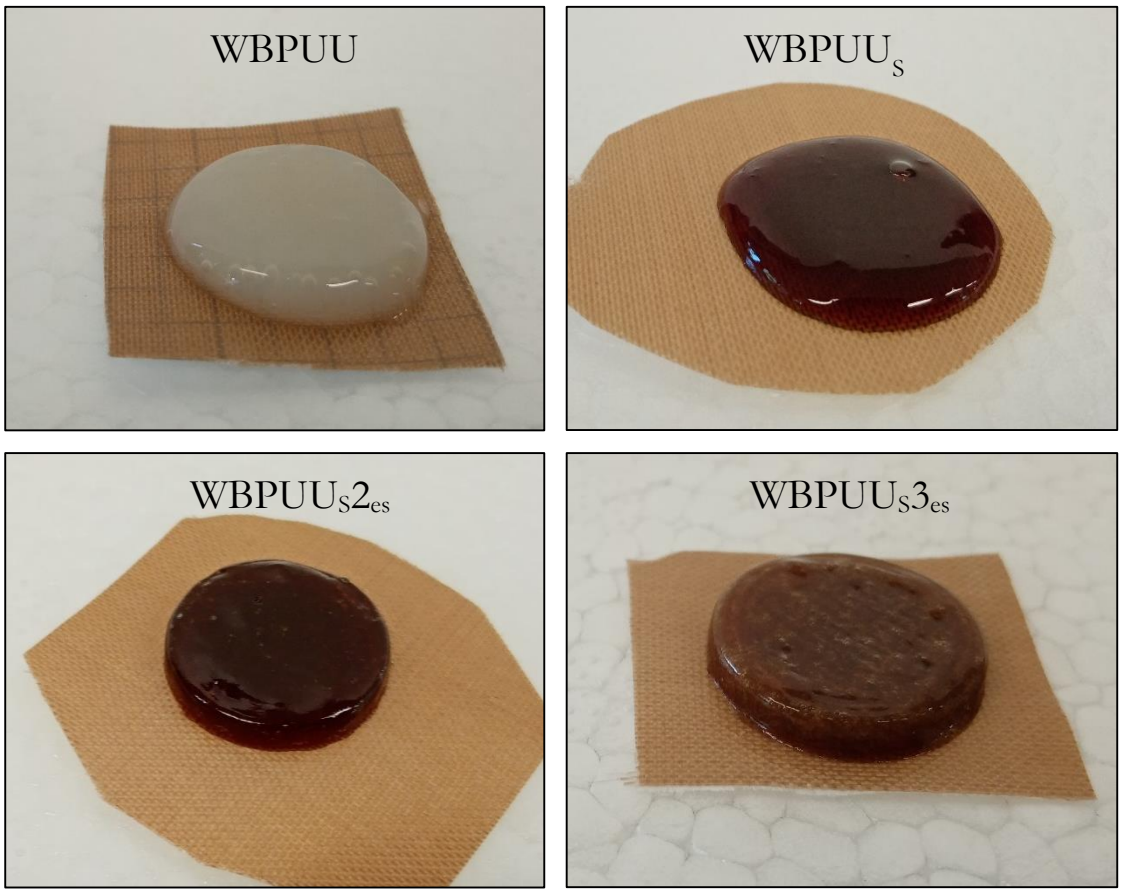

Figure 7.26 DIW 3D-printing of the different prepared inks: WBPUU, WBPUU$_S$, WBPUU$_S$2$_{es}$ and WBPUU$_S$3$_{es}$

Studying the obtained pieces, the addition of *Salvia* extract during the synthesis of the WBPUU matrix did not result in an appreciable modification of the printing performance, presenting both system a good printability but a very poor shape fidelity due to their so viscous behaviour. Additionally, the low yield point of these inks led to the spread of the ink after the printing as well as to the collapse of the 3D construct by its own weight. Regarding the *ex situ* addition of CNC to the systems synthesized with *Salvia* extract, as happened in Chapter 6, the obtained pieces maintain better the shape due to the higher structuration of the inks, resulting in pieces that maintain the given 3D multilayered construct without collapsing. In the case of the system with a 3 wt% of CNC, despite presenting similar shape fidelity compared with WBPUU$_S$2$_{es}$ the printed piece presented a different aspect, owing to

its higher content in CNC. $WBPUU_S3_{es}$ presented a higher elastic behaviour, as was observed for his lower tan δ value, leading to the obtain of an ink with higher structuration. This lower tan δ resulted in a decrease of the merging capacity of the layers, obtaining a printed piece where the printed pattern is clearly recognizable. In contrast, $WBPUU_S2_{es}$ presented a better cohesion between layers due to its more viscous behaviour, resulting in a homogeneous merging of the ink but maintaining a good reproducibility of the CAD construct.

7.3.2.2 Characterization of the printed pieces

In order to study the influence of the addition of *Salvia* extract in the WBPUU based inks apart from the rheology, the main functional groups of neat components and the interactions between *Salvia* extract and WBPUU were studied by FTIR. The spectra of the neat WBPUU, WBPUU/*Salvia* and WBPUU/*Salvia*/CNC_{es} systems as well as the one corresponding to the *Salvia* extract are displayed in **Figure 7.27** whereas an amplification of the N-H and carbonyl region between 4000 and 2000cm^{-1} and 1800 and 1600 cm^{-1} respectively is displayed in **Figure 7.28.**

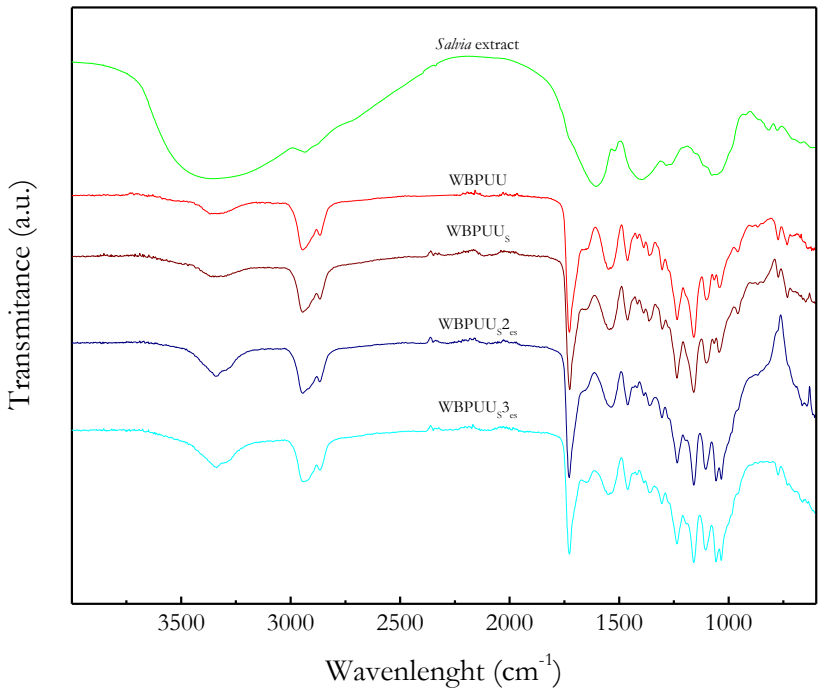

Figure 7.27 FTIR spectra of WBPUU, WBPUU/*Salvia* and WBPUU/*Salvia*/CNC_{es} inks and *Salvia* extract

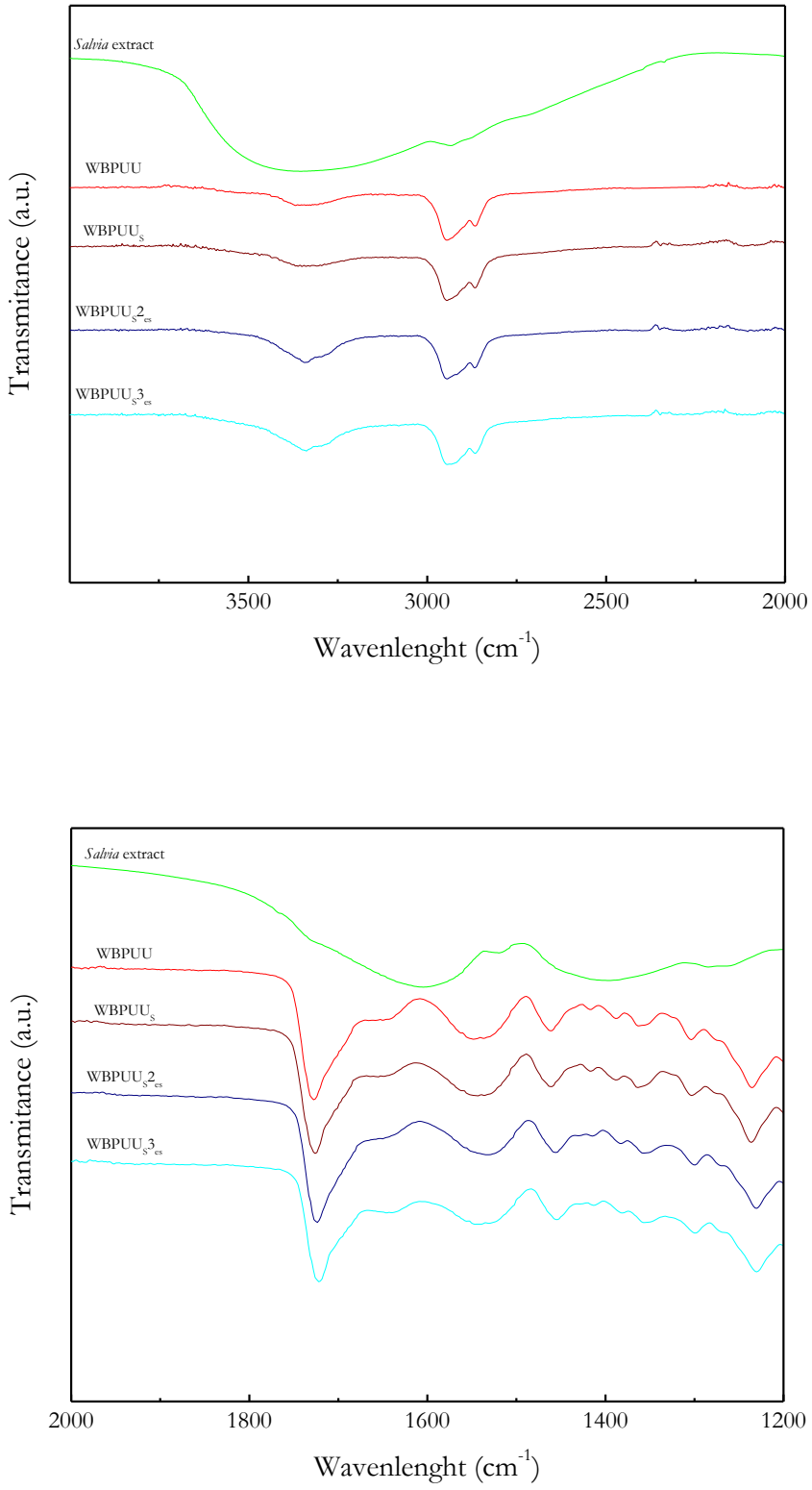

Figure 7.28 Amplification of the FTIR in the 4000-2000 cm^{-1} region (up) and 2000-1000 cm^{-1} region (down)

As was observed in previous chapters, the polyurethane ureas presented two main regions in the ranges 3500-3100 cm^{-1} [37] and 1800-1600 cm^{-1} [38], corresponding to the N-H and C=O of urethane and urea groups respectively. In the case of the neat *Salvia*, a broad peak is observed in the interval between 3500 and 3000 cm^{-1}, related to the hydroxyl groups of the bioactive compounds present in the extract, such as phenolic ones [16]. Additionally, the band situated around ~1700 cm^{-1} is assigned to the C=O of the carboxylic groups of phenolic compounds, whereas the peak situated around ~1590 cm^{-1} corresponded to the C=C of aromatic rings [39].

Analysing the spectra of the WBPUU/*Salvia* and WBPUU/*Salvia*/CNC_{es} systems, an increase of the intensity of the band situated between 3500 and 3000 cm^{-1} was observed, illustrating the overlapping of the signal of the neat WBPUU with the one corresponding to hydroxyl groups presented in the bioactive extract. The band assigned to the C=O of urethane and urea groups [38] for the systems containing CNC is translated towards lower wavelength in the same way as observed previously with the addition of the nanoentities. Regarding the inclusion of *Salvia*, the band corresponded to C=O at the obtained spectrum did not show any displacement with the addition of *Salvia*, showing a similar wavelength than the WBPUU.

Moreover, the influence of the plant extract in the thermal stability of the printed pieces, was studied by TGA. The weight curves and their derivative curves were displayed in **Figure 7.29**, whereas the degradation temperatures of the different systems are displayed in **Table 7.9**. The degradation curve of the *Salvia* extract showed a continuous loss of weigh from 30 ºC. After an initial weight loss corresponding to the humidity loss, most of the weight loss occurred between 150 and 400 ºC, assigned to decomposition of polysaccharides, obtaining a residue higher than 40% remained after the degradation process, as also seen in other plant extracts [40,41]. Contrary WBPUU matrix, the WBPUU containing *Salvia* and the WBPUU/*Salvia*/CNC_{es} nanocomposites showed a two-step degradation as was observed in previous chapters for this type of WBPUU. Despite the addition of CNC by *ex situ* method resulted in an increase of the thermal stability as was observed in Chapter 6, the presence of *Salvia* extract in the WBPUU backbone resulted in an early weight loss of the composites due to the aforementioned lower thermal stability of the *Salvia* extract. Concretely, systems containing *Salvia* extract presented a lower T_o compared with the WBPUU matrix.

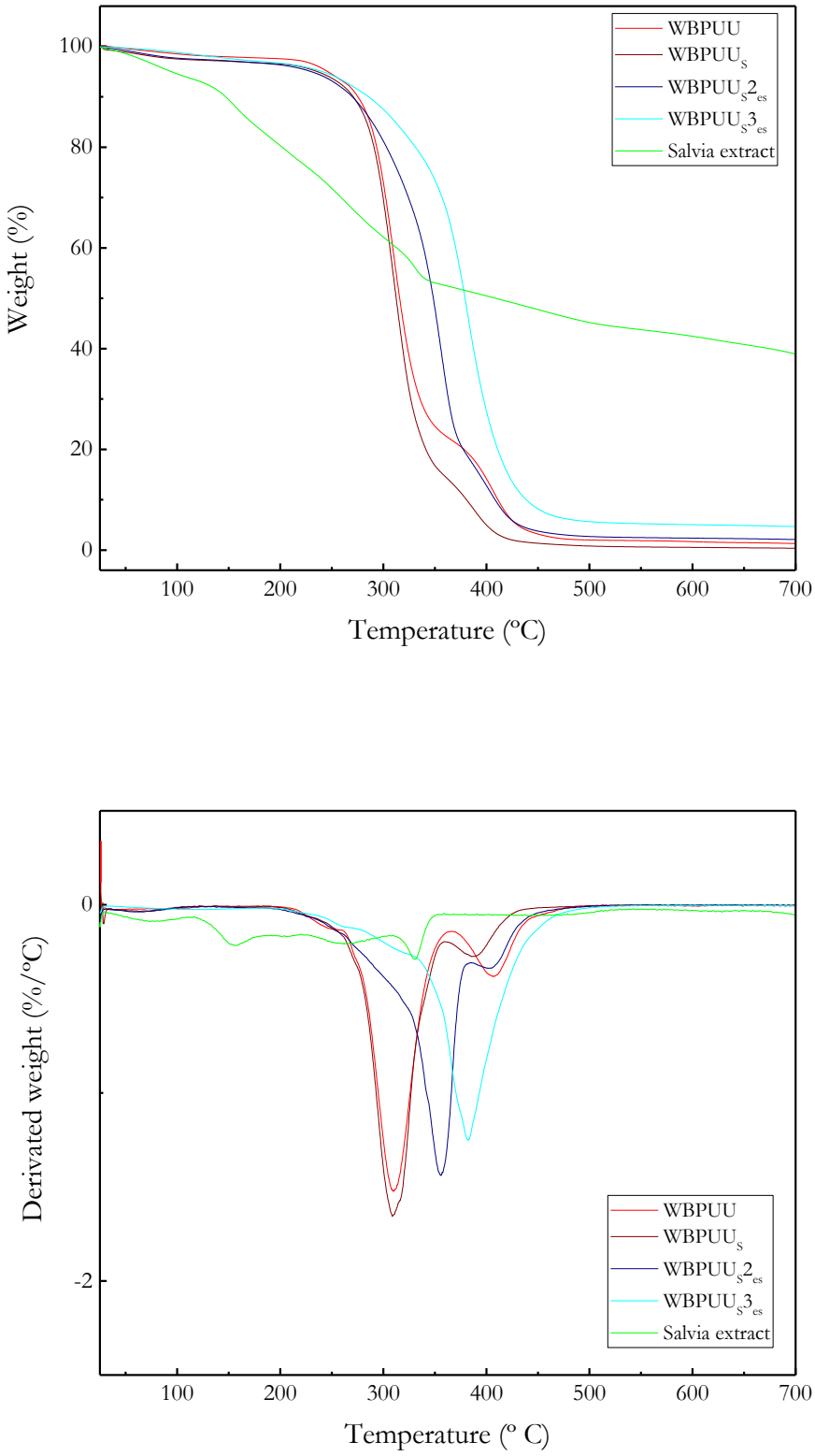

Figure 7.29 Weight curves (up) and DTG curves (down) of WBPUU, WBPUU/Salvia and WBPUU/Salvia/CNC$_{es}$ nanocomposites

Table 7.9 Initial degradation and maximum degradation temperatures of WBPUU, WBPUU/*Salvia* and WBPUU/*Salvia*/CNC_{es} nanocomposites

System	T_0 (°C)	T_d (°C)
WBPUU	246	310
$WBPUU_S$	236	310
$WBPUU_S2_{es}$	232	355
$WBPUU_S3_{es}$	241	382

Analysing the DTG curves, **Figure 7.29** (down), the signal corresponded to the main degradation process in systems containing CNC sweeps towards higher temperatures as a result of the effective interactions between the matrix and CNC and the stabilizing effect of the CNC, being higher the temperature of the peak as the CNC content increased. The addition of *Salvia*, contrary, did not affect the main degradation process, showing $WBPUU_S$ similar T_d compared with the WBPUU matrix.

7.3.2.4 Antimicrobial properties of the WBPUU/Salvia

Finally, antimicrobial test has been carried out by the methodology explained in the 2.2.10 section of Chapter 2. By this way, the prepared $WBPUU_S3_{es}$ scaffolds was tested against Gram negative *Escherichia coli* and Gram positive *Staphylococcus aureus* to demonstrate the antimicrobial activity of the ink. For comparative purpose, a scaffold of the WBPUU matrix without *Salvia* extract has been also tested, as well as the *Salvia* extract in powder form to confirm the antimicrobial properties of the pure extract observed in the literature [16,42]. The results of the obtained halo of inhibition after 24 h is displayed in **Table 7.10**, whereas the images of the samples after the test are displayed in **Figure 7.30** and **7.31** for *E. Coli* and *S. Aureus* respectively.

The WBPUU showed an absence of antimicrobial activity against *E. Coli*, not presenting any sign of inhibition halo. Contrary, in the case of the samples tested against *S. Aureus*, one of the studied samples of WBPUU presented an inhibition halo of 1 mm after 1 day of incubation, as can be observed in **Figure 7.31**, suggesting that the WBPUU system can have some bacteriostatic properties. However, the absence of inhibition zone observed in the other studied samples of WBPUU system suggested that these property was very weak.

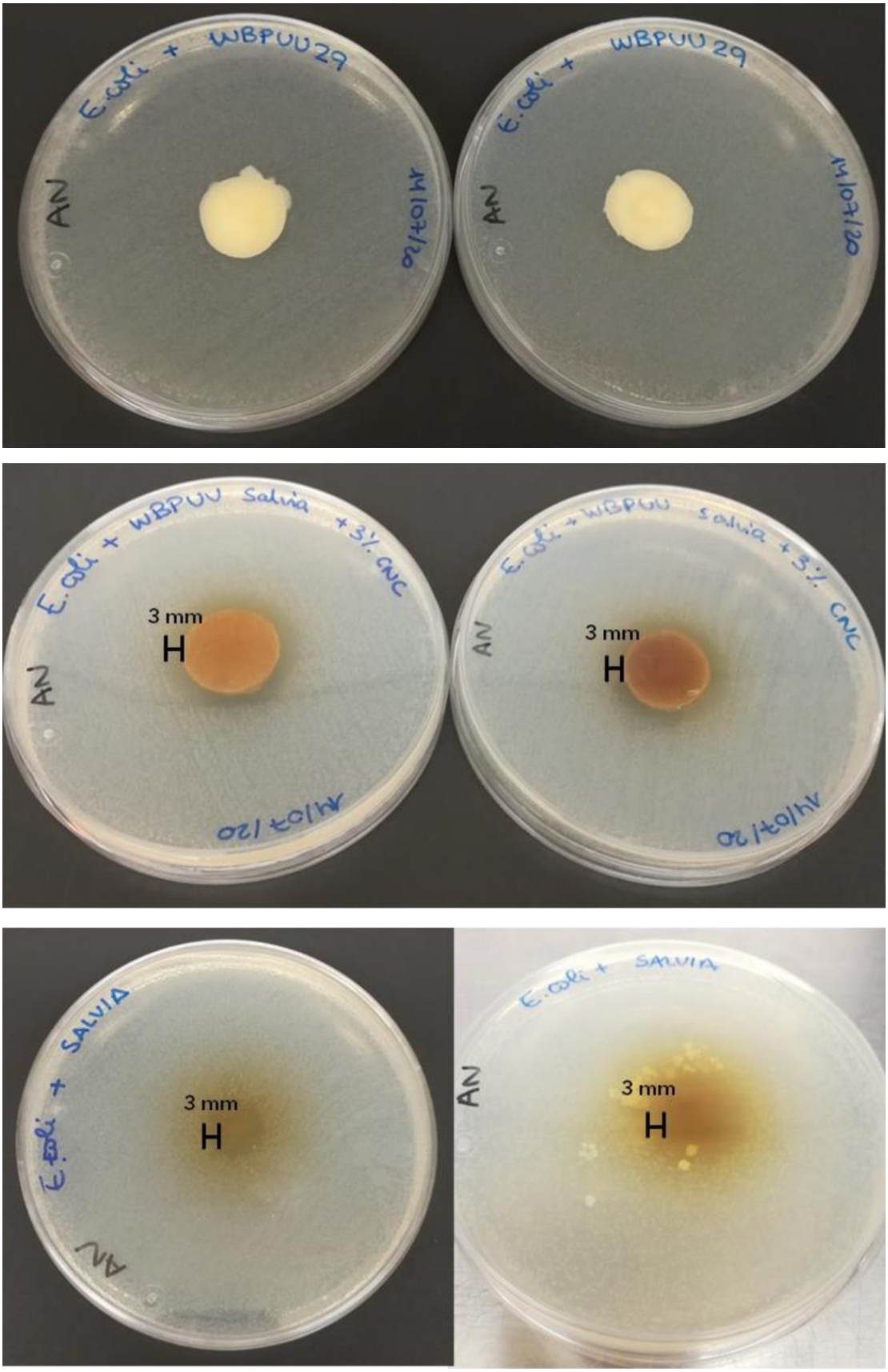

Figure 7.30 Antimicrobial tests of WBPUU, WBPUU$_S$3$_{es}$ and *Salvia* extract against *E. Coli* after 1 day of incubation at 37 ºC

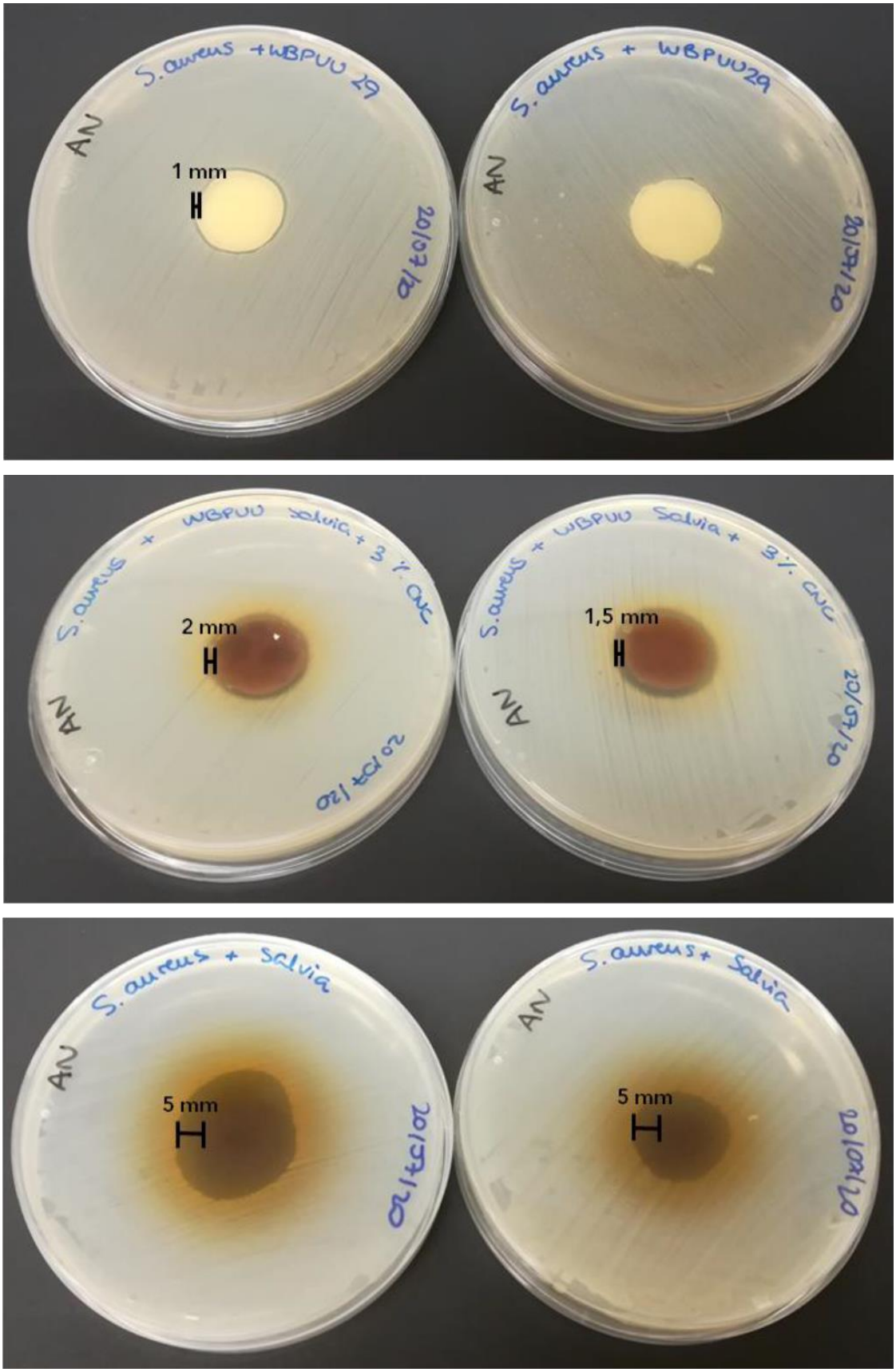

Figure 7.31 Antimicrobial tests of WBPUU, WBPUU$_S$3$_{es}$ and *Salvia* extract against *S. Aureus* after 1 day of incubation at 37 ºC

Table 7.10 Halo of inhibition of the prepared system after 24 h of exposition to *E. Coli* and *S. Aureus*

System	Halo of inhibition after 24h (mm)	
	E. Coli	*S. Aureus*
WBPUU	0±0	0.5±0.5
WBPUU$_S$3$_{es}$	3±0	1.75±0.25
***Salvia* extract**	3±0	5±0

The printed scaffolds containing *Salvia* extract presented after 1 day of incubation clear inhibition halos in all samples, presenting values clearly higher than the WBPUU matrix. These results confirmed the increase of the antibacterial and bacteriostatic properties of the ink containing *Salvia*. Comparing the obtained results for both bacteria, the WBPUU$_S$3$_{es}$ presented higher antibacterial activity against *E. Coli*, showing a higher inhibition halo than the observed one against *S. Aureus*. Additionally, the *Salvia* extract were also tested in the form of powder, so as to confirm the antimicrobial and antibacterial properties observed in the literature. The obtained results confirmed the antibacterial properties of the plant extract, presenting higher inhibition halos than the WBPUU$_S$3$_{es}$ in the case of *S. Aureus*, and the same size in the case of *E. Coli*. The lower amount of *Salvia* extract embedded in the WBPUU compared to the pure extract explain the lower halos of the former.

Anyway, according to the literature the extraction method of the extract plays a major role as far as the obtaining of the higher amount of polyphenolic compounds is concerned. A more effective extraction of the *Salvia* extract than the used one in the present work could lead to the obtaining of extract richer in polyphenolic and other compounds, resulting in an increase of the antibacterial properties of both extract and inks containing the extract.

7.3.3 Conclusions

In this part, WBPUU/*Salvia* extract based inks were prepared in order to obtain printable inks presenting antimicrobial activity. Additionally, CNC was added *ex situ* with the aim of improving the printing performance of the inks.

The rheological properties showed a decrease of the viscosity, yield point and storage modulus with the addition of the *Salvia* extract, suggesting that this plant extract acts as a surfactant when are added during the formation of the particles, leading to the decrease of the rheological parameters. This behavior was confirmed by the DLS and Z potential measurements, where lower particle size as well as more stable dispersion were obtained with

the inclusion of *Salvia* extract in the synthesis of the WBPUU. Regarding the addition of CNC via *ex situ* method, as was observed in Chapter 6, the addition of the nanoentities after the synthesis resulted in an increase of the shape fidelity, obtaining a final piece with optimal appearance. In this case, the $WBPUU_S3_{es}$ exhibits the best results.

Finally, the antimicrobial activity of the WBPUU/*Salvia* system was tested against Gram positive *S. Aureus* and Gram negative *E. Coli,* in order to confirm the viability as potential inks with antibacterial properties. The performed tests showed an increase of the antibacterial activity in the printed pieces from the $WBPUU_S3_{es}$ system compared with the WBPUU matrix, confirming the successful incorporation of the *Salvia* extract, which provided to the printed pieces with this ink antibacterial properties.

7.4 References

[1] M.S. Alhakawati, C.J. Banks, Removal of copper from aqueous solution by Ascophyllum nodosum immobilised in hydrophilic polyurethane foam, J. Environ. Manage. 72 (2004) 195–204. https://doi.org/10.1016/j.jenvman.2004.04.010.

[2] H. Ali, Biodegradation of synthetic dyes — A review, Water Air Soil Pollut. 213 (2010) 251–273. https://doi.org/10.1007/s11270-010-0382-4.

[3] M. Saleem, T. Pirzada, R. Qadeer, Sorption of acid violet 17 and direct red 80 dyes on cotton fiber from aqueous solutions, Colloids Surf. A 292 (2007) 246–250. https://doi.org/10.1016/j.colsurfa.2006.06.035.

[4] E. Forgacs, T. Cserha, G. Oros, Removal of synthetic dyes from wastewaters: a review, Environ. Int. 30 (2004) 953–971. https://doi.org/10.1016/j.envint.2004.02.001.

[5] N.K. Amin, Removal of reactive dye from aqueous solutions by adsorption onto activated carbons prepared from sugarcane bagasse pith, Desalination 223 (2008) 152–161. https://doi.org/10.1016/j.desal.2007.01.203.

[6] M. Moraes, M. Keller, V. Masiero, L. Dolis, G. Villalobos, J. Carla, G. Moraes, G. Maria, Polyurethane foams synthesized from cellulose-based wastes: Kinetics studies of dye adsorption, Ind. Crop. Prod. 85 (2016) 149–158. https://doi.org/10.1016/j.indcrop.2016.02.051.

[7] C. Ding, S. Xu, J. Wang, Y. Liu, X. Hu, P. Chen, Controlled loading and release of methylene blue from LbL polyurethane/poly (acrylic acid) film, Polym. Adv. Technol. 23 (2011) 17–20. https://doi.org/10.1002/pat.2044.

[8] L. Kong, F. Qiu, Z. Zhao, X. Zhang, T. Zhang, J. Pan, D. Yang, Removal of brilliant green from aqueous solutions based on polyurethane foam adsorbent modified with coal, J. Clean. Prod. 137 (2016) 51–59. https://doi.org/10.1016/j.jclepro.2016.07.067.

[9] E.A. Moawed, M.F. El-shahat, Equilibrium , kinetic and thermodynamic studies of the removal of triphenyl methane dyes from wastewater using iodopolyurethane powder, J. Taibah Univ. Sci. 10 (2015) 46–55. https://doi.org/10.1016/j.jtusci.2015.03.008.

[10] R. Rajendran, P. Prabhavathi, S. Karthiksundaram, S. Pattabi, S.D. Kumar, Biodecolorization and bioremediation of denim industrial wastewater by adapted bacterial consortium immobilized on inert polyurethane foam (PUF) matrix: A first approach with biobarrier model, Polish J. Microbiol. 64 (2015) 329–338.https://doi.org/10.5604/17331331.1185230.

[11] H. Lade, S. Govindwar, D. Paul, Mineralization and detoxification of the carcinogenic azo dye congo red and real textile effluent by a polyurethane foam immobilized microbial consortium in an upflow column bioreactor, Int. J. Environ. Res. Public Health. 12 (2015) 6894–6918. https://doi.org/10.3390/ijerph120606894.

[12] S. Kumari, G.S. Chauhan, J.H. Ahn, Novel cellulose nanowhiskers based polyurethane foam for rapid and persistent removal of methylene blue from aqueous solutions, Chem. Eng. J. 304 (2016) 728–736. https://doi.org/10.1016/j.cej.2016.07.008.

[13] E.E. Baldez, N.F. Robaina, J. Ricardo, Separation science and technology study of rhodamine B retention by polyurethane foam from aqueous medium in presence of sodium dodecylsulfate, Sep. Sci. Technol. 44 (2009) 37–41. https://doi.org/10.1080/01496390903182396.

[14] A.T. Paulino, M.R. Guilherme, A. V Reis, G.M. Campese, E.C. Muniz, J. Nozaki, Removal of methylene blue dye from an aqueous media using removal of methylene blue dye from an aqueous media using superabsorbent hydrogel, superabsorbent

hydrogel supported on modified polysaccharide, J. Colloid Interface Sci. 301 (2006) 55–62. https://doi.org/10.1016/j.jcis.2006.04.036.

[15] Y. Huang, H. Yu, C. Xiao, Effects of Ca^{2+} crosslinking on structure and properties of waterborne polyurethane-carboxymethylated guar gum films, Carbohydr. Polym. 66 (2006) 500–513. https://doi.org/10.1016/j.carbpol.2006.04.001.

[16] N. Martins, L. Barros, C. Santos-buelga, M. Henriques, S. Silva, I.C.F.R. Ferreira, Evaluation of bioactive properties and phenolic compounds in different extracts prepared from Salvia officinalis L ., Food Chem. 170 (2014) 378–385. https://doi.org/10.1016/j.foodchem.2014.08.096.

[17] M. Ghorbanpour, M. Hatami, K. Kariman, P. Dahaji, Phytochemical variations and enhanced efficiency of antioxidant and antimicrobial ingredients in salvia officinalis as inoculated with different rhizobacteria, Chem. Biodivers. 13 (2016) 319–330. https://doi.org/10.1002/cbdv.201500082.

[18] A. Santamaria-Echart, I. Fernandes, F. Barreiro, A. Retegi, Development of waterborne polyurethane-ureas added with plant extracts: Study of different incorporation routes and their in fl uence on particle size, thermal, mechanical and antibacterial properties, Prog. Org. Coatings. 117 (2018) 76–90. https://doi.org/10.1016/j.porgcoat.2018.01.006.

[19] Y. Lin, S.J. Hwang, W. Shih, K. Chen, Development of a novel microorganism immobilization method using anionic polyurethane, J. Appl. Polym. Sci. 99 (2005) 738–743. https://doi.org/10.1002/app.22542.

[20] G. Tondi, V. Fierro, A. Pizzi, A. Celzard, Tannin-based carbon foams, Carbon 47 (2009) 1480–1492. https://doi.org/10.1016/j.carbon.2009.01.041.

[21] M.. Ashby, The properties of foams and lattices, Philos. Tramsactions R. Soc. A Math. Phys. Eng. Sci. 364 (2006) 15–30. https://doi.org/10.1098/rsta.2005.1678.

[22] V. Ribeiro, M.A. Mosiewicki, M. Irene, M. Coelho, P.M. Stefani, N.E. Marcovich, Polyurethane foams based on modified tung oil and reinforced with rice husk ash II: Mechanical characterization, Polym. Test. 32 (2013) 665–672. https://doi.org/10.1016/j.polymertesting.2013.03.010.

[23] T. Yuan-Chan, P. Kiatsimkul, G. Suppes, F. Hsieh, Physical properties of water-blown rigid polyurethane foams from vegetable oil-based polyols, Appl. Polym. Sci.

105 (2007) 453–459. https://doi.org/10.1002/app.

[24] T.H. Courtney, Mechanical Behavior of Materials, in: L. Groove (Ed.), 2nd edition, Waveland Press, 2005: p. 733.

[25] T. Calvo, Biobased polyurethanes and nanocomposites: From structure/properties relationship to shape-memory behavior, University of the Basque Country, 2017.

[26] K. Benhamou, H. Kaddami, A. Magnin, A. Dufresne, A. Ahmad, Bio-based polyurethane reinforced with cellulose nanofibers: A comprehensive investigation on the effect of interface, Carbohydr. Polym. 122 (2015) 202–211. https://doi.org/10.1016/j.carbpol.2014.12.081.

[27] M.A. Hubbe, D.J. Gardner, W. Shen, Contact angles and wettability of cellulosic surfaces: A review of proposed mechanisms and test strategies, Bioresources 10 (2015) 8657–8749.

[28] A.F. Afonso, R. Pereira, Â. Fernandes, R.C. Calhelha, A.M.S. Silva, I.C.F.R. Ferreira, S.M. Cardoso, Phytochemical composition and bioactive effects of salvia africana , salvia officinalis 'icterina' and salvia mexicana aqueous extracts, Molecules 24 (2019) 4327.

[29] A. Santamaría-Echart, Synthesis and characterization of waterborne polyurethane and polyurethane-urea towards eco-friendly materials by cellulose nanocrystals and plant extracts incorporation, University of Basque Country, 2017.

[30] L. Tmáková, S. Sekretár, Š. Schmidt, Plant-derived surfactants as an alternative to synthetic surfactants : surface and antioxidant activities, Chem. Pap. 70 (2016) 188–196. https://doi.org/10.1515/chempap-2015-0200.

[31] K. Holmberg, Natural surfactants, Curr. Opin. Colloid Interface Sci. 6 (2001) 148–159. https://doi.org/10.1016/S1359-0294(01)00074-7

[32] S. Salati, G. Papa, F. Adani, Perspective on the use of humic acids from biomass as natural surfactants for industrial applications, Biotechnol. Adv. 29 (2011) 913–922. https://doi.org/10.1016/j.biotechadv.2011.07.012.

[33] J. Lee, M. Kim, C.K. Hong, S.E. Shim, Measurement of the dispersion stability of pristine and surface-modified multiwalled carbon nanotubes in various nonpolar and polar solvents, Meas. Sci. Technol. 18 (2007) 3707–3712.

https://doi.org/10.1088/0957-0233/18/12/005.

[34] T. Sharma, G.S. Kumar, B.H. Chon, J.S. Sangwai, P.E. Program, E. Chemistry, Viscosity of the oil-in-water Pickering emulsion stabilized by surfactant-polymer and nanoparticle-surfactant-polymer system, Korea-Australia Rheol. J. 26 (2014) 377–387. https://doi.org/10.1007/s13367-014-0043-z.

[35] L. Li, Q. Lin, M. Tang, A.J.E. Duncan, C. Ke, Advanced polymer designs for direct-ink-write 3D printing, Chem. Eur. J. (2019) 1–15. https://doi.org/10.1002/chem.201900975.

[36] C.W. Peak, J. Stein, K.A. Gold, A.K. Gaharwar, Nanoengineered colloidal inks for 3D bioprinting, Langmuir 34 (3) (2017) 917–925. https://doi.org/10.1021/acs.langmuir.7b02540.

[37] A.K. Mishra, D.K. Chattopadhyay, B. Sreedhar, K.V.S.N. Raju, FT-IR and XPS studies of polyurethane-urea-imide coatings, Prog. Org. Coatings. 55 (2006) 231–243. https://doi.org/10.1016/j.porgcoat.2005.11.007.

[38] Y. Shi, X. Zhan, Z. Luo, Q. Zhang, F. Chen, Quantitative IR characterization of urea groups in waterborne polyurethanes, J. Polym. Sci. Part A Polym. Chem. 46 (2007) 2433–2444. https://doi.org/10.1002/pola.

[39] Z. Rafiee, M. Barzegar, M.A. Sahari, B. Maherani, Nanoliposomal carriers for improvement the bioavailability of high-valued phenolic compounds of pistachio green hull extract, Food Chem. 220 (2016) 115–122. https://doi.org/10.1016/j.foodchem.2016.09.207.

[40] M. Khan, A.H. Al-marri, M. Khan, N. Mohri, Pulicaria glutinosa plant extract: a green and eco-friendly reducing agent for the preparation of highly reduced graphene oxide, RCS Adv. 4 (2014) 24119–24125. https://doi.org/10.1039/c4ra01296h.

[41] M. Amina, H.M. Al-Youssef, T. Amna, S. Hassan, A.M., El-Shafae, H.Y. Kim, M. Khil, Poly(urethane)/G. Mollis Composite nanofibers for biomedical applications, J. Nanoeng. Nanomanufacturing 2 (2012) 85–90.

[42] A.P.O.P. Cuceu, M. Tofană, S.A. Socaci, C. Pop, A.M. Rotar, L. Salanţă, Determination of antioxidant capacity and antimicrobial activity of selected salvia species, (2016). https://doi.org/10.15835/buasvmcn-fst.

CHAPTER 8

GENERAL CONCLUSIONS AND FUTURE WORK

8. GENERAL CONCLUSIONS AND FUTURE WORK

8.1 General conclusions

This work was dedicated to WBPUU and its capability to be a good candidate for production of pieces by using DIW 3D-printing. The scientific aim of this work was to establish a relationship between the structure of the WBPUU and properties. The technological challenge was to prepare a series of inks suitable for DIW 3D-printing based on a WBPUU dispersion and confirmed. The inks were printable and the quality of the printing performance was adapted.

In this way WBPUU with different PCL/PEG molar ratio in their soft segment were synthesized and characterized in order to analyse the effect of the inclusion of PEG in the properties of the dispersions and films prepared from the dispersions. Regarding the former, the addition of PEG resulted in an increase of the particle size as well as in the decrease of the stability, observing the apparition of a core shell particle structure in the systems containing more amount of PEG. Moreover, the addition of PEG resulted in an increase of the elongation at break as well as in an increase of the hydrophilicity of the films, presenting however a decrease of the thermomechanical stability. Furthermore, systems containing high amounts of PEG showed a physical gelation as a result of the higher particle size and hydrophilicity of PEG, resulting more interesting for their application in DIW 3D-printing. In addition, the influence of the PEG molecular mass into the WBPUU was also studied obtaining that at low molecular mass of PEG (400 g mol^{-1}) the dispersion was too stable whereas at the highest molecular mass (1500 g mol^{-1}) the dispersion was not stable obtaining very poor properties. As a result of this section the system containing a 20 wt% of PEG with a molecular mass of 1000 g mol^{-1} in its SS was the better candidate and selected.

Once the WBPUU ink was selected, the influence of the solid content of the dispersion on the printing performance of the inks was studied by means of rheological measurements so

as to determine the ideal solid content for a successful printing performance. The results showed that the solid content variation pilots the rheological properties obtaining inks with higher viscosity and higher structuration as the solid content increased. However, systems presenting very high viscosity and yield point (WBPUU36 and WBPUU46) were not possible to extrude by DIW 3D-printing. Taking into account this limitations, the system containing 32 wt% of solid content presented the best printing performance.

Moreover, environmental friendly and water dispersible CNC were used as viscosity modulators in order to improve the printing performance of the inks. For that purpose, two strategies were proposed to incorporate CNC to the WBPUU based dispersions, the *in situ* addition of CNC and the *ex situ* one, which differ in the moment that the nanoentities were added to the WBPUU ink. In the former, the CNC are added during the synthesis, taking advantage of the water addition during the phase inversion, whereas the latter contemplated the addition of the nanoentities after the synthesis, dispersing the CNC by vigorous stirring. Different amounts of CNC were added to the inks by both methods and the rheological behaviour of the obtained nanocomposites was studied, as well as the properties of the pieces printed from the inks. The microscopy images of the inks confirmed that the different addition methods resulted in different dispositions of the CNC in the WBPUU particles and dispersion. In the *in situ* method the addition of CNC to the WBPUU prepolymer favours chemical interactions which resulted in a greater increase of the rheological properties. For *ex situ* addition, the nanoentities are disposed around the particles interacting physically. The latter resulted in a slighter modification of the rheological parameters presenting the system with 2 wt% CNC added *ex situ* method lower viscosity and storage modulus than 0.5 wt% CNC *in situ* one. Regarding the increase of the CNC content, as happened with the solid content resulted in an increase of all rheological properties, but in a slighter way. In this case, the system containing 0.5 wt% of CNC *in situ* and the one of 2 wt% of CNC *ex situ* presented the best printing performances. Regarding the influence of the addition method on the properties of the printed piece, the *in situ* addition of CNC resulted in pieces presenting higher Young modulus a thermomechanical stability as a result of the successful reinforcement of the CNC. Contrary, the *ex situ* addition of CNC presented a slighter modification of the mechanical properties and thermomechanical stability due to the lower interactions between the WBPUU and the CNC, presenting in this case a lower increase of Young modulus as well as a lower increase of the thermomechanical stability compared with the *in situ* method.

Two potential applications of the WBPUU inks were proposed and analysed to demonstrate their viability. Regarding the former, in order to obtain porous materials for the absorption of pollutants, scaffolds were prepared from the WBPUU/CNC_{is} system by freeze drying technique. Different amounts of CNC were studied as well as different immersion times in $CaCl_2$ previous to freeze dry, resulting in scaffolds presenting a panel of mechanical properties and morphologies. The improve of printing performance observed for inks containing CNC resulted in scaffolds with homogeneous porosity. Additionally, the inclusion of these nanoentities decreases the porous size, and thus increases the water absorption capacity as well as the rigidity of the scaffold. The immersion in $CaCl_2$ resulted in the formation of a rigid non-porous shell around the scaffold as can be observed by SEM, which resulted in the obtaining of scaffolds with a higher rigidity and additionally, a lower water absorption capacity. Taking into account the obtained water absorption results, the $WBPUU0.5_{is}$ scaffold was tested against the cationic methylene blue dye. The results showed that the selected scaffold absorbed successfully the methylene blue dye, obtaining an interesting absorption efficiency up to 86% in 24 h.

In a second part, *Salvia* extract was added by *in situ* method to a WBPUU based ink in order to obtain printable inks with antibacterial properties. The results showed that the inclusion of *Salvia* extract into the WBPUU ink resulted in a decrease of the particle size as well as in a decrease of the viscosity and storage modulus. In this case, the extract acts as emulsifier, leading to more stable dispersions presenting lower viscosity as well as lower particle size. So as to improve the printing performance of the inks, CNC was added after the synthesis. The *ex situ* addition of CNC gave to the $WBPUU_S$ ink the adequate increase of the viscosity, yield point and storage modulus which allow to obtain interesting printing performance. In this case the $WBPUU_S3_{es}$ ink presented the best results. In addition, antibacterial tests were carried out to the prepared $WBPUU_S3_{es}$ scaffolds against *S. aureus* and *E. Coli* bacteria, where the enhancement of the antimicrobial activity for both bacteria was observed after 24 h if comparing the scaffold containing *Salvia* extract with the one without it.

8.2 Future works

Based on this work and with the aim of continuing with the research in this field, different proposals are displayed, which can complete this work more thoroughly as well as can lead to suitable new outlines for other woks related with this field.

- Taking into account the interesting properties observed in the studied inks as well as the observed good printability, the study of the biocompatibility of the inks could be proposed, so as to analyse their possible implication in the human body. A positive result of biocompatibility, cytotoxicity and cellular adhesion studies can lead to promote some possible biomedical applications. In this context, the study of the viability of the prepared WBPUU/CNC scaffolds so as to promote cellular grown in their structure could represent a good way.

- As was observed in Chapter 7, the WBPUU/CNC printed scaffolds were successfully used in order to remove the cationic methylene blue dye from an aqueous solution, thus, the study of the removal of other cationic pollutants could be carried out, such as some metals like cooper, or other cationic dyes such as for example malachite green. Additionally, give a greater insight into the absorption process of the cationic pollutant by studying the Langmuir isotherm and other methods so as to confirm the chemical reaction between the dye and the WBPUU. Finally, the absorption capacity of the methylene blue by WBPUU/CNC based scaffolds has been studied at neutral pH, so to complete with this study, the absorption capacity of the scaffolds at acid and basic medium should be tested.

- Study the influence of the incorporation of *Salvia* extract by other routes, such as for example the *ex situ* method, that is, after the synthesis of the WBPUU matrix, on the rheology and the dispersion formation. Different combination of addition methods of both CNC and *Salvia* extract could lead to different disposition into the ink and different final properties of the ink. Additionally, the study of the addition of other interesting plants extracts in order to study their potential as additives to provide antibacterial or antimicrobial properties to the ink such as *Melissa* extract, or broccoli extract (Sulforaphane) is proposed.

- In this work, the infusion method was used in Chapter 7 in order to obtain the extract from the *Salvia*. Despite obtaining extract presenting antibacterial properties, the use of different and more adapted methods could lead to the obtain of extract richer in polyphenols that allows to higher antimicrobial activity.

SUPPLEMENTARY MATERIAL

APPENDIX A

ADJUSTMENT OF FLOW EXPERIMENTAL DATA TO RHEOLOGICAL MODELS AND YIELD POINT DETERMINATION

A.1 Objective

The objective of this appendix is to give a more insight view to the adjustment of the experimental data obtained from the flow test of the different inks to theoretical models as well as to the different yield point determination methods. So as to select the method that fits better the experimental data, four theoretical models were proposed and adjusted to the obtained data from the flow test and by means of their R^2, the best one will be selected. Regarding the determination of the yield point, contrary, as explained in the introduction many authors give their own interpretation of the yield point based on the deviation of the G' as a function of the shear stress (σ). In this context, four methods described in **Table 1.3** were selected, and the obtained yield point values were used for the Herschel Bulkley model, which contemplate the presence of the yield point. As happened with the models, the different R^2 values of the adjusted data with the determined yield point values will lead to the selection of the method that fits better with the experimental data.

A.2 Theoretical rheological models

For this study, four rheological models were selected so as to fit with the experimental data: power law model, Herschel Bulkley model, Casson model and Bingham model, which are commonly used so as to describe the rheology of non-Newtonian fluids [1]. The equations of the different used models are displayed in **Table SA.1.**

Table SA.1 Equations of the different studied rheological models

Model	Equation	Determination parameters	References
Power law	$\tau=K\,\dot{\gamma}^{n}$	K and n	[2]
Bingham	$\tau=\tau_O+\mu_p$	μ_p	[3]
Herschel Bulkley	$\tau=\tau_y+K_h\,\dot{\gamma}^{n_h}$	$K_h$and n_h	[4]
Casson	$\tau^{1/2}=k_{OC}^{1/2}+k_c^{1/2}\dot{\gamma}^{1/2}$	k_{OC} and k_c	[5]

A.2.1 Power law model

The power law model also known as the Ostwald de Waele power law, is a mathematical model commonly used so as to describe, but only approximately, the behaviour of a real non-Newtonian fluid. The mathematical expression is showed below:

$$\tau = K\,\dot{\gamma}^{n} \qquad \text{(SA.1)}$$

where τ is refered to the shear stress (Pa), $\dot{\gamma}$ is the shear rate (s^{-1}) , n is the fluid flow behaviour index which indicates the tendency of a fluid to shear thin and it is dimensionless, and K is the consistency coefficient which serves as the viscosity index of the system in Pa s^n. The parameters K and n can be determined from a plot of log τ versus log $\dot{\gamma}$ and the resulting straight line's intercept is log K and the slope is n. In **Figure SA.1** the graphical determination of the n and K parameters of the power law model is illustrated.

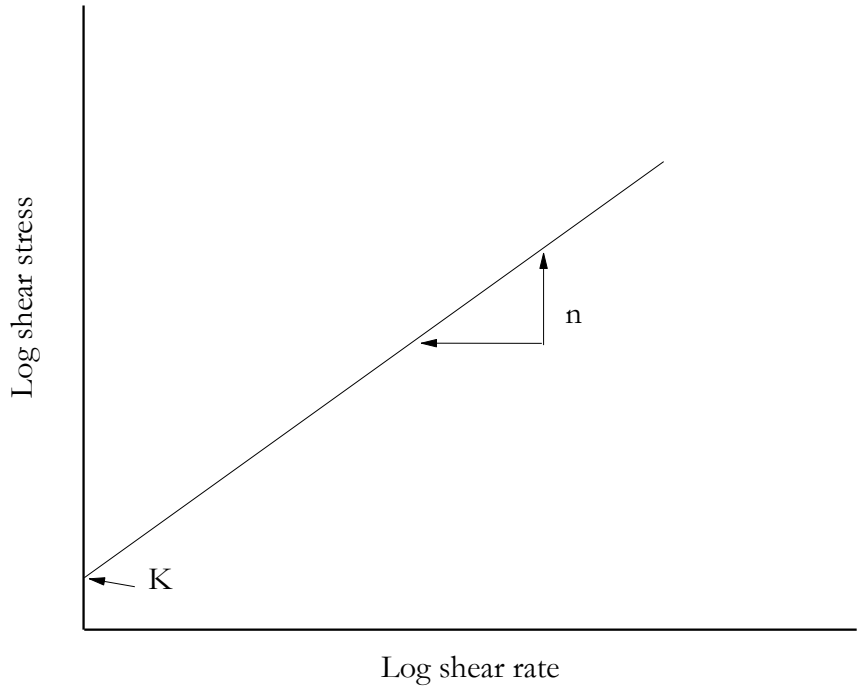

Figure SA.1 Representation of the graphical determination of power law parameters

The power law model gives a good description of the rheological behaviour of non-Newtonian fluids, however, it present drawbacks in high shear rate conditions [6].

A.2.2 Bingham plastic model

The Bingham plastic model is a two parameter model that is widely used in the drilling fluid industry to describe the flow characteristics of many type of non-Newtonian fluids. Mathematically can be described by the following equation.

$$\tau=\tau_0+\mu_p \qquad \text{(SA.2)}$$

where τ_0 is the yield point and μ_p the plastic viscosity. This model is used so as to describe Bingham plastics, which presented a yield point and a plastic viscosity independent of the shear rate.

The principal drawback of this model is the poor accuracy that present at very low shear rate and very high ones as well as its incapacity of describe the behaviour of fluids which presented a viscosity depending on the shear rate.

A.2.3 Herschel Bulkley model

The Herschel Bulkley model is an extension of the Bingham model, but considering a shear rate dependence of the viscosity. Mathematically is described as following:

$$\tau=\tau_y+K_h\,\dot{\gamma}^{n_h} \qquad \text{(SA.3)}$$

where τ is shear stress (Pa), $\dot{\gamma}$ is the shear rate (s^{-1}), τ_y is the yield point (Pa), K_h is the consistency index in Pa s^n and n_h is the flow index and is dimensionless.

This model corrects the deficiency of the Bingham model substituting the plastic viscosity term in the Bingham model by a power law expression. If the yield point is determined by an independent experiment, the K_h and n_h can be determined by linearizing the equation SA.3. In this case the parameters are determined from the plot of $\log(\tau-\tau_0)$ vs $\log\dot{\gamma}$, being the intercept the $\log K_h$ and the slope n_h.

The principal drawback of this method is the challenged concept of yield point [7], where its incorrect determination by an independent experiment can lead to a poor accuracy of the model.

A.2.4 Casson model

The Casson rheological model is a structure based model used to describe the flow behaviour of viscoelastic fluids, presenting a more gradual transition from Newtonian fluid to the yield region. It is described mathematically as the following:

$$\tau^{1/2}=k_{OC}^{1/2}+k_c^{1/2}\dot{\gamma}^{1/2} \quad \text{(SA.4)}$$

where k_{oc} is Casson yield stress (Pa s), k_c is Casson plastic viscosity in mPa.s, τ is shear stress (Pa) and $\dot{\gamma}$ is the shear rate (s^{-1})

The corresponding parameters for the Casson model can be determined from the straight line that is obtained from the plot of the square root of the shear stress ($\tau^{1/2}$) against the square root of the shear rate ($\dot{\gamma}^{1/2}$) with the slope k_c and intercept k_{oc}. The Casson yield stress is calculated as the square of the intercept and the Casson plastic viscosity is the square of the slope.

A.3 Yield point determination methods

As was explained in the introduction, the determination of the yield point, which is a key parameter so as to determine the printability of the inks as well as a necessary data in order to adjust the experimental data to the Herschel Bulkley model, still imply some contradictions in the literature. By definition, the yield point is a measure of the stress at which the network structure of the material starts to break down and hence starts flowing. Hence, inks presenting a yield point will act as a solid at stresses below this point and will flow at higher values.

Table SA.2 Different yield point determination methods (also showed in Table 1.3)

Author	Determination method	References
Lille et al./Cyriac et al.	Deviation of the G' from linearity	[8,9]
Shih et al.	Intercept between G' and G"	[10]
Sharma et al.	10% of deviation of the G' from linearity	[11]
De Graef et al.	Onset of the deviation from linearity of the G*	[12]

All the methods displayed in **Table SA.2** are based on the study of the curve obtained from the storage modulus or the complex modulus as function of the shear stress and only differ in the determination way of the yield point in that curve.

A.4 Experimental part

A.4.1 Yield point determination

With the aim of selecting the yield point determination method that fits better with the experimental data, the experimental values obtained from the WBPUU27 systems were used so as to determine the yield point values by the proposed method observed in **Table SA.2**.

In **Figure SA.2** the calculated yield points are plotted in the curve whereas in **Table SA.3** the yield point values are displayed as well as the R^2 obtained when this values are translated to the Herschel Bulkley model.

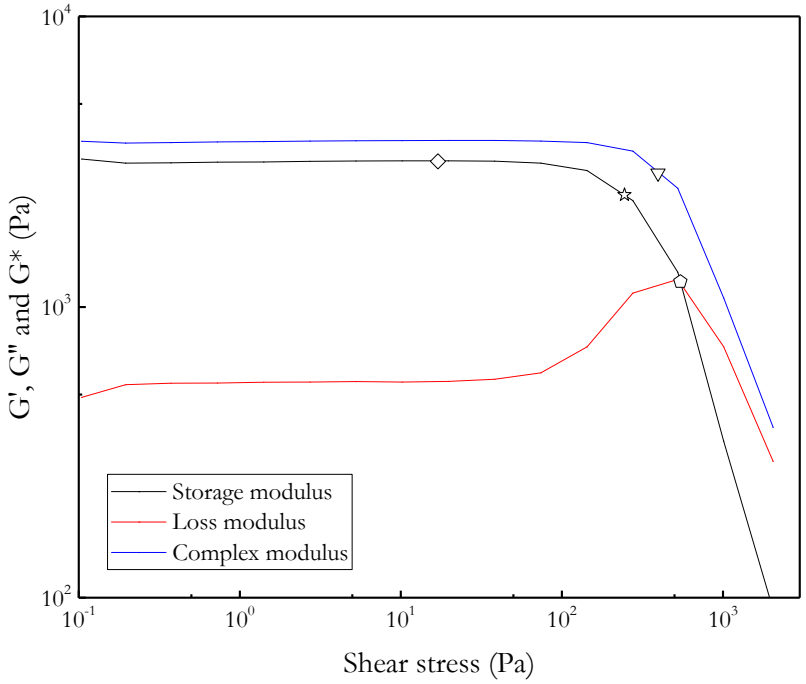

Figure SA.2 Determination of the yield point by different methods presented in the literature: (◇) *Cyriac et al.*, (⬠) *Shih et al.*, (☆) *Sharma et al.*, (▽) *De Graef et al.*

Table SA.3 Yield point values determined from the different methods for WBPUU27 system

Method	Yield point (Pa)	R^2 of Herschel Bulkley model	R^2 of Herschel Bulkley model (above 1 s^{-1})
Cyriac et al.	17	0.97	0.99
Shih et al.	545	0.50	0.92
Sharma et al.	245	0.81	0.99
De Graef et al.	396	0.56	0.93

Analysing the obtained results, the method proposed by *Cyriac et al.* seems to give a better fit with the obtained experimental data, showing the curve constructed by Herschel Bulkley model with this yield point a better R^2 compared with the ones obtained by other methods.

The higher amount of valid data obtained by this method, allowed to have more available data to perform the linear regression, whereas high values, such as the ones obtained by the method proposed by *De Graef et al.*, ruled out a lot of points. The log (σ-σ_y) used for the determination of the K and n index of the Herschel Bulkley model is limited by the σ_y, so high values of yield point resulted in multiple negative data whose log cannot be calculated. That being said, the method *Cyriac et al.* allowed to have more points to represent, and in this case resulted in a better fit of the experimental data, especially at low shear rates, representing better the behaviour of this system of inks as a function of the shear rate.

A.4.2 Adjustment of the experimental data to the rheological models

The experimental data obtained from the rheology flow test were adjusted to the proposed rheological model. In this case the system named as WBPUU27 and studied in Chapter 4 has been selected so as to illustrate the determination of the different parameters and to study the accuracy of the adjustment to the experimental data. In the **Table SA.3** the experimental parameters of the WBPUU27 flow curve are displayed.

Table SA.3 Experimental values of the WBPUU32 system

Shear rate (s^{-1})	Shear stress (Pa)
0.0111	4.0934
0.0154	7.4604
0.0229	12.861
0.0345	22.805
0.0521	39.408
0.0786	57.533
0.119	63.234
0.179	60.985
0.271	61.481
0.409	64.702
0.618	68.622
0.933	73.067
1.41	78.311
2.13	85.194
3.21	91.994
4.86	98.71
7.33	107.33
11.1	118.75
16.7	132.5
25.3	146.02
38.2	163.45
57.6	181.68
87.1	209.41
132	235.77

Regarding the power law model, following the methodology proposed previously, from the plot of log τ and log $\dot{\gamma}$, the regression of the obtained points displayed in **Figure SA.3** gave the following equation $\tau=1.79\ \dot{\gamma}^{0.31}$ with a R^2 of 0.78. As can be observed at low shear rates the experimental data is deviated from the linearity affecting to the adjustment. From this equation the K and n index were calculated obtaining a value of 0.31 for n and 61.65 for K. These parameters were used so as to construct the flow curve proposed by the model which is displayed in **Figure SA.4,** obtaining a R^2 of 0.963 in all the shear rate range and of 0.997 in the range between (1 and 130 s^{-1}). Analysing the obtained results, it can be observed the poor capacity of the power law model to fit with the experimental data at low shear rates due to the null consideration of this systems of the influence of the yield point.

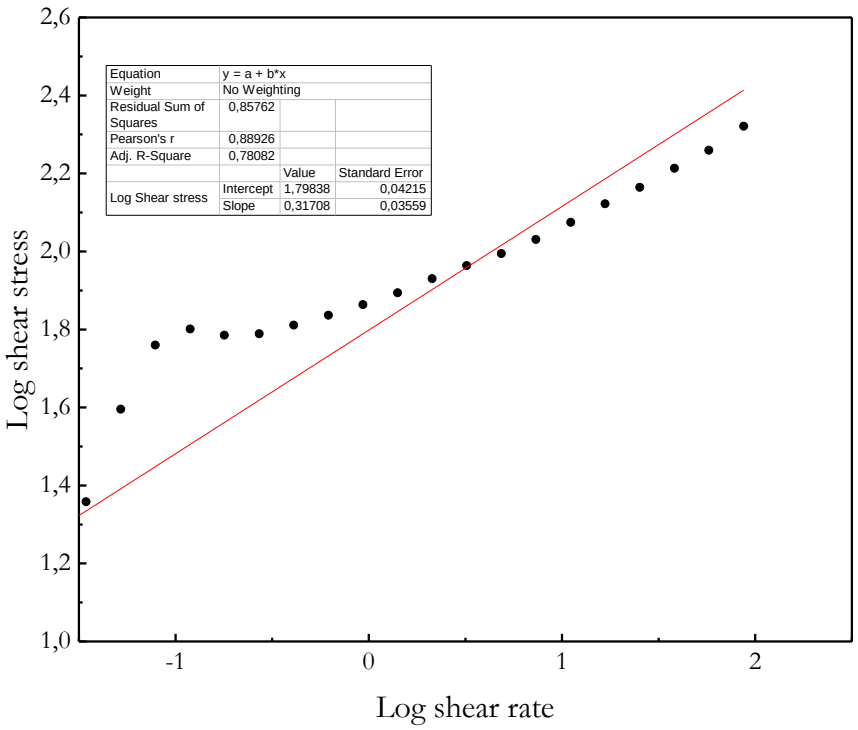

Figure SA.3 Determination of K and n index for power law model

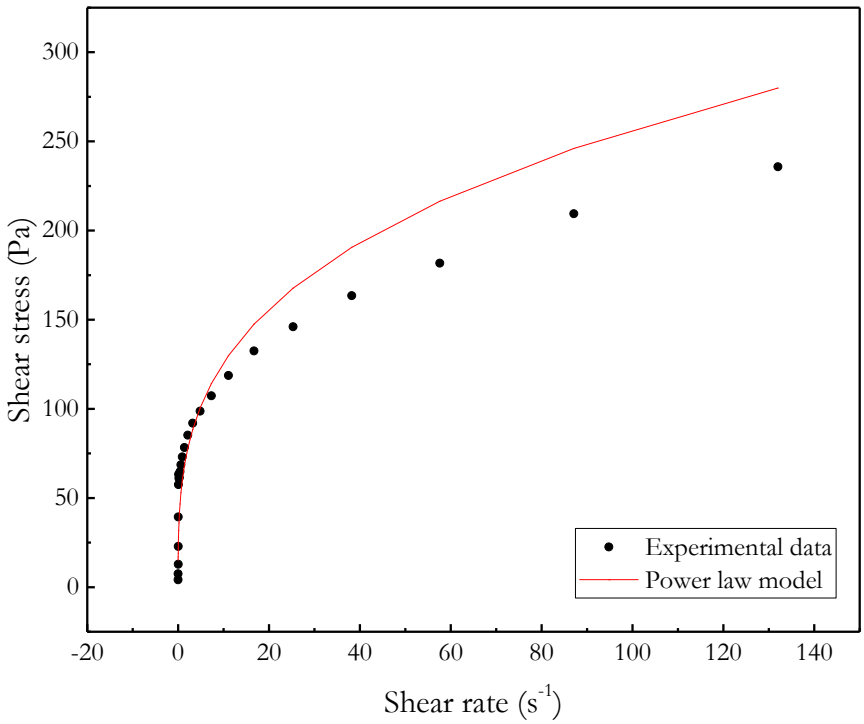

Figure SA.4 Experimental data of WBPUU27 and curve proposed by power law model

Regarding the Bingham model, since its equation did not contemplate a plastic viscosity dependent of the shear rate, as is the case of this type of systems, the adjustment of this model was not carried out since the adjustment will be very poor.

Taking into account the observed shear rate dependence, the Herschel Bulkley model could represent a more accurate model so as to describe the behaviour of the fluid. For the determination of the yield point, taking into account the results observed in A.4.1 section, the method proposed by *Cyriac et al.* is used in this case. From this method, a yield point of 17 Pa was obtained and was used so as to determine the n a K index from the log vs log $\dot{\gamma}$ plot as can be observed in **Figure SA.5.** As a result, a value of 0.249 and 61.39 were obtained for n and K respectively with a R^2 of 0.97. Taking into account the obtained parameters, a flow curve was constructed according to the Herschel Bulkley model, obtaining as a result a good fit with the experimental data, presenting a R^2 of 0.970 in all the shear rate range, and a R^2 of 0.993 in the range between 1-130 s^{-1}. The curve proposed by the Herschel Bulkley model is displayed in **Figure SA.6**.

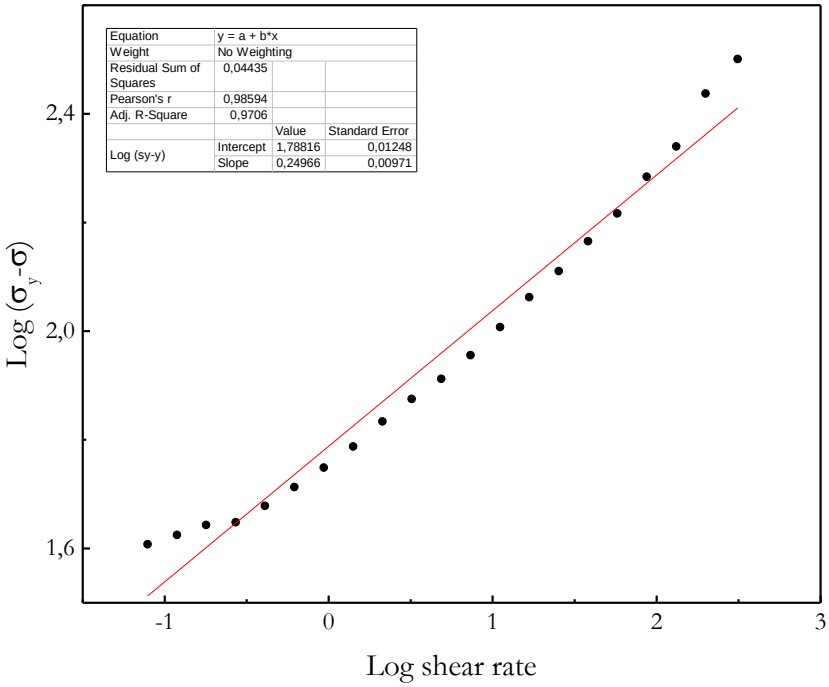

Figure SA.5 Determination of K and n index for Herschel Bulkley model

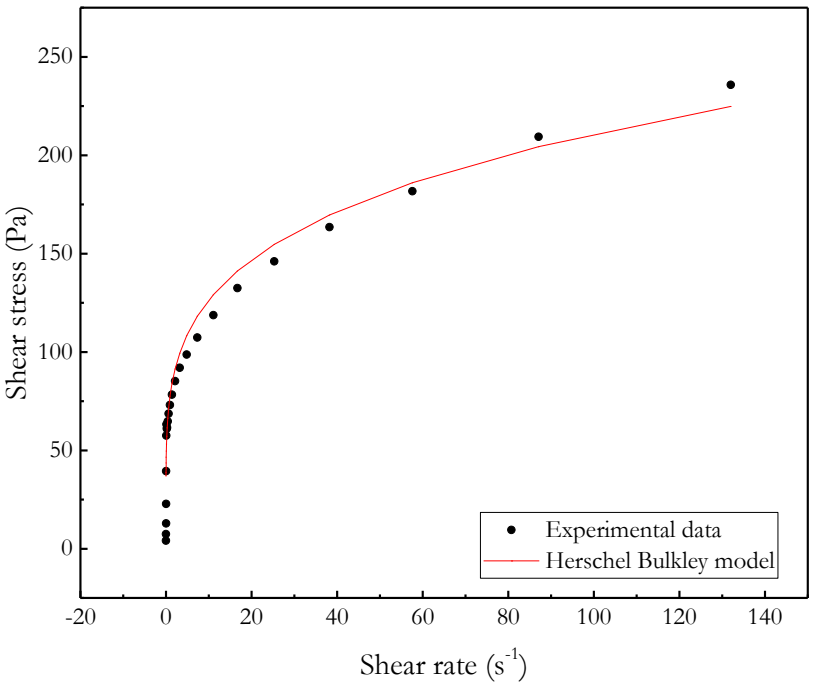

Figure SA.6 Experimental data of WBPUU27 and curve proposed by Herschel Bulkley model

Finally, the experimental data was adjusted to the Casson model. For this purpose, according to the previously explained methodology, the Casson yield point (Pa s), and the Casson plastic viscosity were determined by plotting square root of the shear stress versus the square root of the shear stress. From the obtained curve, which is displayed in **Figure SA.7**, a value of 51.98 and 0.688 were obtained for k_{oc} and k_c respectively. Taking the aforementioned parameters of the Casson model into account, a flow curve was construct obtaining a bad fitting with the experimental data as can be observed in **Figure SA.8**, obtaining a R^2 of 0.83 in all the shear rate range, and of 0.91 in the range between 1-130 s^{-1}.

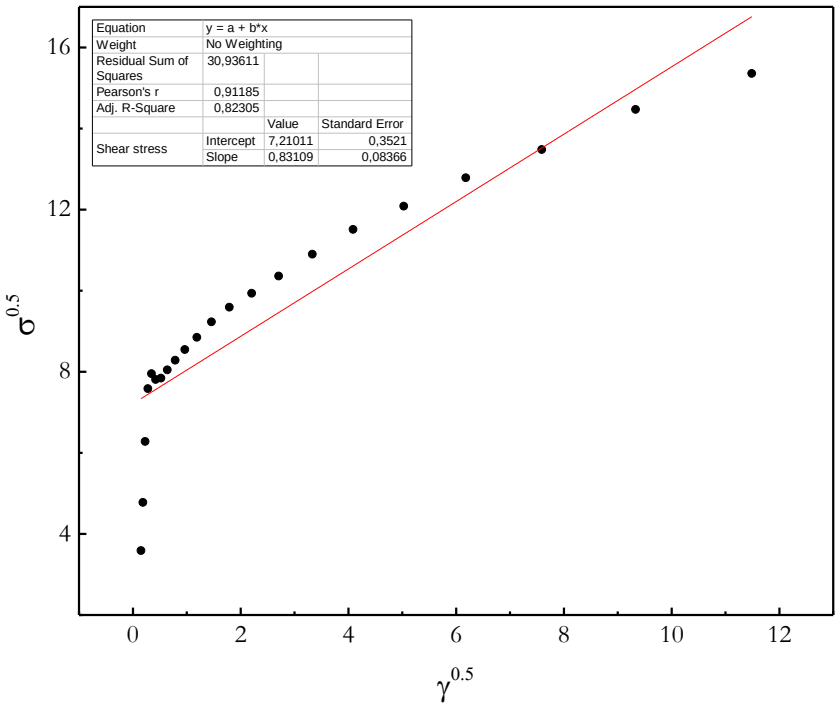

Figure SA.7 Determination of k_{oc} and k_c index for Casson model

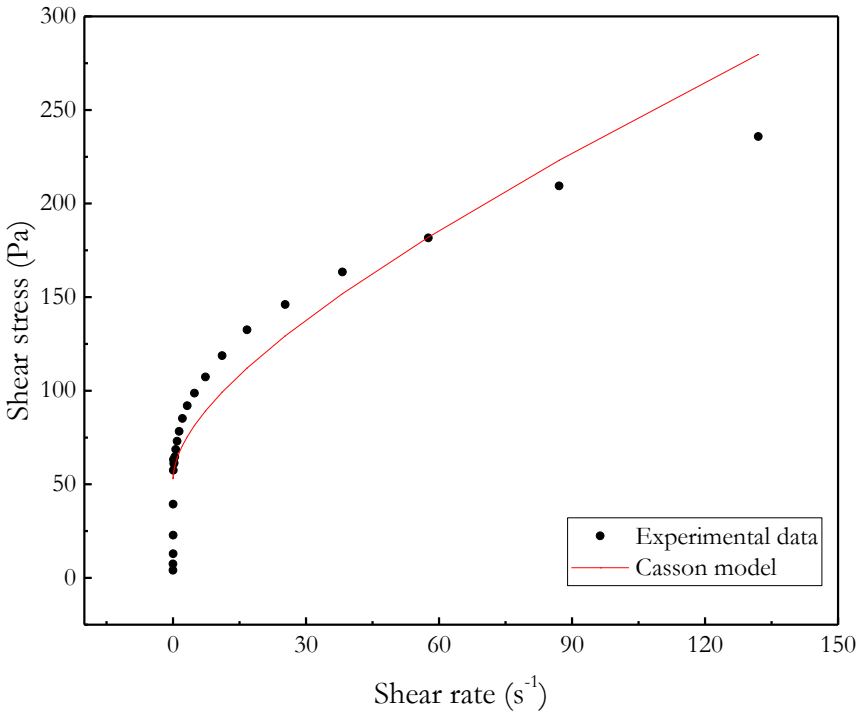

Figure SA.8 Experimental data of WBPUU27 and curve proposed by Casson model

A.5 Conclusions

In this appendix, the process of the selection of the most ideal determination method of the yield point as well as the selection process of the rheological model is displayed so as to give a greater insight into the criteria that has been followed in order to select the used method to characterize the synthesized inks.

For that purpose, several rheological models as well as some yield point determination methods observed in the literature were used so as to fit with the experimental data of WBPUU27 system, and thus select the ideal methods for this concrete WBPUU based inks.

Regarding the determination of the yield point, from among all the tested methods, the one proposed by *Cyriac et al.*, which takes into account the deviation from the linearity in the G' vs σ plot, gave the best fit with the experimental data, resulting in a higher R^2. Methods which consider higher values of yield point resulted in a lower fitting of the experimental data at low shear rate, resulting in a poorer adjustment between the data and the model.

Hence, in this work, the aforementioned method has been used in order to determine the yield point of the WBPUU inks.

Moreover, as far as the selection of the rheological model is concerned, despite power law model presented a quite good correlation with the experimental data, its null consideration of the yield point resulted in a poor fitting at low shear rates. Contrary, the Herschel Bulkley model, which includes the influence of the yield point, gave better fitting in all the range, obtaining the better fit from among all studied rheological models. Thus, this method was used so as to fit all the experimental data obtained from the prepared WBPUU based inks.

Finally, despite in this case the Herschel Bulkley model gave the best adjustment with the experimental data and the yield point determined by *Cyriac et al.* gave a better fit, the nature of the ink rules the selection of the better methods, thus, other systems will be better represented by other models and determination methods.

A.6 References

[1] F.J. Adewale, A.P. Lucky, A.P. Oluwabunmi, E.F. Boluwaji, Selecting the most appropriate model for rheological characterization of synthetic based drilling mud, Int. J. Appl. Eng. Res. 12 (2017) 7614–7629.

[2] M. Reiner, Ueber die Strömung einer elastischen Flüssigkeit durch eine kapillare, Kolloid-zeitshrift 39 (1926) 80–87.

[3] E.C. Bingham, Fluidity and plasticity, New York, 1922.

[4] R. Herschel, W.H., Bulkley, Konsistenzmessungen von gummi-benzollösungen, Kolloid-Zeitshrift 39 (4) (1926) 291–300.

[5] M. Casson, The rheology of disperse systems, Pergamon press, London, 1959.

[6] T.E. Becker, R.G. Morgan, W.C. Chin, J.E. Griffith, Improved rheology model and hydraulics analysis for tomorrow ' s wellbore fluid applications, SPE Prod. Oper. Symp. (2003).

[7] A. Khalili-Garakani, M.R. Mehrnia, N. Mostoufi, Analyze and control fouling in an airlift membrane bioreactor: CFD simulation and experimental studies, Process Biochem. 46 (2011) 1138–1145. https://doi.org/10.1016/j.procbio.2011.01.036.

[8] M. Lille, A. Nurmela, E. Nordlund, S. Metsa-Kortelainen, N. Sozer, Applicability of protein and fi ber-rich food materials in extrusion-based 3D printing, J. Food Eng.

220 (2018) 20–27. https://doi.org/10.1016/j.jfoodeng.2017.04.034.

[9] F. Cyriac, P.M. Lugt, R. Bosman, On a new method to determine the yield stress in lubricating grease on a new method to determine the yield stress in lubricating grease, Tribol. Trans. 58 (2015) 1021–1030. https://doi.org/10.1080/10402004.2015.1035414.

[10] W.Y. Shih, W. Shih, I.A. Aksay, Elastic and yield behavior of strongly flocculated colloids, J. Am. Ceram. Soc. 82 (3) (2004) 616–624. https://doi.org/10.1111/j.1151-2916.1999.tb01809.x

[11] M. Sharma, E. Kristo, M. Corredig, L. Duizer, Food hydrocolloids effect of hydrocolloid type on texture of pureed carrots : rheological and sensory measures, Food Hydrocoll. 63 (2017) 478–487. https://doi.org/10.1016/j.foodhyd.2016.09.040.

[12] V. De Graef, F. Depypere, M. Minnaert, K. Dewettinck, Chocolate yield stress as measured by oscillatory rheology, Food Res. Int. 44 (2011) 2660–2665. https://doi.org/10.1016/j.foodres.2011.05.009.

APPENDIX B

INFLUENCE OF THE CNC ADDITION METHOD IN THE RHEOLOGICAL PROPERTIES OF WBPUU/CNC INKS

B.1 Objective

The objective of this appendix is to provide a supplementary information about the differences between the *in situ* and *ex situ* addition methods of CNC, detailed in Chapters 5 and 6, respectively, as far as rheological properties is concerned. So as to give a greater insight into those differences, in this document the variation of the rheological properties obtained using both methods are plotted as a function of the CNC content to ease the comparison.

B.2 Comparison between the different evolution of the rheological properties when CNC addition by different methods

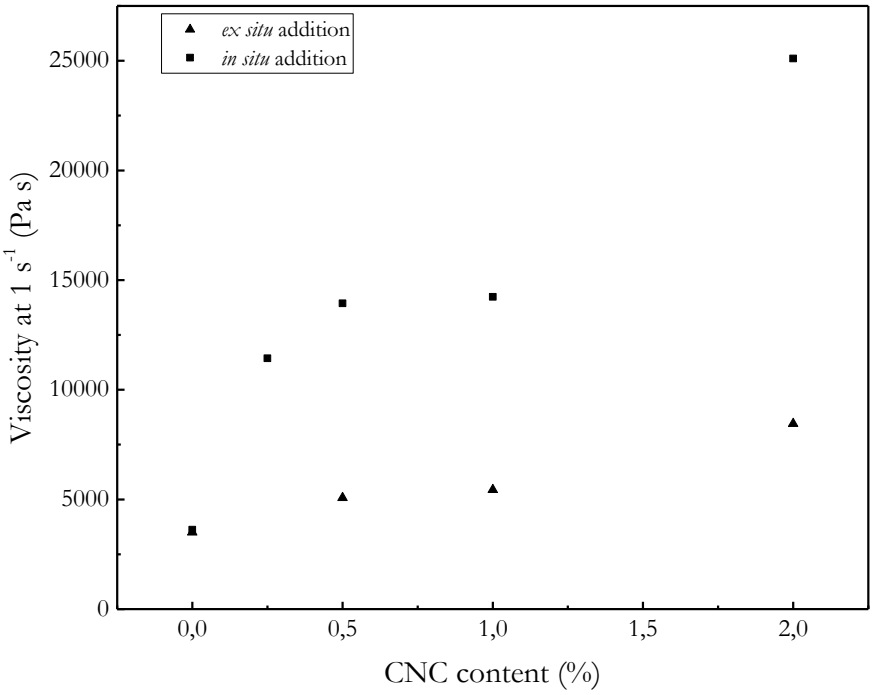

Figure SB.1 Evolution of the viscosity measured at 1 s^{-1} of the WBPUU/CNC nanocomposites obtained adding CNC by different strategies (*in situ* and *ex situ*) as a function of the CNC content

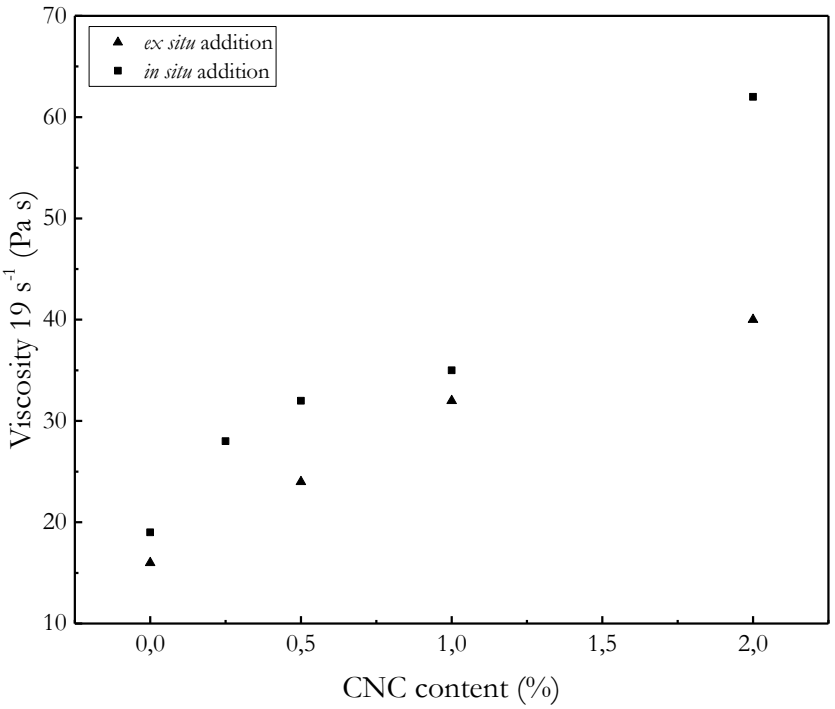

Figure SB.2 Evolution of the viscosity measure at 19 s^{-1} of the WBPUU/CNC nanocomposites obtained adding CNC by different strategies (*in situ* and *ex situ*) as a function of the CNC content

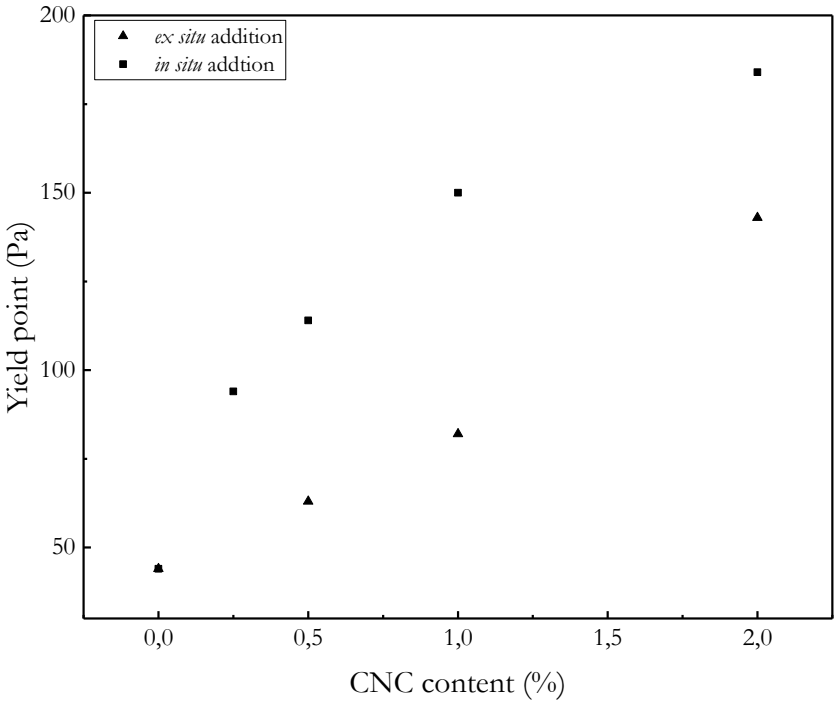

Figure SB.3 Evolution of yield point of the WBPUU/CNC nanocomposites obtained adding CNC by different strategies (*in situ* and *ex situ*) as a function of the CNC content

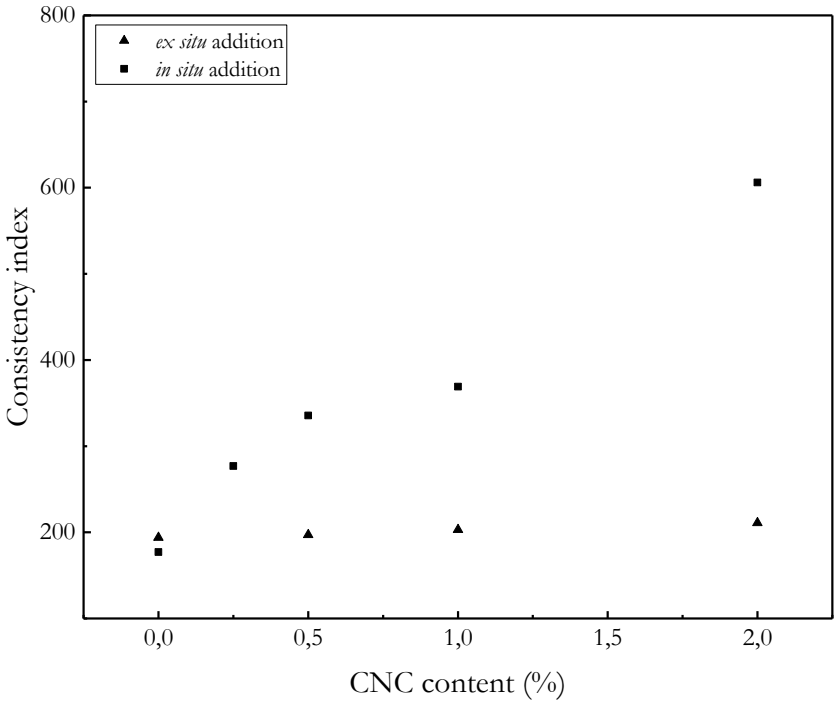

Figure SB.4 Evolution of consistency index of the WBPUU/CNC nanocomposites obtained adding CNC by different strategies (*in situ* and *ex situ*) as a function of the CNC content

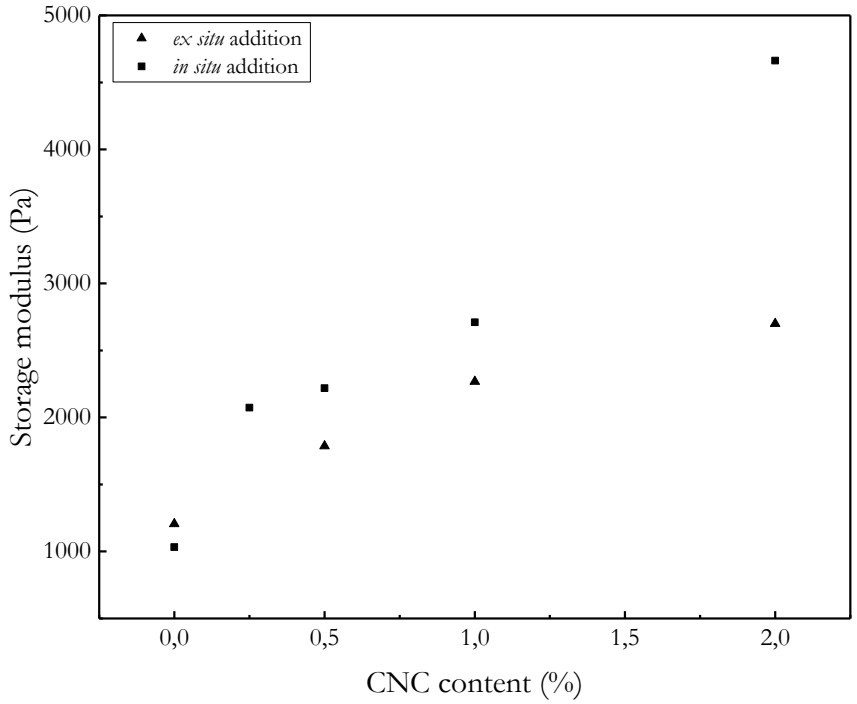

Figure SB.5 Evolution of the storage modulus of the WBPUU/CNC nanocomposites obtained adding CNC by different strategies (*in situ* and *ex situ*) as a function of the CNC content

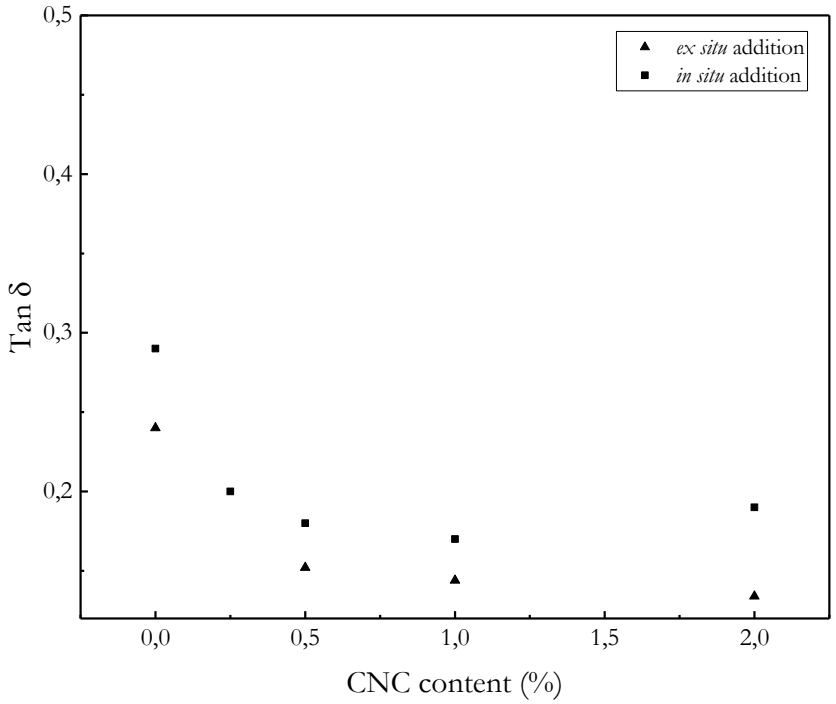

Figure SB.6 Evolution of the tan δ of the WBPUU/CNC nanocomposites obtained adding CNC by different strategies (*in situ* and *ex situ*) as a function of the CNC content

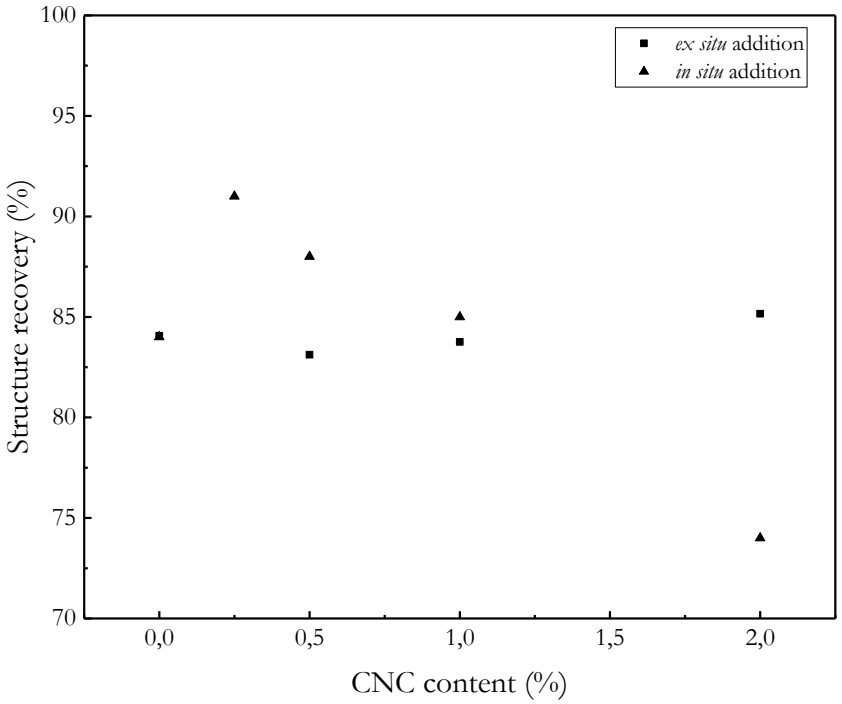

Figure SB.7 Evolution of the structure recovery of the WBPUU/CNC nanocomposites obtained adding CNC by different strategies (*in situ* and *ex situ*) as a function of the CNC content

APPENDIX C

RHEOLOGICAL COMPARISON OF SYSTEMS FROM DIFFERENT CHAPTERS & SHAPE FIDELITY MAPPING OF THE STUDIED INKS

C.1 Objective

The objective of this appendix is to provide additional information of the rheological characterization of the inks obtained in the different chapters. In the first part, the rheological properties of every system which showed good printing performance in the different chapters were represented for comparative purposes. In a second part, **Figure 1.11** of the introduction has been taken as a reference, to stablish an optimal shape fidelity window. The obtained values of the inks studied in this work are displayed in a similar graph where the optimal shape fidelity area observed in the literature was showed. Additionally, the different performed routes in every chapter so as to modify the shape fidelity are displayed.

C.2 Rheological comparison of system presenting good printing performance from every chapters

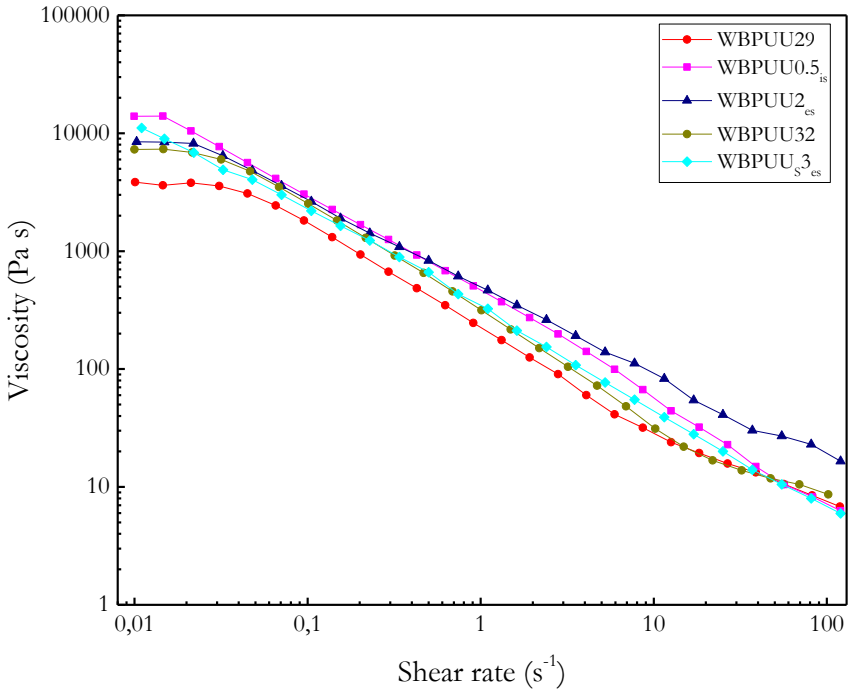

Figure SC.1 Evolution of the viscosity as a function of the shear rate of the systems selected as the ideal formulation for every chapter. (T = 22.5 °C)

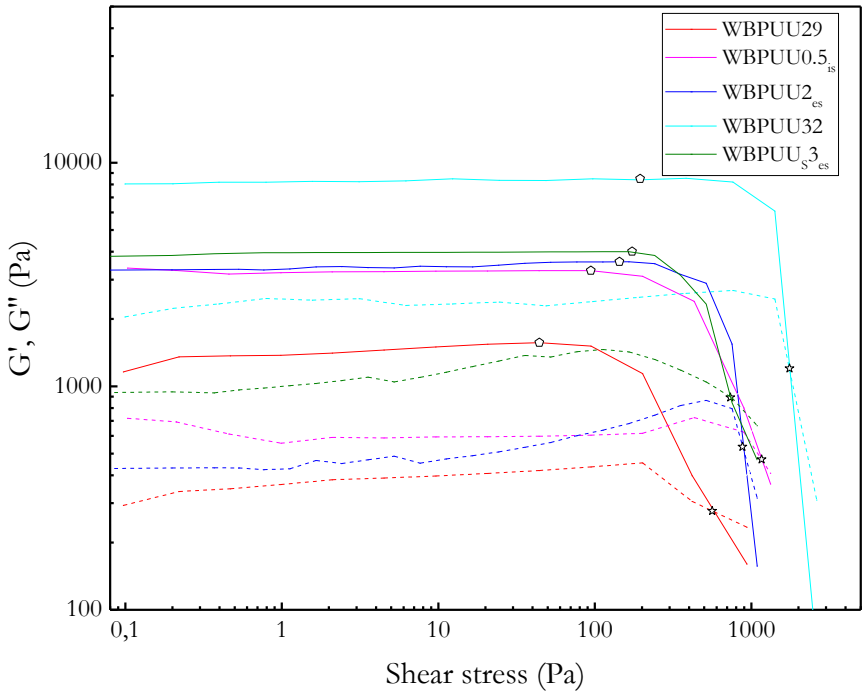

Figure SC.2 Yield point (Cyriac et al.) and flow point (G' = G") determination of the systems selected as the ideal formulation for every chapter. (T = 22.5 °C)

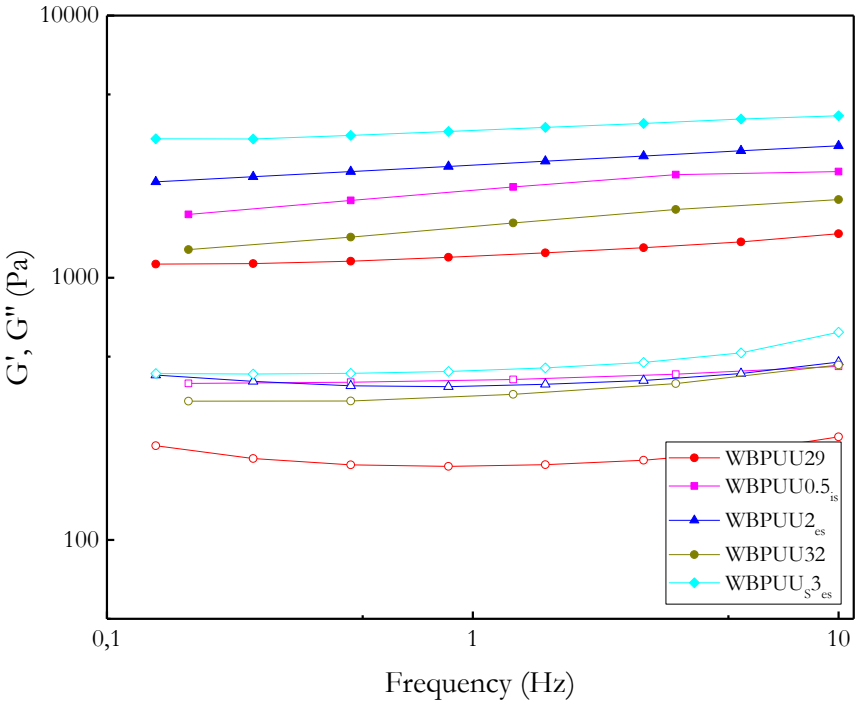

Figure SC.3 (Solid symbol) storage and (open symbol) loss moduli of the systems selected as the ideal formulation for every chapter. (T = 22.5 °C)

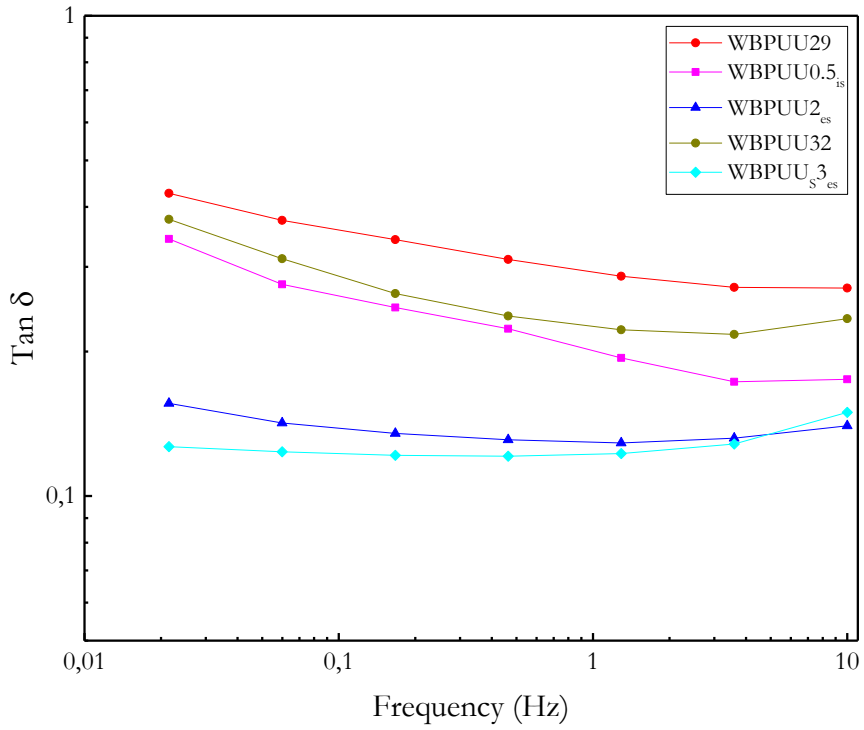

Figure SC.4 Tan δ of the systems selected as the ideal formulation for every chapter. (T = 22.5 °C)

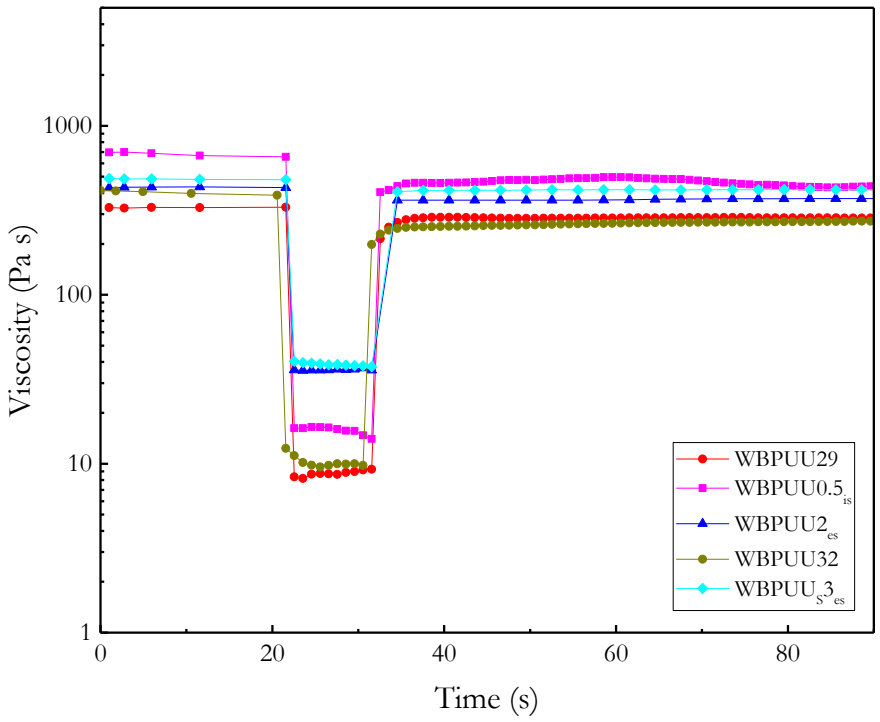

Figure SC.5 Structure recovery of the systems selected as the ideal formulation for every chapter. (T = 22.5 °C)

C.3 Study of the shape fidelity of the inks

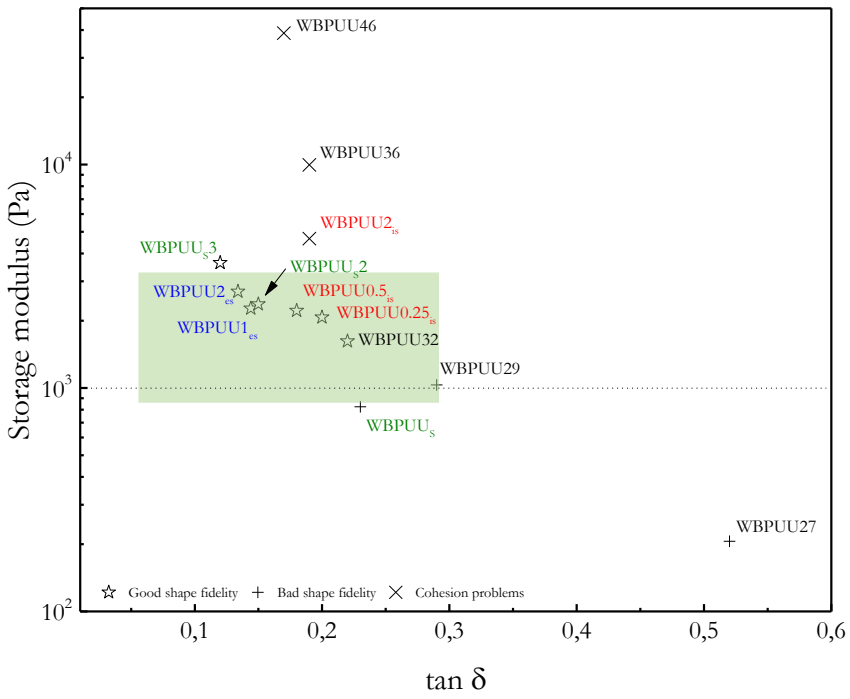

Figure SC.6 Mapping of the studied systems in the different chapters in a storage modulus vs tan δ graph. (…) Good shape fidelity downer limit of the storage modulus proposed by Li et al., the good shape fidelity area of both storage modulus and tan δ obtained from the literature data displayed in the **Figure 1.11** is delimited by the green coloured area. The colour of the samples are referred to the different chapters: solid content variation (black), *in situ* addition of CNC (red), *ex situ* addition of CNC (blue), *Salvia* and CNC *ex situ* addition (green).

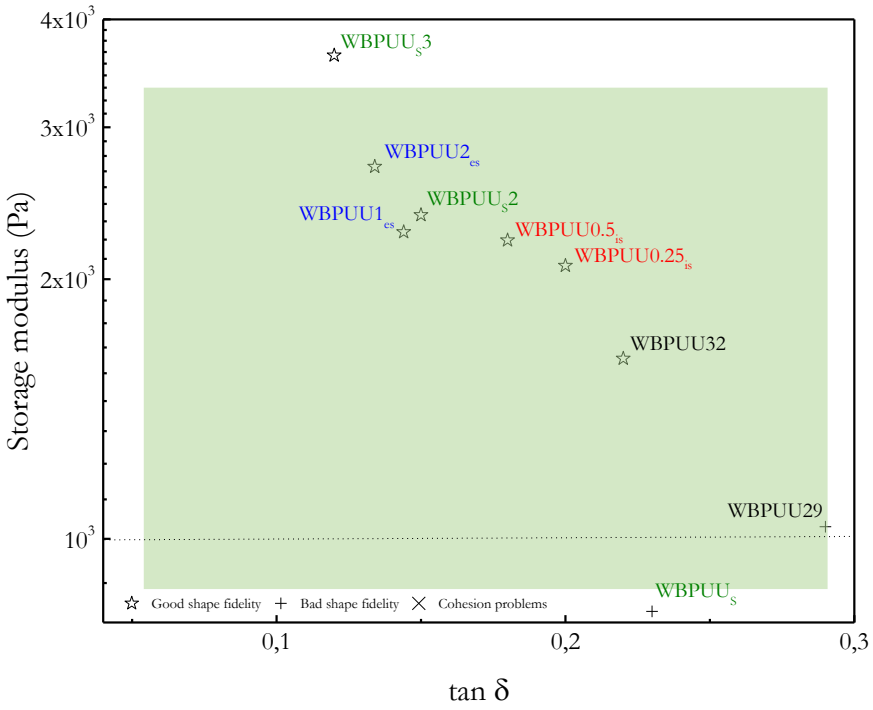

Figure SC.7 Magnification of the **Figure SC.6 i**n the region delimited from the results observed in the literature (green zone)

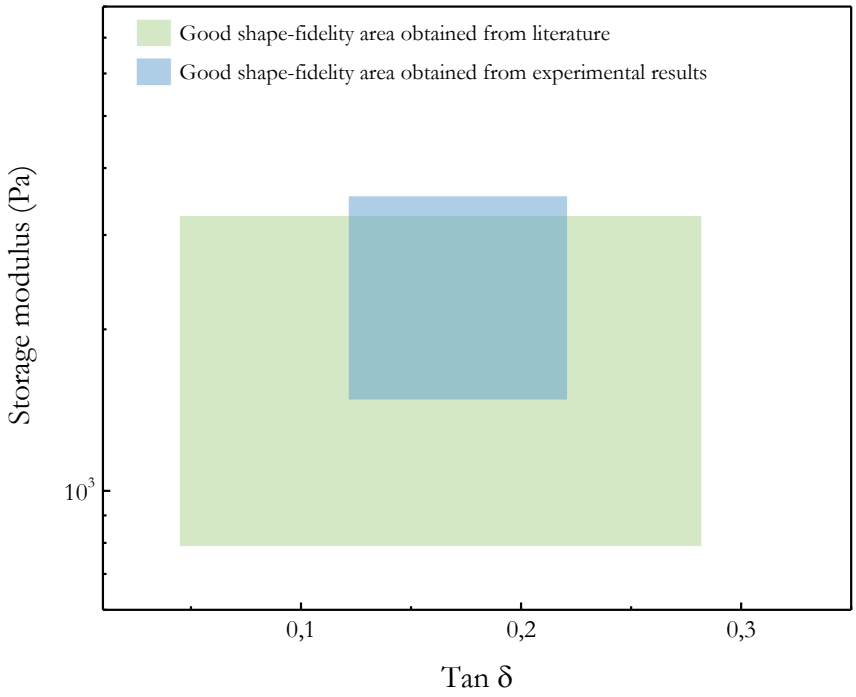

Figure SC.8 Comparison between the good shape-fidelity area obtained from literature and the one obtained from experimental results in a storage modulus vs tan δ plot

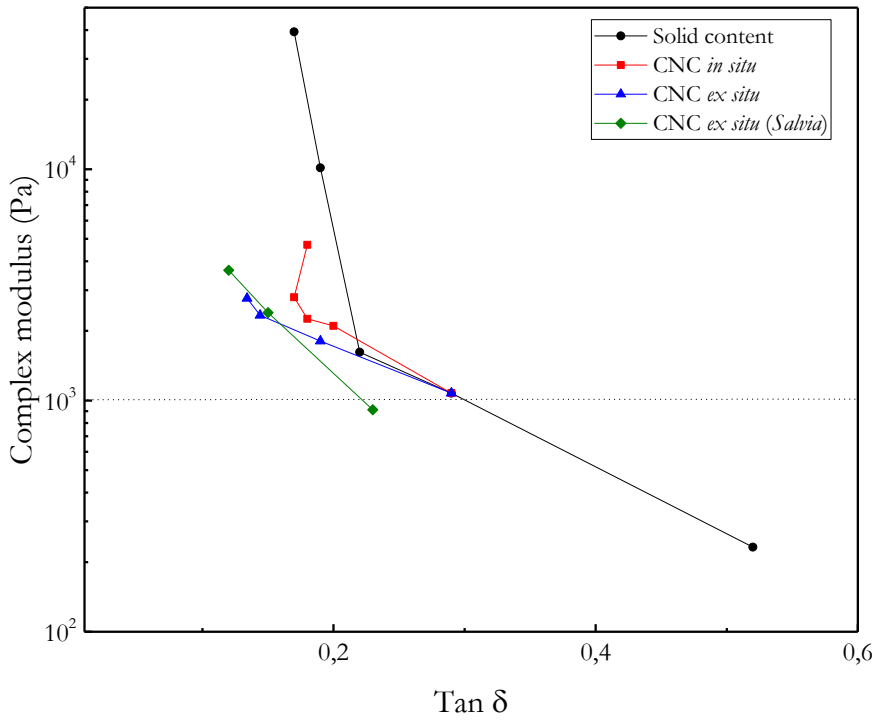

Figure SC.9 Evolution of the different strategies followed in the chapters for the modification of the shape fidelity of the inks. (…) Good shape fidelity downer limit of storage modulus proposed by *Li et al.*

LIST OF TABLES

CHAPTER 1. State of art

CHAPTER 3. Synthesis of waterborne polyurethane urea. Study of the influence of the soft segment composition

CHAPTER 5. *In situ* addition of cellulose nanocrystals to enhance the printing performance of WBPUU based inks

CHAPTER 6. *Ex situ* addition of cellulose nanocrystals to enhance the printing performance of WBPUU based inks

CHAPTER 7. Applications of the printed pieces from PCL/PEG based WBPUU inks via DIW 3D-printing

LIST OF FIGURES

CHAPTER 1. State of art

CHAPTER 2. Materials and methods

CHAPTER 3. Synthesis of waterborne polyurethane urea. Study of the influence of the soft segment composition

CHAPTER 4. Influence of the solid content on the rheology and printing performance of WBPUU hydrogels

CHAPTER 5. *In situ* addition of cellulose nanocrystals to enhance the printing performance of WBPUU based inks

CHAPTER 6. *Ex situ* addition of cellulose nanocrystals to enhance the printing performance of WBPUU based inks

CHAPTER 7. Applications of the printed pieces from PCL/PEG based WBPUU inks via DIW 3D-printing

LIST OF ABBREVIATIONS

WBPU	Waterborne polyurethane
WBPUU	Waterborne polyurethane urea
CNC	Cellulose nanocrystal
CNC_{is}	Cellulose nanocrystal added via *in situ*
CNC_{es}	Cellulose nanocrystal added via *ex situ*
SS	Soft segment
HS	Hard segment
PCL	Polycaprolactone
PEG	Polyethylenglycol
$H_{12}MDI$	4,4'-Dicyclohexyl methane diisocyanate
HDI	1,6-Hexamethylene diisocyanate
IPDI	Isophorone diisocyanate
EG	Ethylene glycol
1,4-BD	1,4-Butanediol
EDA	Ethylene diamine
DMPA	2,2-Bis (hydroxymethyl) propionic acid
MDEA	N-methyldiethanolamine
DABCO	1,4-Diazabicyclo octane
DBTDL	Dibutyltin dilaurate
AM	Additive manufacturing
3D	Three dimensional
SLA	Stereo lithography
FDM	Fused deposition modelling
SLS	Selective laser sintering
3DP	Liquid binding in three-dimensional printing
DIW	Direct ink writing
DED	Direct energy deposition
LOM	Laminated object manufacturing
PCL/PEG	Polycaprolactone/polyethylenglycol

MB	Methylene blue
DLS	Dynamic light scattering
TEM	Transmission electron microscopy
GPC	Gel permeation chromatography
^{1}H NMR	Proton nuclear magnetic resonance
^{13}C NMR	Carbon nuclear magnetic resonance
FTIR	Fourier transform infrared spectroscopy
TGA	Thermogravimetric analysis
DSC	Differential scanning calorimetry
SEM	Scanning electron microscopy
EDS	Energy dispersive X-ray spectroscopy
AFM	Atomic force microscopy
WCA	Water contact angle
E. Coli	*Escherichia coli*
S. Aureus	*Staphylococcus aureus*

LIST OF SYMBOLS

G’	Storage modulus
G”	Loss modulus
Tan δ	Tangent of phase angle
η	Viscosity
σ	Shear stress
$\dot{\gamma}$	Shear rate
σ_y	Yield point
FTI	Flow transition index
K	Consistency index
n	Flow index
$\bar{M}_w$	Weight average molecular mass
T_g	Glass transition temperature
T_m	Melting temperature
ΔH_m	Melting enthalpy
T_0	Initial degradation temperature
T_d	Main degradation temperature
E’	Storage modulus
E”	Loss modulus
E	Young modulus
σ_b	Stress at break
ε_b	Strain at break
W_t	Weight of the sample at time t
W_0	Initial weight of the sample
R	Removal efficiency
C_{24}	Concentration of methylene blue after 24 h
C_0	Initial concentration of methylene blue
σ_{yc}	Stress at the plateau
$\varepsilon_{densification}$	Strain of densification

W_i	Initial plant weight
W_f	Final plant weight
$COOH_{tot}$	Total acid groups content
$Emulsifier_{tot}$	Total emulsifier content
T_gSS	Glass transition of the soft segment
T_mHS	Melting temperature of the hard segment
T_mSS	Melting temperature of the soft segment
ΔHm	Melting enthalpy

List of publications

Authors	J. Vadillo, I. Larraza, A. Arbelaiz, M.A. Corcuera, M. Save, C. Derail, A. Eceiza
Title	Influence of the addition of PEG into PCL-based waterborne polyurethane urea dispersions and films properties
Journal	Journal of Applied Polymer Science
Year	2019
Impact factor	2.520
Rank	32/89 Polymer science (JCR 2019)

Authors	J. Vadillo, I. Larraza, N. Gabilondo, C. Derail, A. Eceiza
Title	Novel solvent-free waterborne polyurethane-urea based ink for extrusion-based 3D printing
Journal	3D Printing & Additive Manufacturing (under revision)
Year	2020
Impact factor	3.579
Rank	16/50 Engineering manufacturing (JCR 2019)

	104/214 Material science multidisciplinary (JCR 2019)
Authors	J. Vadillo, I. Larraza, N. Gabilondo, C. Derail, A. Eceiza
Title	The role of in situ added environmentally friendly cellulose nanocrystals as rheological modulator to improve the printing performance of novel waterborne polyurethane urea based inks for 3D-printing
Journal	Cellulose (submitted)
Year	2020
Impact factor	3.90
Rank	12/89 Polymer science (JCR 2019) 1/21 Material science, paper and wood (JCR 2019) 2/24 Material science, textiles (JCR 2019)

Authors	J. Vadillo, N. Gabilondo, C. Derail, A. Eceiza
Title	Design of shape customized scaffold from waterborne polyurethane urea and environmentally friendly cellulose nanocrystals based ink via 3D-printing
Journal	Under preparation
Year	2021
Impact factor	
Rank	

Authors	J. Vadillo, N. Gabilondo, C. Derail, A. Eceiza
Title	Synthesis of bioactive inks suitable for 3D printing based on waterborne polyurethane urea, cellulose nanocrystals and *Salvia* extract
Journal	Under preparation
Year	2021
Impact factor	
Rank	

List of collaborations

Authors	I. Larraza, J. Vadillo, A. Santamaria-Echart, A. Tejado, M. Azpeitia, E. Vesga, A. Orue, A. Saralegi, A. Arbelaiz, A. Eceiza
Title	The effect of the carboxylation degree on cellulose nanofibers and waterborne polyurethane/cellulose nanofiber nanocomposites properties
Journal	Polymer Degradation and Stability
Year	2020
Impact factor	4.032
Rank	13/89 Polymer science (JCR 2019)

List of communications

Authors	J. Vadillo, I. Larraza, A. Arbelaiz, M.A. Corcuera, M. Save, C. Derail, A. Eceiza

Title	Effect of PCL/PEG ratio on the properties of waterborne poly(urethane-urea) dispersions
Congress	GCNPM2018
Year	2018
Participation	Poster
Place	Kraków

Authors	J. Vadillo
Title	Rheology as a tool to design waterborne polyurethane-urea based bioinks suitable for 3D bioprinting
Congress	II. Jornadas Doctorales de la UPV/EHU
Year	2019
Participation	Poster
Place	Bilbao

Authors	J. Vadillo, I. Larraza, A. Arbelaiz, M.A. Corcuera, M. Save, C. Derail, A. Eceiza
Title	Influence of the molecular weight of poly(ethylene glycol on the properties of PCL/PEG based waterborne polyurethane-urea dispersions
Congress	GCNPM2019
Year	2019
Participation	Poster
Place	Riga

Authors	J. Vadillo, M. Save, A. Eceiza, C. Derail
Title	Study of the correlation between rheological properties and 3D printing

	performance of waterborne polyurethane-urea dispersion
Congress	GCNPM2019
Year	2019
Participation	Oral
Place	Riga

Authors	I. Larraza, J. Vadillo, K. González, A. Saralegi, M.A. Corcuera, A. Arbelaiz, A. Eceiza
Title	Green waterborne polyurethane nanocomposites reinforced with cellulose and graphene synthesis and characterization
Congress	7th International conference on biodegradable and biobased polymers (BIOPOL)
Year	2019
Participation	Poster
Place	Stockholm